University of Sussex

The effects of energy injection into the intergalactic and intracluster media

Owain E. Young

Submitted for the degree of Doctor of Philosophy

University of Sussex

April 2011

Declaration

I hereby declare that this thesis has not been and will not be submitted in whole or in part to another University for the award of any other degree.

Signature:

Owain Young

UNIVERSITY OF SUSSEX

Owain E. Young, Doctor of Philosophy

The effects of energy injection into the intergalactic and intracluster media studied through numerical simulations

Summary

This thesis presents the Millennium Gas suite of simulations - the largest cosmological hydrodynamical simulations to date - and examines the effects of different prescriptions for energy injection and radiative cooling on populations of galaxy clusters. We conclude that the differences between populations of clusters generated by a simulation with an epoch of preheating, and one with a continual injection of energy (feedback), are minimal at the present day (both in good agreement with observations), but that the evolution of the two populations of clusters differs. High redshift observations of cluster gas fractions suggest that continual energy injection is the preferred method.

We examine possible causes of scatter in the cluster gas fraction, but are unable to determine a cause, or combination of causes, of this scatter.

We combine the previously used feedback prescription with the same radiative cooling prescription as was used in the preheating simulation. Although the bimodality is not as clear as in observations, this model produces a sample containing both cool core and non-cool core clusters.

Acknowledgements

This thesis would not have been possible without the help of a great many people, most of whom I will now endeavour to list in an order that seems fitting.

I would like to thank all members of the Sussex Astronomy Centre, but in particular my supervisor - Peter Thomas - for his invaluable guidance, insight and patience throughout my time here; and Chris Short for all his help in modifying Gadget-2 routines and in numerous other areas.

The simulations upon which this thesis is based were run on machines at Durham and Nottingham. I would therefore like to thank Lydia Heck, for her help with COSMA (Durham); and Frazer Pearce for providing data from two Millennium Gas simulations, and computational resources at Nottingham. I would also like to thank Scott Kay for providing the software for reducing the simulated data, and Adrian Jenkins for his initial conditions code.

I am very grateful to those whose observational data I have used for comparison: Steve Allen, Stefano Andreon, Gabriel Pratt, Alistair Sanderson, Alexey Vikhlinin, and particularly Ben Maughan, whose data allowed the comparisons which underpin chapter 4. Without these data, the quality of this thesis would have been greatly reduced.

I would like to thank my parents for their emotional (and financial) support throughout my education, as well as for their proof-reading efforts.

This thesis has been made possible by the funding I received from the Science and Technology Facilities Council.

Contents

List of Tables

List of Figures

Chapter 1

Introduction

1.1 Galaxy clusters

Galaxy clusters are the largest observed, virialised structures in the Universe and, as such, they are extremely useful as cosmological probes. Their mass is typically of the order $\sim 10^{15}\mathrm{M}_{\odot}$, of which the largest component ($\sim 85\%$) is dark matter. The remainder of the mass is the visible, baryonic matter. Most of this ($\sim 90\%$) is in the form of hot gas, with the actual galaxies occupying only $\sim 10\%$ of the baryonic matter (about 1.5% of the total cluster mass - perhaps they aren't well named!). Due to their large masses, the virial temperature of the intracluster medium (ICM) is $\sim 10^7 - 10^8\mathrm{K}$ ($\sim 1 - 8\mathrm{keV}$). Figure 1.1 shows a composite image of a typical galaxy cluster.

Galaxy clusters condense at peaks in the primordial density field through gravitational collapse (e.g. van Albada 1961). This happens in a roughly spherical region of approximately 10 Mpc in diameter. The cosmic baryons within this volume then follow the dynamically-dominant dark matter as it collapses. As the nascent cluster virialises, the baryons trapped in its potential well are heated and form an optically thin, hot, X-ray emitting gas.

1.1.1 Why study clusters?

Since they are the largest virialised objects in the Universe, clusters may be used to study the high mass end of the dark matter halo[1] mass function. Their evolution is highly sensitive to the cosmological parameters, particularly the mean amplitude of mass fluctuations in a sphere of eight comoving megaparsecs, σ_8. They are sensitive probes of dark matter and provide constraints of modified gravity models. This is possible due

[1] A halo being a gravitationally bound clump of dark matter

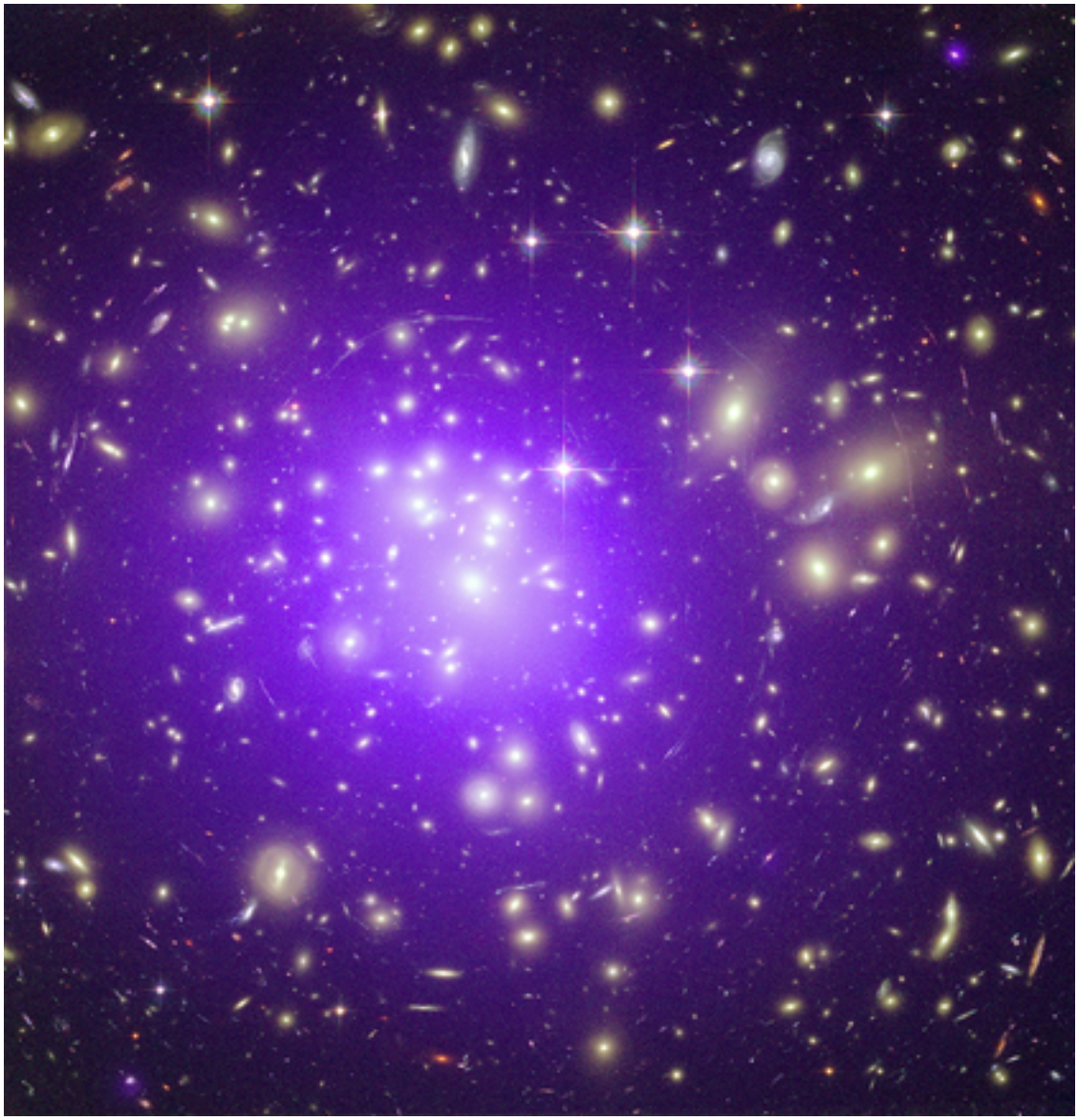

Figure 1.1: A composite image of the galaxy cluster Abell 1689 from the *Chandra* observatory. The galaxies themselves are from optical images, whilst the blue represents X-ray emission from the hot cluster gas

to reliable X-ray mass proxies being developed, notably gas mass (although, as discussed in chapter 4, gas mass may not be a reliable proxy) and, more recently $Y_X \equiv M_{gas}T_X$ (Kravtsov et al., 2006; Maughan, 2007), since this is thought to more closely approximate the thermal energy of the ICM and is not affected as much by cluster-cluster interactions (Poole et al., 2007).

Because of the way in which galaxy clusters form (as well as their large size) they can be thought of as 'snapshots' of the Universe as a whole at the time of their formation. They preserve their density ($\sim$ 200 times the Universe's mean density) and composition, whilst their surroundings are allowed to cool and diffuse. Galaxy clusters represent the bridge between astrophysics and cosmology. Their dynamical properties are principally governed by gravity, but astrophysical processes taking place on the much smaller, galactic, scales still leave an imprint on the diffuse gas which makes up the ICM (e.g. Böhringer and Werner 2010). This dependence on the physics of baryonic matter makes modelling far more complicated.

1.1.2 Observing galaxy clusters

Galaxy clusters were observed (in optical wavebands) as early as the 18th century when Messier (1784) and Herschel (1785) observed collections of galaxies in the regions of the Virgo and Coma constellations (the Virgo and Coma clusters), but it wasn't until the mid twentieth century that the definitive catalogue of Abell (1958, and later Abell et al. 1989) was published. These catalogues contain most of the currently known local clusters, made up of the accumulated observations from nearly 200 years.

Abell's classification method was somewhat arcane. Recognising that apparently neighbouring galaxies could in fact, have a large line of sight separation, he firstly estimated the distance to a cluster candidate by the apparent brightness of its tenth brightest member galaxy, then counting all galaxies within a fixed radius ($\sim$ 2Mpc for all cluster candidates) and less than two magnitudes fainter than the third brightest member galaxy. Finally, he would subtract a mean background count of galaxies. Modern cluster identification techniques make use of refined versions of the Abell method (e.g. Carballo et al. 1995, Bade et al. 1998), with some making use of colour information for cluster candidates (e.g. Gladders and Yee, 2000). Due to cluster galaxies having no star formation, they are typically redder than non-cluster galaxies at similar redshifts. Colour information is especially important for distant galaxy clusters for which the background counts may be much higher than for nearer objects (Gladders et al., 1998). After the galaxies for a cluster candidate

have been found there are two more optical techniques which may be applied to determine if they actually constitute a cluster. Their orbital velocities can be measured, and lensing effects on background clusters may be observed. These measurements indicate the amount of dark matter present in the cluster.

Although they were originally observed in the optical, many cluster observations are now carried out in the X-ray band, since this is the band in which most of the baryonic mass of the cluster emits. Diffuse gas (the electron number density of which varies from $\sim 10^{-4}\text{cm}^{-3}$ in a cluster's outskirts to $\sim 10^{-2}\text{cm}^{-3}$ in the centre), making up the majority of the baryonic matter in galaxy clusters, would normally be difficult to detect, but the large gravitational potential wells associated with galaxy clusters are able to compress this gas and raise its temperature up to 10^8K ($\sim$ 15keV), when it emits in X-rays via thermal Bremsstrahlung (which dominates the emission from clusters with temperatures above $\sim$ 2keV). Thus, the temperature of this gas may be used as a proxy for the depth of the cluster's potential well and therefore its mass ($kT \propto GM/r$).

That galaxy clusters are observable via X-rays was first noted by Felten et al. (1966) via observations of the already optically observed Coma cluster when he noticed an excess of X-ray flux in this region. Similar observations were soon made by Byram et al. (1966) and Bradt et al. (1968), but it was Cavaliere et al. (1971) who first suggested that these X-ray sources and corresponding "associations of galaxies" were linked.

Whilst detailed observations of small numbers of clusters are important for the study of astrophysical processes in clusters, in order to use clusters of cosmology (as well as to study cluster formation and evolution) data for large numbers of clusters are required. To this end, large surveys have been carried out using the instruments on XMM-*Newton* (Jansen et al., 2001; Lloyd-Davies et al., 2010) and *Chandra* (Weisskopf et al., 2002), X-ray telescopes which have been able to gather data for very large numbers of clusters. Future surveys, such as *eRosita* (Predehl et al., 2006) aim to study large numbers of clusters in sufficient detail to study the astrophysical processes therein, as well as to study the properties of the population as a whole.

X-ray observations have shown that there are two distinct populations of galaxy clusters: cool core clusters, and non-cool core clusters. Cool core clusters, as their name suggests, have a core containing cold, dense gas which leads to much of their emission coming from the core region with correspondingly steeper entropy profiles (see figure 1.2).

It is believed that cool core clusters are relaxed objects (e.g. Allen et al., 2008), whereas

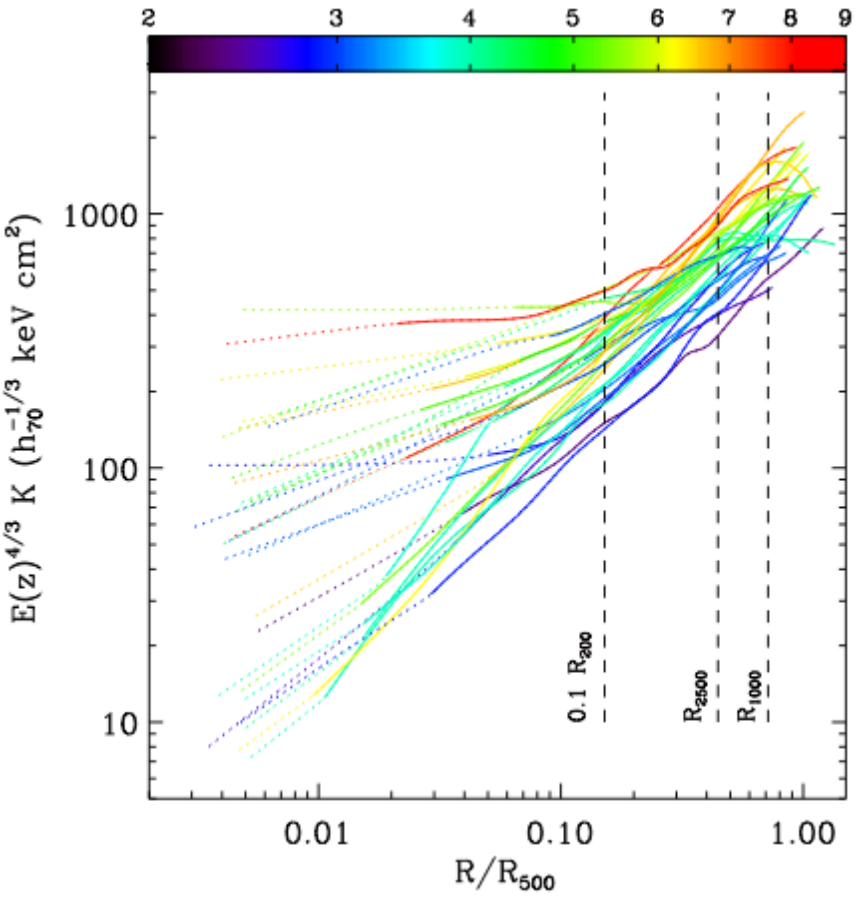

Figure 1.2: Entropy profiles from the REXCESS sample in Pratt et al. (2009a). The lines are colour coded according to spectroscopic temperature. The solid lines show the profiles as derived from direct measurement and the dotted lines show the extrapolations into the central regions assuming an isothermal distribution at the temperature of the innermost data point

non-cool core clusters have been recently disturbed, however the lack of a bimodal cluster population in any cosmological simulations has limited investigation into this area.

Whilst optical and X-ray observations form the backbone of cluster observation, there are two further methods worthy of discussion: gravitational lensing and the Sunyaev-Zel'dovich effect.

The hot gas in galaxy clusters can be indirectly seen in the cosmic microwave background. As CMB photons move through the cluster they can Compton scatter off the much hotter intracluster gas. This can be seen and is referred to as the Sunyaev-Zel'dovich effect (Sunyaev and Zel'dovich, 1970). The Sunyaev-Zel'dovich effect has a huge advantage over studying clusters by more conventional means since it is independent of redshift.

Since galaxy clusters are so massive they warp the space around them. This effect is large enough to be detected as so-called *lensing measurements* and gives another method for cluster detection. In contrast to other cluster detection methods, gravitational lensing measurements rely on the clusters' dark matter components; thus it is possible to observe the behaviour of the dark matter (to some extent) without the baryonic component. This is particularly noticeable in observations of the Bullet Cluster (Markevitch et al., 2004).

Cluster mass estimates

In order to determine the cluster mass function, it is necessary to accurately measure the masses of galaxy clusters. For nearby clusters this is possible by assuming the ICM is in hydrostatic equilibrium and by determining the clusters' gas density and temperature profiles (the data provided by *Chandra* and *XMM-Newton* has allowed this to be done for many nearby clusters), but producing profiles of a sufficient quality for distant clusters requires long observation times, so there are few high redshift clusters with hydrostatic mass estimates.

Where hydrostatic mass estimates are unavailable, cluster masses may be inferred from the relationships between clusters' observable X-ray properties and their total mass (such as those described in section 2.2.3). However, real clusters have been observed to have an excess of entropy in their cores (Ponman et al., 1999; Lloyd-Davies et al., 2000; Finoguenov et al., 2002), which prevents their gas being compressed to high densities and reduces their X-ray luminosity when compared to the self-similar relation. This causes a departure from self similarity; most notably a steepening of the $L_X - M$ relation (Reiprich and Böhringer, 2002; Chen et al., 2007; Vikhlinin et al., 2009; Pratt et al., 2009b) and of the $L_X - T$ relation (Arnaud and Evrard, 1999; Wu et al., 1999; Ettori et al., 2002; Pratt

et al., 2009b).

Unfortunately use of these relations for determining cluster mass has its limitations. There is an intrinsic scatter in these relations and, at present, it is not possible to determine whether a cluster lies above, below, or on the mean relation which can cause its mass to be over or under-estimated. Scatter in relations involving L_X is principally caused by the dense, high luminosity cores of cool core clusters (O'Hara et al., 2006; Chen et al., 2007, for example), although this has successfully been reduced by removing the core regions from the luminosity measurements (Maughan, 2007, for example). Cluster mergers also cause an increase in scatter. Whilst mergers cause the temperature and luminosity of the cluster to be raised, moving them along the $L_X - T$ relation, they also cause clusters to move off the $T - M$ relation (Rowley et al., 2004; Kravtsov et al., 2006; Hartley et al., 2008).

However, $Y_X \equiv M_{gas}T_X$ is very tightly correlated with total cluster mass and appears to be insensitive to cluster mergers. Simulations of Poole et al. (2007) and observations of Arnaud et al. (2007); Maughan (2007); Vikhlinin et al. (2009) confirm that Y_X is a reliable total mass estimate.

Since these scaling relations can be used to determine masses for clusters for which the X-ray data is insufficient for hydrostatic mass estimates, it is important to calibrate them over a large range of redshifts. This would lead to an improvement in our knowledge of the cluster mass function, and therefore the cosmological parameters deduced therefrom, and it should also (when compared to cosmological simulations) lead to a greater understanding of the non-gravitational heating processes.

Low redshift clusters have fairly well calibrated scaling relations (Maughan, 2007, although there seems to be a difference in the scalings for relaxed and unrelaxed clusters), since they also have hydrostatic mass estimates, but scaling relations for distant redshifts are difficult to come by.

1.1.3 Simulating Galaxy Clusters

Simple, linear equations can be readily integrated analytically, so the evolution of systems governed by such equations is simple and quick to study; as are certain special non-linear systems. However, most systems are governed by non-linear equations for which an analytical approach is impossible. In such cases simulations are performed to numerically solve the equations governing the evolution of a system from a defined starting point, until the desired length of time has passed.

Observations of galaxy clusters can give us a great deal of insight, but the dynamical times of such large objects are so long that we are only ever able to see a given cluster at a single instant in its lifetime. In order to understand how they evolve and how they became as they are today, a theoretical approach is required

Galaxy clusters are thought to form via a hierarchical process in which small objects collapse first, but merge with others to form larger and larger objects (Peebles, 1983). Clusters must have, therefore, undergone many of these small mergers throughout their lives in order to grow to the size they are today, each of which will have affected the intracluster medium by inducing shocks and turbulence, as well as affecting a cluster's magnetic field. This whole process is highly non-linear so, in order to study it, we need to make use of large simulations.

The first numerical simulations of galaxy clusters sought to examine the stability and relaxation times of these objects. They typically used a few hundred particles and the only force considered was gravity (Aarseth, 1963; Hénon, 1964; Peebles, 1970; White, 1976). Halos extracted from such simulations were found to have global properties similar to those of the Coma cluster.

As computational techniques advanced, along with the power of computers themselves, simulations started to be performed which could produce haloes containing several thousand particles (e.g. Frenk et al. 1985, Davis et al. 1985) as well as simulations of cosmological volumes (Quinn et al., 1986). These simulations, however, as well as even larger ones containing hundreds of thousands of particles (Tormen et al. 1997, for example) were unable to resolve substructures within haloes, but did provide insight into their accretion history and a power law slope in the density profile was proposed (Warren et al., 1992).

The density profile was further examined by Navarro et al. (1997), who produced a population of haloes, in a cosmological volume, across a large mass range which were then resimulated at a higher resolution. They found that haloes across the whole mass range followed the same density profile (the NFW profile).

Perhaps the pinnacle of N-body simulations was the Millennium Simulation (MS, Springel et al. 2005). This was carried out in a cosmological volume and had an unparalleled resolution such that it was able to resolve not only clusters, but galaxy sized haloes as well.

Most simulations up until the mid-nineties had been N-body simulations in which the only force acting on the particles was gravity. Simulations of this nature are referred to as dark matter simulations, since dark matter interacts only gravitationally. However,

as computational resources continued to increase, large scale simulations examining the effects of the interactions between baryons started to be considered. Baryons, as well as interacting via gravity, also interact with other baryons via hydrodynamic forces and the computational resources required to compute such forces are greater (per particle) than those required for gravity-only computations.

When baryons are included, the additional cluster properties which can be readily determined allow a much better comparison with observations to be made, as well as allowing the study of cluster properties not derivable from dark matter only simulations (baryon fraction, for example).

Hydrodynamical simulations with no additional heating or cooling processes have been shown to reproduce the cluster scaling relations expected for a self-similarly scaled cluster population (e.g. Navarro et al. 1995), but fail to reproduce observed cluster scaling relations.

In order to rectify this, much work has been carried out examining the effects of different heating and cooling processes on scaling relations and on cluster profiles. Radiative cooling has been examined as a mechanism to better reproduce the observed scaling relations (Pearce et al., 2000; Muanwong et al., 2001; Motl et al., 2004; Viola et al., 2007), but alone, radiative cooling fails as, although it steepens the density profiles, creating an entropy excess (when cold gas forms into stars in a cluster's centre and higher entropy gas flows in) and raising the cluster's temperature, it causes too much star formation to occur within the clusters.

To reconcile the negative effects of radiative cooling additional heating processes have been proposed such as the preheating of the gas at a high redshift (e.g. Muanwong et al., 2002; Viana et al., 2003) and a continual injection of energy from star formation and active galactic nuclei (Ettori et al., 2006; Muanwong et al., 2006; Kay et al., 2007). These schemes have both had success in reproducing low redshift cluster scaling relations and profiles, but they produce different predictions for the behaviour of both scaling relations and profiles with redshift. Neither correctly reproduces the observed stellar fractions.

Understanding, and making better models of the cooling, preheating and feedback processes will be important to future simulations of galaxy clusters. Hopefully these will lead to simulations that fit observational data more closely, particularly at high redshift and in the cores of clusters.

1.2 This thesis

This thesis describes the Millennium Gas cosmological simulations - a suite of simulations carried out in the same volume as the Millennium Simulation, but including a baryonic matter component and being performed with a variety of different prescriptions for energy injection and radiative cooling. These are the largest cosmological hydrodynamic simulations yet performed.

Chapter 2 gives an overview of our current understanding of cosmology and structure formation, together with an overview of the methods used to run cosmological simulations.

Chapter 3 introduces the Millennium Gas simulations, details the different physical processes included in each of them, and compares the scaling relations and profiles of clusters generated therein with observations, both at low and high redshift.

Chapter 4 examines the baryon fractions in MG clusters in detail, compares them with observations, defines the cluster gas fraction as a function of cluster mass and redshift, and suggests a preferred model for the evolution of the cluster baryon fraction.

Chapter 5 examines the scatter about the baryon fraction-mass relation and attempts to understand it in terms of other global cluster properties.

Chapter 6 presents a model for reconciling the feedback prescription used in the MG simulations with radiative cooling, together with results from this model and a comparison of them with cluster observations.

Chapter 2

Theory

This chapter describes, in some detail, the principles, concepts and methods which will underpin the rest of the chapters in this thesis. It outlines the current best understanding of the theory of cosmology and structure formation, current techniques employed in cosmological simulations, and the additional physical processes which simulations must include to better reproduce cluster observations.

2.1 Cosmology

Modern cosmology is based on the cosmological principle: on large scales ($> 100h^{-1}$Mpc), the Universe is both homogeneous and isotropic. This is an extension of the Copernican principle and means that, wherever you are in the Universe, it will look the same as if you are anywhere else, and it will look the same in each direction. Observations show us that the cosmological principle is, at worst, a good approximation to the observable region of the Universe we inhabit.

The Wilkinson Microwave Anisotropy Probe (WMAP) results (figure 2.1) show us that at early times, the Universe was homogeneous to the order of one part in 10^{-5}.

In general relativity, the evolution of spacetime under gravity can be written as a metric, the general form of which is given in equation 2.1

$$\mathrm{d}s^2 = g_{\alpha\beta}\mathrm{d}x^{\alpha}\mathrm{d}y^{\beta} \tag{2.1}$$

where x are the coordinates of events in spacetime, $\alpha, \beta = 0, 1, 2, 3$ and 0 is the temporal dimension and 1, 2 and 3 are the spatial dimensions. Under the assumption that the Universe is homogeneous and isotropic, it can be described by the specific form of the

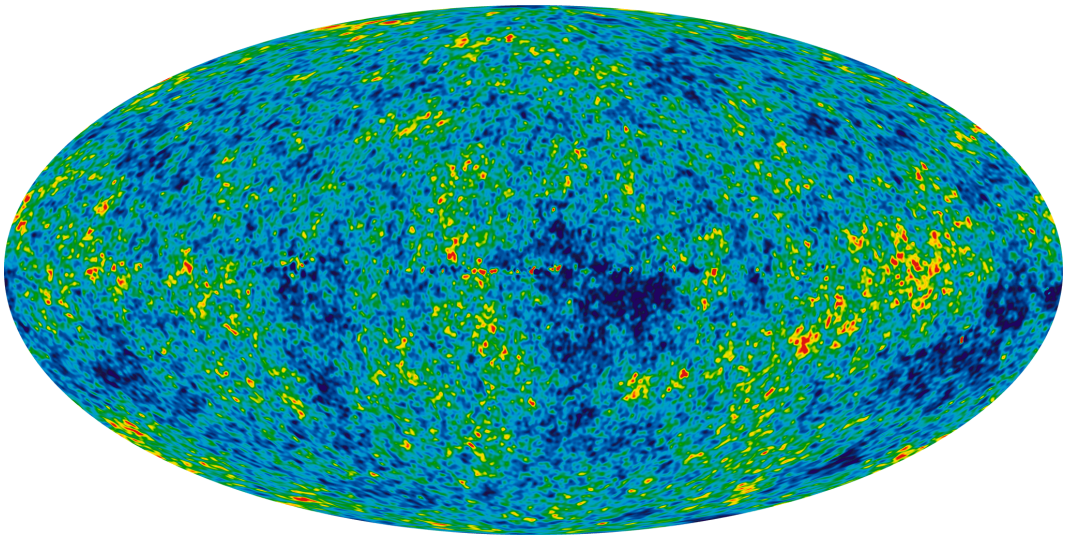

Figure 2.1: The 7 year WMAP full sky map. This is a weighted linear combination of the five WMAP frequency maps, adjusted so as to remove the contribution from our galaxy. The colours represent temperature anisotropies with dark blue indicating regions below the mean temperature and yellow and red regions representing regions above the mean temperature.

metric known as the Friedman-Robertson-Walker-Lemaitre metric:

$$\mathrm{d}s^2 = (c\mathrm{d}t)^2 - a(t)^2 \left[\frac{\mathrm{d}r^2}{1 - kr^2} + r^2(\mathrm{d}\theta^2 + \sin^2\theta \mathrm{d}\phi^2) \right] \tag{2.2}$$

where t is the proper time and c is the speed of light in a vacuum

$a(t)$ and K in equation 2.2 are the *scale factor* and the *curvature* and they are both of huge importance in cosmology.

The curvature describes the geometry of the Universe. In a universe without a cosmological constant, if it is negative, the Universe is said to be open and it will continue to expand indefinitely; if the curvature is zero, the Universe is flat and it will asymptotically approach zero expansion rate at infinite time; and if the curvature is positive the Universe will cease to expand and collapse back on itself. The curvature is closely related to the density of the Universe by equation 2.8.

When the Universe is treated as a perfect fluid (Weinberg, 1972) and using the metric in equation 2.2, the Einstein equations can be reduced to the *Friedman equation*:

$$\frac{\dot{a}^2}{a^2} = \frac{8\pi G\rho}{3} - \frac{kc^2}{a^2} + \frac{\Lambda c^2}{3} \tag{2.3}$$

and the *acceleration equation*:

$$\frac{\ddot{a}}{a} = -\frac{4\pi G}{3}\left(\rho + \frac{3p}{c^2}\right) + \frac{\Lambda c^2}{3} \tag{2.4}$$

where ρ is the density of matter in the universe, G is the *gravitational constant* Λ is the *cosmological constant* and a dot denotes a derivative with respect to time. Originally introduced in order to allow for a static universe, the cosmological constant is responsible for the accelerated expansion we see today.

Equation 2.3 is used to determine the *Hubble parameter*[1]:

$$H(t) = \frac{\dot{a}}{a} \tag{2.5}$$

which describes the local rate of expansion, or the *Hubble flow*.
The *Hubble constant*, H_0, is defined from equation 2.5 as the Hubble parameter *today* ($z = 0$), the current best value for which is $73 \pm 3\text{km s}^{-1}\text{Mpc}^{-1}$ (Spergel et al., 2007).

The Hubble constant is often expressed in terms of the dimensionless quantity h which is defined as $H_0 \equiv h\ 100\text{km s}^{-1}\text{Mpc}^{-1}$. This quantity will be used extensively throughout this thesis.

If one is to ignore the cosmological constant, it is simple to use equation 2.3 to determine the density required to cause the universe to have no curvature:

$$\rho_c(t) = \frac{3H^2}{8\pi G} \tag{2.6}$$

This is known as the critical density and today, $\rho_c(t_0) = 2.78\ h^{-1} \times 10^{11}\text{M}_\odot(h^{-1}\text{Mpc})^{-3}$.

The critical density can now be used to define the *density parameter* Ω:

$$\Omega(t) \equiv \frac{\rho}{\rho_c} \tag{2.7}$$

This definition can then be used in equation 2.3 to see the relationship between the density of the universe and its geometry:

$$\Omega - 1 = \frac{kc^2}{a^2H^2} \tag{2.8}$$

In a universe with a cosmological constant, Ω is split into two parts: $\Omega_m \equiv \rho_m/\rho_c$ and $\Omega_\Lambda \equiv \rho_\Lambda/\rho_c$ where the subscripts, m and Λ denote the matter and cosmological constant densities - $\Omega_\Lambda + \Omega_m = \Omega$.

The currently accepted paradigm for the Universe is the ΛCDM or concordance cosmology. In this paradigm, the Universe has a cosmological constant (Λ), and $\Omega = 1$ (it is flat). Most of the matter density is, however, in the form of *dark matter,* specifically **C**old **D**ark **M**atter, with only a small fraction of the matter density being composed of visible matter (baryons).

[1] from Hubble's law $\boldsymbol{v} = H_0\boldsymbol{r}$ where $\boldsymbol{v}$ and $\boldsymbol{r}$ are the recessional velocity and distance of a galaxy respectively

Table 2.1: The current best values for the ΛCDM parameters as measured with the *WMAP* seven year data in Larson et al. (2011)

Parameter	Value
t_0	$13.77 \pm 0.13 \times 10^9$yr
H_0	70.4 ± 2.5km s^{-1}Mpc^{-1}
Ω_m	0.273 ± 0.013
Ω_Λ	$0.727^{+0.030}_{-0.029}$
$\Omega_b{}^2$	0.0455 ± 0.0028
Ω	$1.0050^{+0.0060}_{-0.0061}$

The values for the cosmological parameters discussed above in ΛCDM are given in table 2.1. All these values are the best values from the five-year WMAP data (Hinshaw et al., 2009).

2.1.1 Redshift

Since the Universe is expanding, all objects at distances sufficient that the Universe's expansion is the primary driver of their motion, are moving away from us. The upshot of this is that the light reaching us from all these objects is shifted towards longer wavelengths. Since this corresponds to light moving towards the red end of the spectrum, this effect is known as *redshift*. Usually denoted by the letter z, in the non-relativistic regime[3], it can be written as

$$z = v/c \tag{2.9}$$

where v is the object's recessional velocity.

When distant objects have no peculiar velocity (no deviations from the Hubble flow) then 2.9 can be rewritten as $z = H_0 d/c$ where d is the object's distance. Redshift has a twofold meaning; an object's redshift is both the distance to said object, and a measure of the expansion factor of the Universe at the time the observed light left the object.

2.1.2 Cosmological Distance Measures

In addition to redshift, there are only two other practical methods for determining the distances to objects outside our galaxy. If an object's absolute luminosity is known, then it can be compared to its observed luminosity; likewise if the object's actual diameter

[3] A relativistic version is $1 + z = \sqrt{\frac{1+v/c}{1-v/c}}$

is known then that can be compared to the measured angular diameter. However, these observed distances and luminosities are dependent on cosmological parameters. For nearby objects (closer than 300Mpc), distances may also be estimated by measuring the parallax - the apparent shift in the object's position in the sky caused by the orbit of the Earth.

The ratio of an object's actual diameter to its observed angular diameter (in radians) is termed the *angular diameter distance,* D_L. Likewise the relationship between an object's bolometric (integrated over all frequencies) luminosity, L, and flux, F, is termed the *luminosity distance.*

These two quantities are closely related to the *comoving distance.* The distance between two nearby objects (with no peculiar velocities) which remains constant with epoch gives a small comoving distance, δD_C. The comoving distance for an object at redshift z is then the integral over all these δD_Cs (Hogg, 1999):

$$D_C = D_H \int_0^z \frac{dz'}{E(z')} \tag{2.10}$$

where D_H is the *Hubble distance* [4], $E(z) = \sqrt{\Omega_M(1+z)^3 + \Omega_k(1+z)^2 + \Omega_\Lambda}$ (Peebles, 1993) and

$$E(z) \equiv \frac{H(z)}{H_0} \tag{2.11}$$

If the Universe is flat, the comoving distance is equivalent to the proper motion distance, D_M, but if the Universe has any curvature this affects D_M. Current measurements suggest that the Universe has zero curvature, so the rest of this thesis will concern only that case.

The proper motion distance can be used to determine the angular diameter distance (the ratio of an object's transverse physical size to its angular size) and the luminosity distance (the relationship between an object's bolometric flux, S, and bolometric luminosity, L, as defined in equation 2.13) as given in equations 2.12 and 2.14.

$$D_A = \frac{D_M}{1+z} \tag{2.12}$$

$$D_L \equiv \sqrt{\frac{L}{4\pi S}} \tag{2.13}$$

$$D_L = (1+z)D_M = (1+z)^2 D_A \tag{2.14}$$

The relationship between these distance measures in the Millennium Gas cosmology can be seen in figure 2.2.

[4] $D_H \equiv c/H_0$

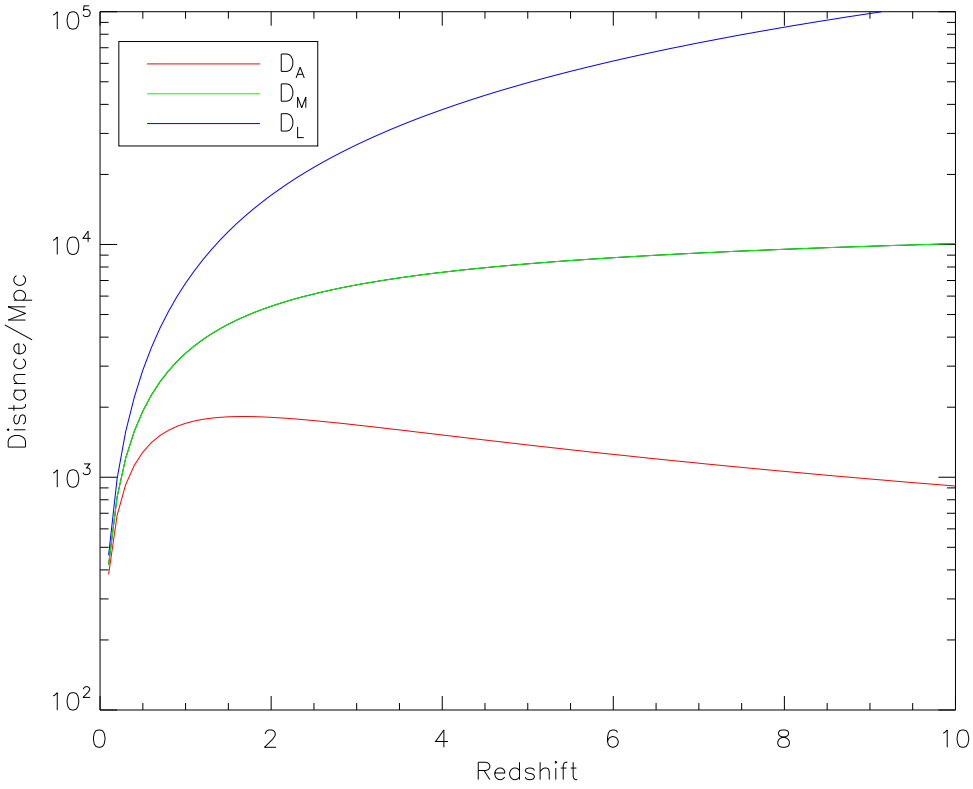

Figure 2.2: Three different distance measures as a function of redshift for a flat Universe with $\Omega_M = 0.25$ and $\Omega_\Lambda = 0.75$, as used in the Millennium Gas simulations

2.2 Structure formation

It was stated above that galaxy clusters form at peaks in the primordial density distribution. This section will begin to justify this statement by explaining the initial formation of galaxy clusters in terms of linear perturbation theory. This is a valid approach when studying the beginnings of cluster formation, before the non-linear effects become too pronounced and it is necessary to use numerical methods.

The primordial density field was largely homogeneous, however there were tiny perturbations. These perturbations were then magnified by the effects of a period of accelerated expansion and, if they were sufficiently massive, could posses a gravitational field of sufficient strength to maintain the density of the perturbation against the subsequent expansion of the Universe. Such perturbations will then be able to collapse through gravitational instability and go on to become the first collapsed objects.

The magnitude of these perturbations can be described by the density contrast, δ:

$$\delta(\mathbf{x}, a) \equiv \frac{\rho(\mathbf{x}, a) - \bar{\rho}(a)}{\bar{\rho}(a)} \tag{2.15}$$

where $\rho(\mathbf{x}, a)$ is the density of the Universe at a point $\mathbf{x}$ and when the scale factor is a and $\bar{\rho}(a)$ is the mean density of the Universe at the same time.

It is now necessary to describe the components of the Universe mathematically. If it is supposed that the Universe is filled with a non-relativistic fluid and a gravitational field (with small perturbations) then it can be described by the continuity equation:

$$\frac{\partial \rho}{\partial t} + \nabla \cdot (\rho \mathbf{v}) = 0 \tag{2.16}$$

the Euler equation:

$$\frac{\partial \mathbf{v}}{\partial t} + (\mathbf{v} \cdot \nabla)\mathbf{v} = -\frac{1}{\rho}\nabla p + \nabla \Phi \tag{2.17}$$

and the Poisson equation for a gravitational field:

$$\nabla^2 \Phi = 4\pi G \rho \tag{2.18}$$

where ρ and p are the density and pressure of the fluid and $\mathbf{g}$ is the gravitational field.

If δ is assumed to be small the approximation $\rho = \rho_0 + \delta\rho$ may be made, where ρ_0 is the underlying, homogeneous density field.

Equations 2.16, 2.17 and 2.18 can be expanded under the above approximation and the higher terms ignored. If δ is supposed to be a plane-wave disturbance, $\delta \propto e^{-i\mathbf{k}.\mathbf{r}}$ (where $\mathbf{k}$ is the comoving wavevector) the gravitational amplification of the density fluctuation may be written as (Peacock, 1999):

$$\ddot{\delta} + 2\frac{\dot{a}}{a}\dot{\delta} = \left(4\pi G\rho_0 - \frac{c_s^2 k^2}{a^2}\right)\delta \tag{2.19}$$

where c_s is the sound speed and depends on the equation of state for the Universe.

The length scale indicating the regime in which gravity prevails over pressure[5] is known as the Jeans length (equation 2.20, Jeans 1902).

$$R_J = c_s\sqrt{\frac{\pi}{G\rho_b}} \tag{2.20}$$

The mass enclosed by the Jeans length is known as the Jeans mass (equation 2.21) and this is an important quantity since only objects with a mass greater than the Jeans mass may collapse to form structures.

$$M_J = \frac{4\pi}{3}\rho R_J^3 \tag{2.21}$$

Thus, combining the equations of mass and momentum conservation with the Poisson equation for a gravitational field lets us analytically follow the evolution of perturbations, provided the fluctuations are sufficiently small and we can make the approximation $\rho = \rho_0 + \delta\rho$ (neglecting higher order terms).

2.2.1 The power spectrum

The power spectrum gives the size of the effect that perturbations have on the density field on different scales. This is strongly correlated with the degree of clustering in the Universe.

The power spectrum is defined from the Fourier transform of a linear density field

$$\delta_{\mathbf{k}} = \frac{1}{V}\int \mathrm{d}^3x\delta(\mathbf{x})e^{i\mathbf{k}.\mathbf{x}} \tag{2.22}$$

where $\delta(\mathbf{x}) = \rho(\mathbf{x})/\rho_0 - 1$ again. The power spectrum is then defined as:

$$P(k) = |\delta_{\mathbf{k}}|^2 \tag{2.23}$$

for all $|\mathbf{k}|$ between k and $k + \delta k$.

If we introduce the smoothed variance:

$$\sigma(M) \equiv \langle(\delta M/M)^2\rangle^{1/2} \tag{2.24}$$

where $M = V\rho_0$, it can be shown that

$$\sigma_n^2 \equiv \frac{V}{(2\pi)^3}\int P(k)|f_k|^2 k^{2n}\mathrm{d}^3k \tag{2.25}$$

[5] or rather the effective pressure caused by the Universe's expansion

The power spectrum defines the effect that perturbations of different scales have on the underlying density field and in its most simple form is a featureless power law:

$$|\delta_{\mathbf{k}}|^2 \propto k^n \tag{2.26}$$

An important cosmological parameter when it comes to cluster formation is σ_8, the amplitude of the linear power spectrum on the scale of 8 h^{-1} Mpc. This particular scale is chosen since a sphere of that radius contains roughly the amount of matter required to build a cluster.

In ΛCDM, structures form hierarchically with the largest objects forming last through a succession of mergers of smaller objects. Galaxy clusters are therefore dynamically young objects and are seldom seen in an unperturbed state. Because of this they are very difficult to treat analytically.

Whilst mature clusters are impossible to describe analytically for reasons mentioned above, at early times, when the size of the density fluctuations is very small, it is possible to analytically describe their behaviour.

2.2.2 Spherical collapse

A very useful analytical model for a forming cluster is the spherical overdensity model, in which the nascent cluster is approximated as a spherical overdense region of the Universe.

This configuration, when it has a radius R and an overdensity $\bar{\delta}$ leads, via Birkhoff's theorem to equation 2.27

$$\frac{\mathrm{d}^2R}{\mathrm{d}t^2} = -\frac{GM}{R^2} = -\frac{4\pi G}{3}\rho_0(1+\bar{\delta})R \tag{2.27}$$

A comparison of equation 2.27 with equation 2.4 suggests that this perturbation evolves as a closed Einstein-de Sitter universe of higher density than its containing universe.

The linear approximation breaks down when δ becomes too large. There are two interesting stages which occur after δ becomes large. The first of these is turnaround. This happens when the sphere breaks away from the general expansion of the Universe and reaches its maximum radius. The time at which this happens and the perturbation's radius can be calculated. The first integral of motion of equation 2.27 gives equation 2.28

$$\frac{1}{2}\left(\frac{\mathrm{d}R}{\mathrm{d}t}\right)^2 - \frac{GM}{R} = E \tag{2.28}$$

where E being less than zero means that the perturbation is bound (analogous to k in the Friedmann equation) and obeys equation 2.29

$$\frac{R}{R_{tr}} = \frac{1}{2}(1-\cos\theta), \frac{t}{t_{tr}} = (\theta - \sin\theta)/\pi \tag{2.29}$$

where R_{tr} and t_{tr} are the radius and time at turnaround.

The second stage is virialisation. After turnaround, the cluster will attempt to collapse into a singularity. This cannot happen since the kinetic energy of the collapse will instead get converted into random motions and the resulting sphere will reach equilibrium. Equilibrium is reached when the potential energy is equal to twice the kinetic energy, as specified by the virial theorem. The radius of this sphere when it is in virial equilibrium is defined as the virial radius of the cluster and is related to the mass by equation 2.30.

$$M_{\Delta} = \frac{4\pi}{3} r_{vir}^3 \rho_{crit} \Delta_c \tag{2.30}$$

where ρ_{crit} is the critical density of the Universe and Δ_c is the overdensity relative to the critical and is cosmology dependent and is given in equation 2.31 (Bryan and Norman, 1998) for a flat universe.

$$\Delta_c = 18\pi^2 + 82x + 39x^2 \tag{2.31}$$

where $x = \Omega(z) - 1$. r_{Δ} is then defined as the radius enclosing a mean overdensity of Δ times the critical density, and M_{Δ} is the mass enclosed in a sphere of radius r_{Δ}.

Whilst the equations above hold for idealised objects, spherical symmetry does not hold in real objects, so the processes become too complex to examine analytically and computers are employed to calculate approximate solutions to the equations.

Cluster formation doesn't end with virialisation. It will continue to attract matter gravitationally and its mass and density will grow accordingly.

2.2.3 Self-similarity

Under the assumption that gravitational shock heating is the only heating mechanism for galaxy clusters, and that the cluster gas is an isothermal sphere, simple scaling relations for cluster properties may be derived (Kaiser, 1986).

$$\rho(r) = \frac{\sigma^2}{2\pi G r^2} \tag{2.32}$$

where σ is the object's velocity dispersion.

If the gas distribution is an isothermal sphere then $k_B T = \mu m_H \sigma^2$,

$$M_{\Delta} = \left(\frac{16\pi G^2}{\mu m_H \Delta^2}\right)^{3/2} H(z)^{-1} T_{\Delta}^{3/2} \propto E_{(}z)^{-1} T^{3/2} \tag{2.33}$$

A cluster's X-ray luminosity is defined by equation 2.34:

$$L_X = \int n_e n_H^2 \Lambda(T) \mathrm{d}V \tag{2.34}$$

where $\Lambda(T)$ is the Bremsstrahlung emissivity and is proportional to $T^{1/2}$. Thus:

$$L_X \propto T^2 E(z) \tag{2.35}$$

The entropy[6] scales as

$$S = \frac{kT}{n_e^{2/3}} \propto TE(z)^{-4/3} \tag{2.36}$$

and it follows from equation 2.35 and equation 2.33 that:

$$Y_X \propto M_\Delta^{5/3} E(z)^{2/3} \tag{2.37}$$

Assuming the gas in a cluster is spherically symmetric and in hydrostatic equilibrium (as appears to be the case in most clusters), the equation of hydrostatic equilibrium may be written:

$$\frac{\mathrm{d}\log\rho_g}{\mathrm{d}\log r} + \frac{\mathrm{d}\log T}{\mathrm{d}\log r} = -2\frac{T_\phi(r)}{T} \tag{2.38}$$

where ρ_g is the gas density and $T_\phi(R)$ is the characteristic temperature of an isothermal sphere of radius r and $T_\phi(r) = GM(r)\mu m_H/2rk_B$. This, in combination with the assumption that the gas is isothermal leads to the beta model for a cluster's X-ray surface brightness (Cavaliere and Fusco-Femiano, 1976):

$$\frac{\mathrm{d}\log\rho_g}{\mathrm{d}r} = \beta\frac{\mathrm{d}\log\rho}{\mathrm{d}r} \tag{2.39}$$

where $\beta \equiv \mu m_H \sigma^2/kT$, and when combined with an isothermal King potential (King, 1962) gives:

$$\rho_g(r) \propto \left[1 + \left(\frac{r}{r_c}\right)^2\right]^{-3\beta/2} \tag{2.40}$$

where r_c is the core radius, and it and β can be considered best-fit parameters.

It is worth comparing the isothermal beta model for the gas density with the Navarro-Frenk-White (NFW) profile for the density of a cluster's dark matter component (Navarro et al., 1995):

$$\rho(r) = \rho_0 \left[\frac{r}{r_c}\left(1 + \frac{r}{r_c}\right)^2\right]^{-1} \tag{2.41}$$

so, the gas density will not exactly follow the dark matter density, particularly in the cluster cores where the gradient of the density profile approaches zero for the beta model, whereas the slope of the NFW profile approaches -1 as $r \to 0$ (meaning it has an infinite central density). At radii much greater than the core radius, the slope of the NFW profile tends towards -3 as the slope of the beta profile tends to -3β.

[6] Where entropy is defined as $S = k_B T/n_e^{\gamma-1}$ where k_B is the Boltzmann constant, n_e is the electron number density and $\gamma = 5/3$ is the ratio of specific heats for a monatomic ideal gas

2.3 Simulations

Outside the regimes described above, analytical treatment of structure formation is impossible. In order to study these regimes, we must use numerical methods to approximate solutions.

2.3.1 N-body Simulations

N-body simulations use a Lagrangian approach to model the gravitational interactions between N gravitationally interacting particles. In the simplest case, particles are given masses (although this is usually constant f'or all particles and therefore are not required to be stored for each particle), positions and velocities (although more properties allow a more sophisticated analysis) and these properties are followed through time to some final state.

The gravitational potential for each particle is defined via equation 2.18 and under the assumption $t' = t + \delta t$ where δt is a small increment in time. Thus, after a time δt a particle will have a new position and velocity:

$$\mathbf{v}' = \mathbf{v} + \frac{\mathbf{F}}{m}\delta t \tag{2.42}$$

$$\mathbf{x}' = \mathbf{x} + \mathbf{v}\delta t \tag{2.43}$$

where δt is given an appropriate value. In cosmological simulations particle positions are given in comoving coordinates such that $\mathbf{x} = \mathbf{r}/a(t)$.

In practice, such an integration scheme is rarely used and Gadget-2 employs a leapfrog method in which the particles' positions and momenta are calculated at interweaving timesteps (see Springel 2005 for a detailed discussion). Such a scheme is preferred since it is more stable over many timesteps than an Eularian integration scheme.

The major problem with scaling N-body simulations to arbitrarily large numbers of particles is that gravity is a long range force so each particle interacts with every other particle in the simulation. This is a particular problem for parallel environments. However, the popularity of N-body simulations in astrophysics has led to several distinct algorithms being developed to efficiently deal with very large numbers of particles (and parallel environments).

The most simple algorithm is the particle-particle method - a simple extrapolation of a two body interaction. In this algorithm the interactions between each pair of particles is calculated explicitly (equation 2.44.

$$\boldsymbol{F}_i = \sum_{i \neq j}^{N} \frac{G m_i m_j}{(\boldsymbol{r}_{ij} + \epsilon)^2} \tag{2.44}$$

where m_i and m_j are the masses of the particles concerned, r_{ij} is their comoving separation and ϵ is the softening length which is described later. The time this algorithm takes to complete scales as the number of particles squared, and is therefore a poor choice for simulations with large numbers of particles.

A more complex method for computing gravitational forces is the particle mesh (PM) method. The basic principle behind this method is that the particles are converted onto a mesh of density values on which the gravitational potential is calculated, and the forces applied to the particles based on their containing cell. The gravitational forces are determined from the mesh of density values in Fourier space via the Fourier transformed Poisson equation:

$$\hat{\Phi} = 4\pi G \frac{\hat{\rho}}{k^2} \tag{2.45}$$

then multiplying by k and calculating the inverse Fourier transform.

There are three common types of basic PM method, but they only differ terms of the smoothing kernel they use. All methods for determining the density at a mesh point follow

$$\rho(\mathbf{x_i}) = \frac{1}{V_i} \sum^{p=1..N} M_p W(\mathbf{x}, \mathbf{x_i}) \tag{2.46}$$

where i is the index of the mesh point, M is the mass of a particle, $\mathbf{x}$ are the positions of the nodes and the particles and W is the smoothing kernel. The smoothing kernel takes different forms depending on the gridding method used.
The Nearest Grid Point (NGB) method assigns the particle's mass to its nearest node (equation 2.47)

$$W(\mathbf{x}, \mathbf{x_i}) = \begin{cases} 1 & \text{for } |\mathbf{x} - \mathbf{x_i}| \leq L/2 \\ 0 & \text{otherwise} \end{cases} \tag{2.47}$$

where L is the grid spacing.

The Cloud In Cell (CIC) method is the most common interpolation function, in which the mass is assigned to the 2 nearest mesh points in each direction (2^3 mesh points in three dimensions), shows in equation 2.48.

$$W(\mathbf{x}, \mathbf{x_i}) = \begin{cases} 1 - |\mathbf{x} - \mathbf{x_i}|/L & \text{for } |\mathbf{x} - \mathbf{x_i}| \leq L \\ 0 & \text{otherwise} \end{cases} \tag{2.48}$$

The third method is the Triangular Shaped Cloud (TSC) in which the mass is assigned

to the three lattice points in each direction (equation 2.49).

$$W(\mathbf{x}, \mathbf{x_i}) = \begin{cases} \frac{3}{4} - \left(\frac{\Delta x}{L}\right)^2 & \text{for } \Delta x \leq L/2 \\ \frac{9}{8}\left(1 - \left|\frac{2\Delta x}{3L}\right|\right)^2 & \text{for } L/2 \leq \Delta x \leq 3L/2 \\ 0 & \text{otherwise} \end{cases} \tag{2.49}$$

where $\Delta x = |\mathbf{x} - \mathbf{x_i}|$ (Bagla and Padmanabhan, 1997). The PM method scales as $N_g \log N_g$ (where N_g is the number of mesh points) rather than the N^2 scaling, but the PM method does a poor job calculating small scale forces.

The Particle-Particle; Particle-Mesh (P3M) method is a combination of the PP and PM methods which avoids the disadvantages of both of its constituents by using the PP method for short range forces and the PM method for long range forces. The long range - short range divide is determined by defining a 'critical distance'. At distances shorter than this, the PP method is used and the PM method elsewhere. This method is inefficient, however, in simulations with a large dynamic range. In such cases the computation time can be dominated by the short range forces. To avoid this problem the PP calculations can be further split up into PP and PM components. This is called an Adaptive P3M (AP3M) method.

A tree method is an algorithm for approximating the long range gravitational forces on a particle. In this method groups of particles at a large distance are approximated as single entities for the purposes of gravitational computations, with groups being ever larger at greater distances. A tree algorithm can be described by the opening criterion - $A = D/d$ which decides whether a group of particles of linear size D at a distance d should be approximated as a single entity - and the grouping mechanism used. Gadget-2 uses the geometrical oct-tree grouping mechanism of Barnes and Hut (1986), but others have since been developed such as the nearest-neighbour pairings (Jernigan and Porter, 1989) and the k-D tree method (Stadel, 2001). The geometrical oct-tree calculated the force on a particle by dividing the space around it into eight equal cells which are recursively divided into sub-cells, with each sub-cell remembering its parent, until each sub-cell contains only a single particle. The opening criterion is then applied to each sub-cell to determine whether or not it should be considered as a single entity or not. It is common for a tree algorithm to be combined with a particle-particle method into a hybrid scheme in which the short range forces are calculated via the particle-particle method. Rather than the N^2 scaling in the particle-particle method, a tree algorithm also has the much more amenable $N \log(N)$ scaling.

In practice, gravity-only simulations require a second force acting on small distances.

Table 2.2: The parameters of the Millennium Simulation (Springel et al., 2005)

Parameter	Value
h	0.75
Ω_m	0.25
Ω_Λ	0.75
Ω_b	0.045
Boxsize	500 Mpc/h
# particles	2160^3
Particle mass	$8.61 \times 10^8 \mathrm{M}_\odot/h$
z_{start}	49

This force acts to reduce the gravitational attraction of particles when they are below a separation. This is known as *gravitational softening* and is included to prevent the forces getting too high at small separations. When this happens the slower, particle-particle interactions come to the fore. Additionally, some N-body codes employ individual timesteps for each particle; these are based on the particles' accelerations, so when two particles get very close together, their accelerations become very large and so their timesteps become very small, making them occupy lots of computational resources. The softening is typically proportional to the mean particle separation.

The most well known cosmological simulation (and the basis for the simulations discussed in this thesis) is the Millennium Simulation (Springel et al., 2005). This was a dark matter only simulation in which the only physical force was gravity. It was carried out in a 500Mpc h^{-1} comoving volume and contained 2160^3 $8.6 \times 10^8 \mathrm{M}_\odot h^{-1}$ particles. The full details of the simulation are included in table 2.2

Real-world observations cannot be reproduced from dark matter-only simulations. Dark matter cannot be directly detected, so it is important to produce simulations which may be tested by observations. Baryons - the visible matter - whilst occupying only a small percentage of the Universe's mass are, therefore, important.

2.3.2 The need for hydrodynamics

Dark matter only simulations are relatively simple. There is a single force, gravity, to contend with and the particles have few properties - position and velocity being the only essential ones.

Baryonic matter, the majority of which is in the form of hot gas, behaves quite dif-

ferently from dark matter. As well as the attractive force of gravity, baryons are able to interfere with each other in other ways; perhaps most importantly by exerting pressure.

Because of the additional calculations required, and the additional information which must be stored by each particle, hydrodynamical simulations are much more computationally expensive than their dark matter counterparts.

2.3.3 Smoothed Particle Hydrodynamics

Hydrodynamical simulations are carried out in one of two ways: Eularian methods, in which space is discretised and the properties of the fluid are functions of time and position; and Lagrangian methods, in which matter is discretised, position becomes a comoving variable and the properties of the fluid are functions of the fluid element and time.

Lagrangian simulations have a distinct advantage when it comes to cosmological simulations: all the particles can be treated the same way under the effects of gravity, the methods are Galilean invariant, and the method is adaptable to the geometry of the system.

The simulations discussed in this thesis are all Lagrangian smoothed particle hydrodynamical (SPH) simulations.

The SPH method that is currently used was put forward initially by Gingold and Monaghan (1977) and independently by Lucy (1977). A Kernel estimation technique is used of the form

$$\langle A(r)\rangle = \int W(r-r',h)A(r')\mathrm{d}^3r \tag{2.50}$$

(for a quantity A, and where h is the smoothing length). Taking the volume $\mathrm{d}^3r \to m_j/\rho_j$ and replacing the integral with a summation gives:

$$\langle A_i\rangle = \sum_{j=1}^{N} \frac{m_j}{\rho_j} A_j W_{ij}(r_{ij},h_i) \tag{2.51}$$

where W_{ij} is short hand for the smoothing kernel $W_{ij} = W(|\boldsymbol{r}_i - \boldsymbol{r}_j|, h)$ depends on the particle separation and the smoothing length, h, and can take several possible forms, but the form used in Gadget-2 is that of Monaghan and Lattanzio (1985):

$$W(r,h) = \frac{8}{\pi h^3}\begin{cases} 1-6\left(\frac{r}{h}\right)^2+6\left(\frac{r}{h}\right)^3, & 0\le\frac{r}{h}\le\frac{1}{2} \\ 2\left(1-\frac{r}{h}\right)^3, & \frac{1}{2}<\frac{r}{h}\le 1 \\ 0, & \text{otherwise} \end{cases} \tag{2.52}$$

It appears as though it is necessary to know ρ_j but, as is traditional, taking $A=\rho$ this problem vanishes leaving:

$$\rho_i = \sum_{j=1}^{N} m_j W(|r_{ij}|, h_i) \tag{2.53}$$

The traditional derivation of the equations of SPH, as given by Monaghan (2005), used a symmetrised kernel with functions for the entropy, temperature and artificial viscosity, but this has a problem: if the quantity over which you integrate is the energy then entropy is not conserved and vice versa.

In SPH each of the particles has a known mass and specific energy and all the other properties must be calculated from all the other particles within a smoothing length. In modern SPH codes this smoothing length is defined, not as a definite distance, but as the radius that encompasses a given number of other gas particles (the number of neighbours may be allowed to vary slightly). The great advantage of this is that the simulations will automatically zoom in on high density regions, typically where interesting stuff is happening, whilst doing the opposite in low density regions. The computational time is concentrated on the regions which contain matter. In addition, if one chooses an exact number of particles to be contained within the smoothing length, then the smoothing length must be calculated from scratch at each timestep, which is time consuming. It is acceptable, however, to allow the number of neighbours to vary slightly so each step only has an approximate number of neighbours, based on the number of neighbours found in the previous step (Ritchie and Thomas, 2001):

$$h_i \rightarrow h_i \left[\alpha + (1-\alpha) \left(\frac{N_{sph}}{N_i} \right)^{1/3} \right] \tag{2.54}$$

where N_i is the actual number of neighbours, N_{sph} is the number to approximate and α is a convergence parameter.

The equations of motion for SPH, as implemented in Gadget-2, are derived through a Lagrangian formulation which better conserves both energy and entropy.

$$L(\boldsymbol{q}, \dot{\boldsymbol{q}}) = \frac{1}{2} \sum_{i=1}^{N} m_i \dot{\boldsymbol{r}}_i{}^2 - \frac{1}{\gamma - 1} \sum_{i=1}^{N} m_i A_i \rho_i^{\gamma - 1} \tag{2.55}$$

where $\boldsymbol{q} = (\boldsymbol{r}_1, ..., \boldsymbol{r}_N, h_1, ..., h_N)$ and the thermal energy acts to provide the motions of the particles. The densities, ρ_i, are functions of $\boldsymbol{q}$ as defined in equation 2.53. The smoothing lengths are calculated by requiring that a fixed mass is contained within the smoothing volume, i.e. $M_{SPH} = (4\pi/3) h_i^3 \rho_i$ which leads to the constraint:

$$\phi_i(\boldsymbol{q}) \equiv \frac{4\pi}{3} h_i^3 \rho_i - M_{SPH} = 0 \tag{2.56}$$

The equations of motion can be obtained (Springel and Hernquist, 2003) from:

$$\frac{\mathrm{d}}{\mathrm{d}t} \frac{\partial L}{\partial \dot{q}_i} - \frac{\partial L}{\partial q_i} = \sum_{j=1}^{N} \lambda_j \frac{\partial \phi_j}{\partial q_i} \tag{2.57}$$

where λ_i are a system of Lagrangian multipliers:

$$\lambda_i = \frac{3}{4\pi}\frac{m_i}{h_i^3}\frac{P_i}{\rho_i^2}\left[1 + \frac{3\rho_i}{h_i}\left(\frac{\partial\rho_i}{\partial h_j}\right)^{-1}\right]^{-1} \tag{2.58}$$

so that

$$m_i\frac{\mathrm{d}\mathbf{v}_i}{\mathrm{d}t} = -\sum_{j=1}^{N} m_j\frac{P_j}{\rho_j^2}\left[1 + \frac{h_j}{3\rho_j}\frac{\partial\rho_j}{\partial h_j}\right]^{-1}\nabla_i\rho_j. \tag{2.59}$$

The gradient of the density field can then be given by equation 2.60

$$\nabla_i\rho_j = m_i\nabla_i W_{ij}(h_j) + \delta_{ij}\sum_{k=1}^{N} m_k\nabla_i W_{ki}(h_i) \tag{2.60}$$

then substituting equation 2.60 into equation 2.59 gives the full equations of motion:

$$\frac{\mathrm{d}\boldsymbol{v}_i}{\mathrm{d}t} = -\sum_{j=1}^{N} m_j\left[f_i\frac{P_i}{\rho_i^2}\nabla_i W_{ij}(|\boldsymbol{r}_{ij}|, h_i) + f_j\frac{P_j}{\rho_j^2}\nabla_j W_{ij}(|\boldsymbol{r}_{ij}|, h_j)\right] \tag{2.61}$$

where

$$f_i \equiv \left(1 + \frac{h_i}{3\rho_i}\frac{\partial\rho_i}{\partial h_i}\right) \tag{2.62}$$

The main problem with SPH is its poor shock capturing ability, caused by its smoothed nature. It is therefore necessary to add a viscosity term to the equations of motion. Fully consistent viscosities do not eliminate the smearing of shocks or the anomalous 'ringing' in the surrounding particles. Therefore alternative implementations (Monaghan and Gingold, 1983, first suggested by) are required and modify equation 2.61 such that

$$\frac{\mathrm{d}\boldsymbol{v_i}}{\mathrm{d}t} = \sum_j m_j\left(\frac{P_i}{\rho_i^2} + \frac{P_j}{\rho_j^2} + \Pi_{ij}\right)\nabla_i W_{ij} \tag{2.63}$$

where Π is the viscosity term, given by equation 2.64.

$$\Pi_{ij} = -\nu\left(\frac{\boldsymbol{v}_{ij}.\boldsymbol{r}_{ij}}{\boldsymbol{r}_{ij} + \epsilon h_{ij}^2}\right) \tag{2.64}$$

in which ϵ is a small number introduced to prevent problems when $\boldsymbol{r_{ij}} = 0$ and ν depends on the particle's densities and smoothing lengths.

Initial Conditions

A simulation needs a starting point. For N-body simulations, this starting point is known as the initial conditions.

To generate these initial conditions, it is usual to take a uniform distribution of particles and perturb them, via the Zel'dovich approximation (Zel'Dovich, 1970)[7], so that they have the desired power spectrum.

[7]This is an approximation to extrapolate linear theory of structure formation into the regime where $\delta\rho/\rho$ is not small

The preferred uniform distribution is a glass. This is a relaxed distribution of particles so if left to evolve under gravity (in the case of a dark matter glass) it will do nothing. A dark matter glass can be generated from any particle distribution by switching the sign of the gravitational forces and allowing the distribution to evolve until the net force on each particle is zero. In practice, a perfect glass cannot be created, but the amplitudes of the fluctuations they contain are much smaller than the imposed fluctuations so this is not a problem. Despite the increased computational cost of generating a glass over that of generating a simple grid of particles, a glass is preferred since it has no preferred direction (as a grid does). When different species of particle are being used, a glass is generated for each of them individually and then they are combined.

2.4 Simulations and Observations

Unfortunately, performing simple hydrodynamical simulations of galaxy clusters, in which the gas is only heated in shocks and adiabatic collapse, will not reproduce observed properties of the central regions of clusters accurately (Allen et al., 2001), typically overestimating the mass for a given cluster's temperature (Muanwong et al., 2002). This overestimation may lead to systematic errors when using galaxy clusters as cosmological probes.

Furthermore, the cooling time of the gas in the cores of clusters is considerably shorter than the age of the cluster. The gas should have therefore cooled completely and should no longer be emitting in the X-ray.

The temperature-mass scaling relation for clusters in a purely adiabatic simulation is identical to that predicted by self-similar scaling (Navarro et al., 1995; Muanwong et al., 2001), but observed scaling relations are significantly steeper than this (e.g. Ettori et al. 2004). The observed luminosity-temperature relation is also found to be steeper than that predicted by a self-similar scaling argument (e.g. White et al. 1997, Pratt et al. 2009b).

2.4.1 The need for (more) additional physics

It is therefore necessary to break this adiabatic state in some way in order to reproduce observations. This is broadly done in up to two ways: adding energy and removing low entropy gas. The latter is done by allowing objects, typically clusters, to radiate their energy away[8] and cool down as they do so leading to the term "radiative cooling" (Pearce et al., 2000; Muanwong et al., 2001; Motl et al., 2004; Viola et al., 2007). Rather than lowering a cluster's temperature, when combined with a star formation prescription,

[8]Simple hydrodynamical simulations make no allowance for radiative transfer of energy

radiative cooling actually raises a cluster's temperature. This happens because, when the low entropy gas cools down into dense clumps, it condenses into stars leaving only higher entropy gas to fall into the void left. Employing a radiative cooling scheme without any additional heating, however has problems; particularly that the stellar fraction in a cluster will grow to be much higher than is observed. A second problem is overcooling in the cluster centres. Whilst some so-called 'cool core clusters' have temperature profiles which decline towards the centre, when there is only radiative cooling and no additional heating this temperature drop is greater than is observed.

The addition of energy is done in one of two ways; either in a single, large event, or a continual injection. A single large event is usually added at a high redshift and affects all gas particles. The magnitude of this heating event is tuned to reproduce certain observations at the present day. This is termed "preheating" (Muanwong et al., 2002; Viana et al., 2003; Ettori et al., 2006) and is justified by assuming a period of much supernova and AGN activity at high redshift. Whilst the exact mechanisms for this preheating differ, the generally employed method is to set an entropy floor, whereby all gas particles with an entropy lower than a specified value have their entropy raised to that value.

Continual energy injection is linked to the position of the matter and affects only gas close to the event. High energy events such as supernovae and active galactic nucleae (AGN) are taken to be the sources of this energy injection in a process termed "feedback" (e.g. Muanwong et al., 2006; Kay et al., 2007; McCarthy et al., 2008; Sijacki et al., 2008; Puchwein et al., 2009, 2010). A realistic feedback prescription is a non trivial problem since physical processes are involved which cannot be resolved in cosmological simulations. Efforts to model energy injection from supernovae have centered around sub-resolution modelling of star formation and subsequent supernovae (e.g. Springel and Hernquist 2003), but the energy requirements to reproduce observed galaxy clusters are such that AGN feedback must also be included and this also requires the inclusion of sub-resolution physics.

The addition of this extra physics is able to bring the temperature-mass relation into good agreement with observations. This suggests that these are important ingredients in the description of galaxy clusters.

2.4.2 Evolution

The above processes affect the evolution of a population of galaxy clusters in different ways. This is certainly expected, particularly in a comparison with feedback and preheating, since a preheating scenario has a particular instant at which a very significant process happens, whereas there is no such "special time" in a feedback scenario.

Previous work, such as Muanwong et al. (2006), has found that the evolution of the cluster scaling relations does indeed vary depending on the particular physical processes involved. This is explored more fully for the Millennium Gas simulations in chapter 3.

Understanding, and making better models of the cooling, preheating and feedback processes will be important to future simulations of galaxy clusters. Hopefully these will lead to simulations that fit observational data more closely, particularly at high redshift and in the cores of clusters.

2.5 Summary

This chapter has detailed the current understanding of cosmology and structure formation, methods for numerical simulations, and has described the additional physical processes which must be considered.

The rest of this thesis builds on this by comparing the differing effects of different physical schemes in hydrodynamical simulations; particularly examining the differences between a single epoch of preheating and a continual injection of energy.

Chapter 3

The Millennium Gas simulations

This chapter introduces the Millennium Gas simulations - a suite of hydrodynamical simulations aiming to add baryons to the Millennium Simulation (Springel et al., 2005, MS) and each incorporating different physical processes:

- GO :- An adiabatic simulation in which gravity is the only heating mechanism.
- PC :- A simulation in which the gas is preheated at redshift 4 and allowed to cool radiatively.
- FO :- A representative sample of re-simulated clusters with feedback taken from the model of Short and Thomas (2009) and no radiative cooling.

The GO and PC simulations are carried out in a comoving cube of length $500h^{-1}$Mpc (as per the Millennium Simulation), containing 5×10^8 $1.42 \times 10^{10}h^{-1}\mathrm{M}_\odot$ dark matter particles and an equal number of $3.12 \times 10^9h^{-1}\mathrm{M}_\odot$ gas particles. These are some of the largest cosmological N-body/hydrodynamical simulations ever carried out.

For both the GO and PC simulations, initial conditions were created at a redshift of 49 by displacing particles from a glass distribution such that they conform to a random realisation of a density field with a ΛCDM linear power spectrum obtained from CMBFAST (Seljak and Zaldarriaga, 1996). These initial conditions were chosen to match those of the Millennium Simulation.

Although the mass resolution is approximately twenty times worse than that of the Millennium Simulation, over 95% of the Millennium Simulation haloes with masses greater than $10^{13}M_\odot h^{-1}$ are within $100h^{-1}$kpc of their MS position and 5% of their MS mass.

The PC and GO simulations both have 160 output redshifts at which all the particle data is written to disk. The gravitational softening is set to $100h^{-1}$kpc until redshift 3, after which it is fixed in physical coordinates leading to a softening of approximately 4%

of the mean interparticle separation; believed to be the optimal choice for hydrodynamical simulations of galaxy clusters (Thomas and Couchman, 1992; Borgani et al., 2006). GADGET-2 (Springel, 2005) is used to run these simulations. It is a massively parallel TreePM N-body/SPH code.

The PC and GO simulations have already been used and results from them published. In each case, the authors took advantage of the large number of objects each simulation produced. They were used by Hartley et al. (2008) who studied the spine of the $L-T$ relation and found that merging clusters get boosted along, but also slightly below the relation. Stanek et al. (2010) used the PC and GO runs to examine the covariance of cluster properties (L_X, f_g, T_{sl}, Y_{SZ} and σ_{DM}), finding positive correlations between all pairs (although the strength of the correlations varies greatly) in the GO run and all but $f_g - \sigma_{DM}$ in the PC run. Additionally, Crain et al. (2007) used the GO run to study cluster baryon fraction, concluding that it does not vary with redshift, nor with mass for well resolved haloes.

Sections one to three each discuss the individualities of the different feedback schemes, whilst section four explains the data reduction, and section five discusses the $z = 0$ differences between each of these simulations. Section six discusses the differences between the predicted evolution of the scaling relations for the PC and FO simulations.

3.1 Gravity only

The GO simulation is the simplest of the MG simulations. In this run the only heating mechanism available to the gas is shock heating via gravitational processes. It does not include any form of gas cooling or star formation.

This run is used as a test for the scaling in the absence of any complex physics and is useful for determining which properties of a cluster are driven by its dynamics and formation history; and therefore, in conjunction with the preheating-plus radiative cooling and feedback simulation, to determine which processes are affected by the additional astrophysical processes included in those simulations.

Since gravity, which has no preferred scale, is the only heating mechanism in this simulation a self-similar cluster population is formed (as has also been shown by Navarro et al. 1995; Eke et al. 1998; Voit et al. 2005; Ascasibar et al. 2006; Muanwong et al. 2006; Stanek et al. 2010).

3.2 Preheating and radiative cooling

The second simulation expands on the GO version through the addition of a radiative cooling scheme, based on the cooling function of Sutherland and Dopita (1993), assuming a fixed metallicity of $0.3Z_{\odot}$ (a good approximation out to at least $z = 1$; Tozzi et al. 2003); a star formation prescription; and an epoch of preheating, attributed to an early burst of star formation.

The preheating scheme works by imposing an entropy floor at high redshift - every particle with an entropy below 200 keV cm^{-2} at this time has its entropy raised to that value (similar to the scheme of Borgani et al., 2002). The entropy of the ICM is raised before the gravitational collapse of groups and clusters, which prevents the gas from forming cold, dense cluster cores. This high-redshift preheating was first suggested by Kaiser (1991) and Evrard and Henry (1991) and an entropy floor is observed in dwarf clusters in the *ROSAT* data (Lloyd-Davies et al., 2000), as well as by Finoguenov et al. (2002). Because only the low entropy gas is heated, the effect of preheating on small objects is far higher than on larger, high entropy objects. This causes a breaking of self-similarity in the cluster population, more in-line with observations than the adiabatic case (Ponman et al., 1999; Lloyd-Davies et al., 2000). This preheating scheme is so extreme that star formation is effectively terminated at $z = 4$.

The star formation prescription allows gas particles to turn into star particles if they meet particular density and temperature requirements. Initially there are no star particles in the simulation, but a gas particle is turned into a collisionless star particle once its temperature drops below 20,000K, its density exceeds 4.2×10^{-27}gcm^{-3} and its density contrast, relative to the universal mean, is greater than 100. Due to the limited resolution of the MG simulations it is not possible to identify individual stars; instead, star particles should be thought of as regions where many stars have formed.

This preheating scheme is certainly a gross simplification, however there is considerable evidence that non-gravitational heating mainly occurs at high redshift (Eisenhardt et al. 2008; Weiner et al. 2009 and others) and the PC run is able to reproduce several observational properties of a low-redshift cluster population, including cluster gas fractions. Unfortunately, this simple model fails to reproduce the observed scatter about the mean scaling relations, particularly in small objects, and fails to produce any cool core clusters. It also produces isentropic cores in galaxy groups, which have not been observed.

3.3 Feedback

Rather than injecting the energy at one specified time, feedback schemes assume that energy injection happens gradually over the course of the simulation. The main contributors to this energy are supernovae and active galactic nuclei.

The feedback run differs from the first two runs in that it is not carried out in a single box; rather it consists of a series of *desimulations* of MG clusters in which the resolution of the cluster itself is high (dark matter resolution equal to the Millennium Simulation; gas resolution equal to the MG simulations - approximately one twentieth of the MS resolution), but the surrounding region has its resolution lowered. This is done since the dark matter resolution required by the semi-analytic model means the computational resources needed to simulate a full box would be very great. We selected 337 clusters, uniformly distributed along the $L - T$ relation and not lying more than $5 - \sigma$ from the mean (see figure 3.2).

The feedback scheme used here is that of Short and Thomas (2009), which differs from others in that the feedback energy is provided by a realistic underlying population of galaxies drawn from a semi-analytic model (SAM). Such models were created in order to better understand the formation of galaxies by taking advantage of large, dark matter-only simulations (Baugh, 2006; Somerville et al., 2008).

Semi-analytic models attempt to 'paste' a realistic galaxy population over an underlying dark matter density distribution, based on the merger history of the dark matter haloes. Critics of SAMs argue that they contain large numbers of free parameters and, because of this, they can predict any given set of observations. Their proponents counter that they allow the study of the effects physical processes on galaxy populations with little computational expense.

Since the model used for these simulations was designed to be used on the Millennium Simulation merger trees it is necessary that the dark matter resolution of the feedback simulations be the same as that of the Millennium Simulation. Only the dark matter resolution is required to be this high. Resolution tests show that the gas resolution may be maintained at the same level as the MG simulations with no loss of accuracy.

A simulation of each cluster is therefore a threefold process. Firstly a dark matter-only simulation is carried out from which the merger trees may be generated. Secondly, the merger trees themselves are generated. Finally the simulation is re-run with gas included and feedback energy provided from the SAMs by using the merger trees. The second and third processes are now discussed in detail.

The merger trees are used to generate a catalogue of galaxies via the L-galaxies SAM of De Lucia and Blaizot (2007). Thus we get 64 redshifts (as in the Millennium Simulation) at which the galaxy properties are saved.

These catalogues are then used to calculate the energy to be injected into the intracluster gas in the following way: all semi-analytic galaxies within a virial radius of the cluster's position at redshift zero are identified and their progenitors are found from the cluster merger trees. The change in the stellar mass, ΔM_{star}, and the change in the central black hole mass, ΔM_{BH}, can be found from the merger trees, as can the interval between semi-analytic outputs Δt. The energy injection from supernovae (type II) is computed using the L-galaxies model for supernova feedback, which assumes the total energy released in a given time interval is proportional to the change in stellar mass in that time interval. Some of this energy is assumed to be used to heat the cold gas in galaxy discs, but the remainder is used to eject gas into the ICM.

Feedback from active galactic nuclei is computed as per Bower et al. (2008) where the energy input over a given time interval is the minimum of:

$$\Delta E_{\rm heat} = \epsilon_r \Delta M_{\rm BH} c^2 \tag{3.1}$$

and

$$\Delta E_{\rm heat} = \epsilon_{\rm SMBH} \Delta E_{\rm Edd}. \tag{3.2}$$

where c is the speed of light in a vacuum, $\Delta E_{\rm Edd}$ is the energy released from a black hole accreting at the Eddington limit in a time Δt, and ϵ_r is the efficiency with which matter is converted into energy just outside the event horizon. ϵ_r is set to 0.1 which is appropriate for accretion onto a vanilla black hole. $\epsilon_{SMBH} \approx 0.02$ parametrises the change from a geometrically thick, advection dominated accretion disk (which leads to efficient jet production and radio-mode feedback) to a geometrically thin, radiation dominated accretion disk (quasar-mode feedback) which happens when $\dot{M}_{BH} = \epsilon_{\rm SMBH} \dot{M}_{Edd}$. This leads to an upper limit on the amount of energy available for heating the intracluster gas. This feedback energy is then coupled to the hydrodynamical simulations in order to track its effect on the properties of the ICM.

When including this feedback, we use same initial conditions as were used for the dark matter only simulation, but with the addition of gas particles with zero gravitational mass. The gas particles are given no gravitational mass so that they have no effect on the previously generated dark matter merger trees from which the feedback energy is calculated.

This approximation is taken in all semi-analytic models. These gas particles are given their true mass for hydrodynamical computations and at output times (at which point the dark matter particle mass is reduced accordingly), so the correct cluster masses may be calculated from the snapshot files. They are included at the resolution of the Millennium Gas simulations (rather than the higher simulation of the Millennium simulation, as for the dark matter) to ease the computational expense required.

At a snapshot time, the feedback energy is injected by introducing temporary galaxy particles, which behave as markers describing where to inject the feedback energy. The merger tree information, as described above, can be used to calculate the feedback and star formation, which is distributed evenly amongst all gas particles within r_{200} of the galaxy particles, by giving them all an equal entropy boost. The galaxy particles are then removed.

It is notable that the injection of feedback energy is not quite a continuous process in these simulations, only happening at output times. The frequency of energy injection, however, has only a negligible impact on the results, provided the time difference between outputs is less than the halo's dynamical time (as tested in Short and Thomas 2009).

3.4 Data reduction

In order to make use of the data generated in these simulations, if must first be reduced into something more usable. This process happens in many stages.

At each output time all the particle data are written out in one or several files. For the GO and PC simulations, in which the whole simulation is carried out at once, the snapshots are written out in 128 separate files based on the particles' positions along a Peano-Hilbert curve[1]. Therefore, for the PC and GO runs, the data reduction can only be parallelised by first rearranging the particle data by position, which is far more useful and means that each datacube can be sent off to its own processor for reduction. This is not necessary for the FO run since the snapshot files are so small (only containing a single cluster in high resolution) that the whole snapshot can be reduced on a single processor in a timely fashion.

The next stage is then to produce friends-of-friends groups within the data cubes. If two particles are within a specified distance, known as the *linking length* (defined here as

[1] Gadget makes use of a Peano-Hilbert curve to distribute the particle data equally amongst processors. Whilst this speeds up the running of the code, it has the downside of arranging the particle amongst the data files in a most un-useful way.

Global properties included in cluster catalogues	
Cluster mass	S-Z y-factor
Cluster radius	Velocity substructure
Position of cluster centre	Stellar/gas/dark matter fractions
Position of maximum dark matter density	Stellar/gas/dark matter velocity dispersions
Position of maximum gas density	Spectroscopic-like temperature
Position of the centroid	Bolometric luminosity and temperature
Substructure statistic	Core radius
Mean velocity	Mass deposition rate

Table 3.1: The global cluster properties calculated at different overdensities for each cluster

10% of the mean inter-particle separation) then they are termed 'friends', and if a sufficient, predefined number of such particles are connected in this way, then they are defined as a friends-of-friends group. These friends-of-friends groups are then used to determine the centres of the clusters by taking the single most gravitationally bound particle.

Once the centres of the clusters have been found it is possible to start creating catalogues of global cluster properties: a list of these properties can be found in table 3.1. This is done by growing spheres out from the cluster's centre, until the desired overdensity is reached, and calculating the properties within that radius. The overdensities used are: 2500, 1000, 500, 200 and the virial overdensity with respect to the critical density at the cluster's redshift.

If two clusters overlap, only the larger of the two objects is stored and the smaller is discarded, as are clusters with fewer than 1000 particles at a given overdensity (corresponding to a minimum mass of $8.61 \times 10^{11} M_{\odot} h^{-1}$ in the FO run and $1.73 \times 10^{13} M_{\odot} h^{-1}$ for the PC and GO run).

The determination of the clusters' positions, masses and stellar/gas/dark matter fraction is self-evident, however other properties (temperatures, luminosities and Sunyaev-Zel'dovich -y factor) require some explanation.

The two included temperatures represent approximations two different observed temperatures. The spectroscopic-like temperature, T_{sl} is a good approximation to the spectroscopic temperature in the Bremsstrahlung regime ($T > 2$keV) (Mazzotta et al., 2004) and is defined in equation 3.3.

$$T_{sl} = \frac{\int \rho^2 T^{1/4} \mathrm{d}V}{\int \rho^2 T^{-3/4} \mathrm{d}V} \tag{3.3}$$

The X-ray luminosity is approximated by the bolometric emission-weighted luminosity, assuming the cooling function of Sutherland and Dopita (1993) and a metallicity of $0.3Z_{\odot}$ (the same cooling function as is used in the PC simulation).

Cluster temperatures are scaled to different overdensities based on the self-similar model, as described in equation 3.4. Likewise for cluster entropy (equation 3.5).

$$T_{\Delta} = \frac{G}{2}\frac{\mu m_H}{k_B}\frac{M_{\Delta}}{r_{\Delta}} \tag{3.4}$$

$$K_{\Delta} = \frac{k_B T_{\Delta}}{n_{e,\Delta}^{\gamma-1}} \tag{3.5}$$

where $n_{e,\Delta}$ is the average electron number density within a radius enclosing a mean overdensity of Δ times the critical density.

$$n_{e,\Delta} = \frac{\Delta \rho_{cr,0} f_b E(z)^2}{\mu_e m_H} \tag{3.6}$$

where $\mu_e = 1.14$ is the mean molecular weight per free electron.

In addition to the global luminosity and temperature values, the catalogues also include the values of the temperatures and luminosities excluding the central core region, where the central core is defined as the central $0.15 \times r_{500}$, where r_{500} is the radius enclosing a spherical region with an overdensity of 500 times the critical density.

The Sunyaev-Zel'dovich y-factor is determined via

$$Y_{SZ} = D_A^2 \int y \, \mathrm{d}A \tag{3.7}$$

where D_A is the angular diameter distance (see section 2.1.2) and y is the Compton y parameter.

$$y = \int \frac{k_B T}{m_e c^2} n_e \sigma_T \mathrm{d}l \tag{3.8}$$

where σ_T is the Thomson cross section and $\mathrm{d}l$ is the line of sight distance through the cluster.

The substructure statistic is defined by a simple centroid shift, given by equation 3.9, in which $\mathbf{x_c}$ is the position of the minimum potential and $\mathbf{x_{com}}$ is the position of the cluster's centre of mass.

$$S = \frac{|\mathbf{x_{com}} - \mathbf{x_c}|}{r_{500}} \tag{3.9}$$

Table 3.2: The raw cluster properties included in radial profiles.

Properties determined for radial profiles	
Total cluster mass	Hot gas mass
Stellar mass	Bolometric temperature
Spectroscopic-like temperature	Entropy

Total numbers of clusters

	Number of clusters	
Redshift	PC	GO
0	20823	25750
0.1	19553	24266
0.2	18165	22313
0.3	16661	20346
0.5	13107	16077
1	5968	7608
1.5	2282	3040
2	633	974
3	28	41

Table 3.3: The numbers of clusters and groups with virial masses above $10^{13}h^{-1}\mathrm{M}_{\odot}$ in the PC and GO simulations

These catalogues can be used in conjunction with the raw data to generate radial profiles (table 3.2) and Gadget files for individual clusters, from which maps may be generated (figure 3.1).

The process of reducing the data is slightly different for the feedback runs. The runs are supposed to generate a single cluster, but due to the increased resolution many more objects ($\lesssim 130$) can also be found if the technique described above is used and the correct cluster is not always obvious. Because of this, we use the positional data from the merger trees required for the feedback model and grow spheres around those centres instead of the cluster centres obtained from a friends-of-friends group.

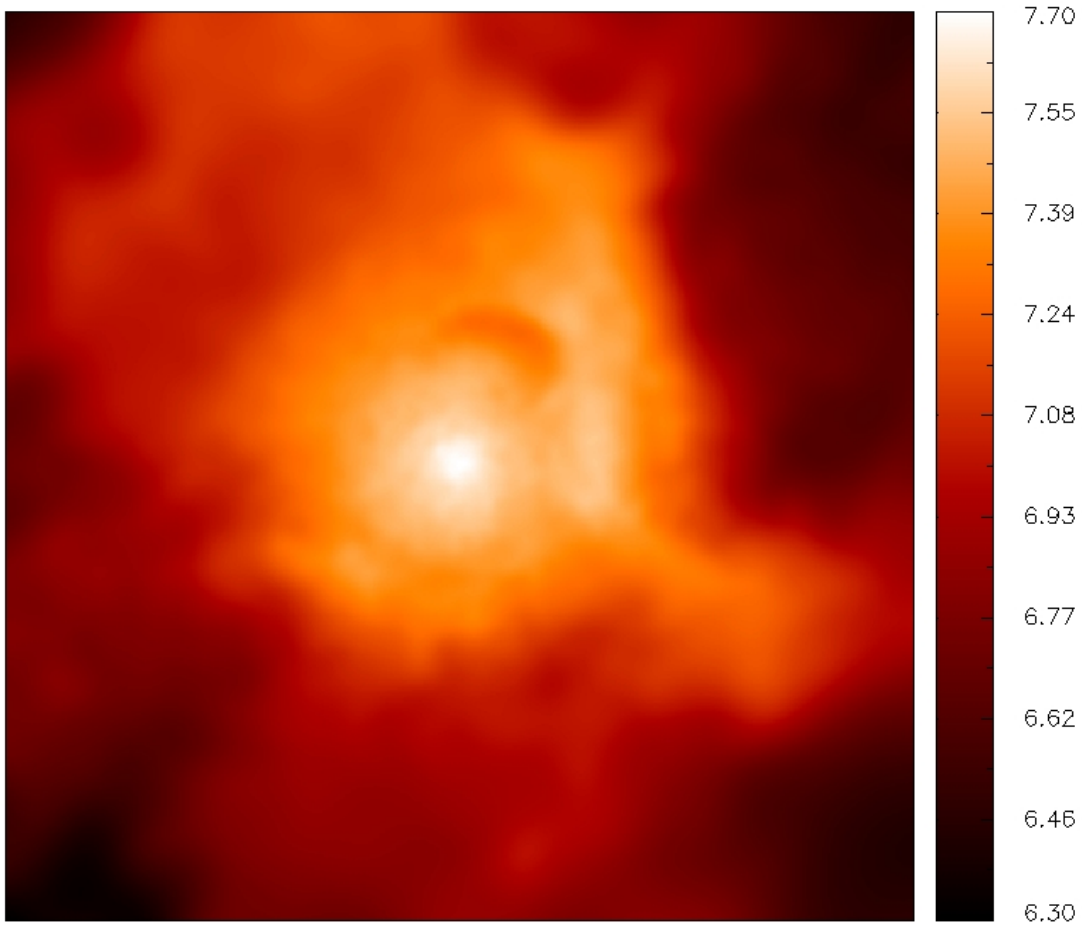

Figure 3.1: A spectroscopic-like temperature map for a typical undisturbed cluster, out to R_{2500}. The colours represent the temperature in keV as indicated by the bar on the right.

Problems with the reduction

Occasionally problems arise in the reduced data which may not be obvious unless cluster maps are viewed.

A problem occurs when there is a small object close to a large one. In this case it is possible for the mass of the small object to be very seriously miscalculated for the larger radii. As the catalogues are being generated and spheres are being grown, if the larger cluster is sufficiently close, when putting down a sphere to enclose a smaller overdensity this may enclose a large part of the very large cluster. This effect can be readily checked for by comparing the mass differences in different catalogues. This problem has been observed in the MG simulations and is corrected for by removing the overlapping clusters.

It may seem that there is a problem with the substructure statistic. A triple cluster system in which a cluster is merging with two others simultaneously may return a very small substructure statistic, despite having a very large amount of substructure. However, this is very rare and we did not come across such an example.

3.5 $z = 0$ Comparison

This section covers the differences between each of the simulations.

3.5.1 Scaling relations

In each of the figures in this subsection, only a subset of the GO and PC clusters have been plotted so that small objects (which are over-represented, relative to more massive objects in the simulation) do not overwhelm the relations and bias the best-fit power laws. Clusters more than 5σ from the best-fit T-M relation are trimmed and the remaining clusters are subsampled in mass, with 400 clusters chosen at random in each decade below a threshold of $3 \times 10^{14} \mathrm{M}_{\odot} h^{-1}$, above which no clusters are discarded. This also makes comparison between the GO and PC runs, and the FO run more meaningful since the sample of desimulated clusters in that run are chosen for being representative examples. This procedure is illustrated in figure 3.2

Figures 3.3 and 3.4 show the X-ray luminosity-temperature relation and X-ray temperature-mass relations, respectively, where the the innermost $0.1 \times r_{500}$ are excluded in the temperature and luminosity measurements, each overlaid with the observational data of Pratt et al. (2009b). The close agreement between the FO and PC runs can be clearly seen,

Table 3.4: The best fit parameters to the power laws in figures 3.3, 3.4 and 3.6 where s is the slope in log space and c is the y-intercept.

	$L-T$	$T-M$	$Y-M$
NC	s = 1.71, c = 0.25	s = 0.64, c = -8.70	s = 1.64, c = -9.52
PC	s = 3.26, c = -1.71	s = 0.57, c = -7.57	s = 1.86, c = -12.63
FO	s = 3.55, c = -2.02	s = 0.52, c = -6.85	s = 1.96, c = -14.06

with the GO run showing slopes closer to those expected from a self-similar population. That the GO simulation appears to be closer to self-similarity comes as no surprise since the only heating mechanism is gravity which has no preferred scale, whereas in the PC and FO runs small objects are preferentially heated. The agreement between the PC and FO runs is also to be expected since they are both tuned to reproduce observed scaling relations at z=0.

Figure 3.5 shows the X-ray temperature and mass relations from the observations of Sun et al. (2009) and Arnaud et al. (2007) with the best fit relations from the GO, PC and FO simulations overlaid. The best fit lines from the FO and PC simulations can be seen to be a much better fit to this observed data, both in the scaling and the slope of the power law, than the GO run. We do not have error bars for the observed data points.

Figure 3.6 shows the $Y_X - M$ relation for each of the MG simulations along with the observational data of Pratt et al. (2009b). The masses of the sample of Pratt et al. (2009b) are calculated from the $Y_X - M$ relation of Arnaud et al. (2007) and therefore all the observational points lie along the mean relation of Arnaud et al. (2007). The slope and the normalisation of this relation can be seen to be in excellent agreement with the FO and PC simulations, whilst the slope from the GO run is lower.

Table 3.4 shows the best fit parameters for each of the power laws listed above.

3.5.2 Profiles

The differences between the $z = 0$ profiles for each of the different runs reiterate some of the differences observed from the scaling relations, as well as some similarities between the GO run and the two runs with additional physics.

Figure 3.7 shows the total mass density for all clusters above 5keV in each of the three Millennium Gas runs. Little difference can be seen between any of the runs (beyond the gravitational softening). This shows that the clusters' dark matter component is little affected by the addition of additional heating and cooling processes. This is to be

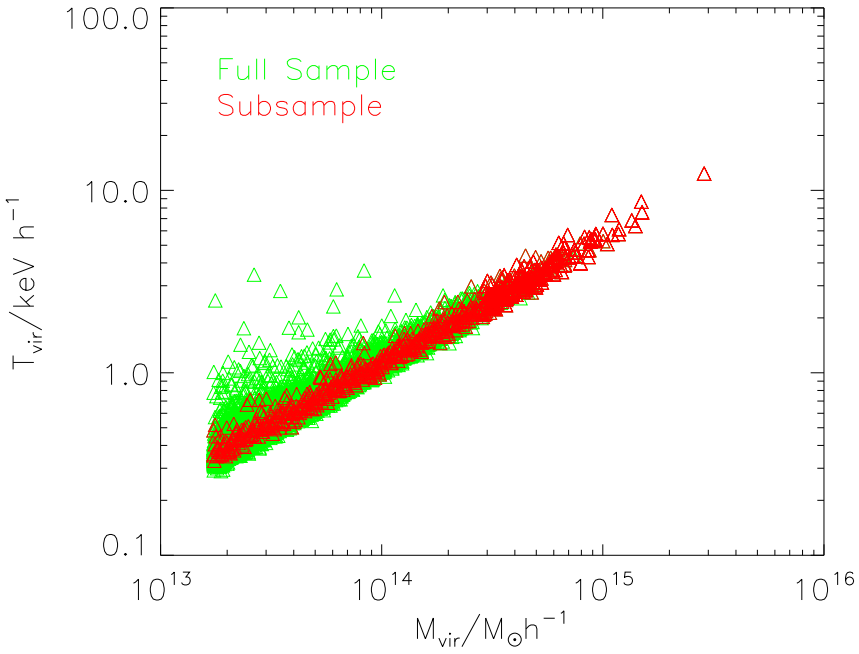

Figure 3.2: An illustration of the subsampling procedure carried out on the PC run. Firstly, clusters lying more than 5σ from the best fit T-M relation are trimmed, then the remaining clusters are sampled such that they are evenly distributed in mass. Above $3 \times 10^{14} M_{\odot}$ all the clusters are included. This is done to prevent the large number of low mass objects causing a bias.

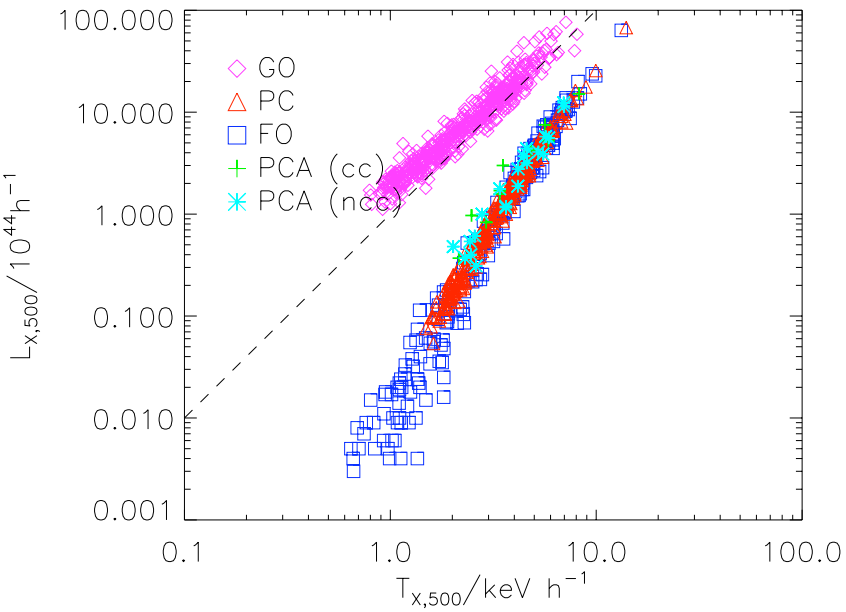

Figure 3.3: The core-excised X-ray luminosity-temperature relation within r_{500} for the GO, PC and FO simulations at z=0 with the observations of low redshift clusters, divided into cool core (cc) and non-cool core (ncc) populations, from Pratt et al. (2009b) overlaid. Note the similarity between the PC and FO runs whilst the GO run has a slope much closer to the self similar value, marked by the dashed line.

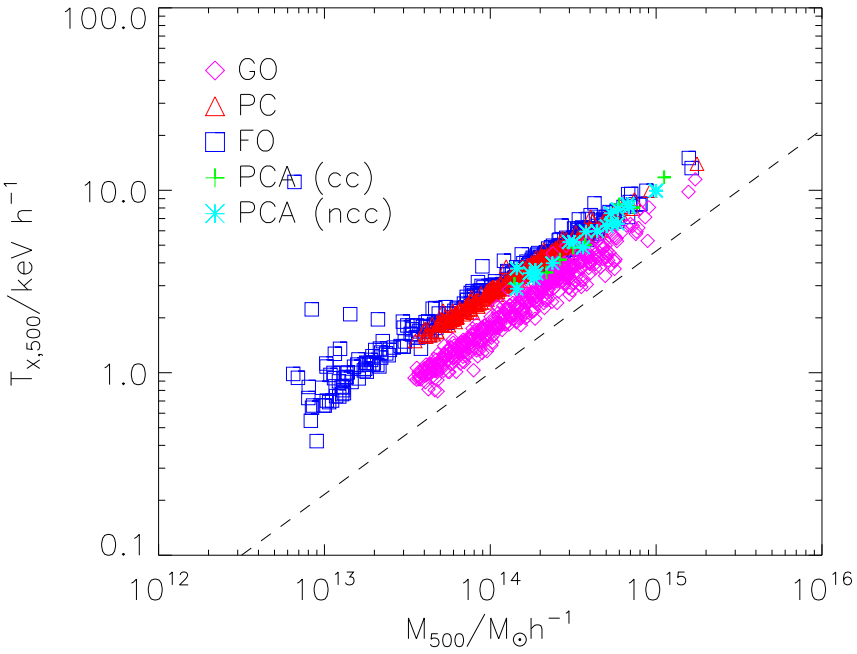

Figure 3.4: The core-excised X-ray temperature-mass relation within r_{500} for the GO, PC and FO simulations at z=0 with the low redshift clusters, divided into cool core (cc) and non-cool core (ncc) populations, from Pratt et al. (2009b) overlaid. The dashed line indicates the self-similar relation.

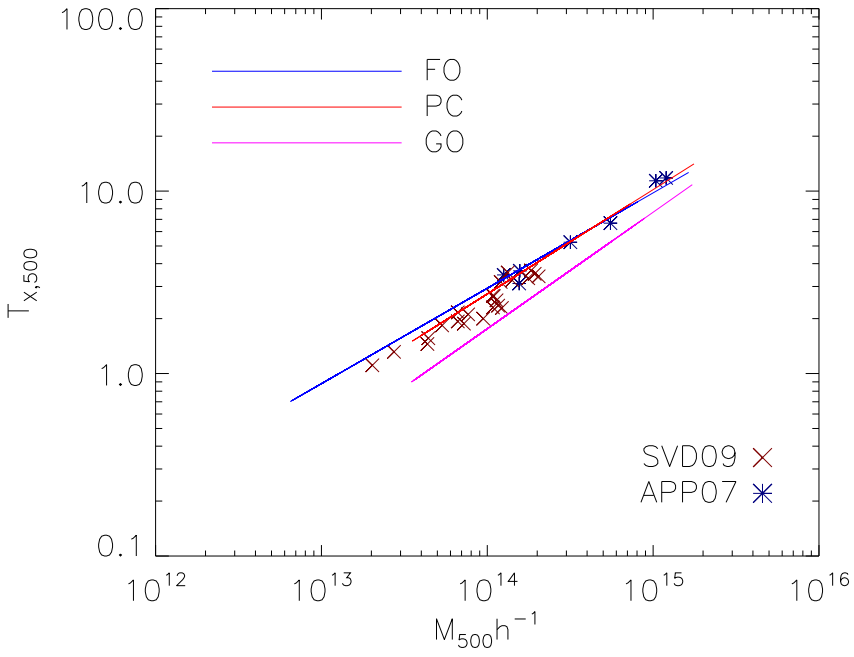

Figure 3.5: The best fit lines from each of the three Millennium Gas simulations on top of X-ray temperature and mass relations within r_{500} for Arnaud et al. (2007) and Sun et al. (2009)

expected since the dark matter is largely unaffected by the gaseous component; and the similarity between the PC and GO runs can be taken as some measure of justification for the assumption, used in the FO run, that the gas has no gravitational mass.

Figure 3.8 is the same as figure 3.7, but shows only the gas density. Here, the difference between the adiabatic and the non-adiabatic runs becomes more apparent. The additional heating processes in the centres of FO and PC have acted to expel more gas, compared the the GO run, and considerably flatter cores can be seen.

Figure 3.9 again shows the difference between the adiabatic and non-adiabatic runs, this time in the spectroscopic-like temperature profiles (for clusters above 5keV again), where the additional heating in the PC and FO runs have raised the central cluster temperature compared to the GO run.

Figure 3.9 shows that all three runs produce clusters whose spectoscopic-like temperature profiles remain flat in the centres (indicating that they're non-cool core clusters), rather than dropping as they would were they cool core clusters. This is to be expected since in the PC run the preheating is so severe that any nascent cool cores will be heated too much to remain cool, and in the FO and GO runs there is no radiative cooling, so cool

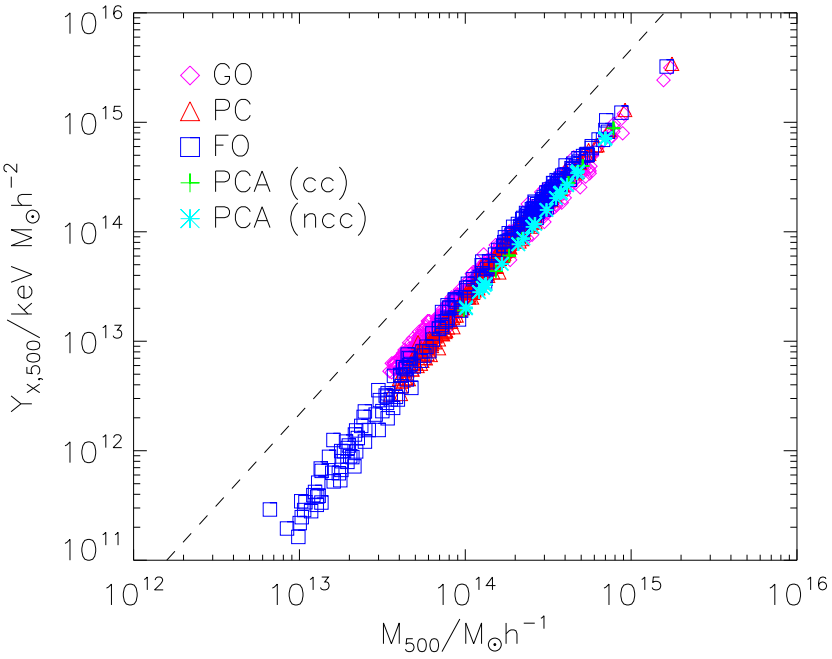

Figure 3.6: The core-excised $Y_X \equiv T_X \times M_{gas}$-mass relation within r_{500} for the GO, PC and FO simulations at z=0 with the low redshift clusters, divided into cool core (cc) and non-cool core (ncc) populations, from Pratt et al. (2009b) overlaid. The dashed line indicates the self similar relation.

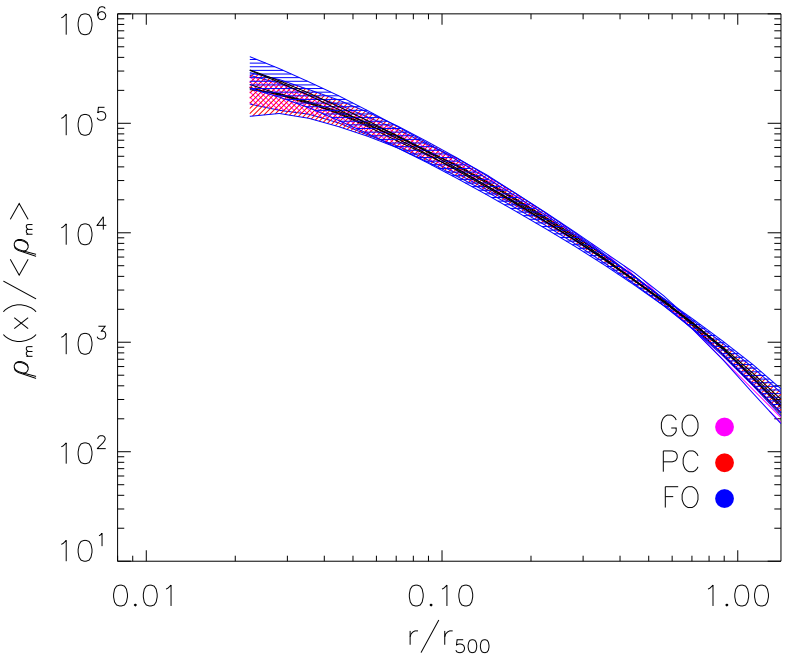

Figure 3.7: The total mass density all clusters above 5keV in each of the three Millennium Gas simulations. The solid lines show the mean relations and the shaded regions show the 1-sigma scatter about it.

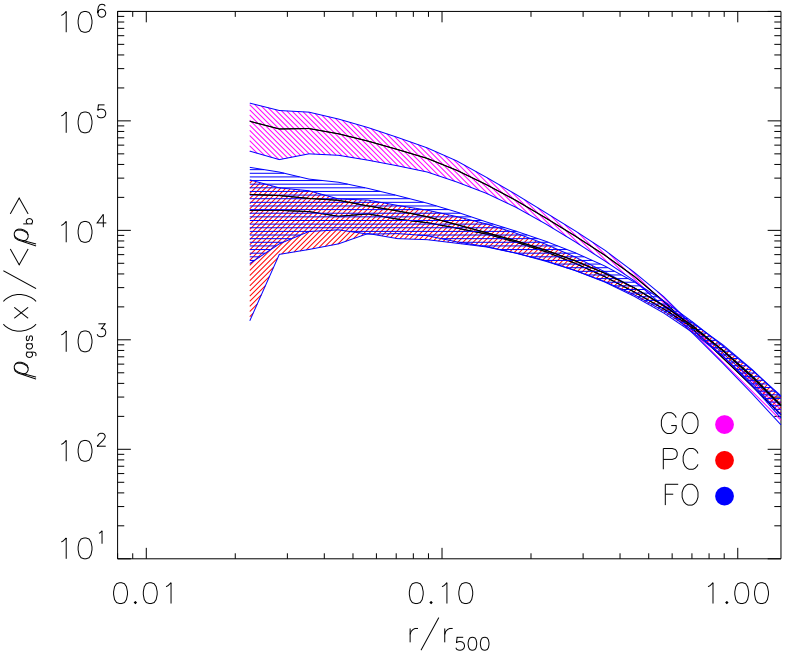

Figure 3.8: The gas mass density in all clusters above 5keV in each of the three Millennium Gas simulations. The solid lines show the mean relations and the shaded regions show the 1-sigma scatter about it.

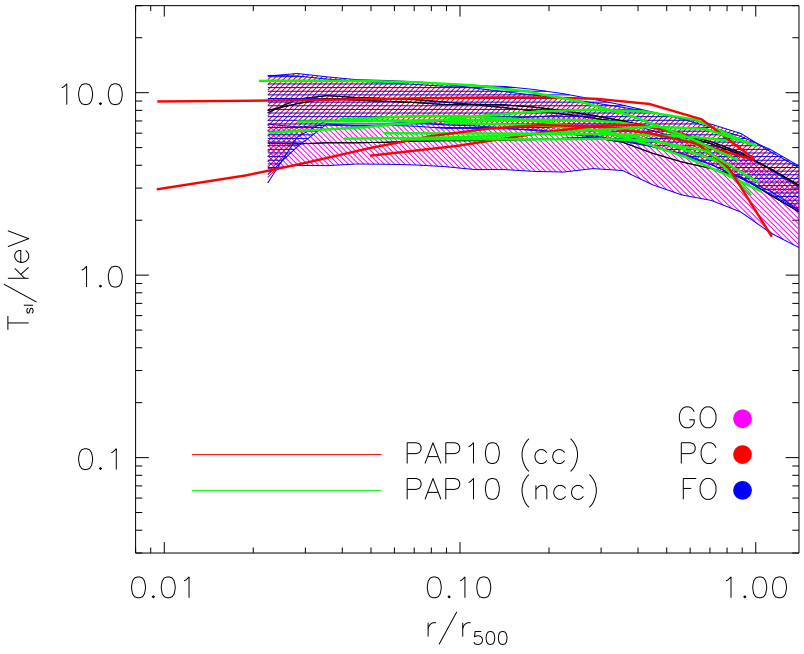

Figure 3.9: The spectroscopic-like temperature profiles for all clusters above 5keV from each of the three Millennium gas runs. The solid lines show the mean relations and the shaded regions show the 1-sigma scatter about it.

cores are unable to ever form.

Figure 3.10 shows the cluster entropy for all objects above 5keV in each of the Millennium Gas simulations. The similarities between the PC and FO simulations, and the effect of the energy injection with respect to the the GO run can be seen again, with the entropy in the cores of the non-adiabatic clusters being much higher than in the adiabatic ones. The profiles for both the PC and the FO runs show typical non-cool core behaviour when they flatten in the cluster centre (c.f. figure 1.2). The behaviour of the entropy profiles in the GO run are more cool core-like than those of the PC and FO runs, but the temperature profiles are still definitely those of non-cool core clusters. Evidence (Vikhlinin et al., 2006; Allen et al., 2008, and others) suggests that observed cool core clusters more closely obey self-similar scaling than non-cool core clusters and, whilst the entropy profiles of clusters found in an adiabatic simulation appear to be more cool core-like than clusters generated from simulations with additional physical processes, their temperature profiles definitely show non-cool core behaviour, indicating that cool cores cannot be formed entirely by unshocked gas, and radiative cooling is required for their development .

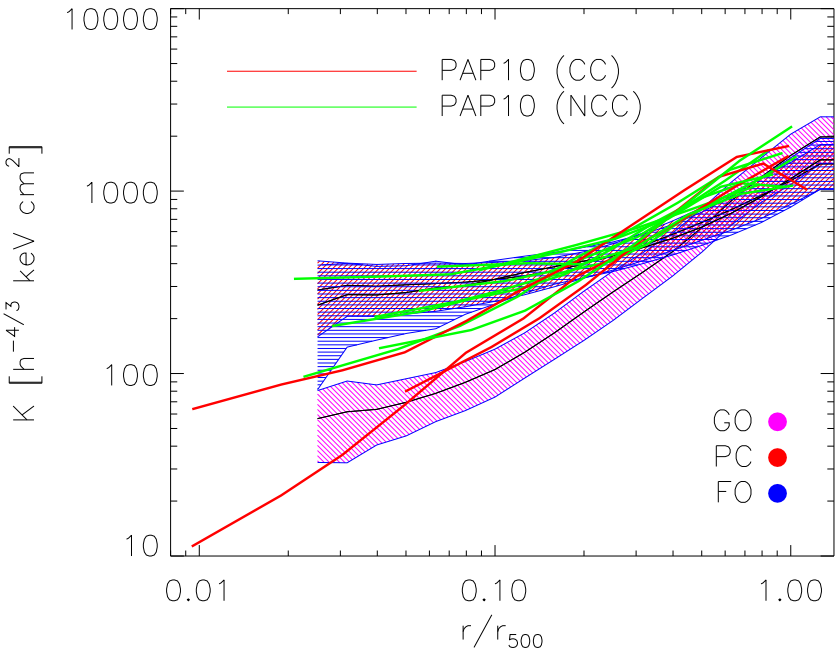

Figure 3.10: The cluster entropy as a function of radius for all objects above 5keV from each of the three Millennium Gas simulations. The solid lines show the mean relations and the shaded regions show the 1-sigma scatter about it.

3.6 Evolution

The results in this section have been published in Short et al. (2010).

Since the differences between the FO and PC runs at $z = 0$ are so slight, in order to discriminate between these two models it is necessary to study the populations of clusters generated in each of the two paradigms at higher redshifts.

Because galaxy cluster properties (particularly their mass function) are highly sensitive to cosmological parameters, they are powerful tools for studying cosmology. However, in order to do this, it is essential to understand the evolution of the mass function with redshift. Since the scalings between mass and observable properties evolve differently in a preheated universe, compared to one with continual feedback, estimates of the evolution of the mass function will differ depending on which model is taken to be true. Therefore understanding which of these heating mechanisms is correct is very important.

The evolution in a population of preheated galaxy clusters is expected to be very different to that of a population of clusters which have been continually heated, as in the FO simulation. Since the heating in the PC simulation occurs at a single time, high redshift scaling relations and profiles for the PC run are expected not to be self-similarly scaled

versions of those at redshift zero. In this simulation, after the entropy floor is imposed at $z = 4$, the core regions are affected more than the outer regions, thus flattening the density profiles (with respect to the adiabatic prediction), as gas is driven out, and raising the normalisation of the temperature profiles.

As the simulation proceeds after this point, these effects lessen as the infall of gas slowly drives the clusters back towards self-similarity. Due to the increased temperatures and entropies, when the cluster accretes gas the effects of shock heating are less than the adiabatic case. The difference between the PC and the GO run will become less and less as the time since preheating increases, eventually becoming indistinguishable at some future time. In contrast, high redshift scaling relations and profiles coming from the FO run are scaled versions of those at redshift zero.

For low redshift clusters, the observational data are sufficient to generate radial profiles and to estimate their masses by assuming hydrostatic equilibrium, as described in appendix A. For high redshift clusters the data are often insufficient for hydrostatic mass estimates (since long observation times are required), so relationships between the cluster mass and X-ray observables are used to determine the clusters' masses. If simulations can match the high redshift scaling relations, then they can be used to constrain them and provide a reliable cluster mass estimate.

Several observational studies of high redshift clusters have been done and their scaling relations described. Ettori et al. (2004) and Maughan et al. (2006) used samples of 28 clusters with $0.4 < z < 1.3$, and 11 clusters with $0.6 < z < 1$ respectively, and masses estimated by assuming a β model. Kotov and Vikhlinin (2005, 2006) and Maughan (2007) were able to use hydrostatic mass estimates, but for small numbers (~ 10) of objects at redshifts higher than 0.4. Pacaud et al. (2007) also used β model mass estimates, and examined a sample of 29 clusters out to $z = 1.05$, with 10 at $z < 0.5$.

Morandi et al. (2007) had sufficient data to measure gas density profiles for 24 clusters with redshifts $0.14 < z < 0.82$. From these measures temperature profiles they determined best-fitting temperature profiles by varying the parameters in their assumed dark matter density profiles. It is noteworthy that, with their larger amounts of data for each object, Morandi et al. (2007) disagreed with those authors using β model mass estimates over mass scaling relations.

There is considerable disagreement between these authors concerning the evolution of these scaling relations. Ettori et al. (2004), Maughan et al. (2006), and Kotov and Vikhlinin (2005, 2006) all agreed on a self-similar evolution for the $M - T_X$ relation;

Kotov and Vikhlinin (2005) and Maughan (2007) also finding self-similar evolution in the $Y_X - M$ relation, however Morandi et al. (2007) found an $M - T_X$ relation slightly below that expected from self-similarity.

Opinion is more divided with relations directly involving luminosity. Vikhlinin et al. (2002), Lumb et al. (2004) Maughan et al. (2006) and Pacaud et al. (2007) all found a self-similar evolution for the $L_X - T_X$ relation, but Ettori et al. (2004) found a negative evolution (with respect to the self-similar), and Kotov and Vikhlinin (2006) and Morandi et al. (2007) found the opposite.

3.6.1 Profile Evolution

Figure 3.11 shows the evolution of the mean scaled profiles of the ten most massive clusters in the PC (top panels) and FO (bottom panels) and the difference between them can be seen to be in agreement with the above reasoning; the PC clusters show substantial evolution in their scaled profiles due to the $z = 4$, preheating having a much greater effect on the clusters' cores than their outer regions, whilst the FO clusters evolve, more-or-less, self-similarly (see section 2.2.3). The behaviour shown in figure 3.11 is not particular to the most massive objects, but only these are plotted since this is a simple way to select the same objects in each snapshot. That the entropy injection in the FO run does not cause the evolution of the cluster profiles to deviate from self-similarity demonstrates a degree of self regulation in the feedback model supplying the energy.

3.6.2 Scaling Relation Evolution

In accordance with the difference in the evolution of cluster profiles in the PC and FO simulations, the evolution of the scaling relations in the PC and FO simulations are also different. Where scaling relations must be used to determine cluster masses from observable cluster properties (as is usual when considering high redshift objects), scaling relations taken from the PC and FO run will give different mass estimates for the same observation, and therefore different estimates of the cluster mass function.

To be able to determine the correct cluster masses and the correct cluster mass function for high redshift objects, it is important to decide which of the scaling relation is correct. This is done by comparing the high redshift results of the two simulations with the cluster observations of Pratt et al. (2009b) and Maughan et al. (2008).

The sample of Maughan et al. (2008) was chosen for comparison since it was one of the largest high-redshift cluster samples available (containing 115 *Chandra* clusters), it

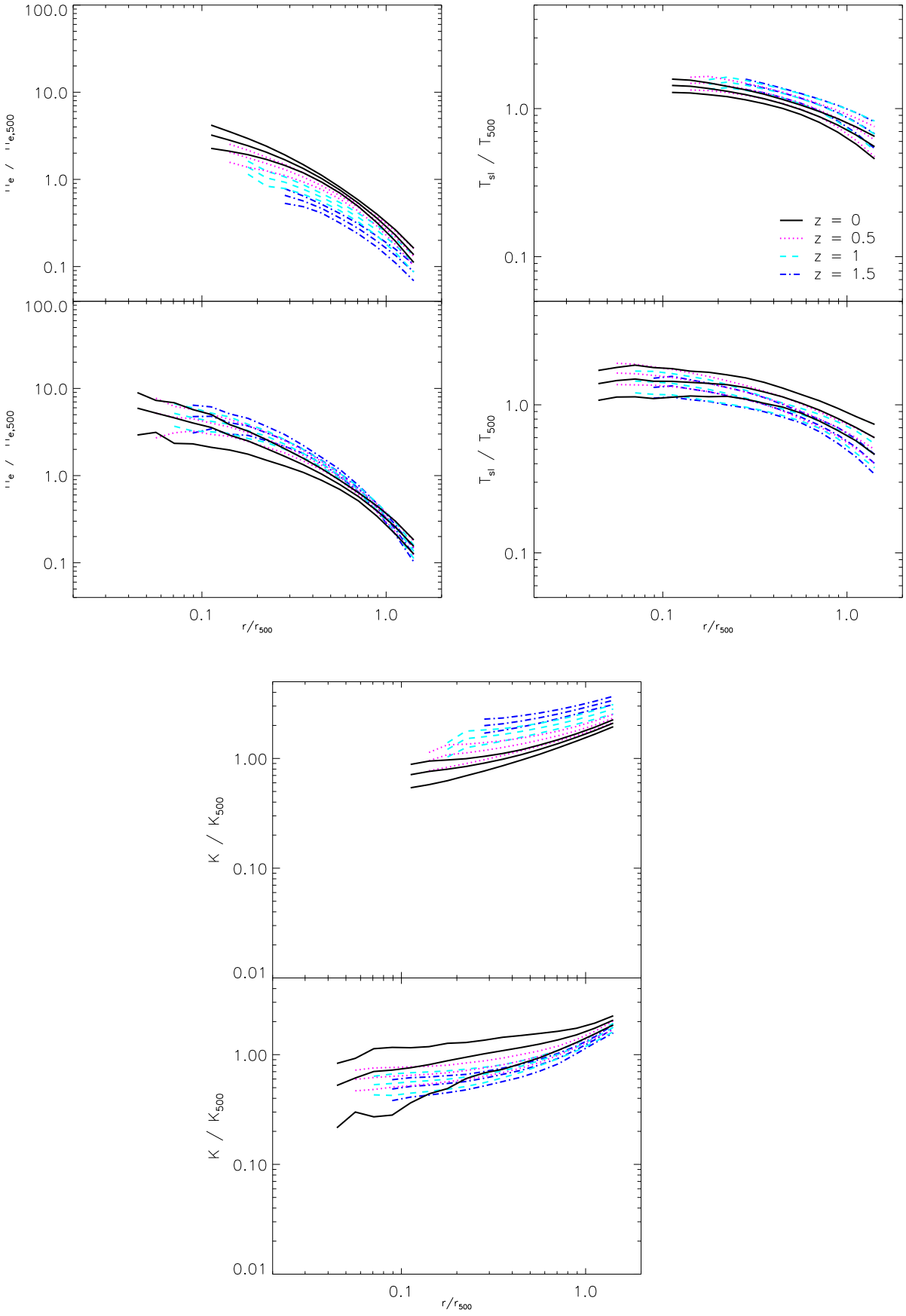

Figure 3.11: The scaled electron number density (left), spectroscopic-like temperature (middle) and entropy (right) profiles for the ten most massive clusters in the PC (top panels) and FO (bottom panels) simulations at four different redshifts showing the difference in the evolution of objects in the two models.

covers the broadest redshift range (0.1 <z <1.3) of any available sample and the temperatures and luminosities are defined in the same way as those in the simulated cluster catalogues. Caution must be taken with this sample (as with any high-redshift sample) as it is susceptible to selection biases which limit the strength of any comparisons made.

Each model predicts opposite senses of evolution in the scaling relations with the FO model showing positive evolution in the $Y_X - M$, $L_X - M$ and $L_X - T_{sl}$ (with the PC model showing negative evolution) and negative evolution in the $T_{sl} - M$ relation (with the PC model showing positive evolution).

It is, however, difficult to determine which model produces scaling relations which are closer to those observed since the number of observed high-redshift clusters is too small to readily constrain the slope and normalisation of high-redshift scaling relations. This is illustrated for the T-M relation in figure 3.12, and the L-T relation in figure 3.13.

However, when higher quality data becomes available it may be possible to use it as a discriminator between the PC and the FO models; for example, the XCS will soon be available and will become the largest X-ray selected cluster sample yet, with clusters selected with well defined criteria out to $z \simeq 1.5$. Comparison between our simulated cluster samples and such an observational sample as this should yield exciting results.

3.7 Conclusions

This chapter has presented the Millennium Gas suite of cosmological simulations - the largest hydrodynamical cosmological simulations to date - and explained the methods used for the data reduction.

Direct comparisons of the results for each simulation were then made and they show that there is a good agreement between the PC and FO simulations at redshift zero, and with observational data for non-cool core clusters. None of the simulations were able to produce cool core clusters, although the entropy profiles for the GO clusters were more cool core-like than those of the PC and FO clusters. That neither the GO nor FO runs are able to produce cool core clusters indicates that radiative cooling is required for the production of cool core clusters.

The evolution of the scaling relations for the PC and FO simulations was then discussed. The evolution of both the scaling relations and the profiles for these runs differs, with the PC clusters showing considerable evolution and the FO clusters appearing to evolve as scaled versions of those at $z = 0$. These two predictions for the evolution of the scaling relations was then compared with high redshift observations, but the observational

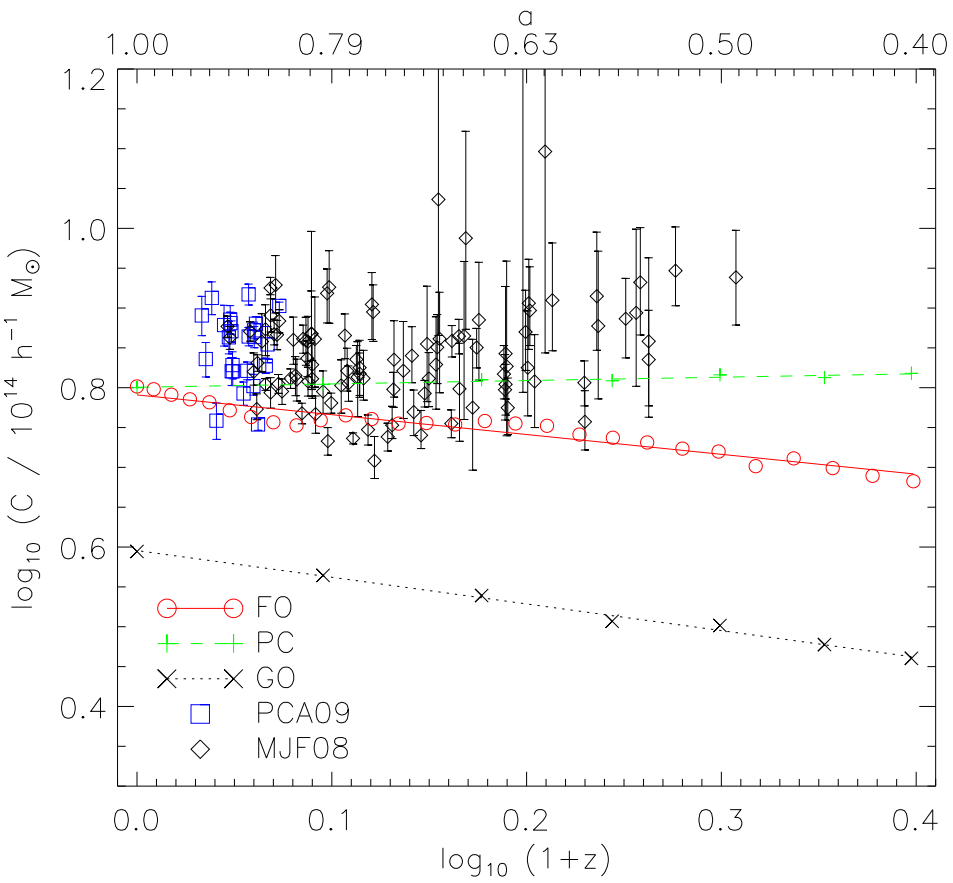

Figure 3.12: The evolution of the normalisation of the T-M relation for the PC and FO simulations with the data of Pratt et al. (2009b) and Maughan et al. (2008)

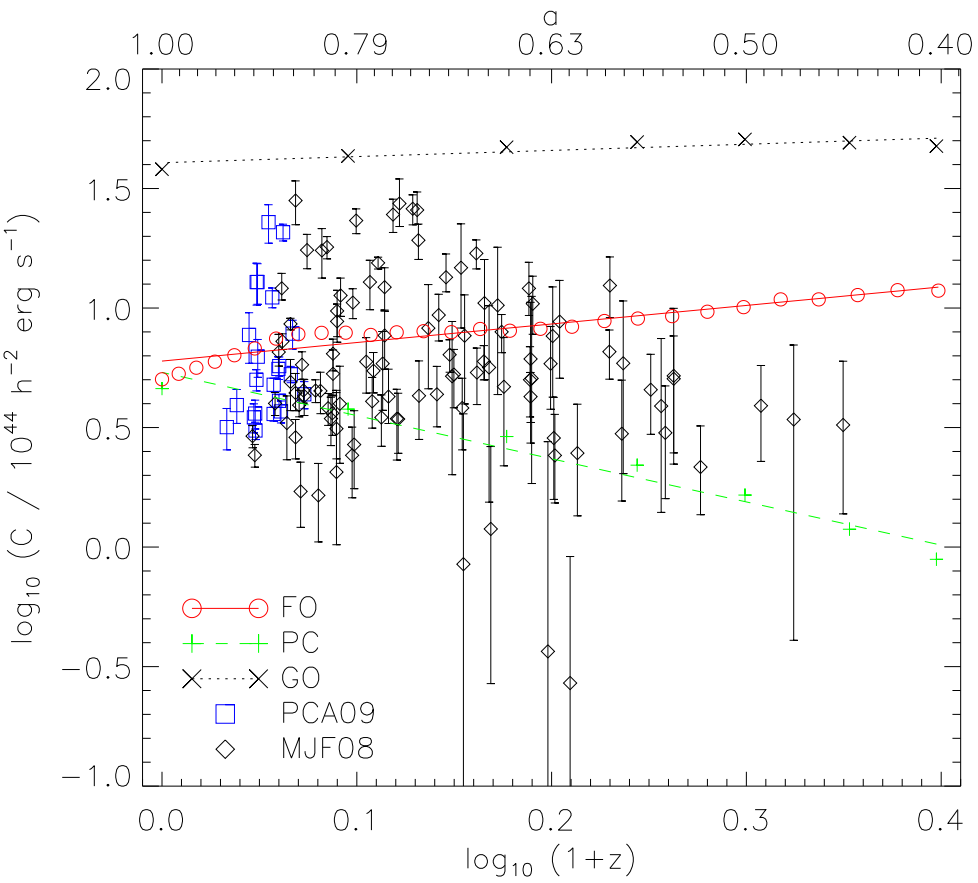

Figure 3.13: The evolution of the normalisation of the L-T relation for the PC and FO simulations with the data of Pratt et al. (2009b) and Maughan et al. (2008)

data are not sufficient to determine which model is preferred.

Chapter 4

Baryon fractions in clusters of galaxies: evidence against a preheating model for entropy generation

This chapter has previously been published in Young et al. (2011).

4.1 Introduction

The hot gas fraction of clusters of galaxies was first used as a cosmological probe by Allen et al. (2002), and later refined in Allen et al. (2004) and Allen et al. (2008). These papers show quite conclusively that the gas fraction can be used to derive cosmological parameters that are in agreement with the concordance ΛCDM cosmology. A similar result was obtained by LaRoque et al. (2006) in a joint X-ray, Sunyaev-Zel'dovich analysis. Subsequently, a more sophisticated analysis that properly takes into account selection effects, and combines mass, X-ray luminosity and temperature observations of 238 clusters at $z \leq 0.5$, reached similar conclusions (Mantz et al., 2010a,b), as did a study by Ettori et al. (2009) of 60 clusters extending to $z \sim 1.3$.

However, as has been pointed out by Sadat et al. (2005), the above conclusion relies very heavily upon the assumption that the gas fraction in the clusters used in the study is independent of both mass and redshift. We show in this chapter that using different models for entropy generation in the intracluster medium (ICM) can lead to variations in hot gas fractions in simulated clusters that are at least as great as those that one obtains

by using an incorrect cosmology in the observational data analysis. We argue, therefore, that, at present, it is more useful to fix the cosmology to the concordance value and to use the data to constrain cluster physics. By doing so we conclude that the data favour a model of continual energy injection into the ICM from galaxies rather than a widespread preheating episode at high redshift.

In the future, once the physical models of the ICM become more refined, and with the large statistical samples of clusters generated by *eROSITA*, it should be possible to do a combined analysis that constrains both the cluster physics and the cosmology simultaneously.

Section 4.2 describes our results first on gas fraction profiles, then scaling relations, and finally the evolution of each of these. The conclusions of the chapter are summarised in Section 4.3.

4.2 Results

In this section we first discuss the radial profiles of the hot gas fractions of clusters at the present day. We then characterise the dependence of the hot gas fraction upon cluster mass, and investigate the scatter about that mean relation. Finally, we look at the variation of the hot gas fraction with redshift.

4.2.1 Profiles

Differential hot gas profiles

Figure 4.1 shows the differential gas mass fraction profiles for clusters in three temperature ranges, $kT_{\rm sl} > 5\,{\rm keV}$ (upper, green regions), $2.5\,{\rm keV} < kT_{\rm sl} < 5\,{\rm keV}$ (middle, cyan regions) and $kT_{\rm sl} < 2.5\,{\rm keV}$ (lower, magneta regions). The curves are plotted out to beyond r_{500} (the radius at which $\Delta = 500$), which is the region accessible to X-ray observations.

For the GO run the gas fraction plateaus at a value of 0.16–0.17 at about $0.3\,r_{500}$, although there is a very slow increase at larger radii (beyond the right-hand edge of the plot). This is less than the global baryon fraction of 0.18: conversion of kinetic energy into heat, together with continual stirring of the gas by the motion of dark matter structures, allows the gas to pick up energy at the expense of the dark matter (e.g. Pearce et al., 1994). This is particularly evident in the cluster cores: for the largest clusters, r_{500} is of order $1\,h^{-1}{\rm Mpc}$; therefore the drop in baryon fraction in the core of the clusters occurs on a scale significantly larger than the force softening ($25\,h^{-1}{\rm kpc}$).

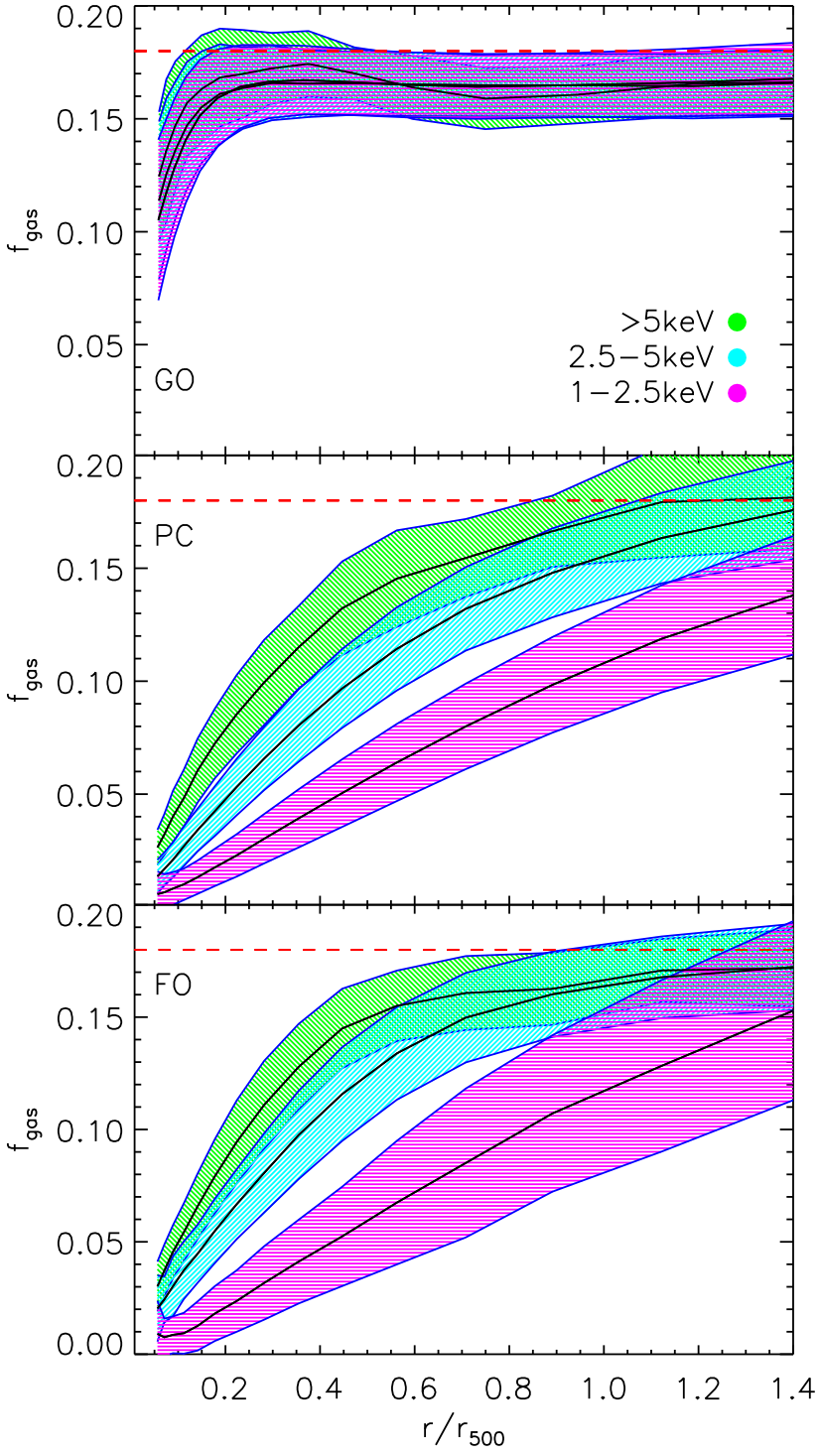

Figure 4.1: Differential hot gas fraction profiles. The solid lines show the mean relations and the shaded region the 1-sigma scatter. The upper, green regions correspond to clusters with spectroscopic-like temperatures above 5 keV; the middle, cyan regions to 2.5−5 keV and the lower, magenta regions to clusters in the range 1−2.5 keV. Profiles are only plotted for radii greater than the gravitational softening length. The dashed line in each case shows the cosmic mean.

In the PC and FO runs, gas has been expelled from the cluster cores and pushed to larger radii. The effect is more pronounced at lower masses: thus the gas profiles of clusters with $kT_{\rm sl} < 2.5\,{\rm keV}$ are still steeply rising at r_{500}, while for $kT_{\rm sl} > 5\,{\rm keV}$ the profiles are approximately constant beyond this radius. The inconstancy of the gas fraction is both a nuisance, requiring careful calibration before we can use clusters as cosmological probes, and a useful test of any model of entropy generation in the ICM.

Comparison with observations

Rather than plotting differential profiles, observational studies tend to report the cumulative gas fractions, averaged within some radius. Figures 4.2 and 4.3 show the cumulative gas fraction profiles in the FO run compared to several different observational studies (Vikhlinin et al., 2006; Allen et al., 2008; Pratt et al., 2009a). We have only plotted simulated clusters in temperature ranges corresponding to those of the various observational data sets. To save space, we do not show the results from the PC run—these are similar.

All three observational studies plot the gas fractions using a different ordinate. The top panel, from Vikhlinin et al. (2006), uses overdensity relative to the critical density. They looked at 13 *Chandra* clusters with a range of temperatures upwards of about 1.5 keV for which the data extend out to large radii. The simulated and observed clusters agree at the outer limit of the data, but the former fall more rapidly as one moves into the cluster centre.

The middle panel shows data from Allen et al. (2008). They again study *Chandra* clusters, but they focus on the inner regions of 42 hot ($kT_{\rm sl} > 5\,{\rm keV}$) systems. As can clearly be seen, the simulated clusters lie well below the observations within r_{2500}.

Both the above studies focus on bright, relaxed systems (those that are likely to be labelled cool core, or CC). By way of contrast, the REXCESS survey (Böhringer et al., 2007; Pratt et al., 2009a), shown in the lower panel of Figure 4.3, is sample of 33 nearby galaxy clusters from *XMM-Newton*, selected so as to sample a broad range of luminosities and with no bias towards any morphological type. The temperature range here is 2-9 keV with the more massive clusters lying towards the upper edge of the observed band, and the least massive ones towards the bottom. Here the simulations are much more successful in reproducing the observed profiles, providing a fair match to the non-cool-core (NCC) population out to the limit of the observations. They fail to reproduce CC clusters (those with flattened baryon fraction profiles in their inner regions), however these are much less frequent than in the relaxed samples.

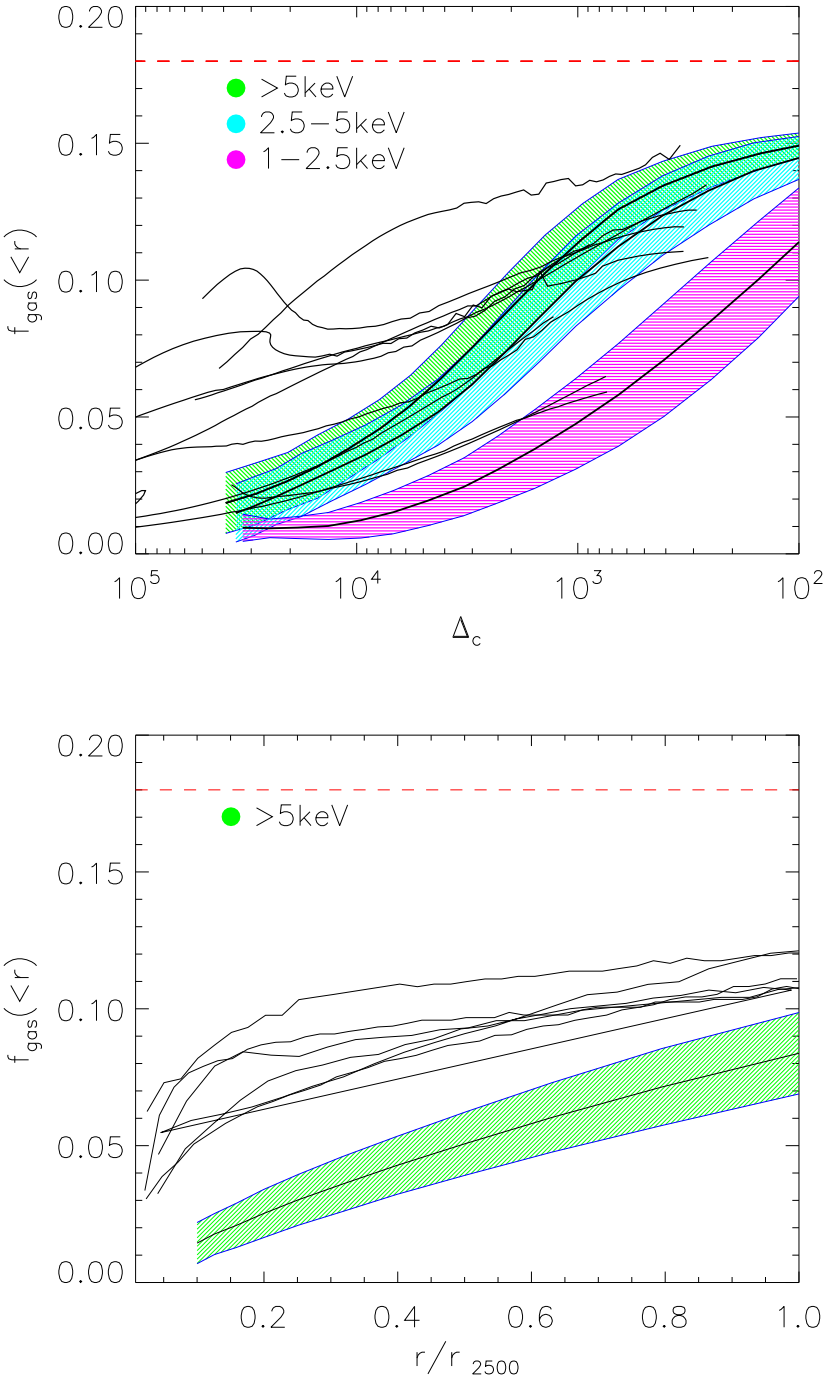

Figure 4.2: Comparison of the cumulative hot gas fraction profiles in the FO run with those of Vikhlinin et al. (2006, upper panel) and Allen et al. (2008, lower panel). In both cases the coloured bands refer to the 1-sigma spread of profiles seen in the simulations: upper, green ($kT_{\rm sl} > 5\,{\rm keV}$); middle, cyan ($2.5\,{\rm keV} < kT_{\rm sl} < 5\,{\rm keV}$); lower, magenta ($1\,{\rm keV} < kT_{\rm sl} < 2.5\,{\rm keV}$). The profiles of simulated clusters are only plotted for radii greater than the softening length. The observational data are shown by black lines.

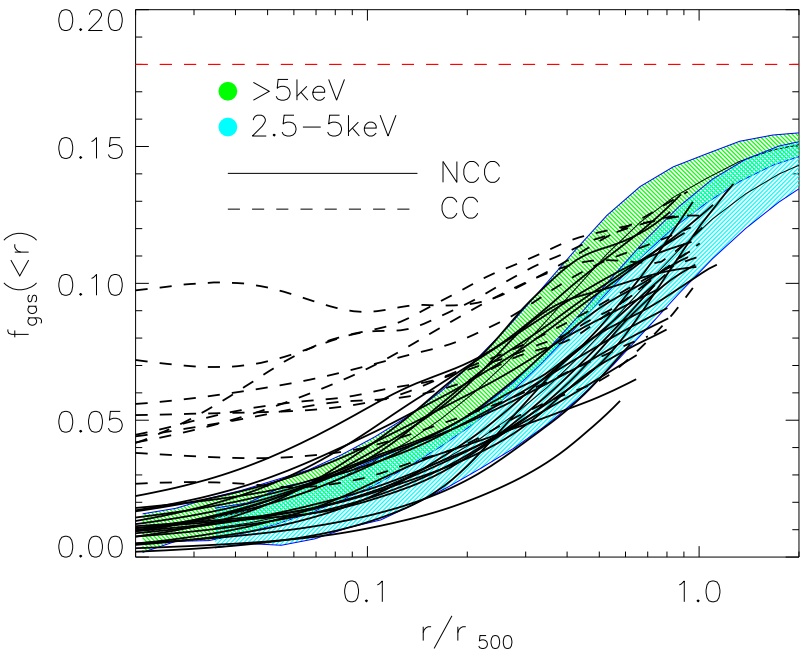

Figure 4.3: Comparison of the cumulative hot gas fraction profiles in the FO run with those of Pratt et al. (2009a). The coloured bands refer to the 1-sigma spread of profiles seen in the simulation: upper, green ($kT_{\rm sl} > 5\,{\rm keV}$); middle, cyan ($2.5\,{\rm keV} < kT_{\rm sl} < 5\,{\rm keV}$); lower, magenta ($1\,{\rm keV} < kT_{\rm sl} < 2.5\,{\rm keV}$). The profiles of simulated clusters are only plotted for radii greater than the softening length. The observational data are shown by black lines with solid and dashed lines corresponding to non-cool-core and cool-core clusters, respectively.

We conclude that our simulated clusters provide a fair match to the hot gas fractions in typical NCC clusters, but fail to reproduce the higher gas fractions seen in the central regions of the brighter, CC clusters.

The results for our adiabatic halos agree with other previous simulations (e.g. Kravtsov et al., 2005; Ettori et al., 2006; Crain et al., 2007). Direct comparison of the other runs is more difficult because we use different feedback models.

Qualitatively, we see a similar behaviour in the profiles of the hot gas fraction to previous work, but the baryon fraction profile is very different in our FO run because of the much reduced stellar fraction. The integrated baryon fractions within r_{500} are considered in Section 4.2.2.

4.2.2 Scaling relations

Cumulative hot gas fractions

Figure 4.4 shows the cumulative gas fraction within a radius of r_{500} as a function of total mass. The GO points are consistent with a constant value of 0.162, slightly smaller than the universal mean of 0.18. By contrast, both the PC and the FO runs have hot gas fractions that are strong functions of mass, because the feedback processes are more effective in lower-mass clusters and evacuate more of the gas.

Figure 4.5 contrasts the hot gas fractions for the FO run within three different radii corresponding to enclosed overdensities of $\Delta = 200$, 500, and 2500 (the PC run gives similar results). In each case the mass has been measured within the corresponding radius. As expected from the radial profiles, the gas fraction is an increasing function of scale radius (i.e. decreasing overdensity). Note that, for a fixed enclosed mass, the variation in enclosed gas fraction is relatively modest: e.g. at $M_\Delta = 10^{14}\,h^{-1}\,\mathrm{M}_\odot$ it varies from 0.07 for $\Delta = 2500$ to 0.10 for $\Delta = 200$. This is much less than the variation seen if a fixed overdensity is used to measure the mass, e.g. for $M_{500} = 10^{14}\,h^{-1}\,\mathrm{M}_\odot$, the enclosed gas fraction increases from 0.04 to 0.11 as the overdensity drops from 2500 to 200.

In Figures 4.4 and 4.5, we fit the hot gas fraction scaling relations with models of the form

$$\log_{10} f = \log_{10} f_0 + s(\mu - \log\,(1 + \exp(\zeta\mu))/\zeta), \tag{4.1}$$

where $\mu = \log_{10}(M/M_0)$ and f_0, M_0, ζ and s are fitting parameters. In log space, this represents a line of constant slope, s, at masses well below M_0, bending over to a constant value of f_0 at high masses. For low enclosed overdensities we would expect f_0 to tend towards the universal baryon fraction of 0.18, although we do not impose this as a con-

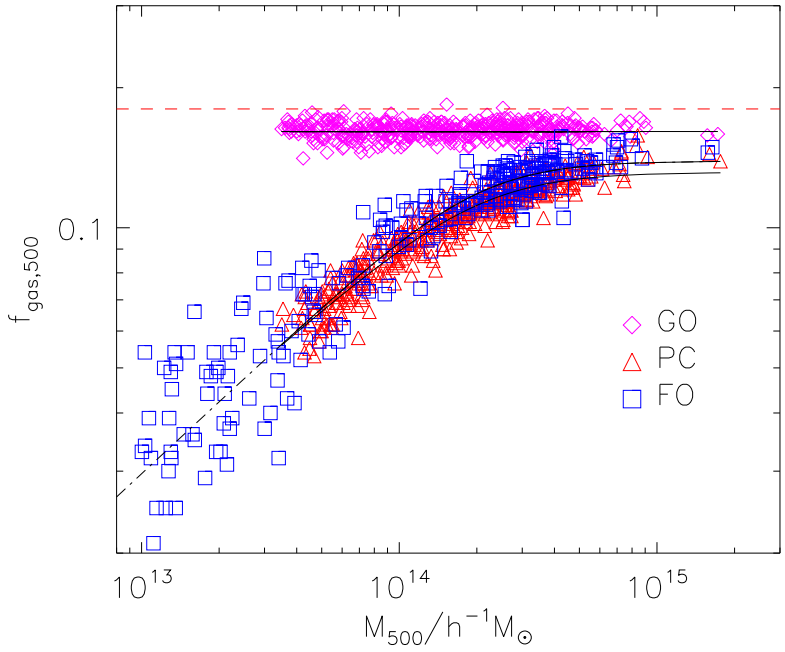

Figure 4.4: The cumulative hot gas fraction within r_{500} as a function of total mass. The solid lines show the best-fitting mean relations, as described in the text and Table 4.1. Extending the fit to the whole range of the FO data, as shown by the dot-dashed line, makes almost no difference to the fit. The dashed line shows the mean baryon fraction in the simulation.

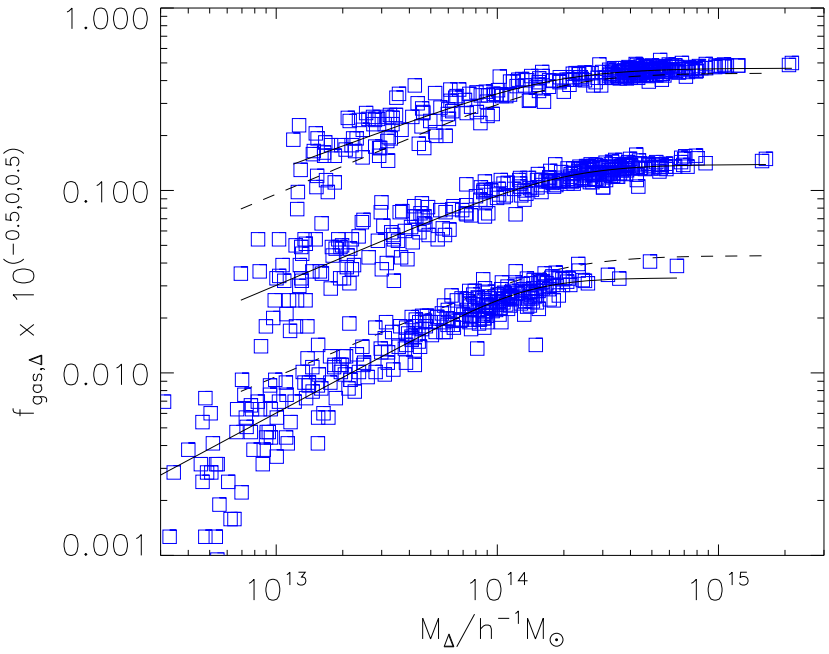

Figure 4.5: The baryon fraction within three different radii for the FO run: r_{200} (upper), r_{500} (middle) and r_{2500} (lower). For clarity, the upper and lower data points have been shifted by 0.5 dex. The solid lines show the best-fitting mean relations and the dashed lines the best-fitting mean relation for the r_{500} data.

Table 4.1: Model parameter fits to the hot gas fractions as a function of mass, as described by Equation 4.1 with a fixed value of $\zeta = 4$. Here $m = \log_{10}(M_0)$. Typical 1-sigma errors in f_0, m and s are 0.005, 0.2 and 0.04, respectively. For the GO run there is no discernible mass-dependence in the hot gas fractions and so only the mean value is recorded in column f_0. The final column gives the root-mean-square scatter in dex of the data points about the best-fit line.

Model	Overdensity	f_0	m	s	σ
GO	2500	0.158			0.036
	500	0.161			0.018
	200	0.163			0.013
	500\2500	0.164			0.026
	200\500	0.166			0.033
PC	2500	0.103	14.15	0.590	0.048
	500	0.134	14.26	0.519	0.041
	200	0.150	14.43	0.363	0.027
	500\2500	0.161	14.28	0.393	0.037
	200\500	0.180	14.10	0.263	0.044
FO	2500	0.126	14.25	0.650	0.124
	500	0.143	14.26	0.552	0.061
	200	0.148	14.21	0.472	0.058
	500\2500	0.163	14.13	0.492	0.076
	200\500	0.173	13.72	0.512	0.066

straint. ζ is a parameter that controls the abruptness of the transition between the two regimes. The data are not always sufficient to independently constrain all the parameters, and in particular ζ: for that reason we use a fixed value of ζ when recording our fits. The best-fit models are shown as solid lines in the figures, and the parameters are listed in Table 4.1, along with the scatter about the best-fit relation.

Figure 4.6 shows the cumulative hot gas fractions in the FO run within r_{2500} and r_{500} as a function of mass. The shaded region shows the 1-sigma spread about the mean relation from the simulation and the points are observational data from the sources listed in the figure caption. Concentrating first on the upper panel, it is apparent that there are systematic differences in the reported hot-gas fractions that cannot be attributed solely to statistical error. In particular, the Allen et al. (2008) data lie significantly above those

of the other studies. This may be because they concentrated on regular, CC clusters that are likely to lie towards the upper edge of the distribution. Even given these observational inconsistencies, however, the simulations show a much greater variation in gas fraction with M_{2500} than do the observations. It would seem that in the FO run (and the PC run is similar) we have ejected too much material from within this radius in small clusters, and too little in large ones.

Moving out to r_{500}, as shown in the lower panel of the figure, the simulations and observations are in better agreement. There is again a suggestion that the observational data would prefer higher gas fractions than the simulations below a cluster mass of of $5 \times 10^{13} h^{-1} \mathrm{M}_{\odot}$, but the scatter in the observational measurements is large. At higher masses, the two show a similar trend of increasing gas fraction with cluster mass, although the simulated values are perhaps slightly too high. This is presumably because the mean baryon fraction that we have used in the simulations, 0.18, is higher than the current WMAP best fit value of 0.168.

Differential hot gas fractions

The profiles of Figure 4.1 suggest that the differential gas fraction between radii of r_{2500} and r_{500} may provide a measure that is more independent of mass than the cumulative gas fractions of the previous section.

In Figure 4.7 we show differential gas fractions, r_{2500}-r_{500} and r_{500}-r_{200}, for the FO model (once again, the PC run gives similar results). Both are higher than the equivalent cumulative measures, although the universal gas fraction is reached only for the most massive clusters ($M_{200} > 3 \times 10^{14}\, h^{-1}\, \mathrm{M}_{\odot}$) at radii $r > r_{500}$. Clearly the differential gas fraction at larger radii, r_{500}–r_{200}, is more nearly constant and so provides the more accurate probe of cosmology, but observationally the inner annulus, r_{2500}–r_{500}, provides a compromise between eliminating the depleted inner region and having enough counts to enable a reliable X-ray determination of the gas density. The observational data from Sanderson et al. (2003), Vikhlinin et al. (2006) and Sun et al. (2009), plotted in Figure 4.8, present a confused picture. The Sanderson et al. (2003) data broadly mimic the simulations, but the statistical scatter in their data is very large. Vikhlinin et al. (2006) report the smallest error bars for their data and find differential gas fractions that increase strongly with mass, but which lie below the simulated values; whereas, at lower masses, the Sun et al. (2009) data seem to require hot gas fractions that are decreasing, or at best flat, as a function of mass. We conclude that these differential measurements are not yet

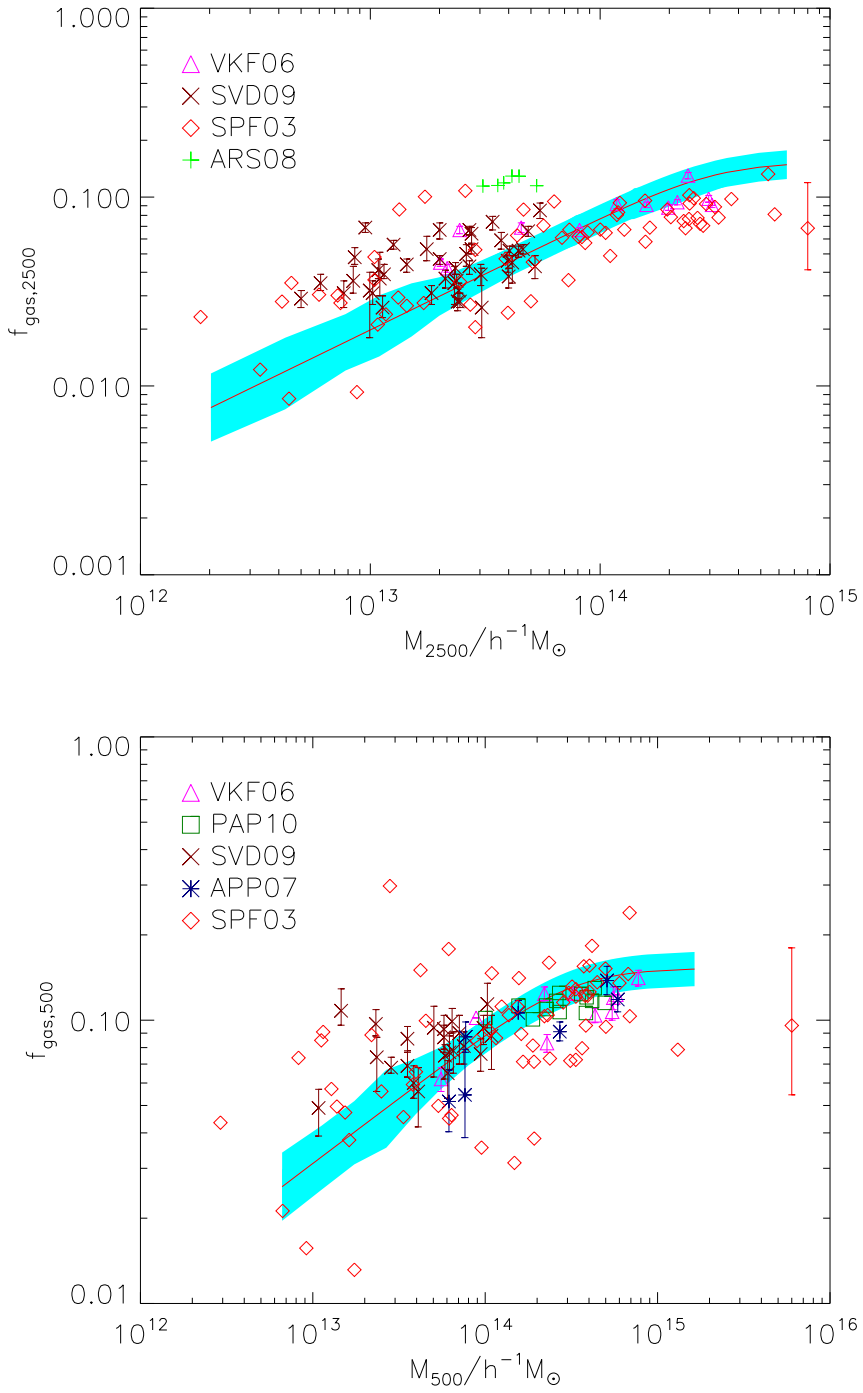

Figure 4.6: The cumulative hot gas fraction versus mass relations for the FO run as compared to observations. The upper and lower panels refer to overdensities of 2500 and 500, respectively. The shaded regions are the 1-sigma spread in the simulated clusters. The symbols represent observational data from Sanderson et al. (2003), Vikhlinin et al. (2006), Arnaud et al. (2007), Allen et al. (2008), Sun et al. (2009) and Pratt et al. (2009a). For the Sanderson et al. (2003) clusters we show one fake data point on the right-hand edge of the plots with typical 1-sigma (statistical) error bars. For the other samples, we include the error bars on the plotted points, apart from Allen et al. (2008) and Pratt et al. (2009a) since we do not know the uncertainties in their measurements.

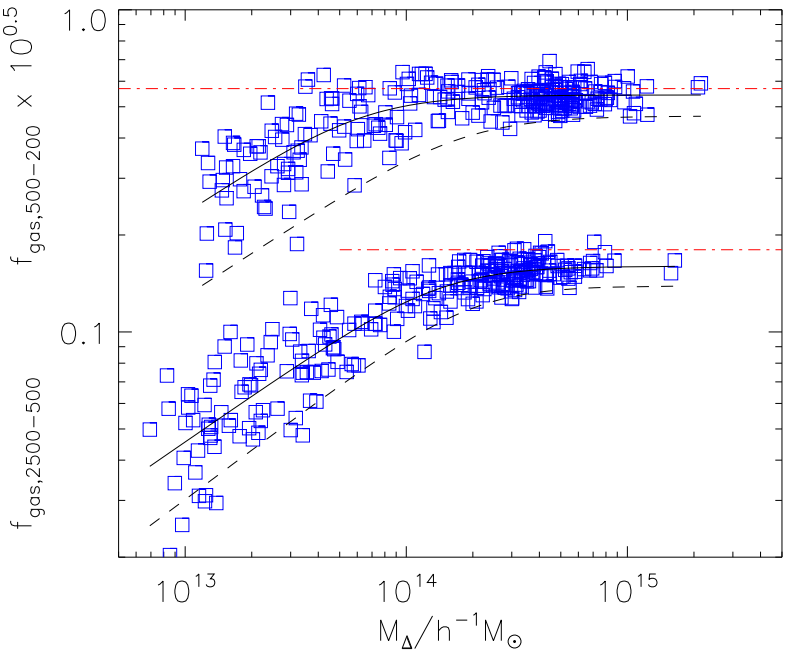

Figure 4.7: Differential hot gas fractions for the FO runs: between r_{2500} and r_{500} (lower points), and between r_{500} and r_{200} (upper points). The upper points have been shifted up by 0.5 dex, for clarity. In each case, the mass has been taken to be that at the outer edge of the differential range. The solid lines show the best-fit mean relation and the dashed lines show the best-fit relation for the equivalent cumulative gas fraction measure. The dash-dotted lines show the mean baryon fraction in the simulation.

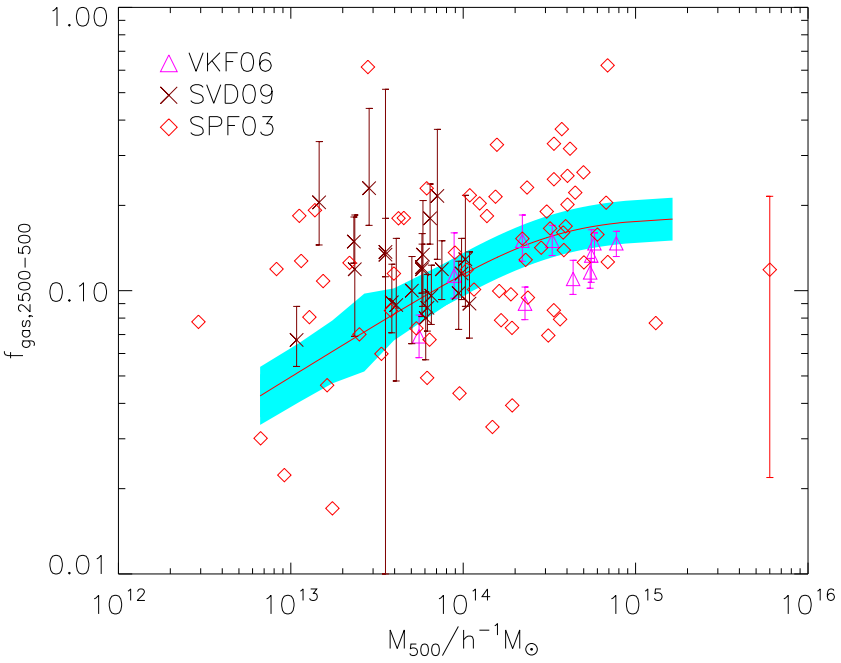

Figure 4.8: The differential hot gas fraction in the annulus contained between r_{2500} and r_{500} for the FO run as compared to observations. The shaded region is the 1-sigma spread in the simulated clusters. The points are taken from Sanderson et al. (2003), Vikhlinin et al. (2006) and Sun et al. (2009). For the Sanderson et al. (2003) clusters we show one fake data point on the right-hand edge of the plot with typical 1-sigma (statistical) error bars. For the other samples, we draw the error bars on the plotted points.

Table 4.2: As for Table 4.1 but for the baryon fractions rather than the hot gas fractions. ζ = is fixed at 4 for the PC and 8 for the FO run. For the GO run there is no star formation and so the values are the same as reported in Table 4.1.

Model	Overdensity	f_0	m	s	σ
PC	2500	0.141	14.32	0.250	0.061
	500	0.161	14.44	0.307	0.037
	200	0.168	14.49	0.271	0.030
	500\2500	0.174	14.29	0.362	0.035
	200\500	0.188	14.10	0.269	0.042
FO	2500	0.156	14.92	0.251	0.069
	500	0.150	14.48	0.308	0.052
	200	0.157	14.41	0.291	0.044
	500\2500	0.167	14.25	0.357	0.053
	200\500	0.181	13.94	0.333	0.058

sufficiently robust to provide useful constraints.

It is interesting to note that both the PC and FO models have higher differential gas fractions at large radii than does the GO model. The injection of entropy has removed gas from the cores of the clusters and pushed it out to larger radii, between r_{500} and r_{200}. In a steady-state, the higher entropy in these runs would ensure that they have a lower gas density than in the GO model: we conclude that on large scales, although still within the virial radius, the clusters are not in dynamical equilibrium.

Baryon fractions

The baryon fractions are also well-fit by the model given in Equation 4.1 with parameters as listed in Table 4.2. Because clusters are large systems with deep potential wells, it is often stated that they should enclose a representative sample of the Universe, and in particular that they should contain the Universal fraction of baryons. Indeed, we find this is approximately true, with only a small baryon deficit within r_{200}.

Observationally, the baryon fraction is hard to determine because of the difficulty in measuring the contribution from dwarf galaxies and from intracluster light (stars that have been stripped from galaxies). This latter component may comprise as much as 40 percent of the total light of the cluster (Bernstein et al., 1995; Gonzalez et al., 2000; Feldmeier et al., 2002, 2004; Gonzalez et al., 2005; Krick et al., 2006; Zibetti et al., 2005). Except

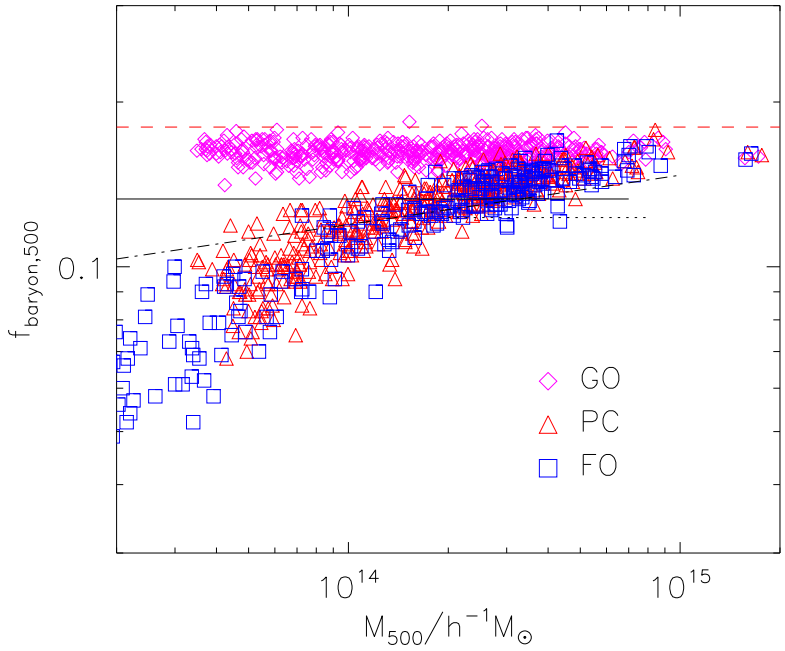

Figure 4.9: The cumulative baryon fraction versus mass. The solid and dotted lines show the mean relations (approximately independent of mass) from Gonzalez et al. (2007) and Laganá et al. (2008), respectively; the dash-dotted line shows that from Giodini et al. (2009). The red dashed line is the universal mean.

for the brightest X-ray clusters, the measurement of total mass is also problematic.

Gonzalez et al. (2007, hereafter GZZ07), in a sample of 12 groups and clusters spanning a wide mass range, find that the baryon fraction is independent of mass and averages to 0.133 within r_{500}. Laganá et al. (2008, hereafter LLA08) with a smaller sample of 5 high-mass clusters find a slightly lower value of 0.123 (the mean of their quoted numbers, weighted by the inverse square of their errors). On the other hand Giodini et al. (2009, hereafter GPF09), in a sample of 41 clusters drawn from Vikhlinin et al. (2006), Arnaud et al. (2007) and Sun et al. (2009), find that the baryon fraction is a slowly-increasing function of mass. The baryon fractions for our FO and PC clusters are compared to these observations in Figure 4.9

The observations and the simulations approximately agree for cluster masses of 1–$3 \times 10^{14} h^{-1}\,\mathrm{M}_{\odot}$. However the simulations show a strong variation with cluster mass, even more so than that of GPF09. This difference is attributable mainly to differences in star formation, as described below.

Stellar fractions

Both our PC and our FO models have much more modest star formation than do many previous simulations (e.g. Borgani et al., 2004; Ettori et al., 2006; Kay et al., 2007; Nagai et al., 2007; Davé et al., 2008; Fabjan et al., 2010; Puchwein et al., 2010). In particular, the FO run takes its star-formation rate from the highly-successful L-Galaxies semi-analytic model. The mean stellar fraction in our high mass clusters in the FO run agrees well with the observations of both GZZ07 and LLA08; the results of GPF09 are slightly higher. However, we do not find such a strong increase in stellar fraction in low-mass clusters as is seen in both GZZ07 and GPF09. The upper panel in Figure 4.10 shows the stellar mass-fraction within r_{500} as a function of mass for both the PC and the FO runs, with the trend from GZZ07 shown as a solid line and that from GPF09 as a dotted line. This comparison suggests that we considerably underestimate star formation in groups. The lower panel shows a similar plot for r_{200} with data from Andreon (2010). He finds lower stellar fractions but a similar steep increase with decreasing mass.

Before dismissing our FO model as unrealistic, however, we note the following:

- As pointed out by Balogh et al. (2008), the GZZ07 data is incompatible with any model that forms galaxies via hierarchical mergers unless there is an unreasonably large star-formation rate in groups at late times.

- The L-Galaxies model produces correlation functions for the galaxy distribution that are consistent with observations with no evidence for a suppression at small separations (Kitzbichler and White, 2008). It is difficult to reconcile this with the need to greatly increase the stellar fraction in groups.

The other simulations mentioned above also predict a slow variation of stellar fraction with mass, although they mostly have stellar fractions that are higher than ours, agreeing with the observations on group scales but having stellar fractions that are too high on cluster scales. For example, the clusters of Ettori et al. (2006) have a stellar fraction of about 0.05 within r_{500}. The equivalent fraction for massive clusters ($kT_{\rm sl} > 5\,{\rm keV}$) in our own runs is 0.02 for PC and 0.013 for FO. [1]

We conclude that, although the observations are not yet sufficiently robust, stellar mass fractions provide an important test of, and discriminant between, different galaxy formation models.

[1] Ettori et al. (2006) choose to give stellar fractions in terms of the mean baryon fraction, $Y = M_{\rm star}/M_{\rm total}/f_{\rm b}$. The stellar fractions quoted in their paper are thus a factor of 5.6 larger than those listed here.

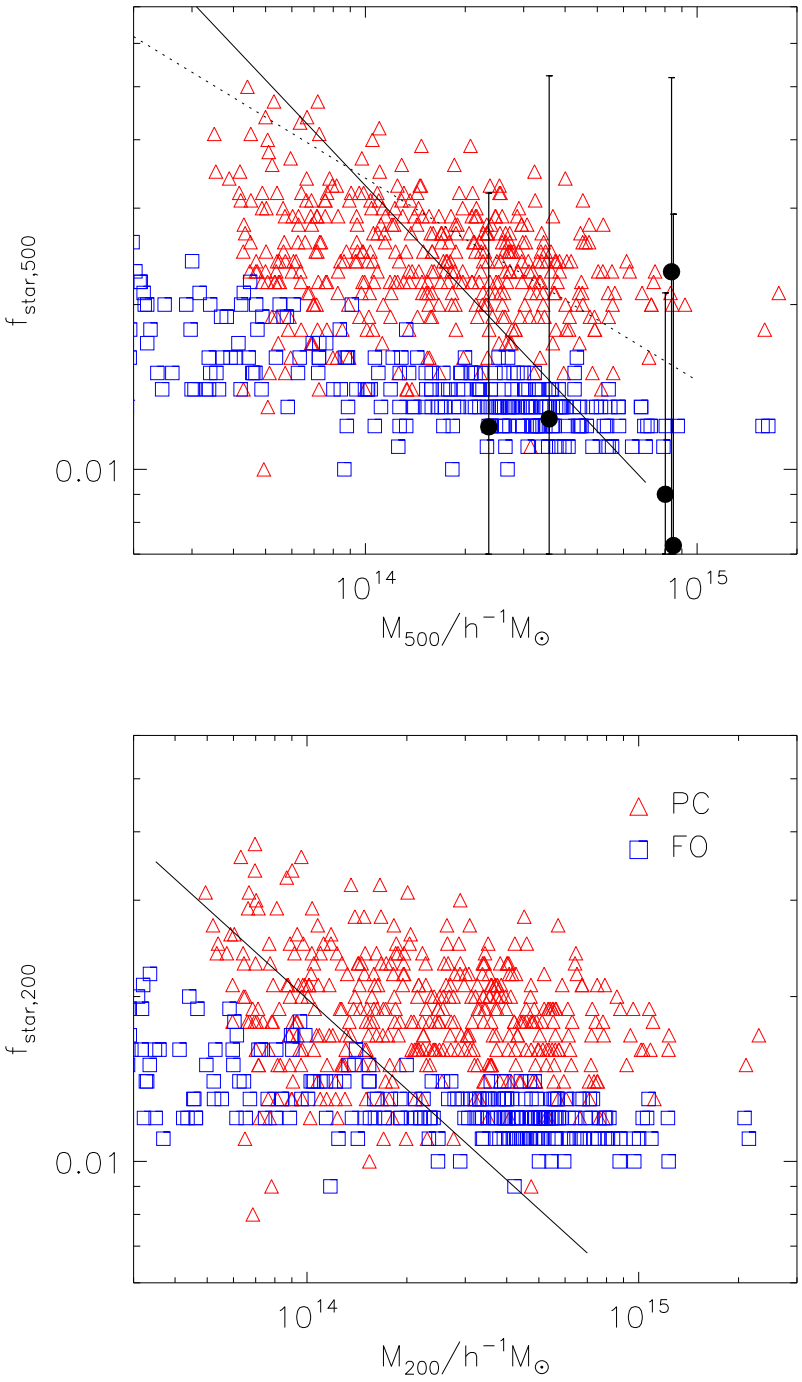

Figure 4.10: The cumulative stellar fraction versus mass. The upper panel shows the stellar fractions within r_{500}; the black dots are observed clusters from LLA08, the solid line shows the observed relation from GZZ07, and the dotted line that from GPF09. The lower panel is the stellar fraction within r_{200}, with the solid line showing the observed relation from Andreon (2010).

Scatter in the scaling relations

In this section we briefly investigate why some clusters have slightly more hot gas, and others slightly less, than other clusters of the same mass (a more in-depth investigation is given in chapter 5). Our purpose in doing this is two-fold: firstly to understand the physical reason for this scatter, and secondly to suggest corrections that can be applied to the observations to better allow gas fraction to be used as a probe of cosmology.

First note that, as is evident from Figure 4.4, the mean gas fractions in the GO run are independent of mass. However, there is scatter about the mean gas fraction that we might hope to relate somehow to the physical properties of the cluster.

We have checked for correlations of the scatter with every conceivable physical quantity (including substructure, merging history, angular momentum, etc.) and find many weak correlations, but no strong one. Figure 4.11 shows a positive correlation with concentration, i.e. more concentrated clusters have a greater gas fraction than the average within r_{2500}. Likewise, clusters that form earlier have a greater gas fraction than those that form later. The correlation coefficients for these two relations are 0.29 and -0.23, respectively. These may be two aspects of the same relation as concentration shows a negative correlation with formation time. Appendix B describes how we measure each of these for the clusters in our simulation. Both are correlated with cluster mass, but it turns out that they are more strongly correlated with each other.

The physical mechanism that may drive the correlations seen in Figure 4.11 is unclear: it primarily affects the core of the cluster as the correlations get weaker if one measures the gas fraction within larger radii. It may be that the degree of gravitational pre-heating is greater in systems that form later (see, e.g., Mo et al., 2005).

Other quantities that we have tested include the halo angular momentum, merger history and substructure. Once the primary correlation of gas fraction with mass is removed, none of these show any correlation with the residual gas fraction.

Observationally, of course, an excess core gas fraction is associated with an increase in X-ray luminosity. Thus, as shown in Figure 4.12, the excess luminosity of a cluster above the mean $L_{\rm X}$-$T_{\rm sl}$ relation is correlated with the presence of excess gas in the cluster. The correlation coefficients in this case are 0.51 and 0.73 for the PC and for the FO run, respectively. A similar result was found for the PC run by Stanek et al. (2010). This correlation may serve to reduce the scatter from the major outliers in the gas fraction-mass relation.

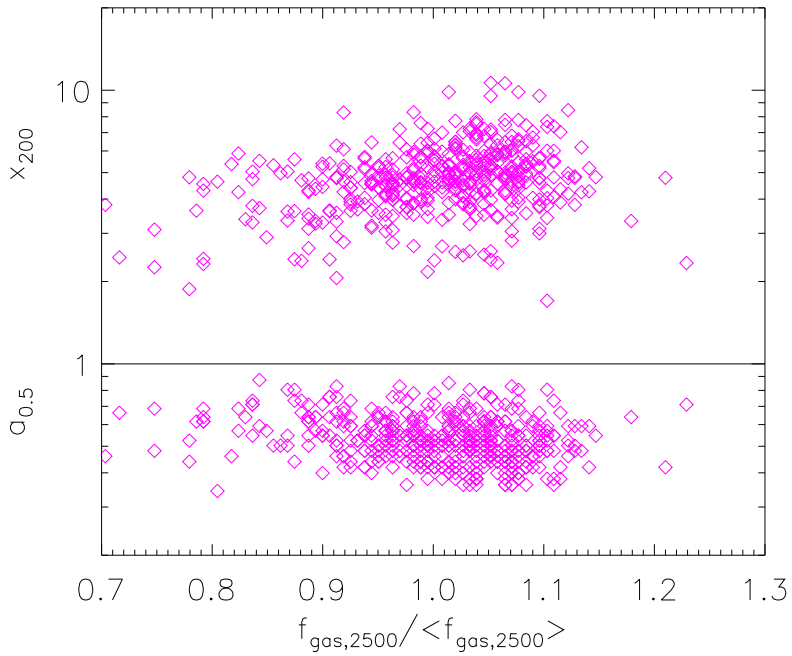

Figure 4.11: The strongest correlations of the scatter in the mean gas fraction within r_{2500} for the GO run. The upper points show the cluster concentration, and the lower points the expansion factor of the Universe at the time that the cluster had accumulated half its final mass.

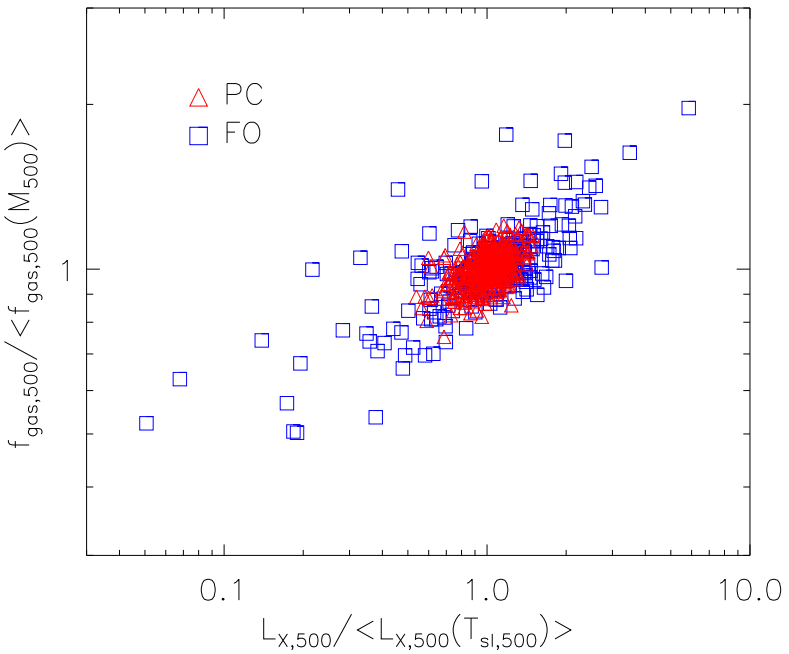

Figure 4.12: The deviation from the mean gas fraction-mass relation plotted against the deviation from the mean luminosity-temperature relation. Properties are measured within a radius of r_{500}. Shown are the ratio of the measured quantities compared to that of the best-fitting mean relation.

4.2.3 Evolution

Profiles

Figure 4.13 shows the evolution of the cumulative gas fraction profiles of the 10 most massive clusters, for each of the runs.

Looking first at the GO run in the upper plot, it can be seen that the gas fraction within r_{500} remains largely constant over time: this is to be expected for self-similar evolution. As the effective resolution increases (i.e. the ratio of the smoothing length to r_{500} decreases) so the gas fraction within the cluster core can be seen to be depleted, though still much higher than in the other two runs.

In the PC simulation, the gas fractions at high redshift are much reduced over their present-day values. This is because a large amount of energy has been injected into the ICM at early times, expelling gas from the clusters. Subsequently, the gas falls back into the clusters as the Universe evolves and tends towards (but falls far short of) self-similar evolution. In other words, the early entropy injection becomes relatively less important in more massive systems at late times.

This is in contrast to the behaviour in the FO run. Here we have continual injection of energy so that gas fraction profiles remain constant over time. Although our simulation takes its level of feedback from a semi-analytic model, nevertheless it seems to have achieved a homologous evolution.

Thus, although the PC and FO clusters have indistinguishable gas profiles at the present day, they look very different in the past. This casts doubt on the use of the measured gas fraction as a cosmological probe, but instead opens the possibility that it can be used to determine the nature of the feedback mechanism: in particular to distinguish between early (PC) and continual (FO) heating.

Scaling relations and comparison with observations

Figure 4.14 shows the hot gas fractions within r_{500} at a redshift $z = 1$ for clusters in our three simulations. For comparison, we also plot high-redshift systems ($0.8 \leq z \leq 1.3$) from a catalogue of clusters observed with *Chandra* compiled by Maughan et al. (2008). Note that Maughan et al. (2008) do not themselves present $f_{\rm gas}$ values. To compute them, we first determine the total mass, M_{500}, from the supplied values of $Y_{\rm X}$ (where $Y_{\rm X}$ is defined as the product of the gas mass within r_{500} and the spectroscopic-like temperature in the spherical annulus $0.15\,r_{500} < r \leq r_{500}$) by using the $Y_{\rm X} - M_{500}$ relation derived from the sample of Vikhlinin et al. (2006). This is the procedure adopted by Maughan

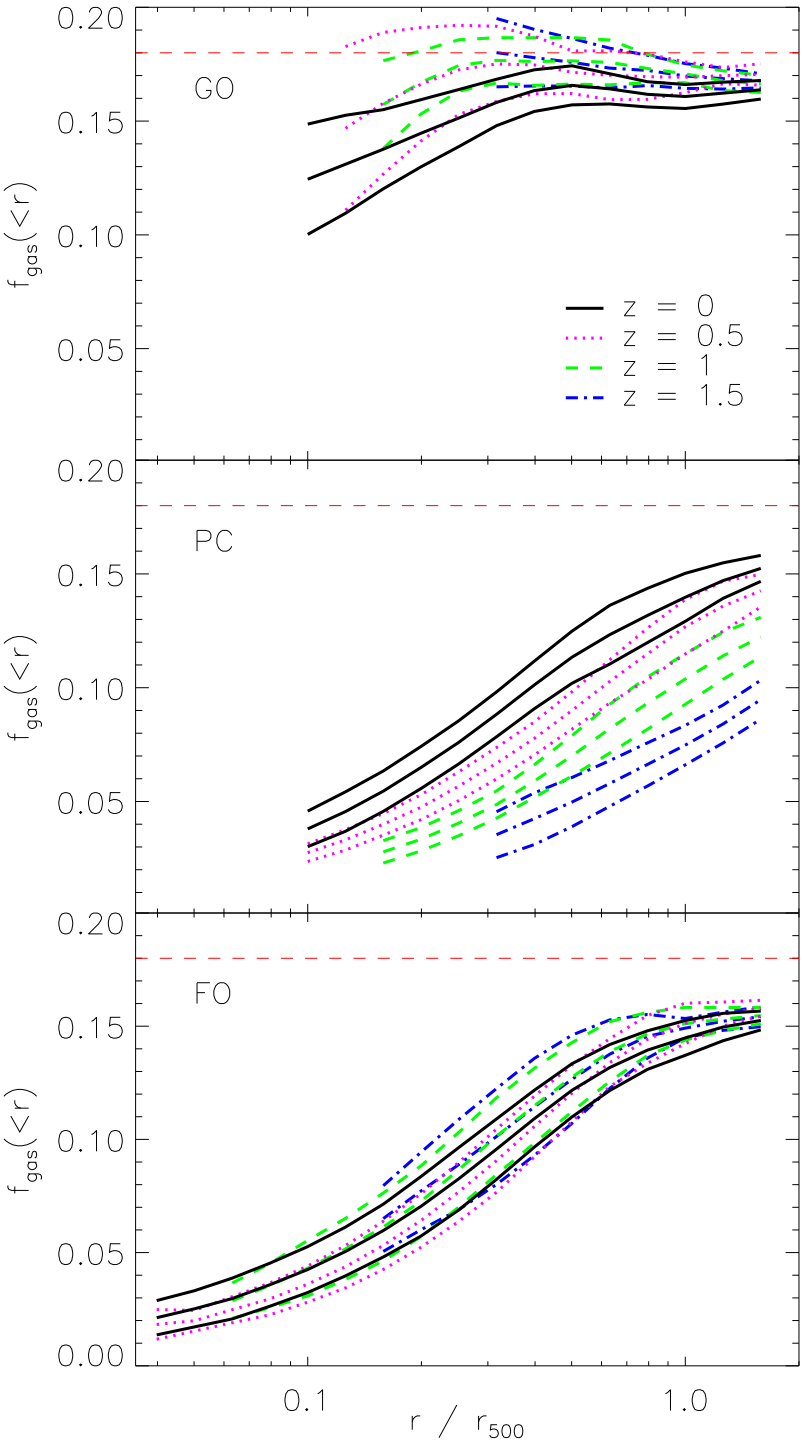

Figure 4.13: The evolution of the cumulative gas fraction profiles of the 10 most massive clusters. In each case the dot-dashed blue, dashed green, dotted magenta and solid black lines correspond to z =1.5, 1, 0.5 and 0, respectively. The middle line of each set is the mean of, and the upper and lower the 1-sigma spread in, the gas fraction profiles. The red dashed line is the universal mean.

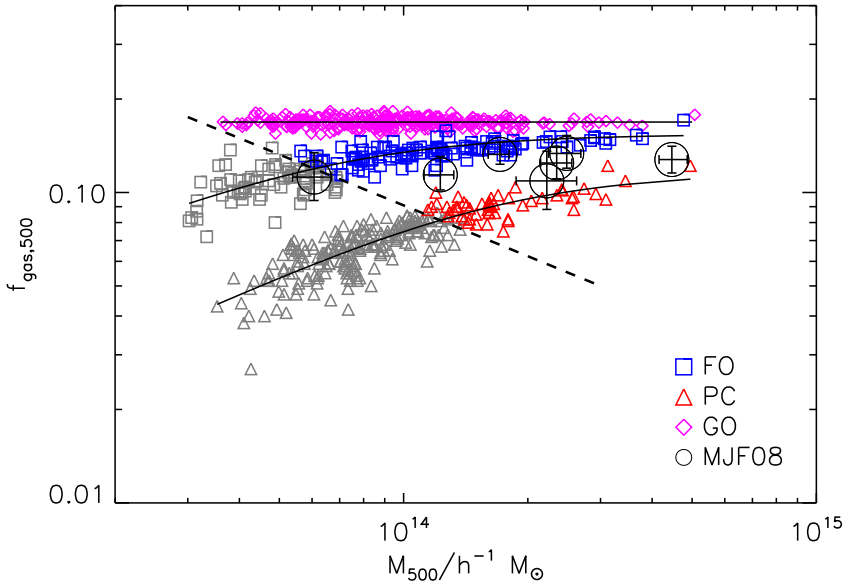

Figure 4.14: Gas fractions within r_{500} at $z = 1$ as a function of total mass. The solid lines show the best-fit mean relations. The black circles are high-redshift clusters ($0.8 \leq z \leq 1.3$) from the observational dataset of Maughan et al. (2008). The dashed line illustrates the effect of imposing a typical survey flux limit of $6.5 \times 10^{-14}\,\mathrm{erg\,s^{-1}\,cm^{-2}}$ at $z = 1$; only clusters to the right of this line would actually be observed by such a survey (the observed cluster slightly to the left of this line is at a lower redshift $z \approx 0.8$).

et al. (2008, see their Equation 4). The gas fraction then follows upon taking the ratio of the gas mass interior to r_{500} (tabulated in their paper) to the total mass. The errors on the observational data points in Figure 4.14 are computed using the supplied statistical errors on the gas mass and the core-excised temperatures. We compute errors on f_{gas} in this way, rather than using the errors on Y_{X}, because the gas mass and temperature are independent measurements.

The different evolutionary behaviour of the gas fraction profiles is reflected in that of the mean gas fractions: the PC clusters have significantly smaller gas fractions at early times than those in the FO run. On the whole, the predictions of the FO model provide a closer match to the observational data than those of the PC model, but it seems as if some of the observed data points lie below the lower edge of the FO $f_{\mathrm{gas}} - M_{500}$ relation. This could be because the mean cosmic baryon fraction in our simulations is higher than that measured by WMAP. If we were to repeat our simulations with the measured value of f_{b}, we would expect all relations in Figure 4.14 to be shifted downwards, improving the agreement between our FO model and the observations.

However, we note that the observational mass estimates may be lower than the true mass, because they are derived from a $Y_X - M_{500}$ relation that was calibrated using clusters with hydrostatic mass estimates. Simulations have shown that the assumption of hydrostatic equilibrium can bias such mass estimates low by $\sim 10-20\%$ (Rasia et al., 2006; Kay et al., 2007; Nagai et al., 2007; Burns et al., 2008; Piffaretti and Valdarnini, 2008; Meneghetti et al., 2010), because of additional pressure support provided by subsonic bulk motions in the ICM and/or non-thermal components. This would imply a small systematic over-estimate of the gas fraction, so the observational data points in Figure 4.14 should be shifted downwards and to the right. Another potential source of systematic error is that the masses of high-redshift clusters in the sample of Maughan et al. (2008) were determined by assuming self-similar evolution of the $Y_X - M_{500}$ relation.

It is also important to consider the effect of source selection on our results. Observational cluster selection is based on X-ray flux, so may be biased towards systems with higher baryon fractions, particularly at high redshift. It is not possible to quantify this effect precisely using the archival sample of Maughan et al. (2008) since their selection function is unknown. A simple way of estimating the impact of selection effects on our findings is to ask the question: given a typical flux-limited survey, which of our simulated clusters would actually be observed? For illustrative purposes, we choose a flux limit of $6.5 \times 10^{-14}\,\mathrm{erg\,s^{-1}\,cm^{-2}}$, equal to that of the WARPS survey (Horner et al., 2008) from which many of the objects in the Maughan et al. (2008) sample are drawn. The effect of imposing this flux limit at $z = 1$ is shown by the dashed line in Figure 4.14; only objects to the right of this line would be observed by a WARPS-like survey. Note that one of the clusters from Maughan et al. (2008) lies slightly to the left of this line; this is because it is at a lower redshift, $z \approx 0.8$. The important point to note is that, for both the PC and FO runs, there is only a narrow mass range where the bias is significant, with most clusters in the two samples remaining unaffected. Even if we took a much higher flux limit, it would require greatly increased scatter about the PC $f_{\mathrm{gas}} - M_{500}$ relation for consistency with the observations, which is not intrinsic to the model.

The best-fit parameters to the scaling relation of Equation 4.1 are shown as a function of redshift in Figure 4.15. In the case of the GO run, we fit only the mean value of the gas fraction, f_0, which is well-determined. For the other two runs, the shaded regions show the 1-sigma allowed parameter range determined from monte-carlo markov chain fitting. The parameters show considerable scatter, but this scatter is highly correlated. So while it is formally possible for both the PC and FO clusters to have the same value of f_0 at

Table 4.3: Best fit straight lines to the evolution with redshift of the gas fraction model parameters shown in Figure 4.15. These fits take the form $p = p_0 + s_p z$, where p is the parameter, p_0 its value at $z = 0$, and s_p the slope of the relation with redshift.

Parameter	Model	p_0	s_p
m	PC	14.23	0.00
	FO	14.30	-0.44
s	PC	0.53	0.08
	FO	0.51	0.01
$\log_{10} f_0$	PC	-0.870	-0.065
	FO	-0.834	0.022

$z = 1$, for example, the other parameters must adjust themselves so as to maintain the difference in gas fraction seen in Figure 4.14.

The solid lines in the upper three panels of Figure 4.15 show straight-line fits to the evolution of each of the parameters with redshift – note that we fit to $\log_{10} f_0$ rather than f_0 as it is the former that appears in Equation 4.1. These fits are listed in Table 4.3 and are used in the following section when comparing our model predictions with observations.

From the straight-line fits shown in Figure 4.15, the mean gas fraction within r_{500} can be predicted for clusters of given mass and redshift using Equation (4.1). This prediction is compared to observed gas fractions from the sample of Maughan et al. (2008) in Figure 4.16. What is plotted here is the ratio of the observed gas fraction to the predicted one, so that perfect agreement would correspond to a value of unity, independent of redshift, but with some scatter due to the cluster-to-cluster variation and measurement error. The data are presented in this way since the gas fraction is a function of both cluster mass and redshift. The error bars are computed using the errors on the observed gas fractions (see above for details of how these were determined from the data of Maughan et al. 2008), accounting for the fact that the error on the total mass introduces an extra uncertainty when computing the theoretical prediction for the gas fraction.

It is immediately apparent that observations favour the FO prediction over the PC one, i.e. limited evolution in gas fraction since $z = 1$. This is shown in Table 4.4 where we list the allowable parameter ranges for straight line fits to the data both in linear and in $\log y$–$\log(1 + z)$ space, where y is the ratio of observed to predicted gas fraction within r_{500}.

In making these fits, we treat the scatter about the mean relation as an unknown,

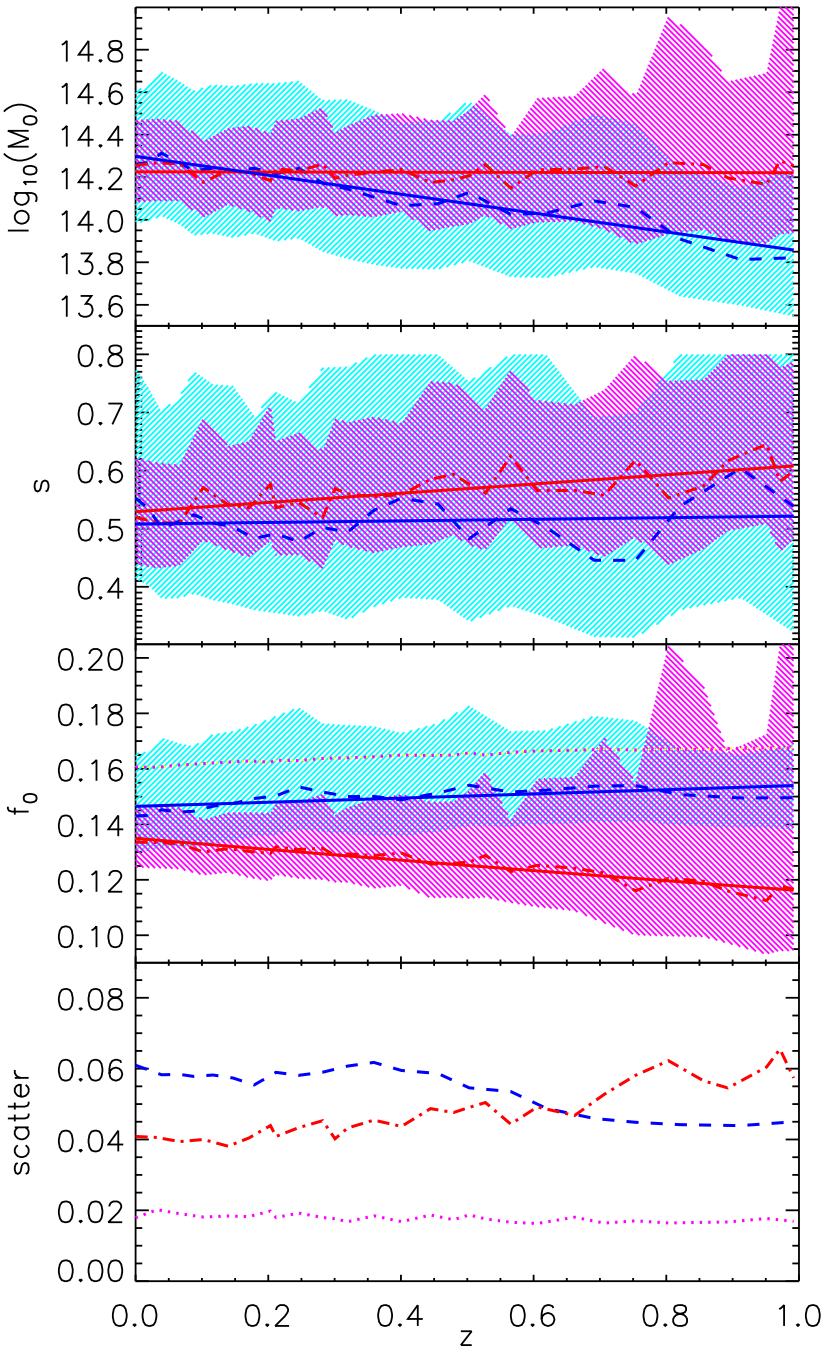

Figure 4.15: Evolution of the fitting parameters of Equation 4.1 for the gas fraction within r_{500}: GO (dotted, magenta on yellow), PC (dash-dotted, red on magenta) and FO (dashed, blue on cyan) lines. The shaded region in each case shows the 1-sigma allowed parameter region. The lowest panel shows the rms scatter in dex about the best-fit relation. The solid lines in the upper three panels show the best fit linear relations to the redshift evolution of the parameters.

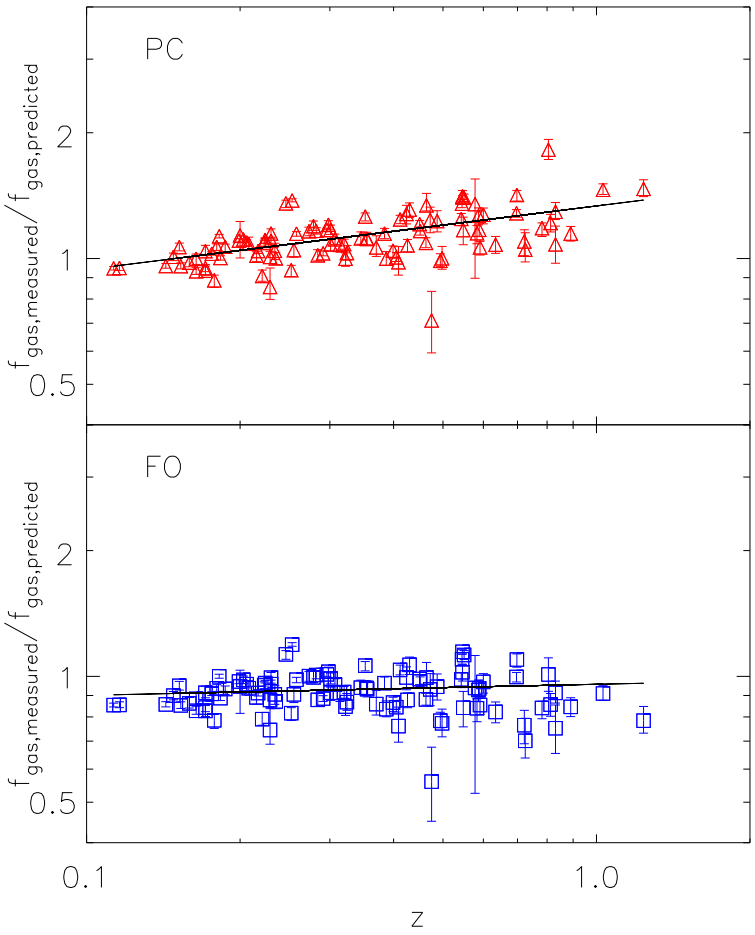

Figure 4.16: Ratios of the observed hot gas fractions within r_{500} from Maughan et al. (2008) to our model predictions. The solid lines show the best straight-line fits in $\log y$–$\log(1+z)$ space.

Table 4.4: Best fit straight lines to the observed versus predicted hot gas ratios seen in Figure 4.16 in linear and in $\log y$–$\log(1+z)$ space. The allowed 1-sigma parameter ranges are calculated assuming that the expected variance about the best fit is equal to the observed one. The scatter is the root-mean square scatter about the best-fit line after allowing for the observational errors. In the log-log plots, the scatter is expressed in dex.

Model	const	slope	scatter
PC linear	0.960 ± 0.022	0.436 ± 0.064	0.074
log	0.126 ± 0.012	0.152 ± 0.020	0.028
FO linear	0.923 ± 0.019	0.002 ± 0.050	0.071
log	-0.019 ± 0.012	0.026 ± 0.020	0.034

$\sigma_{\rm scatter}$, independent of mass and redshift. The data are not good enough for a more sophisticated model, and that is likely, anyway, to make little difference to the fit. Given observational data, y_i, and errors, σ_i, we estimate the scatter as

$$\sigma^2_{\rm scatter} = \frac{\frac{1}{N-2}\sum_i \frac{(y_i - y_{i,\rm fit})^2}{\sigma_i^2} - 1}{\frac{1}{N}\sum_i \frac{1}{\sigma_i^2}}, \tag{4.2}$$

where $y_{i,\rm fit}$ are the best-fit values. We iterate to convergence in $\sigma_{\rm scatter}$, at each stage minimising the chi-squared statistic

$$\chi^2 = \sum_i \frac{(y_i - y_{i,\rm fit})^2}{\sigma_i^2 + \sigma^2_{\rm scatter}}. \tag{4.3}$$

Note that the scatter about the best-fit line is, in each case, lower than that seen in the simulations (as shown in the bottom panel of Figure 4.15). Formally, therefore, neither of the models is a good fit. However, it seems unlikely that the true scatter in $f_{\rm gas}$ will be below that seen in the PC simulation. The uncertainty in the observed $f_{\rm gas}$ values is hard to determine, particularly at high-redshift, so it is quite possible that the size of the error bars has been over-estimated, leading to an under-estimate of the intrinsic scatter.

For the PC simulation, the slope of the observed to simulated gas fraction ratio is incompatible with a horizontal line with high significance. The difference between the best-fit values at $z = 0.1$ and $z = 1$ is about 6 times the scatter. Even if we were to account for observational bias in flux-limited samples towards clusters with higher baryon fractions, especially at high redshift, this is simply too large a difference to be explained by selection effects alone (recall our discussion of Figure 4.14). We conclude that the PC model can be ruled out as a viable cause of entropy generation in the ICM.

The FO simulations, on the other hand, are perfectly consistent with a constant ratio of approximately unity. The slightly lower mean hot gas fraction for the observations as compared to the simulations can be explained by the fact that the latter have a higher mean baryon fraction than the *WMAP* 7-year value.

We note that the analysis of Ettori et al. (2009) has many clusters in common with Maughan et al. (2008), but lists total masses and gas fractions that are often in disagreement. We are not certain why this is but note that there are differences in the analysis of the data, particularly in the cluster outskirts. We have repeated the analysis described in this section with the data of Ettori et al. (2009) but the data are much less constraining, principally because they quote much larger error bars. Nevertheless, one should bear in mind that systematic errors in the assumptions made in the data analysis could be degenerate with differences in the simulated ICM physics.

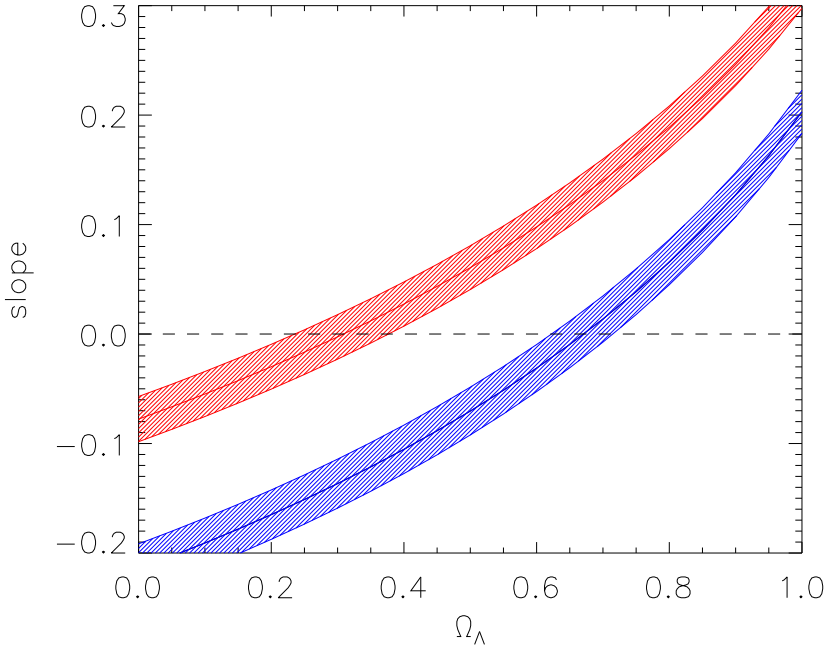

Figure 4.17: The relationship between the slope in log-space of the observed/simulated gas fraction ratio as a function of redshift and the value of Ω_Λ. The upper, red curve is for the PC run and the lower, blue curve for the FO run. The shaded regions show the formal 1-sigma confidence regions.

Looking at the problem in reverse, one could ask what errors could be introduced into the determination of cosmological parameters by the choice of an incorrect physical model for the evolution of the ICM. It is not possible to make a precise prediction for this using the current simulations as we only have access to a single realisation with a particular set of cosmological parameters. Nevertheless, fixing the simulated clusters to be the same, Figure 4.17 shows the effect of changing the observed cluster gas fractions in response to different values of Ω_Λ (fixing $\Omega_\Lambda + \Omega_\mathrm{m} = 1$). From this, it can be seen that using an incorrect physical model can have a dramatic effect, larger than that induced by changing cosmological parameters within any reasonable range.

The analysis described in this section is necessarily very naive. A full treatment would require a detailed understanding of the selection function of observed clusters, modelling of the scatter in the scaling relations as a function of redshift, and of the mean relations as a function of cosmological parameters. Nevertheless, none of this is likely to alter the basic conclusion that both observed clusters and those derived from our FO model show little evolution in hot gas fractions within r_{500} out to $z \approx 1$, whereas the PC model predicts a

strong decline.

4.3 Conclusions

In this chapter, we investigated the baryon content of clusters of galaxies in simulations using a variety of physical models for the intracluster medium:

- GO – gravitational heating only with no radiative cooling. The purpose of this model is to test which aspects of the simulation evolve in a self-similar way and to provide a comparison for the other two runs.

- PC - universal preheating to $200\,\mathrm{keV\,cm^2}$ at $z = 4$, plus radiative cooling and star formation. This represents widespread and early heating by objects that lie below the resolution limit of the simulation.

- FO - feedback taken from a semi-analytic model, including heating from both supernovae and active galactic nuclei, but without radiative cooling. The motivation for this model is to test heating from a realistic galaxy population that matches both the luminosity function and the black hole mass function of the current-day Universe.

The differential hot gas fraction profiles of clusters in the GO simulation are approximately constant at radii greater than $0.2\,r_{500}$, lying at 90 per cent of the cosmic mean. In the other two simulations, the profiles rise steeply from a low value in the cluster core before bending over to an approximately constant value at large radii: for the most massive clusters, $kT_{\mathrm{sl}} > 5\,\mathrm{keV}$, this occurs well within r_{500}.

The cumulative hot gas fraction profiles of our clusters in both the PC and FO runs lie well below those of the regular, cool-core (CC) clusters observed by Vikhlinin et al. (2006) and Allen et al. (2008). However, they provide a fair match to the non-cool-core (NCC) clusters found in the REXCESS representative cluster survey (Pratt et al., 2009a).

When we look at integrated gas fractions within fixed radii, the agreement with observations is mixed. The total gas fraction within r_{2500} shows a stronger variation with cluster mass in the simulations than is seen in the observations. On the other hand, the agreement within r_{500} is much better, at least on scales above $5 \times 10^{14}\,h^{-1}\mathrm{M}_{\odot}$. There is a small offset but that can be explained by the fact that we adopt a mean baryon fraction in our simulations that is higher than the current best-fit value from WMAP, respectively 0.18 and 0.168.

A more slowly-varying function of mass is provided by the differential gas fraction between r_{2500} and r_{500}. Unfortunately, the scatter in the observational data is currently too large to allow any meaningful comparison with the simulations.

In agreement with previous work, our simulated clusters show a much smaller dependence of stellar fraction on mass than is seen in observations. Our stellar fractions within r_{500} are about 0.013 for massive clusters, $M_{500} > 10^{15}\,h^{-1}\mathrm{M}_{\odot}$, in the FO run, similar to observed values. The PC run gives slightly higher values, 0.02, whereas previous simulations can have stellar fractions as high as 0.05 (i.e. as much as a third of all the baryons within the cluster turned into stars). On the other hand, for lower-mass clusters, $M_{500} \sim 5 \times 10^{13}\,h^{-1}\mathrm{M}_{\odot}$, our mean stellar fractions of 0.015 (FO) and 0.03 (PC) are much lower than the observed value of about 0.05. We note that there is some theoretical difficulty in understanding such a steep dependence of stellar fraction on cluster mass, and that the observational determination of this mass fraction is difficult, especially in low-mass systems. While this should prove a fruitful line of investigation in the future, it is probably too early to draw firm conclusions about the validity of the models.

We have fitted the gas fractions as a function of mass to relations of the form given by Equation 4.1, with the results shown in Table 4.1. The scatter about these mean relations is lowest for the GO run and significantly larger for the PC, and especially the FO runs. Unfortunately, the observational data are too poor to provide an accurate measure.

For the GO run, we might expect that the scatter about the mean gas fraction-mass relations has a physical origin in the formation history of the clusters. Indeed, there is a weak correlation/anti-correlation of gas fraction with concentration/formation time (most strongly with the expansion factor at the time that the cluster had accumulated half its current mass). The strongest correlation that might be used observationally to correct for scatter in the gas fractions is that between deviation from the mean L_X-T_{sl} relation and the excess gas fraction.

Although the gas fraction profiles are very similar for both the PC and FO runs at $z = 0$, their evolution is very different. In the former gas is heated and expelled from the clusters at early times, so that the gas is depleted at high redshift and gradually falls back into the cluster over time. By contrast, the continual injection of energy in the FO run leads to evolution that is close to self-similar.

The evolution of halo gas fractions can therefore be used as a strong discriminant between models. We compare our simulated clusters with the compilation of *Chandra* clusters from Maughan et al. (2008). The observational data are fully-consistent with

the FO predictions and disagree with the evolution seen in the PC simulation with high significance. We need to be a little careful in interpreting these results as this is a highly biased sample that may well contain a disproportionate number of luminous clusters at high-redshift. However, the scatter in gas fraction is sufficiently small that, even if we only observed those clusters with high baryon fractions at high redshift, the disagreement between the observations and the PC prediction would still be significant. We conclude that the observations favour continual heating, as in our FO model, over significant pre-heating at high redshift.

A corollary of the strong dependence of gas fraction evolution on the physics of entropy generation is that it becomes very difficult to use the gas fraction as a probe of cosmology. The differences caused by uncertain gas physics currently swamp those caused by reasonable changes in cosmological parameters. In the future, as both observational data for high-redshift clusters and models of the ICM improve, a joint analysis should be undertaken that considers variations in both cosmological parameters and cluster physics.

The main limitation to our present study is that the absence of cooling in our FO simulation leaves us unable to model CC clusters. Whilst that does not significantly affect the gas fractions when integrated out to r_{500}, it would be clearly desirable to also reproduce the full range of gas fraction profiles at smaller radii. We are working on ways to introduce cooling into the FO scheme without leading to excess production of cooled gas in CC clusters.

Chapter 5

Scatter in the hot gas fractions

This chapter concerns the investigation into the causes of the scatter in the hot gas fraction for our simulated galaxy clusters. Techniques for determining the relationships containing the least scatter are discussed, followed by an explanation of how to identify the causes of the deviations from this relationship. The potential causes of scatter in the gas fraction are discussed, then examined for Millennium Gas clusters.

5.1 Introduction

Galaxy clusters are the largest virialised objects in the Universe. They form by condensing at overdensities in the early Universe and eventually freeze out of the Universe's expansion to leave a snapshot of the Universe at the time of their formation (as detailed in chapter 1). On account of their large size, they are thought to contain a representative sample of the Universe at their formation time, in particular (as far as this chapter is concerned) the gas fractions of clusters are often used to constrain the universal baryon fraction (Grego et al. 2001; Ettori et al. 2003; Allen et al. 2004 and first discussed by White et al. 1993).

It has been shown in both observations (Evrard, 1997; Vikhlinin et al., 2006; Andersson et al., 2010) and simulations (e.g. Bialek et al. 2001), however, that there is not only a variation in the gas fraction with cluster mass, but there is also a considerable amount of scatter about this relation.[1]

Whilst the mass dependence poses potential problems with the use of clusters as estimators of the universal baryon fraction, it is not insurmountable. As can be seen in figure 5.1, and also in McCarthy et al. (2007) and Allen et al. (2008), there is a mass threshold

[1] It has also been reported - in the simulations of Crain et al. (2007) and the observations of Gastaldello et al. (2007) - that there is no dependence on the gas fraction with mass, but Crain et al. (2007) are only considering the adiabatic case and the results of Gastaldello et al. (2007) show huge scatter.

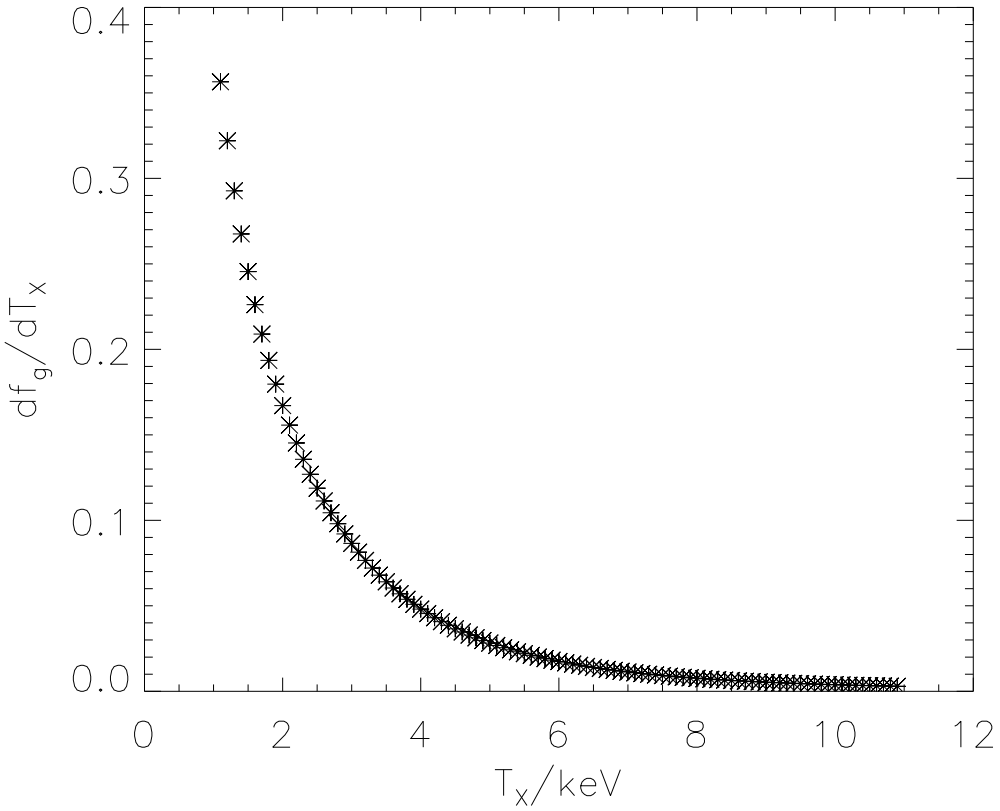

Figure 5.1: The slope of the hot gas fraction - bolometric temperature relation in varying temperature bins for the PC simulation. A flattening can clearly be seen at higher tempertaures, but there is some debate as to the exact temperature above which the gas fraction is constant.

above which the gas fraction ceases to vary (4keV in McCarthy et al. 2007, 5keV in Allen et al. 2008). It is possible, therefore, to assume there is no mass dependence for sufficiently large clusters, with the added convenience that they are more readily observed than their smaller relatives.

The scatter about the gas fraction - mass relation is a more subtle problem. Since the causes of this scatter are unknown, it is not possible to know whether an observed cluster has a high, low, or middling gas fraction for its mass. It is likely that, since the baryons are the only directly observable component of the cluster, observations (particularly those at high redshift where photon counts may be small) are systematically favouring those clusters with positively scattered gas fractions. Unless this effect is corrected for, it will lead to overestimates in the universal baryon fraction.

In order to eliminate this potential bias, it is therefore necessary to infer a cause, or causes, of this scatter in the gas fraction. There is no theoretical work published on this subject.

5.2 Method

The Millennium Gas simulations provide an excellent opportunity to study the causes of the scatter in the gas fraction. The large number of objects contained in these simulations allows a robust statistical study of the scatter to be performed. The challenge is then to find a method to study this large, multi-dimensional dataset and the correlations between relevant variables in a rigourous and quantitative manner.

We use a technique, similar to principal component analysis (PCA), but in which we can fix a particular variable and determine the appropriate combination of the remaining variables to minimise the scatter.

PCA is a procedure for transforming a number of possibly correlated variables into a smaller number of uncorrelated variables - principal components. The first principal component corresponds to the direction (in the space of the dataset) containing the maximum variation, the second principal component corresponds to the direction of the second largest variation and so-on, with each principal component being orthogonal to all the others. Thus, one ends up with a number of principal components equal to the number of dimensions of the original dataset.

5.2.1 Determining the contributions to the scatter

PCA is useful when looking at each relationship within a dataset, however, when one wants to examine only the variation in a single variable caused by the other variables it is useful to use a different analysis.

Suppose one wishes to minimise the scatter in the quantity x_i (figure 5.2). It is necessary to minimise the scatter in:

$$f = \min_{\alpha_j, c} \sum_d \left(x_i - \sum_{i \neq j} \alpha_j x_j - c \right)^2 \tag{5.1}$$

Where d runs over all the data points and α_j and c are undetermined coefficients which will be chosen to minimise the function. At its minimum, $\alpha \partial f / \partial c = 0$ or $\partial f / \partial \alpha_k = 0$:

$$\frac{\partial f}{\partial c} = 0 \rightarrow \sum_d \left(x_i - \sum_{j \neq i} \alpha_j x_j - c \right) = 0 \tag{5.2}$$

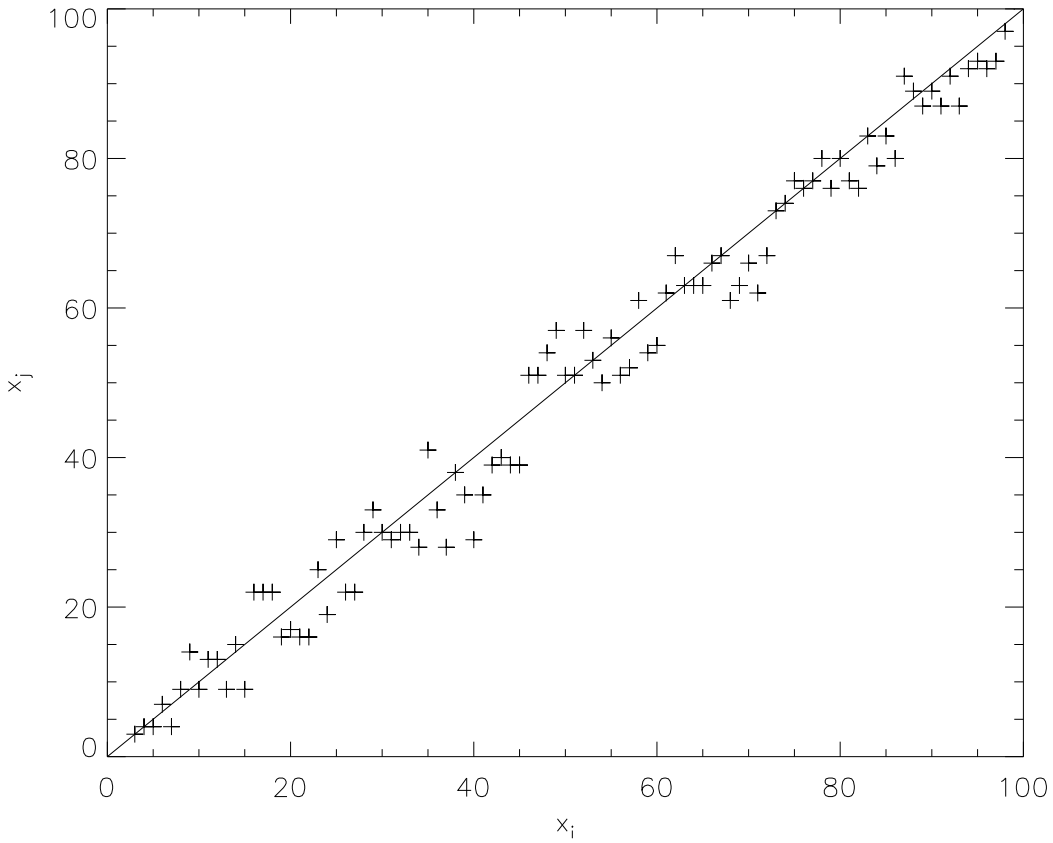

Figure 5.2: Variable x_i has some dependence on variables x_j and some scatter thereabouts

$$\frac{\partial f}{\partial \alpha_k} = 0 \rightarrow \sum_d \left(x_i - \sum_{j \neq i} \alpha_j x_j - c \right) x_k = 0 \tag{5.3}$$

Equation 5.2 can then be rewritten as equation 5.4

$$\sum_d c = \sum_d x_i - \sum_{j \neq i} \alpha_j \sum_d x_j \tag{5.4}$$

leading to:

$$c = \bar{x_i} - \sum_{j \neq i} \alpha_j \bar{x_j} \tag{5.5}$$

where $\bar{x}$ is the mean of x.

Now the expression for c from equation 5.5 can be substituted into equation 5.3 to give equation 5.6

$$\sum_d \left[(x_i - \bar{x_i}) - \sum_{j \neq i} \alpha_j (x_j - \bar{x_j}) \right] x_k = 0 \tag{5.6}$$

and, since $\sum (x_j - \bar{x_j}) = 0$, this leads (perhaps postulatively) to:

$$\sum_{j \neq i} \sum_d (x_j - \bar{x_j})(x_k - \bar{x_k}) \alpha_j = \sum_d (x_i - \bar{x_i})(x_k - \bar{x_k}) \tag{5.7}$$

This is now a linear algebra problem we must solve to get the values of α_j which determine the combination of the $N - 1$ variables in an N variable dataset such that the scatter in a given variable, with respect to all the others is minimised. Code for doing this, based on pre-existing linear algebra libraries in contained in appendix C.

The practical use of this is to take datasets containing the variable of interest together with those variables believed to be correlated with it. The contributions of the variables to the scatter can then be readily examined.

5.2.2 Merger trees

Since mergers are important events in cluster histories, these must be defined and quantified. This is done via merger trees. Merger trees are created from raw particle data and describe the evolution of galaxy clusters in terms of their interaction with other clusters.

As the Millennium Gas simulations are carried out in the same box as the Millennium Simulation, we are able to use its merger tree information which has already been generated.

Merger trees for the Millennium Simulation are generated in postprocessing as opposed to on the fly, therefore the only data available from which to construct the merger trees is that at the written snapshots.

The full method for creating these merger trees is described in Springel et al. (2005), but is briefly summarised here.

There are several stages to constructing a merger tree, the first of which is to locate friends-of-friends groups with a linking length of 0.2 times the average inter-particle separation, which are then decomposed, using the SUBFIND algorithm (Springel et al., 2001), into gravitationally bound haloes[2] and subhaloes[3], which are the objects used to construct the merger trees. These substructures are overdense regions within the friends-of-friends group. Substructures with fewer than 20 particles are not considered to be genuine, and such particles are termed 'unbound'. The unbound material typically makes up 10% of the mass of a friends-of-friends group (Springel et al., 2001) with the subhaloes being composed of the remaining 90%. These gravitationally bound haloes (aggregations of subhaloes) and subhaloes are the objects the merger tree attempts to track.

The next step is then the determination of a descendant for each (sub)halo residing in a future snapshot - usually the subsequent snapshot. This procedure is done recursively until the present day. The halo merger trees are stored in such a way that is optimal for walking backwards from lower redshift haloes. A schematic for a merger tree is shown in Figure 5.3

5.2.3 Matching clusters

Merger trees have been created for the Millennium Simulation and, since the Millennium Gas simulations are carried out using the same initial conditions, it is possible to use the Millennium merger trees to describe the evolution of Millennium Gas clusters.

The Millennium Gas clusters are matched with Millennium haloes at redshift 0 by a two stage process:

Firstly, extract all the halos from the Millennium database with a mass greater than, or roughly equal to the mass of the smallest cluster in the cluster catalogue. There will typically be more haloes than objects in the catalogue due to the higher resolution in the Millennium Simulation.

Secondly, loop over each cluster finding the closest halo with a mass approximately equal to that of the cluster of interest.

If a cluster has no suitably massive halo within a tenth of its virial radius then it is assumed that it cannot be matched and is ignored in further analysis. This happens because of discontinuities in the way the merger trees are stored in the database. Objects

[2] Cluster-sized objects

[3] Roughly galaxy-sized objects

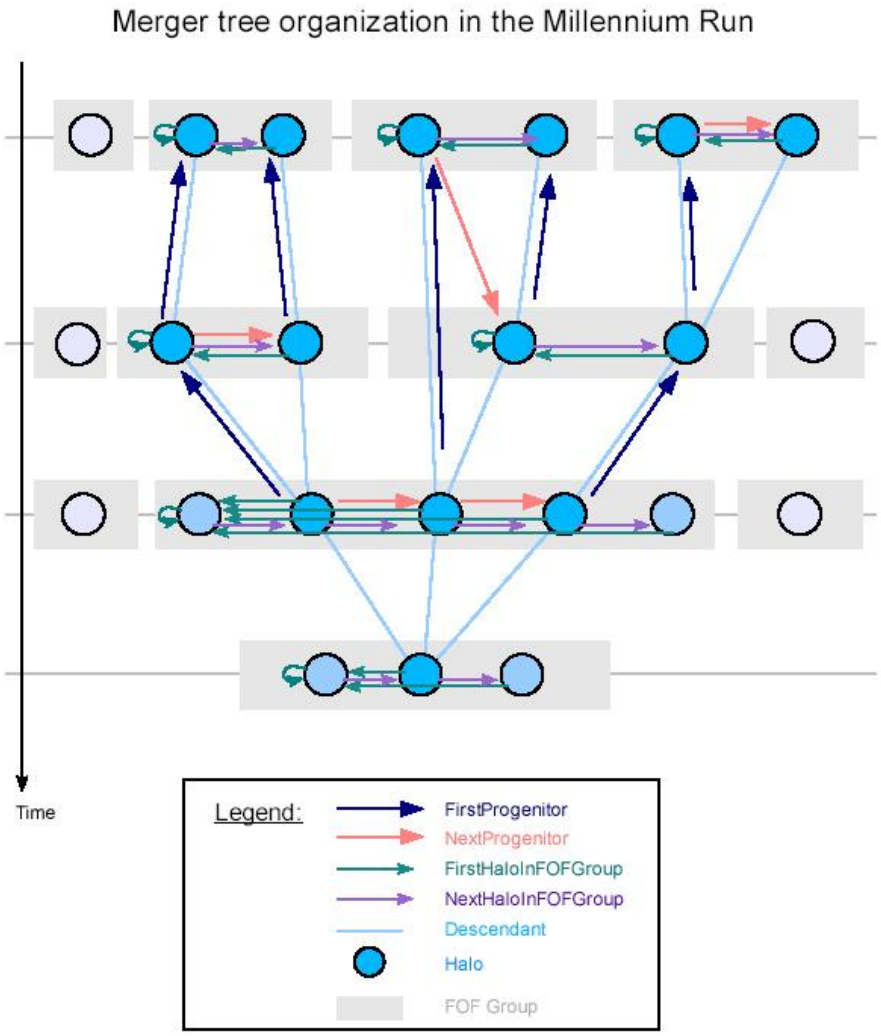

Figure 5.3: The merger tree organisation in the Millennium Simulation database. The lowest object is at a low redshift with horizontal lines of haloes representing higher redshift snapshots whilst more massive objects appear on the left within their FOF group. The distinction between the haloes and the FOF groups can be clearly seen. The position of the halo in the FOF group is required for semi-analytic galaxy formation models.

occasionally 'disappear' from one snapshot to the next (reappearing at a later snapshot). This appears to happen occasionally when objects interact and SUBFIND will mistake two distinct objects for one single one. This method typically returns a halo for 95% of the clusters.
The merger trees for the matched halo are then assumed to apply to the cluster and used when examining its evolution.

Definitions of mergers and formation times

In order to test the effects of mergers on the simulated clusters, it is necessary to define what is meant by a merger. The same is also true of cluster formation times.

All the definitions we propose are based on the numbers of particles[4] in the relevant halo in the merger trees for the Millennium Simulation.

The definitions of formation times are as follows:

1. The snapshot[5] by which the number of particles in the halo's main progenitor has reached a certain fraction of the final number of particles. Fractions used are 0.2, 0.3 and 0.5.

2. The snapshot by which the total mass of all the halo's progenitors has reached a certain fraction of the halo's final number. The same ratios as above are used. SQL queries to extract these numbers can be found in appendix D

3. The time of the last major merger, as defined by the snapshot at which the number of particles in the main progenitor increases by the fractions above. The SQL query for this is contained in appendix E

5.3 Mergers and accretion as causes of scatter

In this section, as well as the next, we discuss potential causes of the scatter. Correlations with these potential causes and the scatter itself are shown in section 5.5.

Galaxy clusters acquire their mass, both the dark and baryonic components, via two processes; accretion of the surrounding cosmic matter and via mergers. Each of these processes is likely to have a different effect on the final cluster gas fraction.

[4]Number of particles is used in preference to mass since one of the quirks of the merger trees for the Millennium Simulation is that not all haloes have masses, although they do all have a particle number.

[5]There only exists merger tree information for each Millennium snapshot, not each timestep.

Matter continuously accreted onto the cluster will have a baryon fraction of close to the cosmic value (0.18) and so a cluster formed entirely of accreted matter is likely to have a gas fraction of close to the cosmic value. If this argument is extended back to the first objects to have formed, they will all have a gas fraction of close to the cosmic mean and so any mergers between such objects will not alter the gas fraction of the final object. This can be seen in the GO simulation in which cluster gas fraction scales self similarly.

In the PC run, at a redshift of just over 4 (just before the preheating event), the cluster gas fraction shows this self similar behaviour. Just after preheating, the gas fraction in these already-formed objects will be lower, and will show a mass dependency[6]. They will, however, continue to accrete the surrounding matter, which will raise their gas fractions. Thus, objects with a greater proportion of their mass already formed into clusters at $z = 4$ will have acquired less of their mass via post-preheating accretion, and will therefore have lower gas fractions than objets which have done more post-preheating accretion.

We therefore suggest that the amount of matter accreted since $z = 4$ (for the PC run - this will be more complicated for the FO run) will have an effect on the scatter in the present day gas fraction (equation 5.8).

$$\frac{f_g}{\bar{f}_g} = \frac{f_{g,cosmic}}{\bar{f}_g} + \frac{M_{z=4}(f_{g,z=4} - f_{g,cosmic})}{M_{z=0}\bar{f}_g} \tag{5.8}$$

where $\bar{f}_g$ is the mean gas fraction of a cluster of mass M at $z = 0$, and $f_{g,z=4}$ is the gas fraction of a cluster of mass M, immediately following preheating.

Clusters also grow via mergers. In the FO and PC simulations, where gas fraction is a function of cluster mass, these mergers will affect the gas fraction of the formed object. The argument goes as follows:
Suppose cluster B merges with cluster A, where, for the sake of argument cluster A is more massive than cluster B. Since cluster B has a lower gas fraction, the gas fraction of the merged cluster will then have a gas fraction lower than A's original gas fraction (and higher than B's), thus being offset from the mean relation. This effect may, however, be very small. If the masses of the two clusters are very different then the effect will also be small since both the total mass and the gas mass of the merged cluster will be very close to that of cluster A (equation 5.9). If, however, clusters A and B are of very similar mass then their gas fractions will also be very similar and so the gas fraction of the merged cluster will be little different to that of either A or B, but may still be lower than that of a cluster of mass equal to the sum of the masses of A and B.

[6] At such a high redshift, all clusters will have $M << M_0$.

$$f_{g,final} = \frac{f_{g,A}M_A + f_{g,B}M_B}{M_A + M_B} \tag{5.9}$$

As explained in chapter 4, section 4.2.2, hot gas fraction is linked to total cluster mass via:

$$\log_{10} f = \log_{10} f_0 + s(\mu - \log\left(1 + \exp(\zeta\mu)\right)/\zeta) \tag{5.10}$$

where $\mu = \log_{10}(M/M_0)$ and f_0, M_0, ζ and s are fitting parameters as laid out in table 4.1.

There must then exist an optimal mass ratio for a merger such that the difference between the gas fraction of cluster A (the more massive cluster) and the gas fraction of the merged cluster is maximised.

For the purposes for which we now use equation 5.10, in the regime $M << M_0$ when the change in gas fraction with mass is most pronounced: $f = sM/M_0 + f_0$.

Therefore, to determine the maximum fractional change in the gas fraction through mergers, it is necessary to maximise equation 5.11; where both M_A and M_B are much lower than M_0 and $\nu \equiv s/M_0$[7].

$$\Delta f_g = \frac{\nu(M_A^2 + M_B^2) + f_0(M_A + M_B)}{f_0(M_A + M_B) + \nu(M_A + M_B)^2} \tag{5.11}$$

where Δf_G is the ratio of the gas fraction of a cluster that has accreted all of its mass, and one of the same mass which has formed via the merger of two smaller objects.

As can be seen from figure 5.4; this mechanism doesn't appear to lead to any great change in the merged cluster's gas fraction. However, the accretion of many small objects could have a much greater effect since it would be similar to merging with a larger object with the gas fraction of a smaller one.

We only study the PC and FO runs for correlations between mergers and formation time since clusters in the GO run show gas fractions independent of mass, and no change in this relation with redshift.

The effects of cluster formation on the gas fraction were studied by Tittley and Couchman (2000). They report that hierarchically formed clusters had lower gas fractions than non-hierarchically formed clusters, suggesting that a cluster's gas fraction can be lowered by multiple mergers with smaller objects. The reason for this is unlikely to be linked to that outlined above since the simulations of Tittley and Couchman (2000) were adiabatic

[7] s has a value of 0.363 for the PC run at an overdensity of 200 (we use 200 here since only it is presented in the Millennium Simulation database from whence we get our figures) and of 0.472 for the FO run. f_0 has values of 0.150 and 0.148 and M_0 has values of $10^{14.43}$ and $10^{14.21}$ respectively.

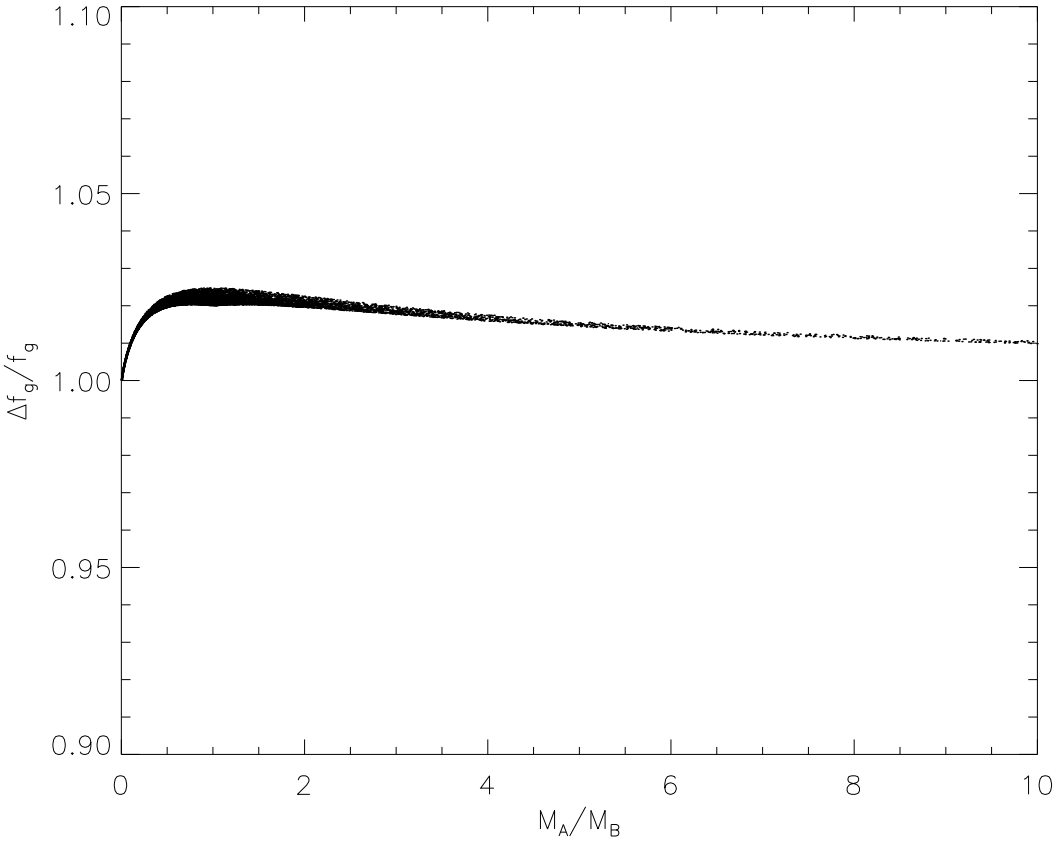

Figure 5.4: The results of a Monte-Carlo simulation calculating the different fractional changes in the gas fraction against the change in mass of the cluster for groups and clusters in the mass range $10^{11} - 10^{15} M_{\odot}$ (well below M_0) using the parameters from the FO simulation. It can be seen that this process is highly sensitive to the particular masses of merging clusters and that a slight difference in initial mass can lead to a relatively large change in the change in the gas fraction. The same plot made with the PC parameters is very similar.

and there was therefore no dependence of cluster gas fraction on mass. Tittley and Couchman (2000) also suggest that there may be increased scatter in lower mass clusters, but we do not find this in our sample.

5.4 More Potential Causes of Scatter

Angular momentum

It is suggested in Dai et al. (2010) that there is a correlation between cluster gas fraction and the cluster's circular velocity. This, along with the cluster's angular momentum was examined as a possible source of scatter in the Millennium Gas clusters.

Substructure

Substructure, as defined via a centroid shift is also examined as a possible cause for the scatter. Clusters with a high substructure are thought to be be either undergoing mergers, or to have recently merged since a large shift in the centroid would seem to indicate a large mass discrepancy in a particular direction.

Concentration

Cluster concentration is determined from the cluster mass at two different radii, typically R_{2500} and R_{500}, by fitting an NFW profile (Navarro et al., 1995) in which the parameters are determined from the two pairs of masses and radii.

5.4.1 Observing scatter

It is likely that there are certain properties of clusters which, whilst not causing the scatter, are nonetheless correlated with it. These properties, if they are observable, are potentially of use in removing any bias in universal baryon fraction measurements caused by the scatter.

Excess luminosity

The most obvious observable property likely to indicate scatter in the cluster gas fraction is lumonosity. Since the baryons are the only luminous component of a galaxy cluster, it is to be expected that an excess of baryons will be likely to cause an excess in the luminosity of a cluster of a particular mass. Likewise a lower than expected luminosity for a given mass is likely to be indicative of a lower than average (for that mass) gas fraction.

Table 5.1: All the global cluster properties considered when examining the scatter in the gas fraction-mass relation divided into fundamental and derived, structural and observable properties.

Fundamental properties			Derived properties
Structural	Observable	Structural	Observable
M_Δ	K_Δ	Concentration	$L_{X,\Delta_1}/L_{X,\Delta_2}$
R_Δ	$L_{X,\Delta}$	$f_{gas,\Delta_1-\Delta_2}$	$T_{sl,\Delta_1}/T_{sl,\Delta_2}$
$f_{gas,\Delta}$	$T_{sl,\Delta}$	$f_{star,\Delta_1-\Delta_2}$	$T_{X,\Delta_1}/T_{X,\Delta_2}$
$f_{star,\Delta}$	$T_{virial,\Delta}$	r_s	$T_{virial,\Delta_1}/T_{virial,\Delta_2}$
Substructure	$T_{X,\Delta}$	$f_{baryon,\Delta}$	Residual $T - M_\Delta$
Velocity substructure		$f_{baryon,\Delta_1-\Delta_2}$	Residual $L - T_\Delta$
P_Δ			
$M_{200}(z=4)$			
$0.2, 0.3, 0.5 \times M_{200}(z=0)a$			

5.5 Results

In the majority of cases results for the PC and FO runs are very similar, so we only present the results for the PC run, unless there is any significant difference between the two. The GO run does differ, but we do not present its results for properties it produces which are known to be poor matches to observations.

5.5.1 Definition of formation time

We have used two different definitions of formation time - one based on the time by which the main progenitor of a cluster has accumulated a given fraction of its final mass, and one based on the time by which the total mass of all progenitors has reached a given fraction of the cluster's final mass. We now show that differences between these definitions and final mass fractions, by examining the relationship between cluster concentration and different formation times.

There is a strong correlation between each fraction used when the definition is based on the total mass of all progenitors, but it is noteworthy that definitions based on the main progenitor and definitions based on the total mass are not strongly correlated (a correlation coefficient lower than 0.8). It is also true that the only two fractions of the main progenitor mass which show a strong correlation are the 0.2 and 0.3; neither shows

a strong correlation with 0.5.

The lack of strong correlations between the total mass and the mass in the main progenitor definitions indicates that these are two quite distinct phenomena and any correlations with formation time may be dependent on the definition used.

Figure 5.5 illustrates the difference between basing the definition of formation time on the mass of the main progenitor and the total mass of all progenitors for the three different final mass fractions. It can be seen that, as well as the expected difference in normalisation, the increased scatter in the main progenitor definitions is evident, particularly for the definitions based on 20% and 30% of the final cluster mass. When defined as 50% of the cluster's final mass there is more scatter than when a smaller fraction is used; additionally there is less of a difference between the definitions based on the mass of the main progenitor and the total mass of all progenitors.

5.5.2 Causes of scatter

Every one of the above-mentioned possible causes of the scatter, shows little correlation with the observed scatter. The best correlation is with the concentration, although the correlation is weak (figure 5.8). The absence of any correlation with the mergers (figures 5.6 and 5.7) is in agreement with the reasoning above. The effect of the accretion of many small objects over a cluster's history could, if they happen in a short enough time span, have the same effect as the merger with a large cluster which still had a low gas fraction, however this effect also fails to explain the scatter in the gas fraction-mass relation (figure 5.9). We could not reproduce the results of Tittley and Couchman (2000) and found no correlation between the gas fraction in the GO run and formation time, nor between the scatter and total cluster mass.

It is noteworthy that, while there is a reasonable correlation between the cluster's concentration and its formation time, the formation time does not correlate with the scatter, as can be seen in figure 5.6.

Since no correlation can be seen between the scatter and the clusters' recent merging histories, we expect that there is also no correlation with substructure since that is higher in disrupted clusters (Kay et al., 2007) and we do indeed find this (figure 5.8).

The purpose of using our method for studying correlations is that the scatter can be examined in terms of a combination of other variables. Since simply examining the correlation coefficients for the residual gas fraction against every other variable yields

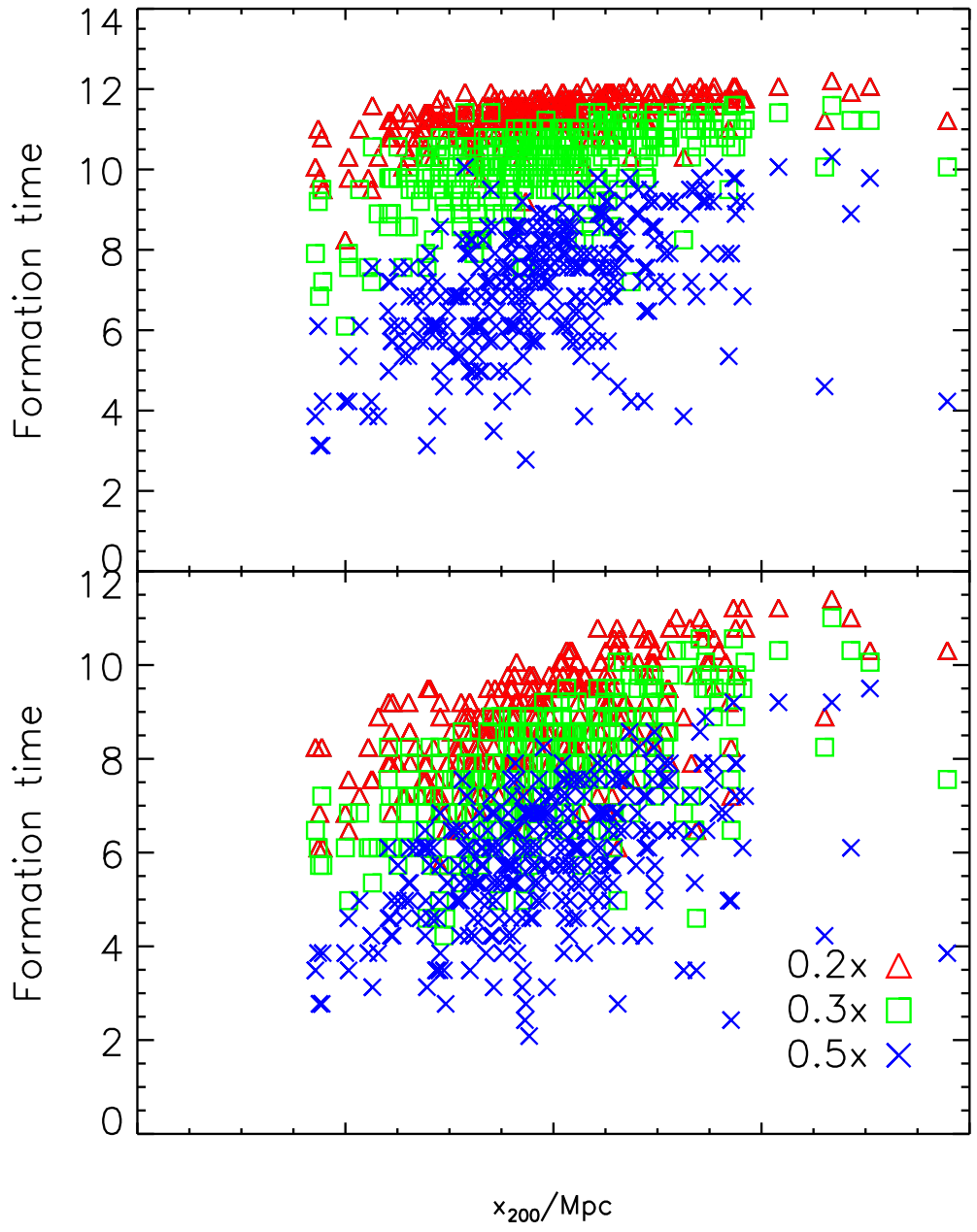

Figure 5.5: The cluster formation time as defined by the fraction of the total mass of all progenitors (top panel) and the mass of the main progenitor for the PC run (bottom panel). x_{200} is the value of r_{500} taken from the fitted NFW profile.

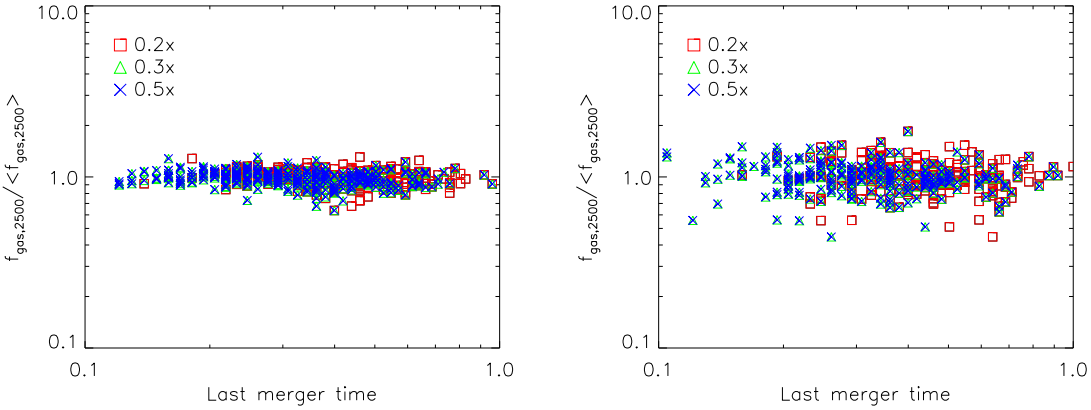

Figure 5.6: The effect on the residual mass fraction within r_{2500} of the time of a cluster's last major merger as defined as a jump in the mass of the cluster's main progenitor by a fraction of 0.2, 0.3 and 0.5 times its final mass for the PC run (left) and FO run (right). The GO run is not shown since it is qualitatively identical to the PC run.

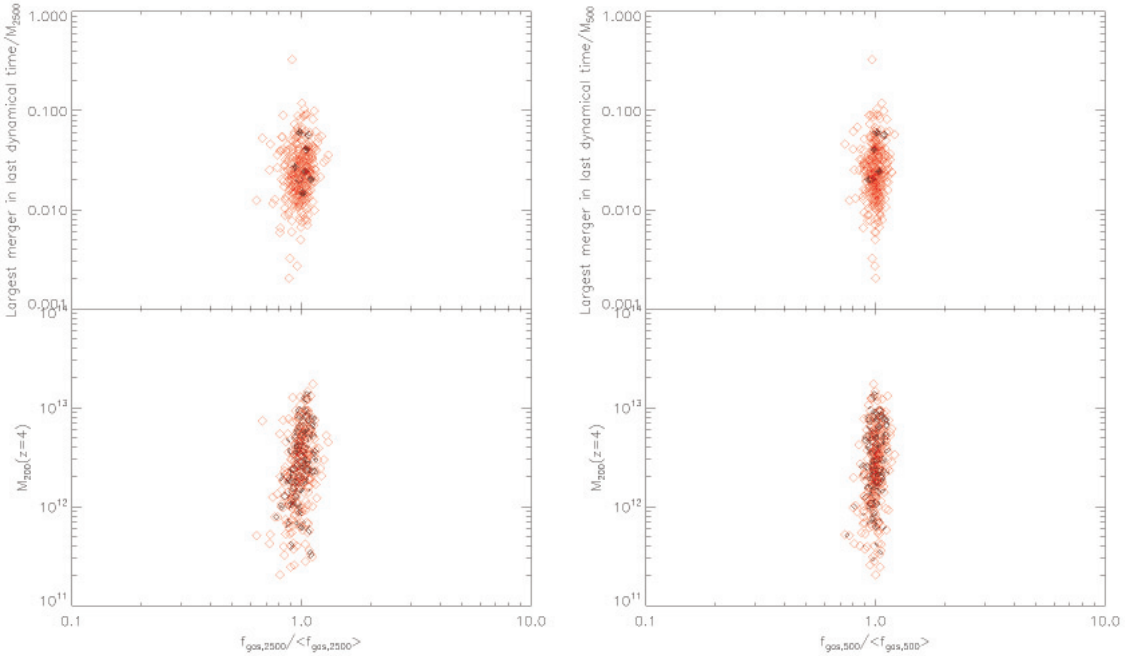

Figure 5.7: The residual gas fraction within R_{2500} (left) and R_{500} (right) plotted against the fractional change in the cluster's mass in the last dynamical time (top panel) and the cluster's M_{200} at redshift 4 (bottom panel) both for only the PC run since the others are not sufficiently different to merit inclusion.

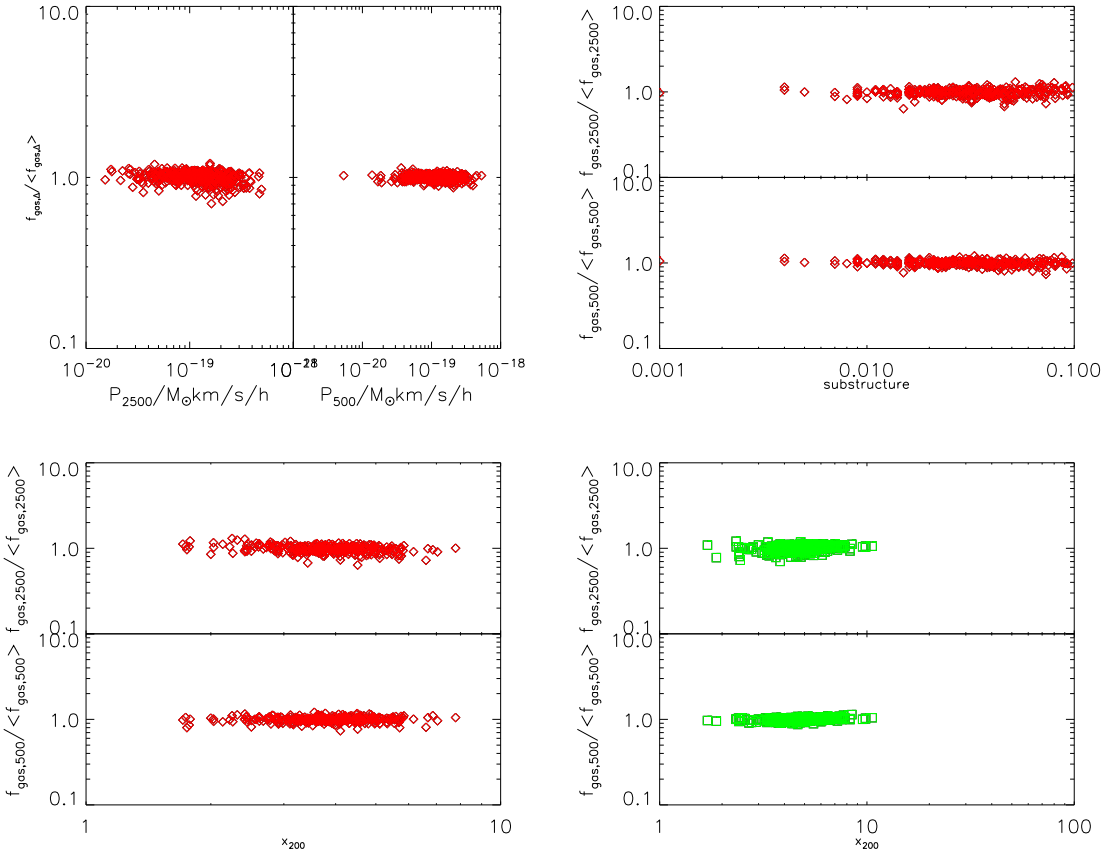

Figure 5.8: The residual gas fraction as a function of angular momentum (upper left) within R_{2500} (left) and R_{500} (right), as a function of substructure (upper right) within R_{2500} (upper panel) and R_{500} (lower panel) and as a function of concentration (bottom left) for the PC run (as a function of concentration for the GO run, bottom right). The results of the FO run are very similar to those of the PC run, as are the results of the GO run for angular momentum and substructure.

no strong correlations[8], we utilise this approach in the hope that it might indicate a combination of variables which correlate strongly with the scatter.

Unfortunately we also had little success with this method when applied to this particular problem. Our hope with this method was that it could take a relationship between a given variable and the residual gas fraction and indicate other variables which might be included in the relation to reduce its scatter, and in so doing improve its correlation. However, the relationships we examined involving the residual gas fraction and just one other variable had slopes so close to zero that any decrease in the scatter we were able to achieve did not improve the correlation significantly.

[8]Where we call a strong correlation one with a correlation coefficient above 0.8

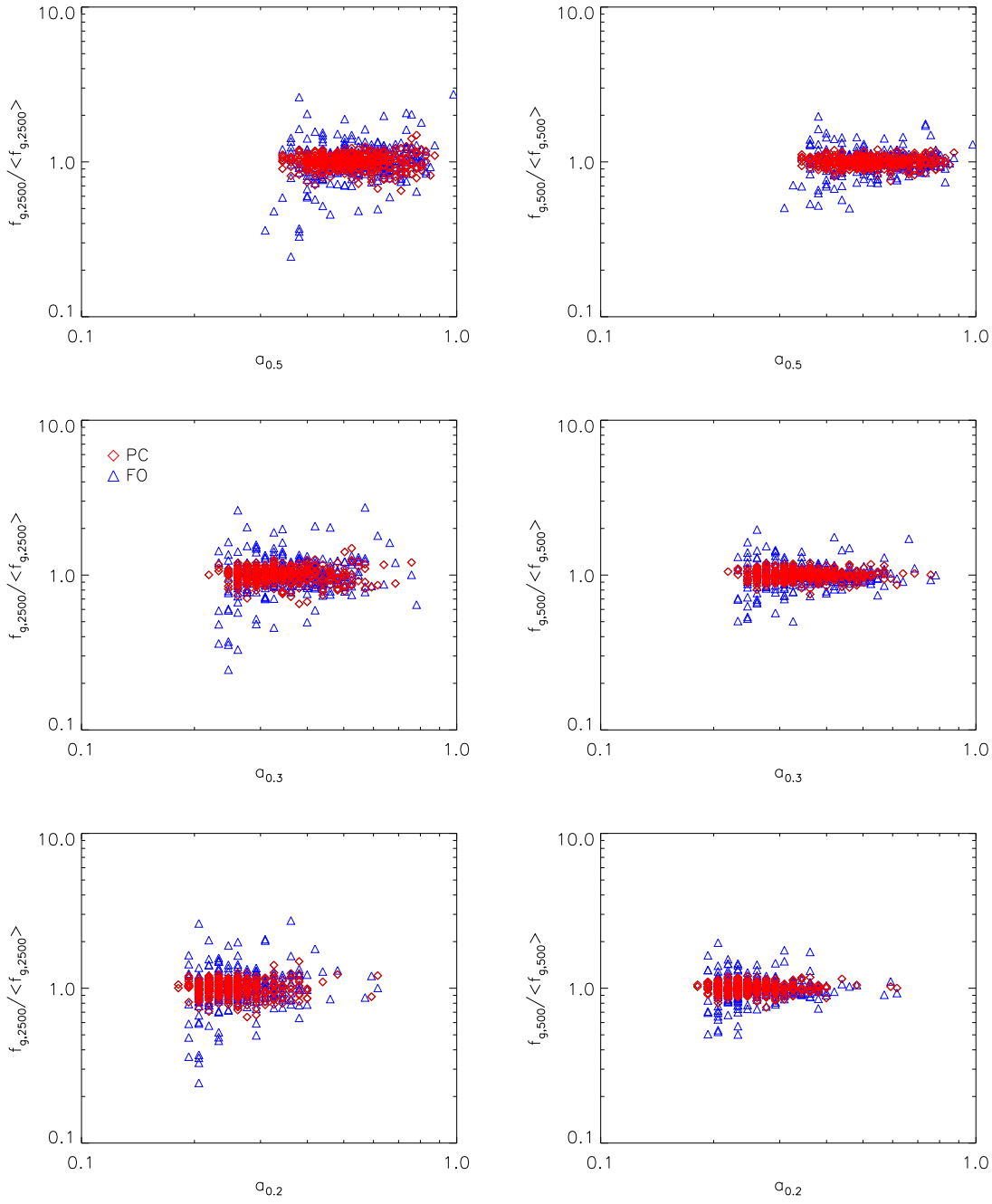

Figure 5.9: The residual gas fraction within R_{2500} (left column) and R_{500} (right column) as a function of the time at which the main progenitor acquired 0.5 times its final mass (top row), 0.3 times (middle row) and 0.2 times (bottom row)

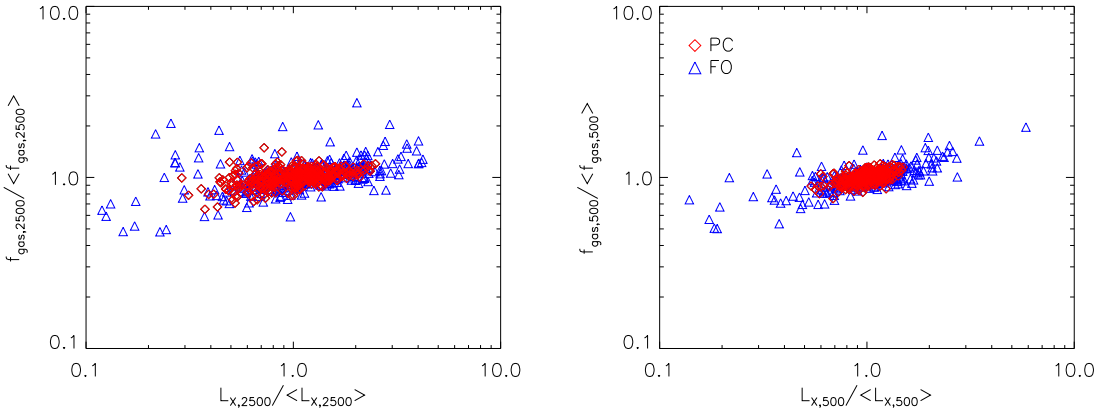

Figure 5.10: The residual gas fraction plotted against the residual luminosity within R_{2500} (left) and R_{500} (right) for the PC and FO runs. The correlations differ significantly depending on radius used, although neither correlation can be considered good, although the correlation coefficient for the FO run within R_{500} is higher at slightly above 0.7.

5.5.3 An observable indication of scatter

The strongest correlation we found with the scatter was with the scatter in the $L_X - T_{sl}$ relation (figure 5.10), although the correlation was not strong (correlation coefficient of 0.71). As discussed above, this was expected since baryons are the luminous component of galaxy clusters so an excess in luminosity must mean an excess in the luminous component of a cluster. It is interesting to note that the correlation is much weaker within R_{2500} than within R_{500}, indicating that other drivers of the scatter are acting in the cluster cores.

Since the residual gas fraction (for the FO run within r_{500}) shows a definite, although not strong, correlation with the scatter about the $L_X - T_{sl}$ relation, we may now use this as a starting point from which to deduce a stronger correlation with residual gas fraction. Using the techniques described in section 5.2.1 we found that the scatter about this relation can be minimised by the addition of the scatter about the $T_{sl} - M_{tot}$ relation, although this itself is not correlated with the residual gas fraction. Since there is already a definite slope in the relation (unlike in the examples in which we were looking for causes of scatter), the reduction in scatter caused by the addition of a third variable has a positive effect, raising the correlation coefficient to 0.88, when the variables are raised the to the appropriate powers, as shown in figure 5.11. Whilst an improvement in the correlation is seen within r_{500}, a greater (percentage wise) improvement in the correlation coefficient is seen within r_{2500} indicating that the addition of the residual temperature has a greater effect in the cluster core. This can be compared to the effect of simply multiplying the two

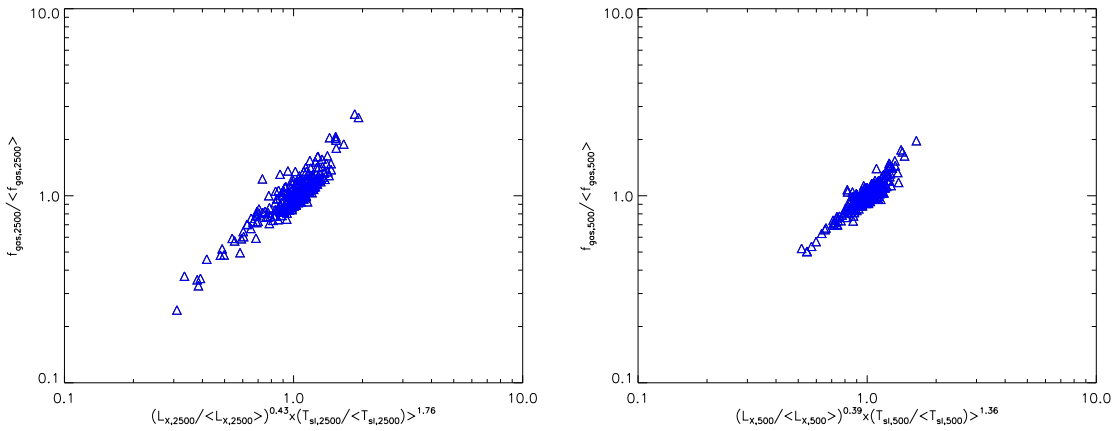

Figure 5.11: The residual gas fraction versus the product scatters in $L_X - T_{sl}$ and the $T_{sl} - M_{tot}$ relations, raised to the powers indicated by equation 5.7.

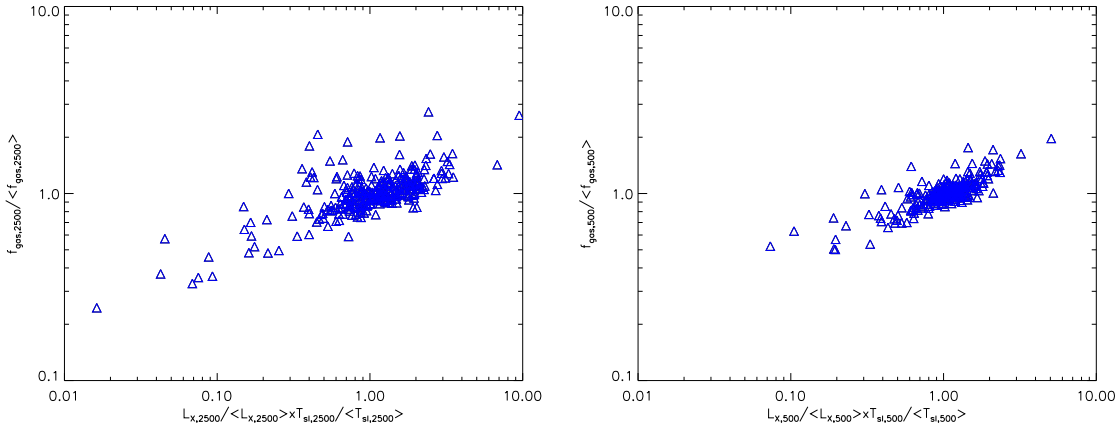

Figure 5.12: The residual gas fraction versus the scatter in the $L_X - T_{sl}$ relation multiplied by the scatter in the $T_{sl} - M_{tot}$ relation within r_{2500} (left) and r_{500} (right) for the FO run. The improvement in the correlation when compared to figure 5.10.

variables without these powers (as in figure 5.12) improves the correlation (a correlation coefficient of 0.80), but not to the same degree as when the variables are raised to the appropriate power.

5.6 Conclusions

Cluster gas fraction is not independent of total cluster mass, however we broadly agree with the observations of McCarthy et al. (2007) and Allen et al. (2008) that the gas fraction in high-mass clusters ($\gtrsim$ 6keV) is broadly constant with mass, albeit with some scatter.

We examined every conceivable variable likely to be correlated with the scatter in the

gas fraction-mass relation and we were, unfortunately, unable to determine any particular variable (or group of variables) strongly correlated with the scatter and likely to cause it.

Care should be taken when examining correlations with cluster formation times since we have shown that the strength (or otherwise) of correlations with formation time (with variables known to correlate with formation time, particularly concentration) can vary greatly depending on the definition of formation time used. Because of this we used several definitions of cluster formation time when searching for causes of scatter in the gas fraction-mass relation; none of which yielded any positive results.

There is little difference in the the PC and FO runs in their correlations with residual gas fraction, but the GO run differs. This is to be expected since the $z = 0$ PC and FO runs are very similar.

We found the scatter did not depend on a cluster's recent merger history, despite a simple theoretical argument suggesting that recent mergers could affect a cluster's gas fraction by up to 2%. This was surprising and points to mergers being, at best, a second order effect in producing scatter.

We did find that there was a definite correlation between the scatter about the $f_{gas} - M_{tot}$ relation and the scatter about the $L_X - T_{sl}$ relation for the FO simulation and, although this was itself not strong, we found that the correlation between the scatter about the $f_{gas} - M_{tot}$ relation and the product of the scatter about the $L_X - T_{sl}$ relation and the scatter about the $T_{sl} - M_{tot}$ was strong, despite there being no correlation with the scatter about $T_{sl} - M_{tot}$. This is the most interesting result we have obtained as it suggests that there may be a systematic, observational bias towards selecting those systems with higher than average gas fractions. To quantify the extent of this effect is, however, difficult since it requires high quality spectroscopic-like temperature, X-ray luminosity and total mass data.

A possible reason that we were unable to find a cause for the scatter could be the populations of clusters we were examining were not bimodal (only containing non-cool core clusters). The presence of both cool core and non-cool core clusters in a population will give rise to an increase in the scatter about the baryon fraction-mass relation which would manifest itself in those cluster properties driven by core processes, such as ratios of cluster properties within the core and without.

Chapter 6

Feedback, radiative cooling and additional heating

This chapter will seek to introduce radiative cooling to the feedback model, described in chapter 3, to produce the feedback-plus-cooling (FC) model. Simply allowing clusters to cool radiatively in this model does not have the desired effect since too much cooling happens in the central regions and not enough further out. This is the overcooling problem.

Attempts to overcome this are discussed: decoupling the hot gas from the cold, and including additional heating mechanisms (affecting only the cold gas) to counter the effects of overcooling.

This extra heating is required because of a mismatch between the cooling rates of the gas in the semi-analytic model underpinning the feedback prescription, and that in the simulation.

6.1 Feedback and radiative cooling

The majority of the baryonic material in galaxy clusters takes the form of hot gas forming the intracluster medium, with the remainder having formed into stars. The material for ongoing star formation and black hole growth - and hence feedback - comes from this hot gas.

Simulations including only radiative cooling, but neglecting any sort of feedback prescription, are effective at depleting the hot gas component in galaxy clusters as it forms into stars, but this results in the excessive growth of galaxies (Cole, 1991) and overcooling in cluster centres (Balogh et al., 2001). An additional heating source is therefore required to counterbalance these undesirable effects of radiative cooling.

Cooling and feedback are in some ways linked since, for star formation (which leads to supernova feedback) and black hole growth (AGN feedback) to occur, the hot gas must be allowed to cool into star formation regions and onto black holes. It is therefore unrealistic to assume a feedback model without radiative cooling[1]. Several cooling mechanisms have been proposed based on this reasoning (e.g. Kay 2004).

It was shown in chapter 4 that continual energy injection into the intracluster medium produces a better fit to high redshift observations than a preheating model. However, the feedback model considered in that chapter has a serious limitation - there is no radiative cooling included. The upshot of this is that the cluster population generated by the FO model contains no cool core clusters. The aim in this chapter is to combine radiative cooling with the feedback model of Short and Thomas (2009).

It is known from observations (Maughan et al., 2008; Pratt et al., 2009a; Sanderson et al., 2009) that there exist two distinct populations of galaxy clusters: cool-core clusters (CC) and non-cool-core clusters (NCC). However, hydrodynamical simulations are unable to produce these two distinct populations. The preheating and feedback Millennium Gas simulations, as detailed in chapter 3, are moderately successful at producing NCC clusters, but are unable to produce CC clusters. In the case of the feedback runs, this is because of a lack of radiative cooling, and in the precool run it is the extreme preheating event causing the evaporation of cold, dense clumps.

Other simulations have similar problems. Whilst some (e.g. Kay et al. 2007) are able to produce cool core clusters via radiative cooling and others suffer from the same problems as the Millennium Gas simulations, none are able to produce two distinct populations.

6.1.1 Overcooling

A problem with including radiative cooling in the FO runs is that of overcooling, in which the gas in the centres of the clusters cools to lower temperatures than are observed. This can clearly be seen in the entropy profile in figure 6.1. Comparing this profile with those of Pratt et al. (2009a) shows the problem. This problem is caused by the cooling routines for the simulation (as described in chapter 3) and that assumed by the semi-analytic model from which the feedback is taken. Together they produce an unstable situation which leads to a cooling catastrophe.

We examine two methods of overcoming the overcooling problem: a 'decoupling' of hot and cold gas within the simulation (Pearce et al., 2000); and an extra heating mechanism

[1]The Short and Thomas (2009) feedback scheme inherently assumes a galaxy scale cooling model which it acquires from the underlying semi-analytic model.

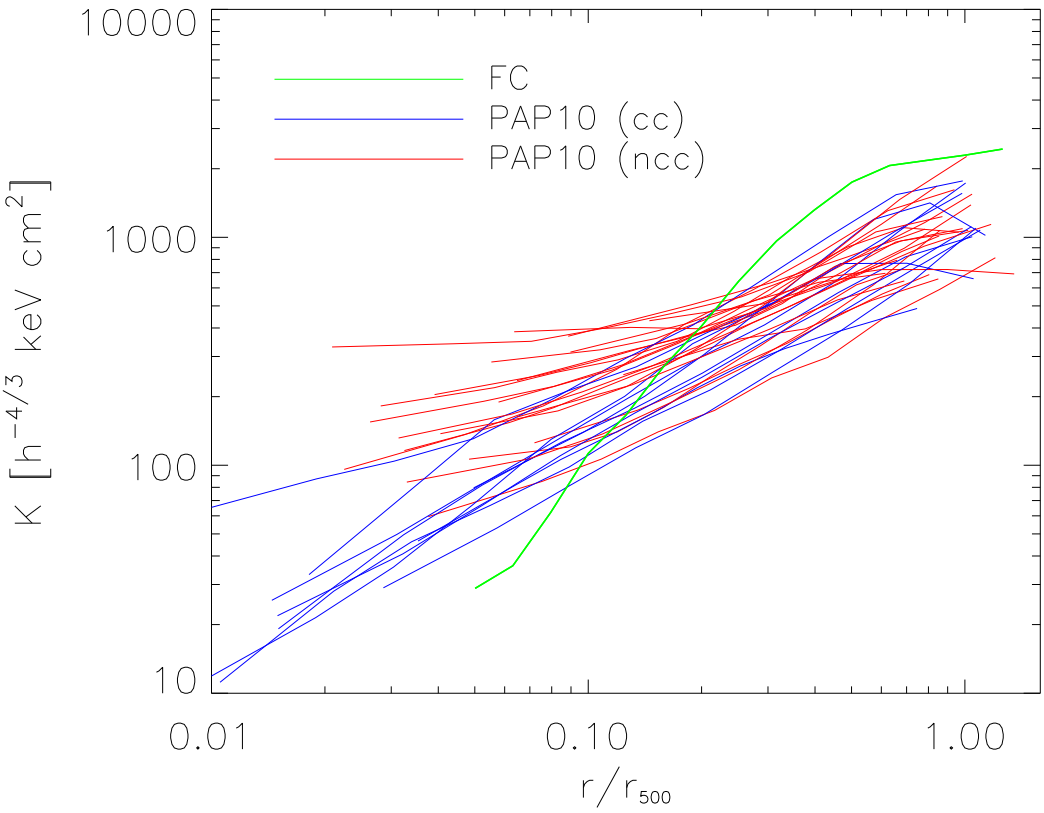

Figure 6.1: The entropy profile for a z=0, 2 $\times 10^{14} h^{-1} \mathrm{M}_{\odot}$ cluster when simulated with feedback and radiative cooling. The steepening of the profile at small radii is an indicator of overcooling in the cluster's centre. The green line represents the simulated cluster, and the red and blue lines represent the cool core and non-cool core clusters from Pratt et al. (2009a).

specifically targeting the cold, dense gas in the centres of clusters.

6.1.2 Decoupling

Decoupling is thought to occur within the ICM, where cold clumps of gas may be seen amidst the surrounding hot gas (Salomé et al., 2006). In these cases, some mechanism (possibly magnetic fields) is preventing conduction between the cold and hot gas.

Computationally, we implement this by forbidding hot gas particles ($\gtrsim 20,000$K) from 'seeing' cold gas particles and so they are not included in calculations of their SPH properties. The opposite is not true, however, leaving the cold gas particles to be heated up by their hotter neighbours.

Since cold particles are able to heat up through interactions with their hot neighbours, there comes a time by which they are no longer classified as 'cold', and then a two way interaction with the hot particles is allowed. Decoupling then behaves as a damper, preventing hot gas from cooling at too fast a rate in the hope of eliminating the overcooling problem.

Figure 6.2 shows the difference in the entropy profile for a cluster with $M_{500} = 2 \times 10^{14} h^{-1} M_{\odot}$. Comparing this figure with figure 1.2 shows a much closer agreement than does figure 6.1, however the slope of the power law is still too steep . An additional heating mechanism is needed to raise the cluster's entropy in the centre of this cluster, whilst leaving its entropy at r_{500} unchanged.

The normalisation in the decoupled entropy profiles are lower than those without decoupling. This is an effect of the decoupling on the gas cooling. When decoupling is not included, some gas can cool very quickly down to very low temperatures, so is not considered when producing entropy profiles (for which only 'hot' gas is considered). When decoupling is included, the gas cools more slowly, so cooling gas can still be considered 'hot' despite being cooler than its surroundings and will act to lower the mean temperature and entropy of the cluster.

6.2 Additional Heating

Another way to prevent overcooling is simply to raise the temperature of the cold particles. When employing such a scheme, decoupling has no effect since the gas is not allowed to cool sufficiently for it to be decoupled.

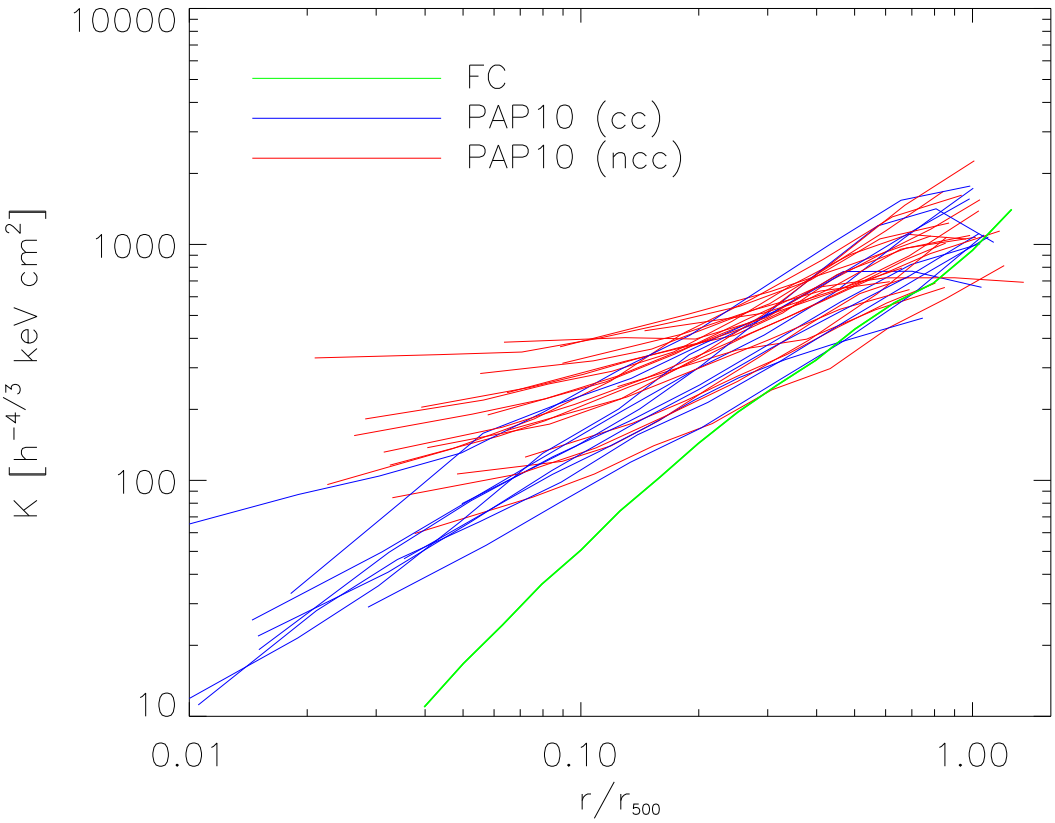

Figure 6.2: The entropy profile for a z=0, 2 $\times 10^{14} h^{-1} \mathrm{M}_{\odot}$ cluster when the hot and cold gas is decoupled. The agreement with figure 1.2 is much better than that of figure 6.1. The green line represents the simulated cluster and the red and blue lines represent the cool core and non-cool core clusters from Pratt et al. (2009a).

6.2.1 Mechanisms for additional heating

We initially examined several distinct mechanisms for heating the cold gas before deciding on a particular model. These models are described below:

- Additional heating based on the cold particle's potential.

  The particle's potential energy can be linked to an equivalent temperature via equation 6.1 and this value is added to the temperature of each cold particle. Particles are defined as 'cold' if their temperature is below a given value (typically a few tens of thousands of Kelvin). In addition, only particles with a high density contrast are heated to prevent spurious heating of the inter-cluster gas at each timestep.

$$\phi = \frac{2k_B T}{\mu m_H} \tag{6.1}$$

- Additional heating based on the velocity dispersion of the surrounding particles.

  For each gas particle, a list of dark matter neighbours within its smoothing length is found and their velocity dispersion is calculated. This is then converted into an effective temperature via equation 6.2. If a gas particle's temperature is low and its density contrast high (as above), then its temperature is raised by this amount.

$$\sigma^2 = \frac{k_B T}{\mu m_H} \tag{6.2}$$

- Additional heating based on the virial temperature of the parent halo.

  This is only done at each output time since the friends-of-friends trees are required to obtain information about the parent halo. For each halo, its virial temperature is calculated all the cold gas particles contained therein are raised by this temperature.

- Imposing a temperature profile for the cluster.

  Vikhlinin et al. (2006) provide a model for a given cluster's temperature profile (equation 6.3 and figure 6.3). This is imposed on the cluster by denying each particle the ability to fall below the predicted temperature allowed by its distance from the cluster centre. This is done at each timestep, however, since it requires information about the parent halo, the minimum temperature for a particle can only be calculated at an output time, potentially leading to problems if a particle travels a large radial distance between outputs. In practice, this does not appear to be a problem.

$$\frac{T(r)}{T_{mg}} = 1.35 \left[\frac{(x/0.045)^{1.9} + 0.45}{(x/0.045)^{1.9} + 1} \right] \left[\frac{1}{1 + (x/0.6)^2} \right] \tag{6.3}$$

  where $T(r)$ is the temperature at a radius r, T_{mg} is the gas mass weighted temperature of the cluster and $x = r/R_{500}$

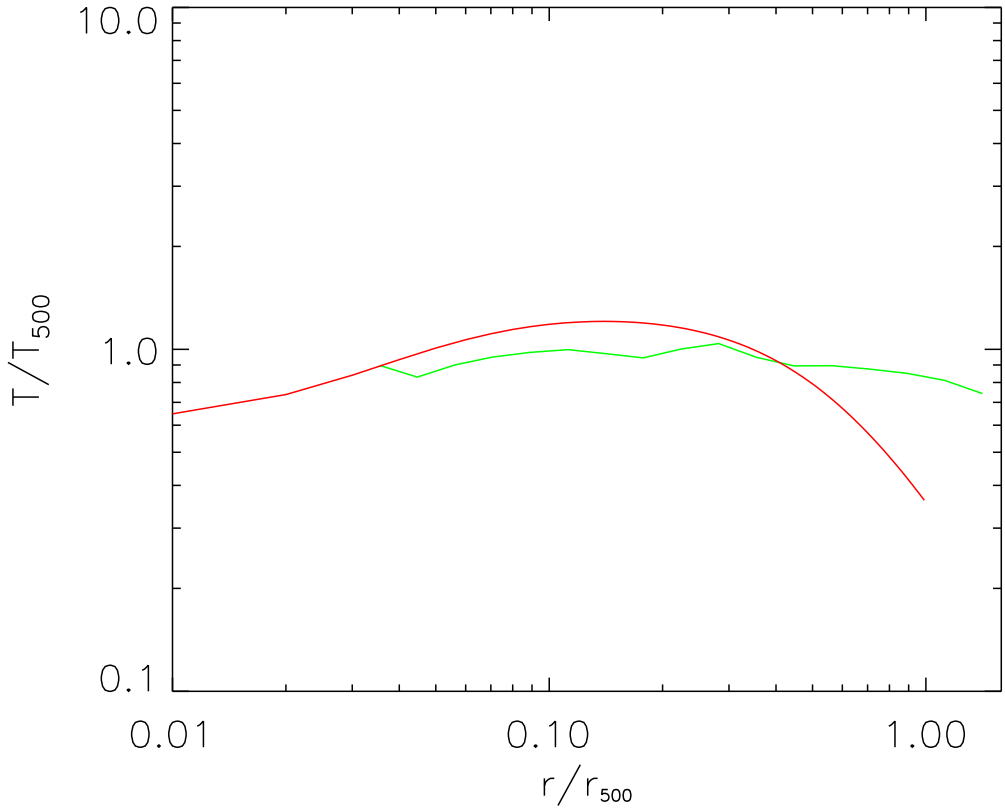

Figure 6.3: A plot of the temperature profile as described by equation 6.3.

Figure 6.4 shows that this profile is fully consistent with the observational data of Pratt et al. (2009a).

We tested these methods by producing temperature profiles for a cluster (believed, due to it being relaxed, to possess a cool core) for each of these additional heating schemes.

The first three of these mechanisms do little to address the overcooling problem, producing profiles qualitatively similar to those produces without any additional heating (figure 6.5), however the imposition of a temperature profile is successful in preventing overcooling (figure 6.6), although raising the central temperature profile well above that of a cool core cluster. We therefore use this as our starting point and apply further refinements.

There is a significant problem with all the heating mechanisms we examined, and that is the amount of additional energy required. This is typically several times that supplied by the semi-analytic feedback prescription and is a serious problem for the model, since the additional heat cannot reasonably be explained by a poorly-targeted heating from the feedback. It is therefore necessary to make modifications to our model in order to bring down the amount of energy it requires, whilst allowing it to produce convincing cluster

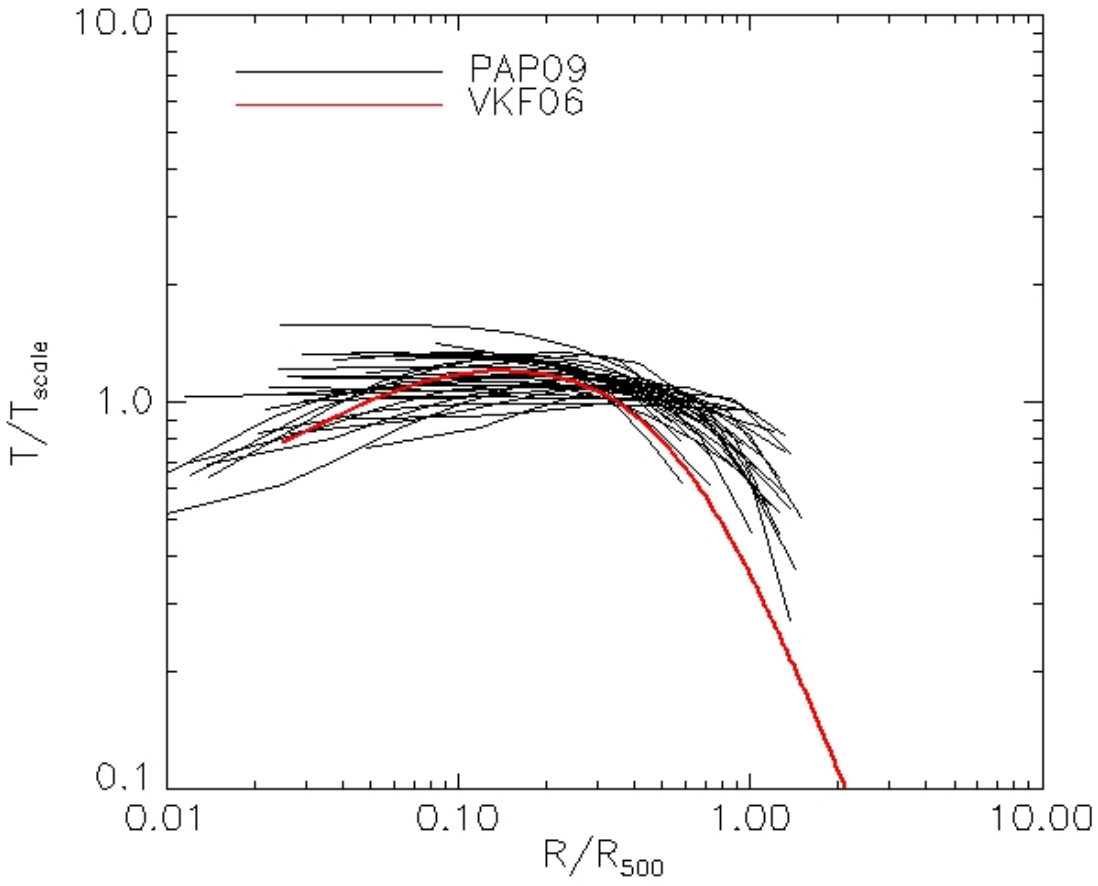

Figure 6.4: The temperature profiles from Pratt et al. (2009a) with the model temperature profile from equation 6.3. The theoretical profile can be seen to resemble the profile of a cool-core cluster and is fully consistent with this observational data

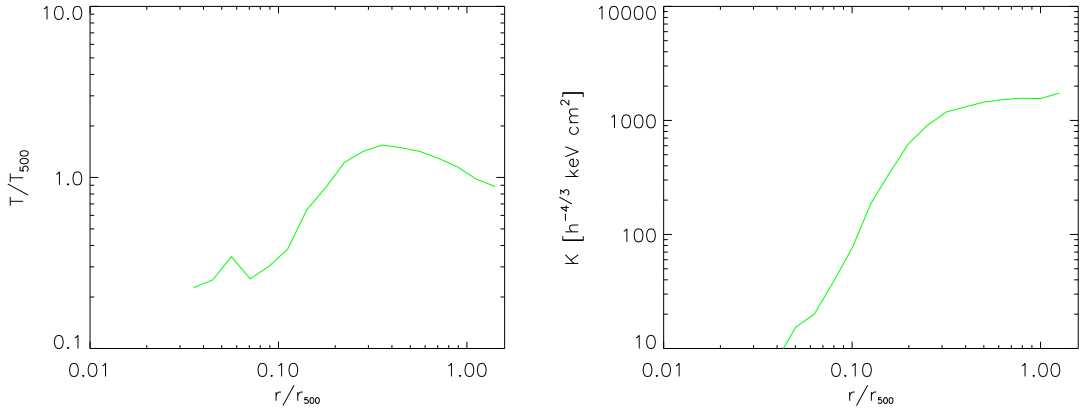

Figure 6.5: The temperature (left) and entropy (right) profiles of a cluster in which the cold gas is heated by an amount based on the particles' potentials. This cluster is still suffering from overcooling. Profiles produces when the heating is based on the velocity distribution of the neighbouring particles and on the parent halo's virial temperature are qualitatively the same.

profiles. These refinements are now discussed.

6.2.2 Further Refinements

To try to reduce these high energy requirements, as well to produce cool core profiles, many refinements to our model are considered:

- Heating particles when they're below a fraction of their minimum temperature.
  As can be seen in figure 6.3, observed clusters show scatter about the imposed temperature profile. If trying to impose the profile on a cluster naturally lying below this profile, a lot of energy will be expended heating particles which have not overcooled. To compensate for this, we try allowing particles to cool to a pre-defned fraction of the imposed temperature, before being heated back up. This allows for some of the observed scatter in the temperature profiles.

- Heating particles to a non-cool core temperature profile
  To prevent a cooling catastrophe and excessive energy input, particles must be sufficiently heated that they are removed from the cooling flow. To this end, we try imposing the profile of a non-cool core cluster. In the outer regions, this is the same as that in equation 6.3, but flattening in the center, at the maximum temperature

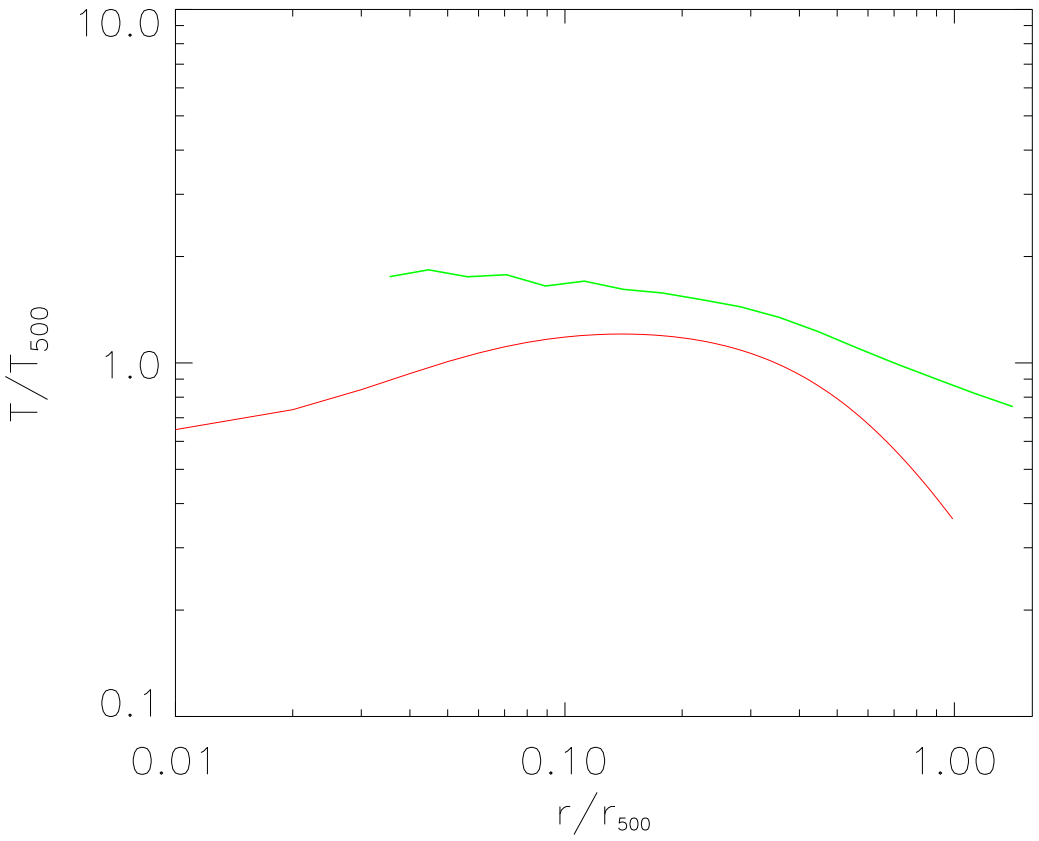

Figure 6.6: The temperature profile for a cluster in which a minimum temperature is imposed as per equation 6.3. The red line shows the imposed temperature profile. The cluster's temperature drops below this since, in a simulation timestep, the cooling occurs after the heating.

the profile achieves:

$$\frac{T(r)}{T_{mg}} = \begin{cases} 1.35 \left[\frac{(x/0.045)^{1.9}+0.45}{(x/0.045)^{1.9}+1}\right] \left[\frac{1}{1+(x/0.6)^2}\right] & r > 0.16 r_{500} \\ 1.21 & r \leq 0.16 r_{500} \end{cases} \tag{6.4}$$

and heating a particle to this temperature, should it fall below the value allowed by the cool core profile.

- Heating particles to a multiple of their minimum temperature.

  Similar to above, we try a mechanism whereby if a particle falls below its minimum temperature, it is heated to a multiple of its minimum temperature.

- Heating only central particles.

  Examining the temperatures (internal energies) of the particles comprising a cluster, it can be seen that the only particles suffering from overcooling reside within the innermost $0.1 r_{500}$. Therefore, we choose to heat only the particles within this radius and those outside this radius receive no additional heating.

- Heating only very cold particles.

  When particles overcool, they drop far below the virial temperature of the cluster, so an additional heat source acting on only these cold particles has the potential to prevent overcooling whilst having little effect on the rest of the gas. It is well known (Lloyd-Davies et al., 2000; Ponman et al., 1999) that gas in clusters rapidly cools down to about 10,000K. This provides a lower limit on the temperature of the gas, and the precise value of the threshold temperature at which to designate gas as 'cold' has little effect, provided it is well below the cluster's virial temperature.

- Allowing the metallicity to evolve.

  The histories of energy injection in all the simulated clusters show that a large amount of additional energy gets injected at very high redshifts ($\gtrsim 10$). At such redshifts the additional energy can be as high as 20 times that injected via the semi-analytic feedback by that redshift. This suggests that the temperatures to which we are raising the gas at these redshifts is not high enough to remove it from the cooling phase meaning that it will rapidly re-cool, only to be heated and cool again on the next timestep.

  We believe that this is a problem with the cooling function at high redshifts. The imposed cooling function assumes a constant, universal metallicity of $0.3 Z_{\odot}$. At high

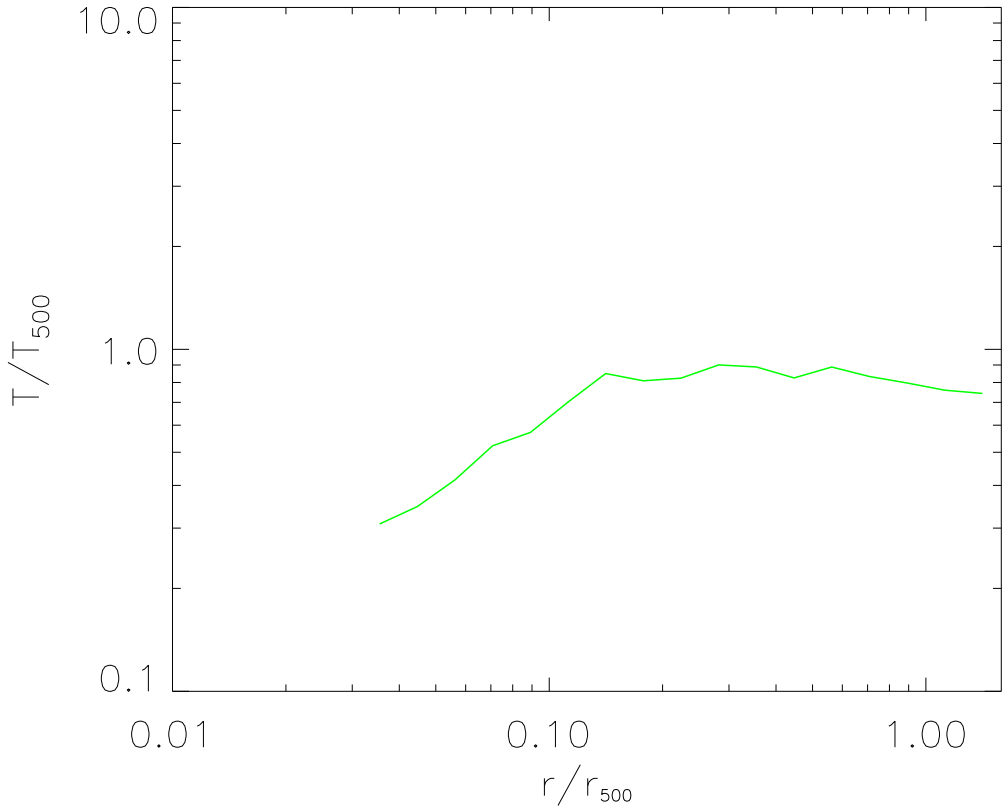

Figure 6.7: The temperature profile for the same cluster as above, when only particles with temperatures below 30,000K are raised to the imposed temperature profile.

redshifts, however, this metallicity is far too high (Connolly et al., 1997; Balestra et al., 2007) - leading to high rates of radiative cooling. To correct for this, we move to the simple linear model of universal metallicity evolution of Muanwong et al. (2006).

We determined that heating central particles (and not those at large radii) was an important refinement to make, since this would help target only those particles which are likely to overcool. We could also determine that, when a particle is heated, it should be heated sufficiently that it will be removed from any cooling flow. Heating only cold particles up to $\approx T_{vir}$ lowers the temperature profile - pushing it towards a cool core, although with a degree of overcooling (figure 6.7). This effect did not occur in all objects, however. When run on a second test cluster (chosen at random), this cluster did not become cool core-like, as can be seen in figure 6.8.

Our final heating model is, therefore, to raise the temperatures of cold particles ($T < 30,000K$) within $0.1r_{500}$ of the cluster centre up to a large multiple of the tem-

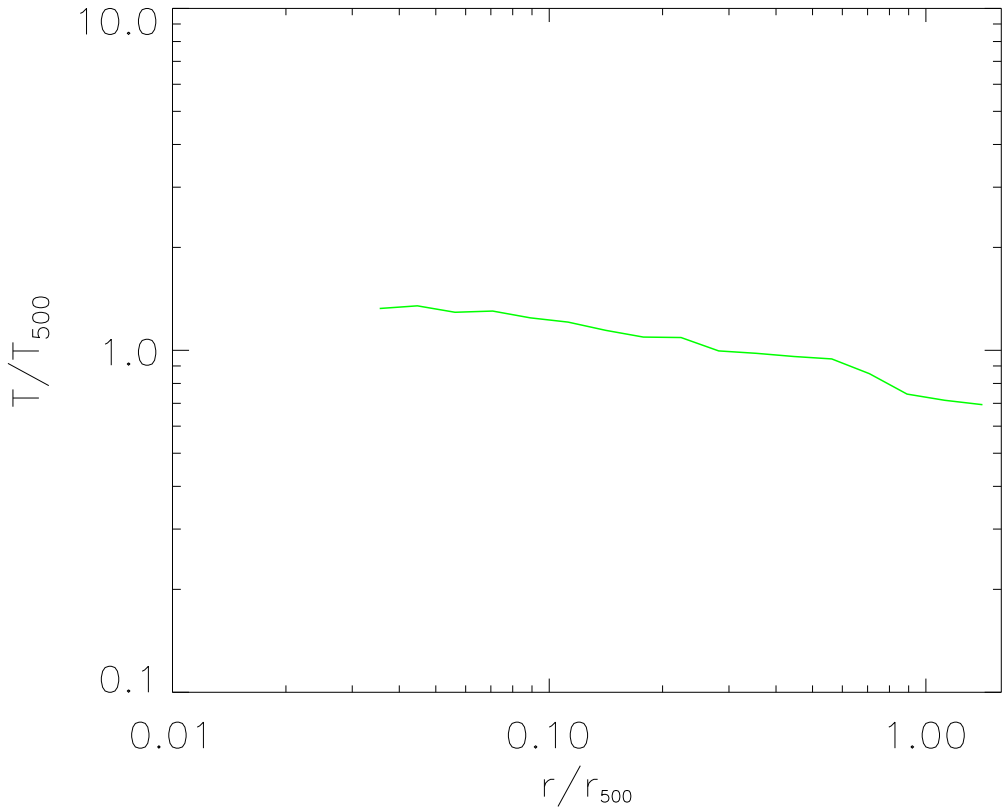

Figure 6.8: The temperature profile for another test cluster when only particles with temperatures below 30,000K are raised to the imposed temperature profile. In this case, the profile does not become cool core-like.

perature profile for a non-cool core cluster. Since the temperature profile in the region we heat the particles is not a function of radius, this is indistinguishable from raising these particles to a large multiple of the gas mass weighted temperature ($6 \times T_{mg}$ - chosen to minimise the energy requirements). This large temperature increase is required to stop these previously cold clumps of gas from cooling back down and causing another cooling catastrophe - as happens when the gas is heated by smaller multiples of T_{mg}. In addition to the refinements to the heating mechanism, we also include an evolving metallicity. This has little effect on the cluster profiles, but greatly improves the energy requirements of the model - particularly at high redshift.

It is noteworthy that imposing a condition whereby cold particles are raised to approximately T_{mg} and not allowed to cool results in very similar results as this scheme. This indicates that there are certain regions near the cluster cores in which cooling is extremely efficient, even for gas at the virial temperature. This is part of the cooling flow problem (Peterson and Fabian, 2006). Any additional heating mechanism has to be able to counteract this extremely efficient cooling.

We now present a population of galaxy clusters simulated with this model.

6.3 A bimodal cluster population

Running the FC model with the extra heating on a population of 22 clusters with masses between $2 \times 10^{14}\mathrm{M}_{\odot}h^{-1}$ and $9 \times 10^{14}\mathrm{M}_{\odot}h^{-1}$ (the properties of which are tabulated in table 6.1) successfully produces both cool core and non-cool core clusters (which can be seen in figures 6.9, 6.11 and 6.13) as have been observed by Maughan (2007); Pratt et al. (2009a); Sanderson et al. (2009), for example.

6.3.1 Cluster classification

We classify clusters as cool core or non-cool core based on the power law slopes of their inner $r < 0.15r_{500}$ temperature and entropy profiles. It is the case in well-behaved clusters that, for a cool core, they will have steep entropy and temperature profiles, with the opposite being true for non-cool core clusters. In our sample, all clusters with an inner temperature profile slope greater than 0.08 are considered cool core. The corresponding entropy profile slope threshold is ~ 0.4. Whilst there is no clear bimodality in our cluster sample (figures 6.17 and 6.18), the majority of objects fall, undisputedly, into one class or the other, with only a few lying close to the dividing line.

Table 6.1: The FC cluster sample. The cluster I.D.s together with their masses, substructures, classifications and their recent mass jumps.

i.d.	$M_{500}/10^{14}h^{-1}M_{\odot}$	classification	substructure	$M_{z=0.4}/M_{z=0}$
1356	8.69	CC	0.024	0.76
2562	7.23	NCC	0.036	0.87
1302	6.89	NCC	0.040	0.50
1714	5.69	CC	0.10	0.27
1435	5.44	NCC	0.047	0.61
2037	5.32	NCC	0.027	0.50
1177	5.23	CC	0.080	0.47
1336	5.17	CC	0.028	0.77
1032	5.10	CC (merging)	0.25	0.10
2142	4.53	CC	0.028	1.02
1662	3.78	NCC	0.13	0.55
1412	3.78	NCC	0.11	0.47
2022	3.64	NCC	0.038	0.63
1112	3.57	NCC	0.023	0.47
1545	3.31	NCC	0.036	0.74
1373	3.23	NCC	0.075	0.63
1510	3.01	CC	0.045	0.62
1527	2.81	NCC	0.065	0.62
1066	2.57	CC	0.059	0.69
1442	2.47	CC	0.051	0.51
1763	2.30	CC	0.048	0.71
3145	2.26	NCC	0.034	0.39
2401	2.23	NCC	0.075	0.48

6.3.2 Results

Figures 6.9 and 6.10 show the clearest difference between the cool core and the non-cool core clusters. All the profiles obey a power law of roughly equal slope (typically $1.0 \lesssim s \lesssim 1.1$ - slightly lower than observed) outside the central $0.15R_{500}$, but therein the profiles of the non-cool core clusters flatten off, whereas those for the cool core clusters maintain their power law right into the centres.

Figures 6.11 and 6.12 again show the difference between the two classes and how cool core clusters are named. As for the entropy profiles, the temperature profiles outside the centre are similar for both the cool core and non-cool core clusters, but within this radius the profiles for the non-cool core clusters flatten off, whereas the profiles of the cool core clusters reach a peak and then descend towards the centre. The simulated temperature profiles, whilst qualitatively agreeing with observations, differ in that their peak occurs much further away from the cluster centres.

Figures 6.13 and 6.14 show the gas-mass density and electron number density profiles. Again, there is a good agreement with observations and the difference between the cool core and non-cool core clusters can be seen.

The cumulative hot gas fraction profiles (figures 6.15, 6.16) are not as good a match to observations as are the density and entropy profiles, but they also show a clear distinction between cool core and non-cool core clusters; the latter are a reasonable match to observed hot gas fraction profiles - although not as good a match as those of the FO simulation (figure 4.3). The worsening of this match to observations appears to be caused by the additional heating mechanism. In a model without the additional heating, but with cooling, the hot gas fraction profiles display the same shapes as those observed, but scaled to small values as the hot gas condenses into stars. That this behaviour is not seen when the additional heating is included suggests that the additional heating not only counteracts this, but does it too efficiently. This indicates that additional tweaking of the model is required.

We investigate the bimodality of the population by examining the power law slopes of the spectroscopic-like temperature and entropy profiles for our simulated cluster sample (figures 6.17 and 6.18). These plots show a distinction in the power law slopes of the two populations, but do not show a clear gap between the slopes of the two populations, as was shown by Sanderson et al. (2009) who produce a similar plot with the observational results of 20 clusters taken with the *Chandra* X-ray satellite. They found a clear bimodality in their sample and state that it can be explained by thermal conduction redistributing heat

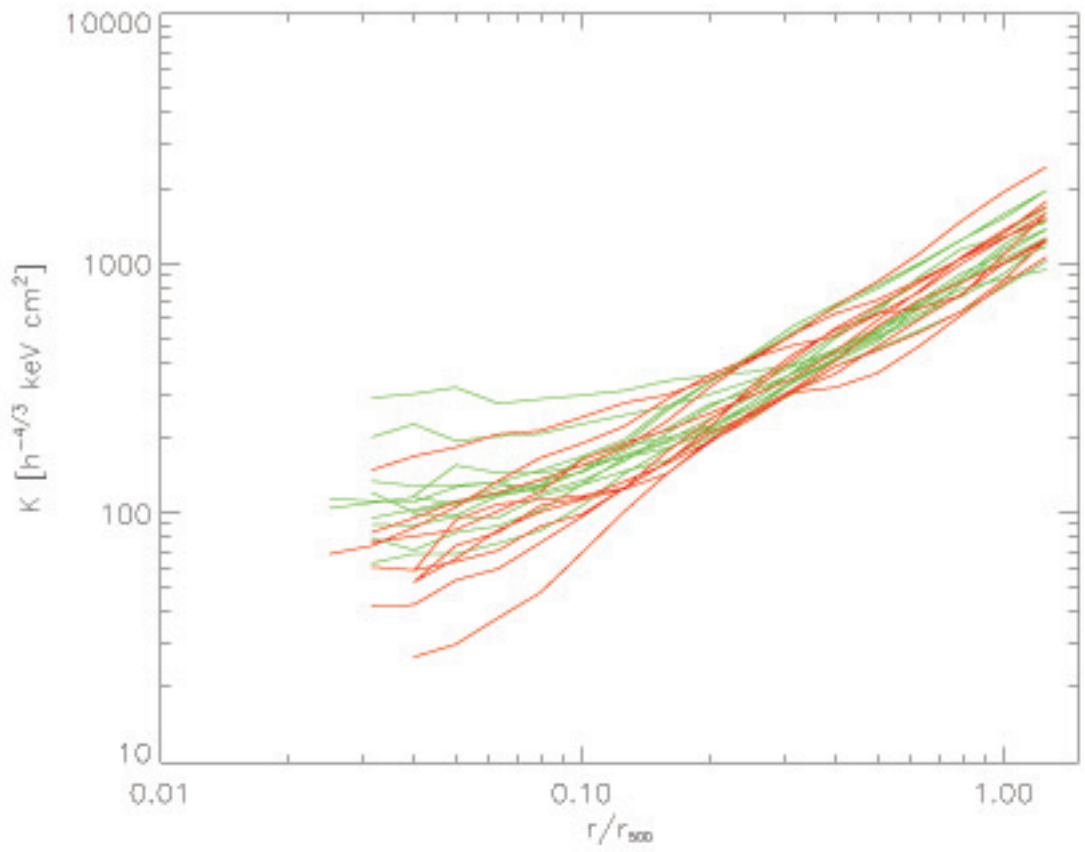

Figure 6.9: The entropy profiles for a sample of clusters simulated using our final model. The green lines represent non-cool core clusters and the red lines the cool core clusters. The change in the lines' colours towards the cluster centres represents the extent of the gravitational softening. The difference between the cool core and non-cool core clusters are clearly illustrated by the deviation of the two groups of profiles at low radii ($r < 0.15r_{500}$) where the cool core clusters maintain a (roughly) power law slope and the non-cool core cluster flatten off.

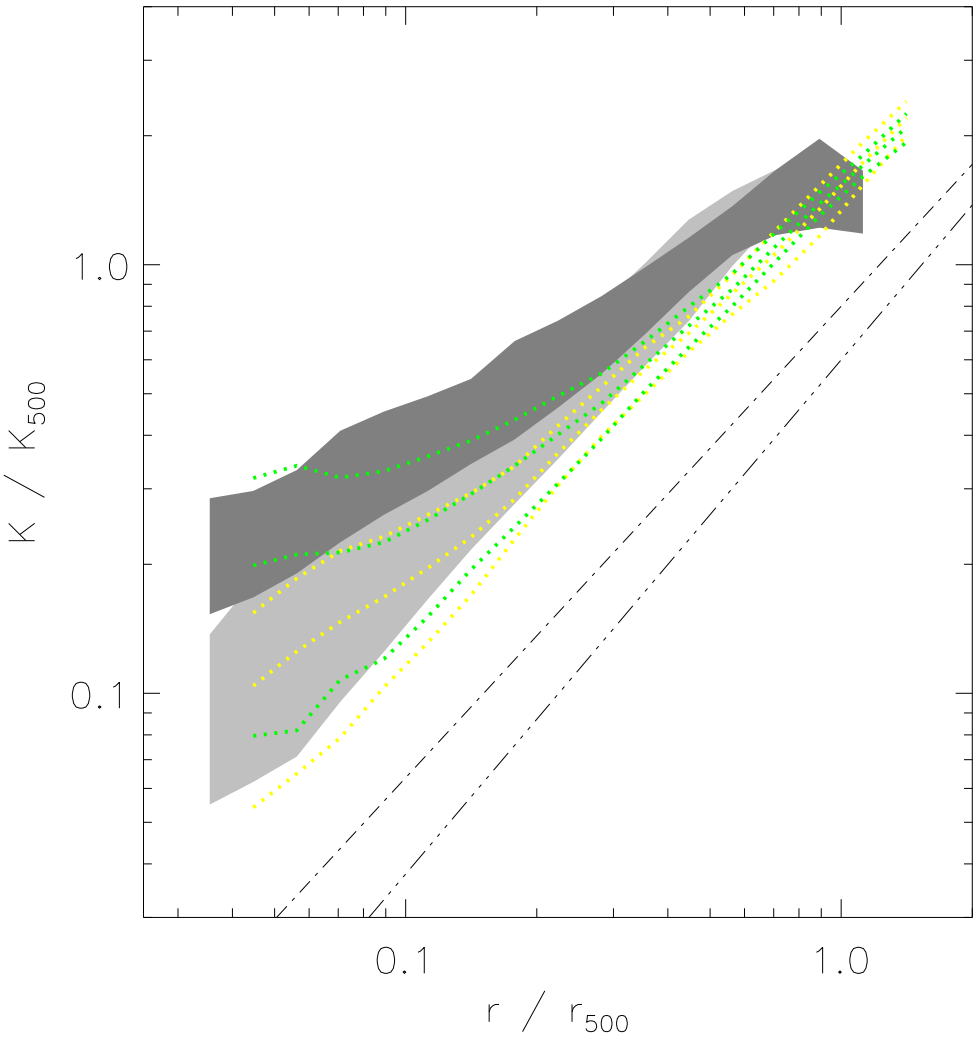

Figure 6.10: The mean entropy profiles with 1σ deviations from the simulated CC (yellow) and NCC (green) clusters on top of the mean and 1σ deviation of the observational data of Pratt et al. (2009a) for cool core (light grey) and non-cool core (dark grey) clusters. The dot-dashed and dot-dot-dot-dashed lines indicate power-law slopes of 1.1 and 1.2 respectively.

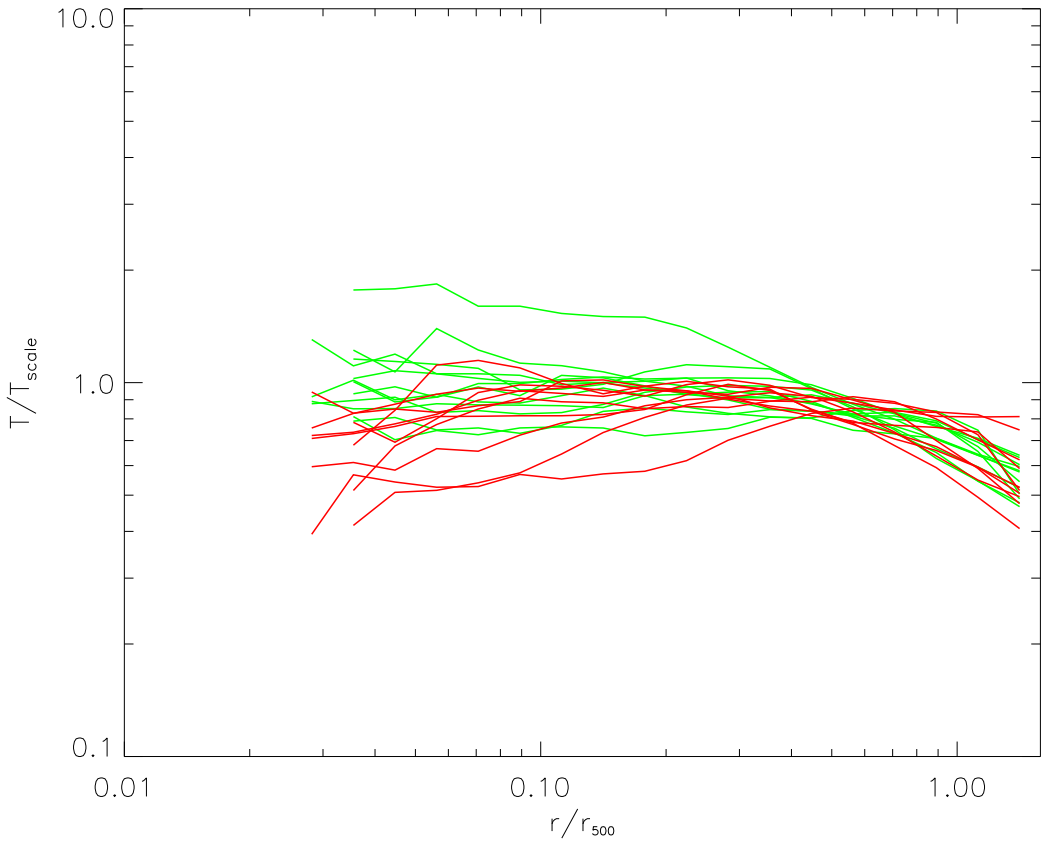

Figure 6.11: The spectroscopic-like temperature profiles for a sample of clusters simulated using our final model. The green lines represent the non-cool core clusters and the red lines the cool core clusters. The change in the lines' colours towards the cluster centres represents the extent of the gravitational softening. The downwards slope of the temperatures of the cool core clusters give them their name and the difference between them and the non-cool core clusters can be clearly seen.

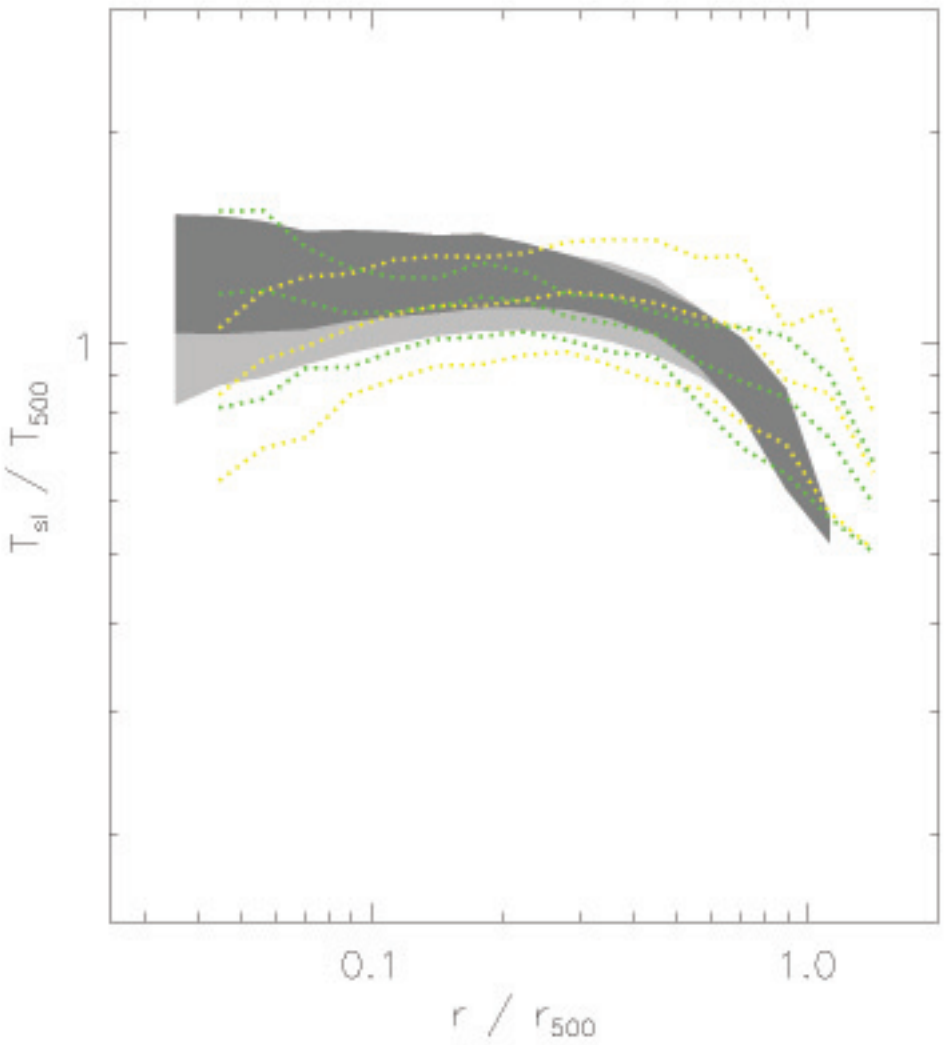

Figure 6.12: The mean spectroscopic-like temperature profiles and 1σ scatter for the CC (yellow) and NCC (green) clusters overlaid on the mean and 1σ deviation of the observational data of Pratt et al. (2009a) for cool core (light grey) and non-cool core (dark grey) clusters.

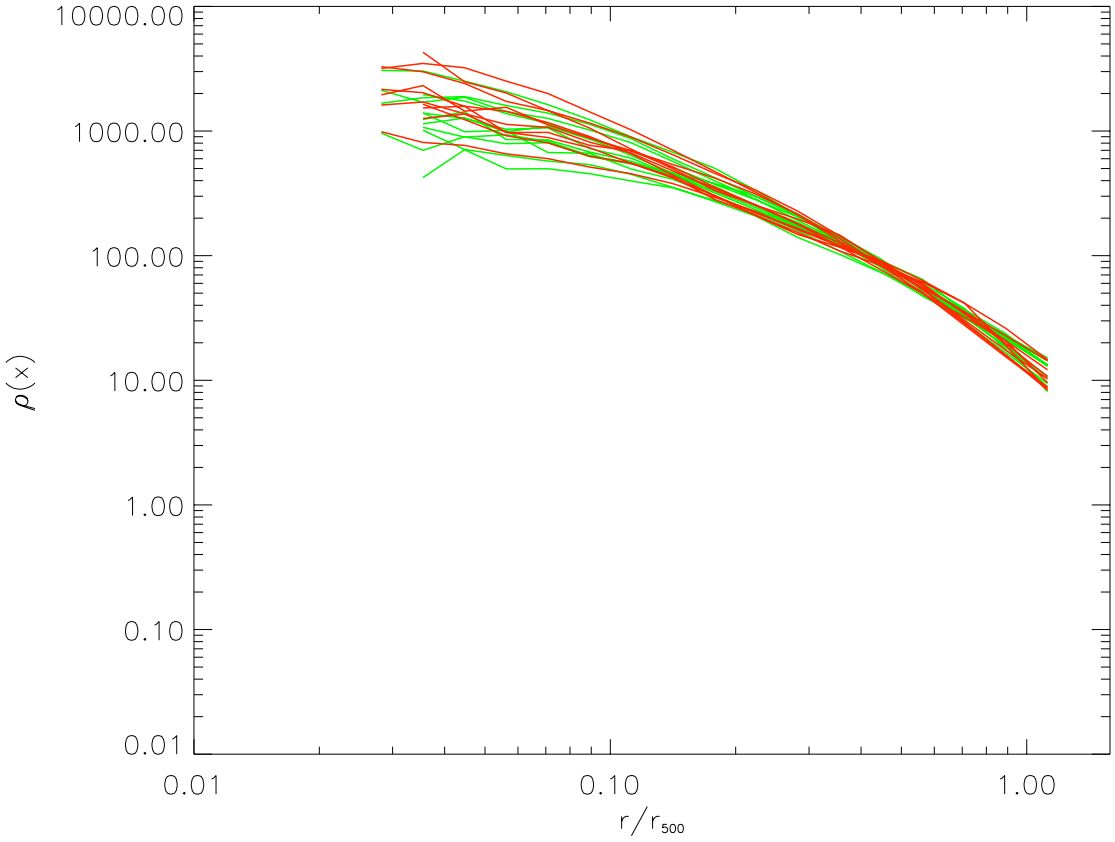

Figure 6.13: The gas-mass profiles for a sample of clusters simulated using our final model. The green lines represent the non-cool core clusters and the red lines the cool core clusters. The change in the lines' colours towards the cluster centres represents the extent of the gravitational softening. The difference between the two classes of object can be seen again in the cluster centres where the non-cool core clusters have flattened central density profiles compared to the more NFW-like cool core clusters.

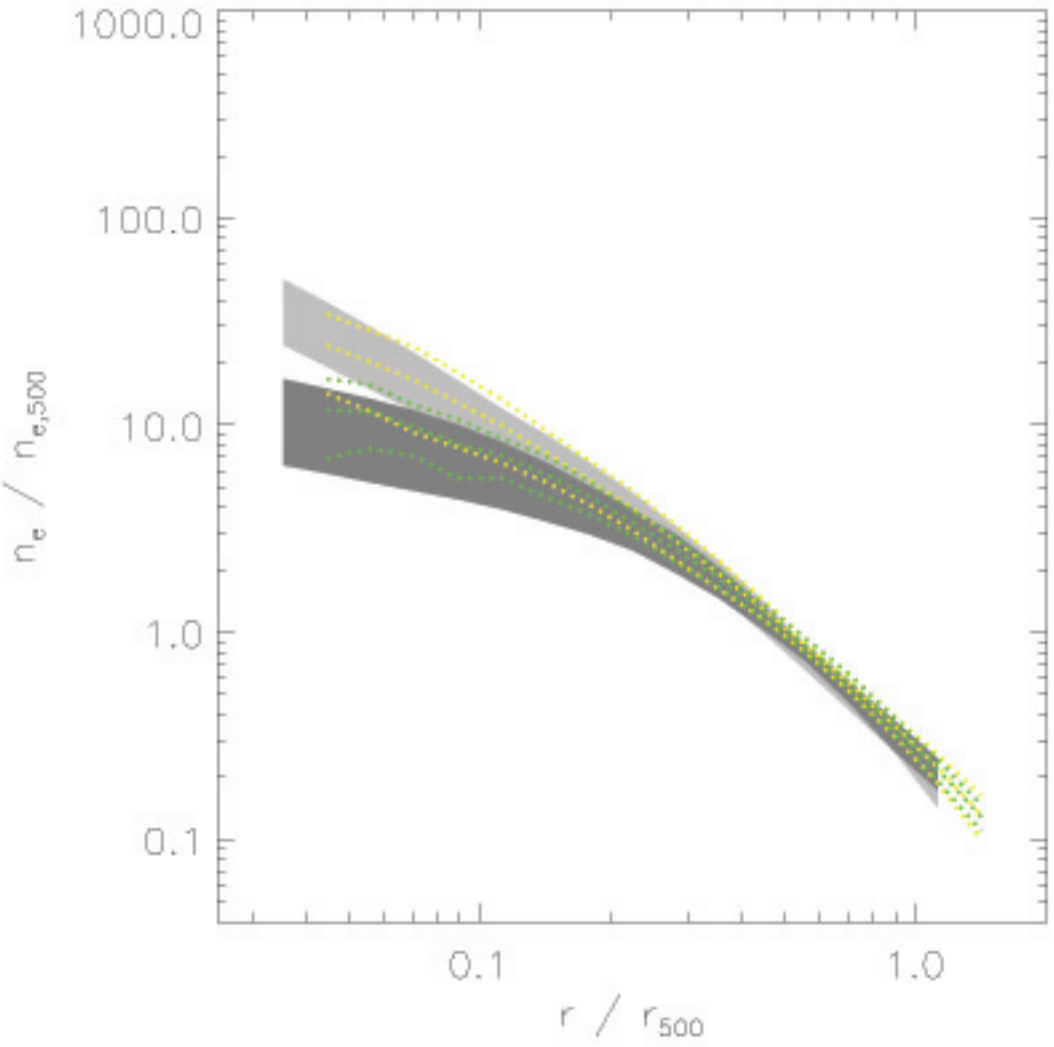

Figure 6.14: The mean electron number-density profiles and 1σ scatter for the CC (yellow) and NCC (green) clusters overlaid on the mean and 1σ scatter in the observational data of Pratt et al. (2009a) for cool core (light grey) and non-cool core (dark grey) clusters.

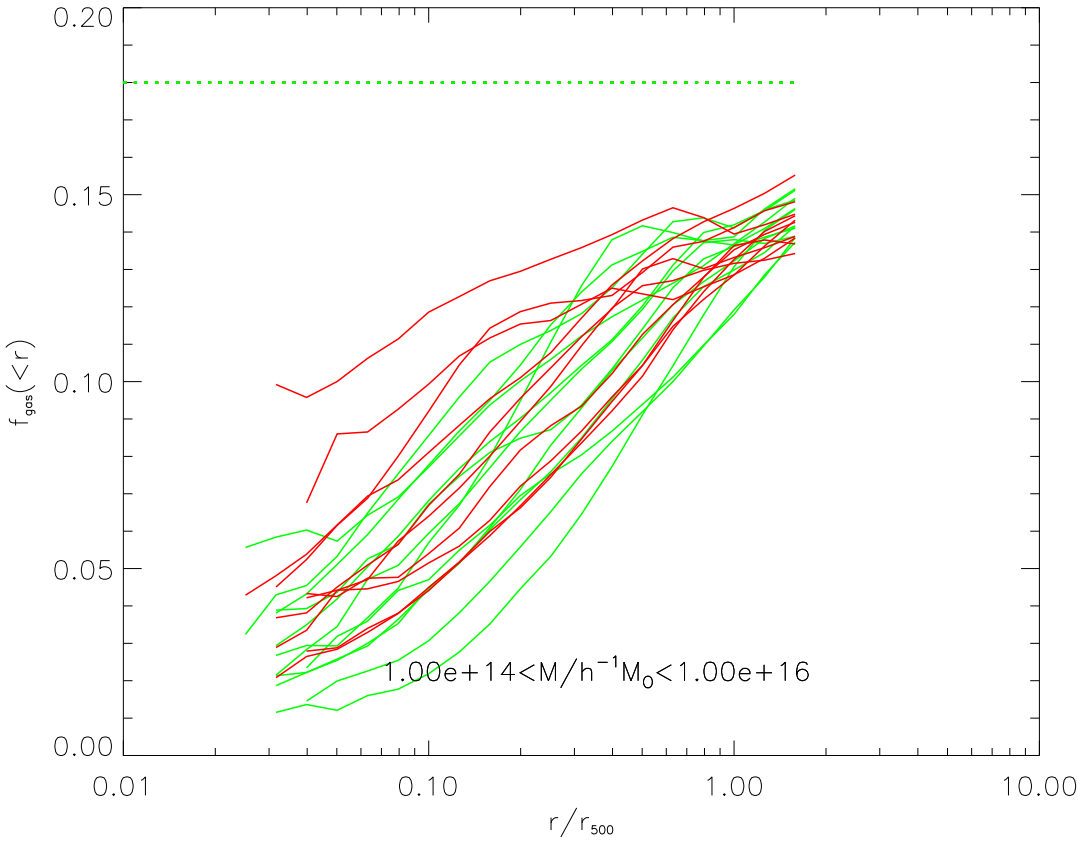

Figure 6.15: The cumulative gas fraction profiles for a sample of clusters simulated using our final model. The green lines represent the non-cool core clusters and the red lines the cool core clusters. The change in the lines' colours towards the cluster centres represents the extent of the gravitational softening. This plot shows a difference between the cool core and non-cool core clusters where the profiles of the cool core clusters are higher within the central $0.15R_{500}$ than those of the non-cool core clusters. There is, however, a large amount of scatter in the profiles of both classes and there appears to be less central flattening in the cool core clusters than was observed in the REXCESS sample (figure 4.3).

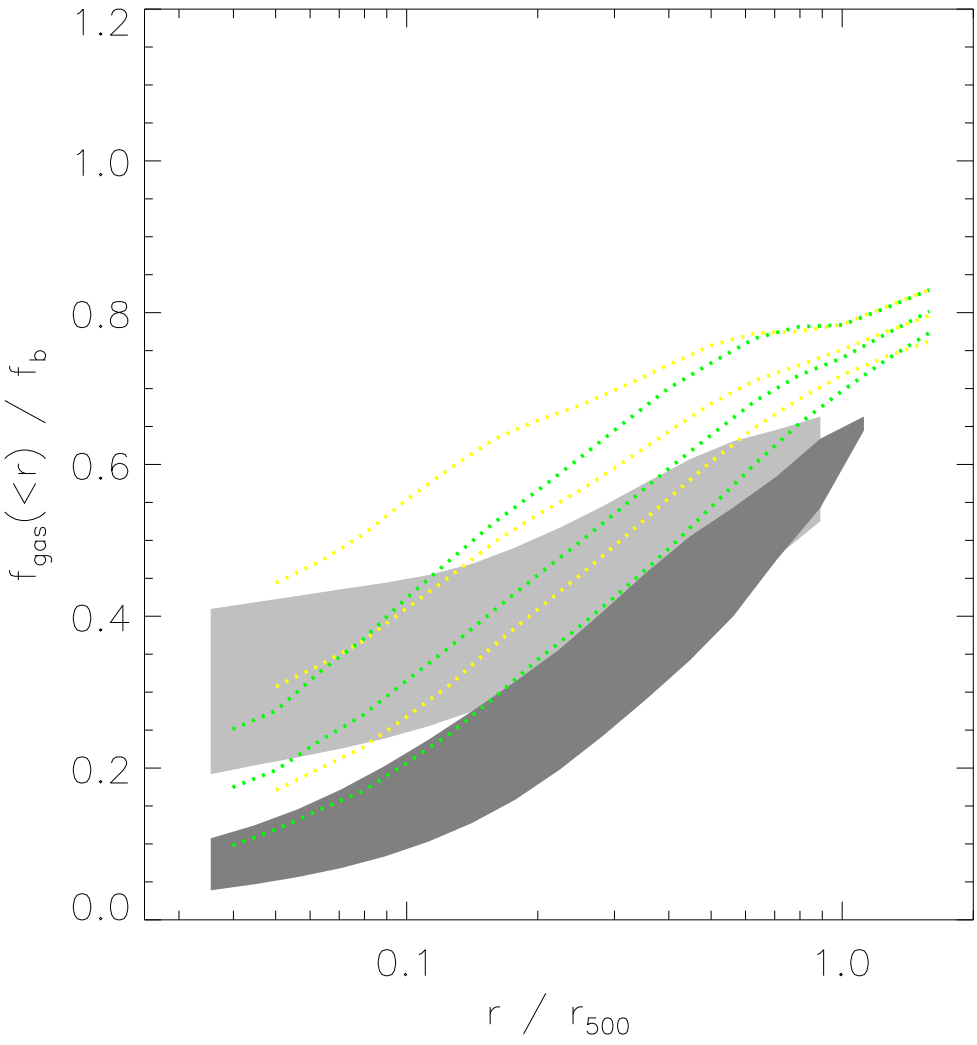

Figure 6.16: The mean gas fraction profiles and 1σ errors for the CC (yellow) and NCC (green) clusters overlaid on the mean and 1σ scatter in the observational data of Pratt et al. (2009a) for cool core (light grey) and non-cool core (dark grey) clusters.

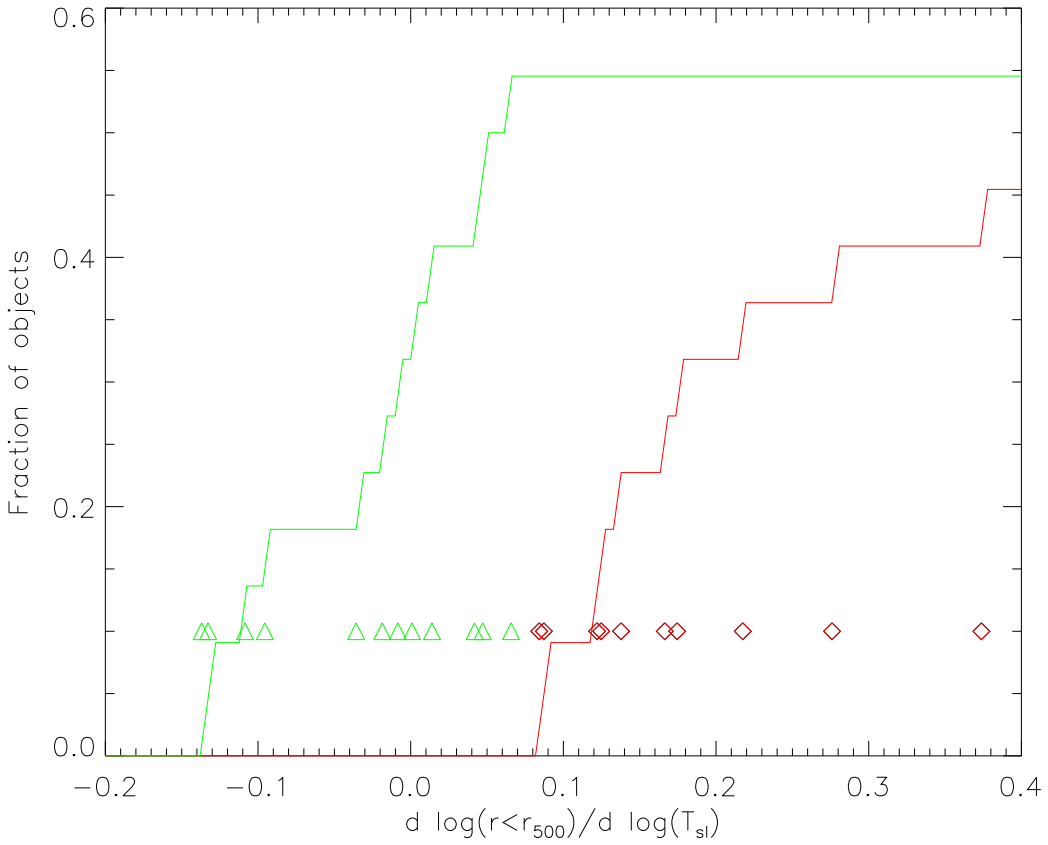

Figure 6.17: The slopes of the inner spectroscopic-like temperature profiles for the simulated clusters. Green triangles represent the non-cool core clusters and red diamonds, the cool core clusters. The distinction between the two classes can be seen, although there is not a clear gap between the populations.

within the gas. If a cluster has a steep entropy profile then its core cooling rate is very fast and heat from the outskirts cannot be conducted into the core quickly enough to prevent the temperature declining, whereas if a cluster has a shallow entropy profile then its cooling rate is lower and the rate at which heat can be conducted to the cluster's core is sufficiently high that it can offset the cooling. They suggest a cutoff value (2/3) of the slope of the entropy profile, above which a cluster will tend towards a cool core and above which it will tend to a non-cool core. Our results do not reproduce such a clear bimodality. This is unsurprising if the argument of Sanderson et al. (2009) is to be believed, since our model does not include conduction.

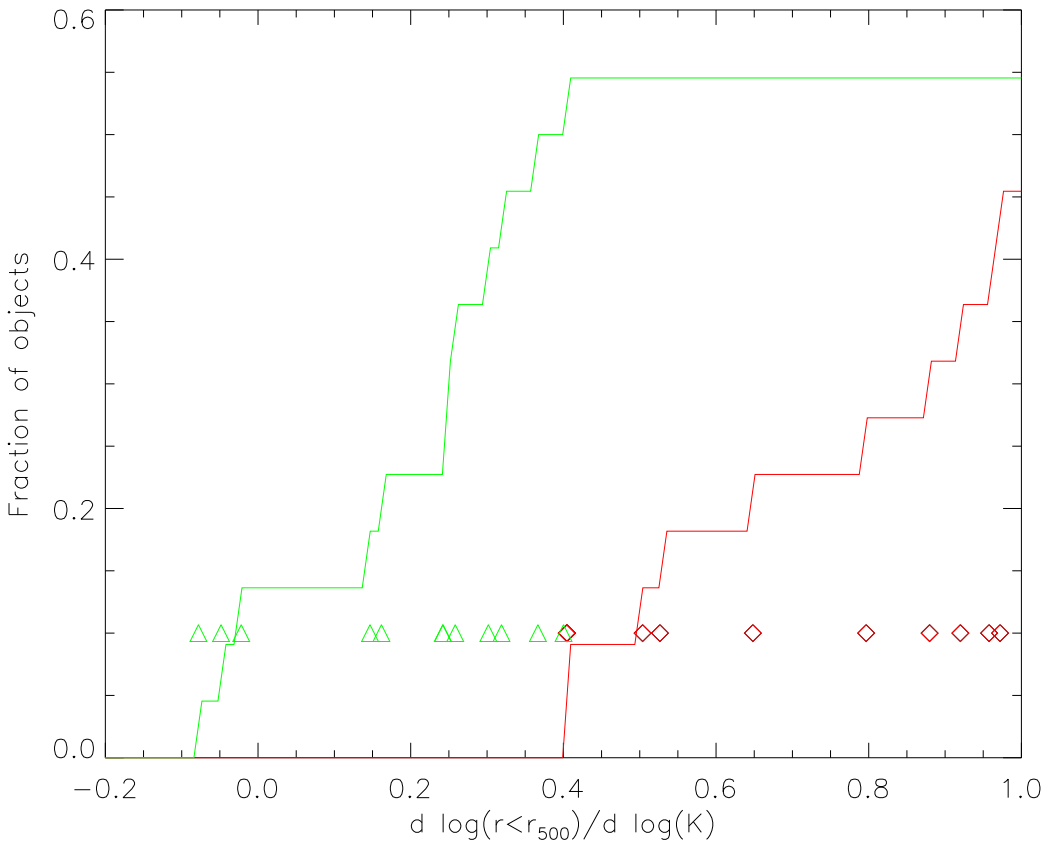

Figure 6.18: The slopes of the inner entropy profiles for the simulated clusters. Green triangles represent the non-cool core clusters and red diamonds, the cool core clusters. The distinction between the two classes can be seen, although there is not a clear gap between the populations.

6.3.3 Formation Histories

Cool core clusters are believed to be relaxed objects (Vikhlinin et al., 2006; Allen et al., 2008, e.g.). We now examine whether or not our sample supports this assertion by examining correlations between a cluster's "cool core-ness" - quantified by the power law slopes of its inner ($r < 0.15r_{500}$) entropy and temperature profiles - with its substructure statistic and its recent change in mass.

We define the recent change in mass as the maximum change in cluster mass since $z = 0.4$. We do this because when clusters undergo major mergers their masses oscillate whilst they attempt to virialise. The result of this is that, at $z = 0$, the masses of such clusters are often lower than they have previously been (similarly they may be higher at $z = 0.4$) and therefore simply comparing their masses at $z = 0$ and $z = 0.4$ suggests they have been less perturbed than they have been.

It is apparent from figure 6.19 that there is no correlation between a cluster's "cool core-ness" and these two measures of relaxation, although there is a band in mass jump between 0.4 and 0.55 within which clusters are much more likely to have non-cool cores. That there exists a band in which clusters are more likely to have cool cores, rather than a cutoff value between the two regimes is an effect of the symmetry between the merger of a larger cluster with a smaller one and vice versa. A closer examination of the formation histories of these objects shows that they had recent mergers with much more massive objects. This is equivalent to the more massive object undergoing a minor merger and therefore having a high $M_{z=0.4}/M_{z=0}$.

The merger histories for randomly selected cool core and non-cool core clusters is shown in figure 6.20. This figure gives an indication of the differences in formation histories for the two classes of object.

The difference in substructure statistics between cool core and non-cool core clusters is only slight, although there is a suggestion that non-cool core clusters have slightly higher substructure statistics, with the exceptions of the two aforementioned clusters which have been the minor objects in mergers with much larger objects.

There is one non-cool core cluster falling outside this range. An examination of its formation history shows that it underwent a major merger at $z \simeq 0.9$ from which it had not fully recovered before undergoing a second, smaller merger. The formation history of this object is shown in figure 6.21. This object illustrates the difficulty in attempting to define the extent to which clusters are relaxed in a simple way.

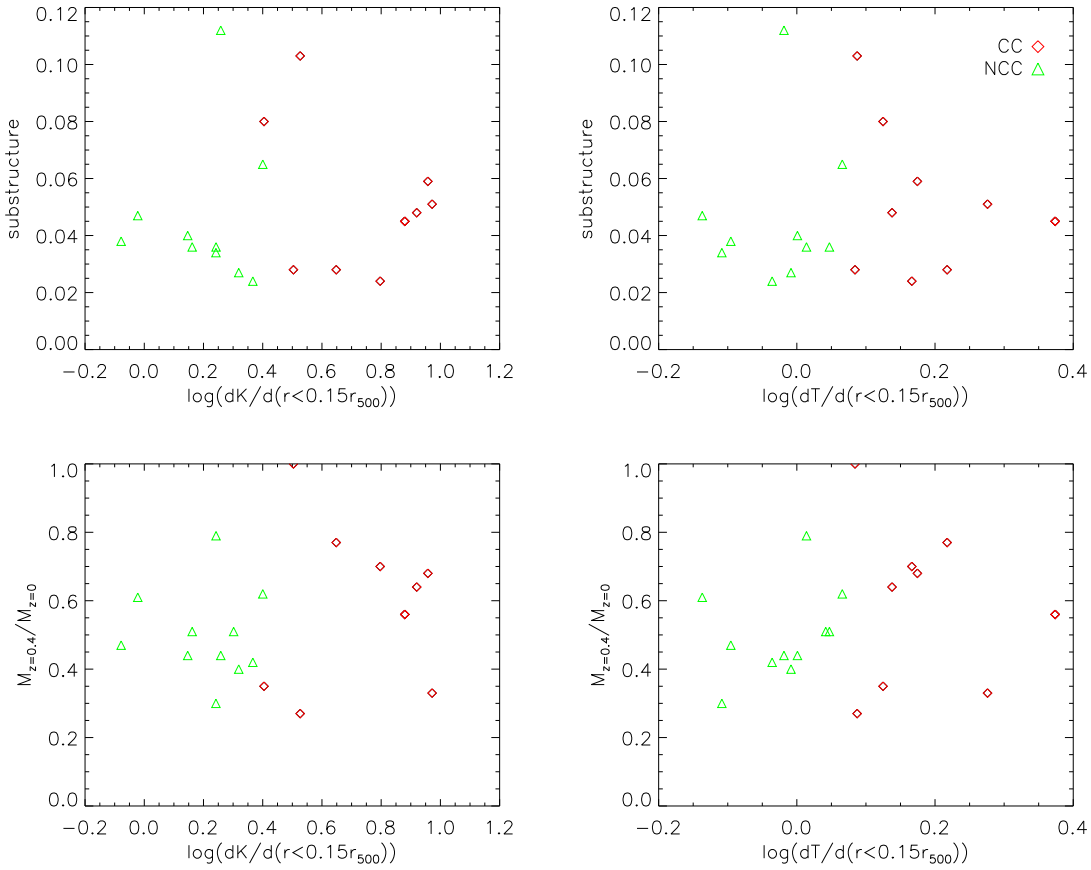

Figure 6.19: Power law slopes of temperature profiles (right) and entropy profiles (left) against substructure (top) and maximum fractional jump in M_{500} since $z = 0.4$ (bottom). Green triangles represent non-cool core clusters and red diamonds represent cool core clusters. The high substructure values and low fractional mass changes for two cool core clusters should not be trusted since they are the result of a recent merger with a much larger object.

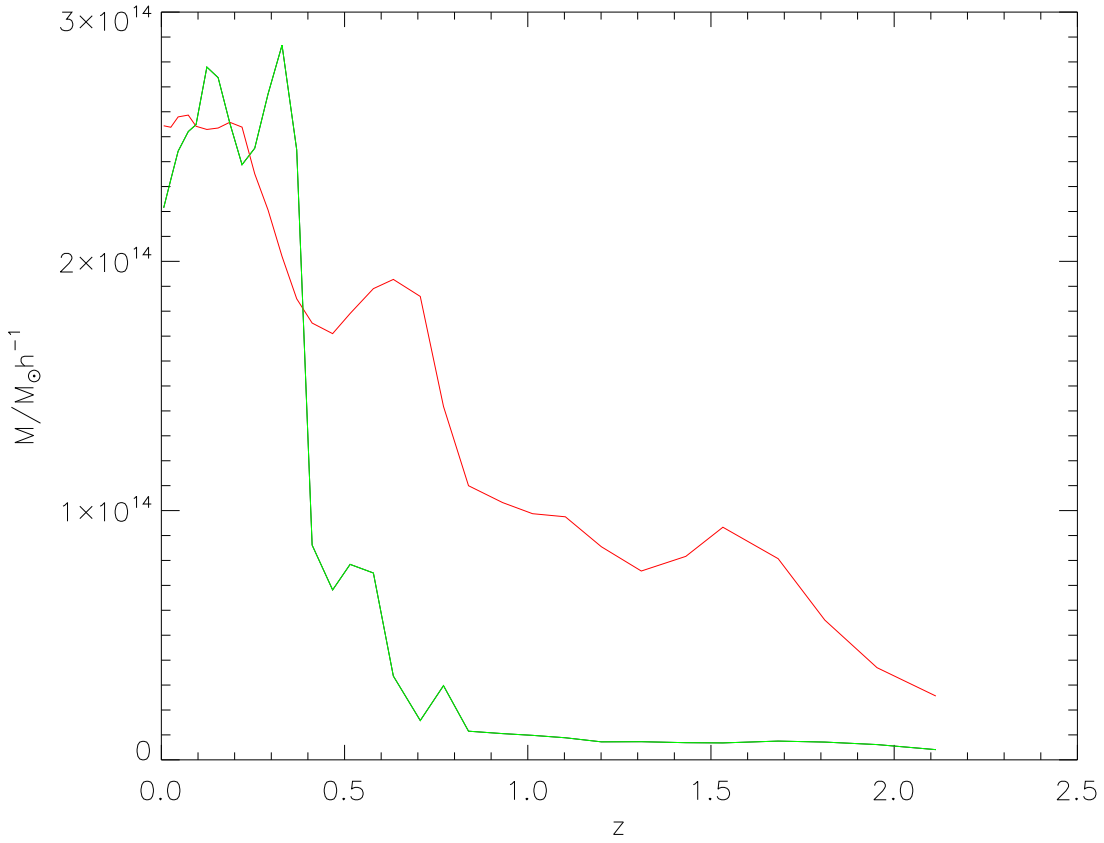

Figure 6.20: Typical merger histories for a cool core (red) and non-cool core (green) clusters. The formation history for the cool core cluster is a lot smoother than that of the non-cool core cluster which had a major merger at a redshift of approximately 0.4

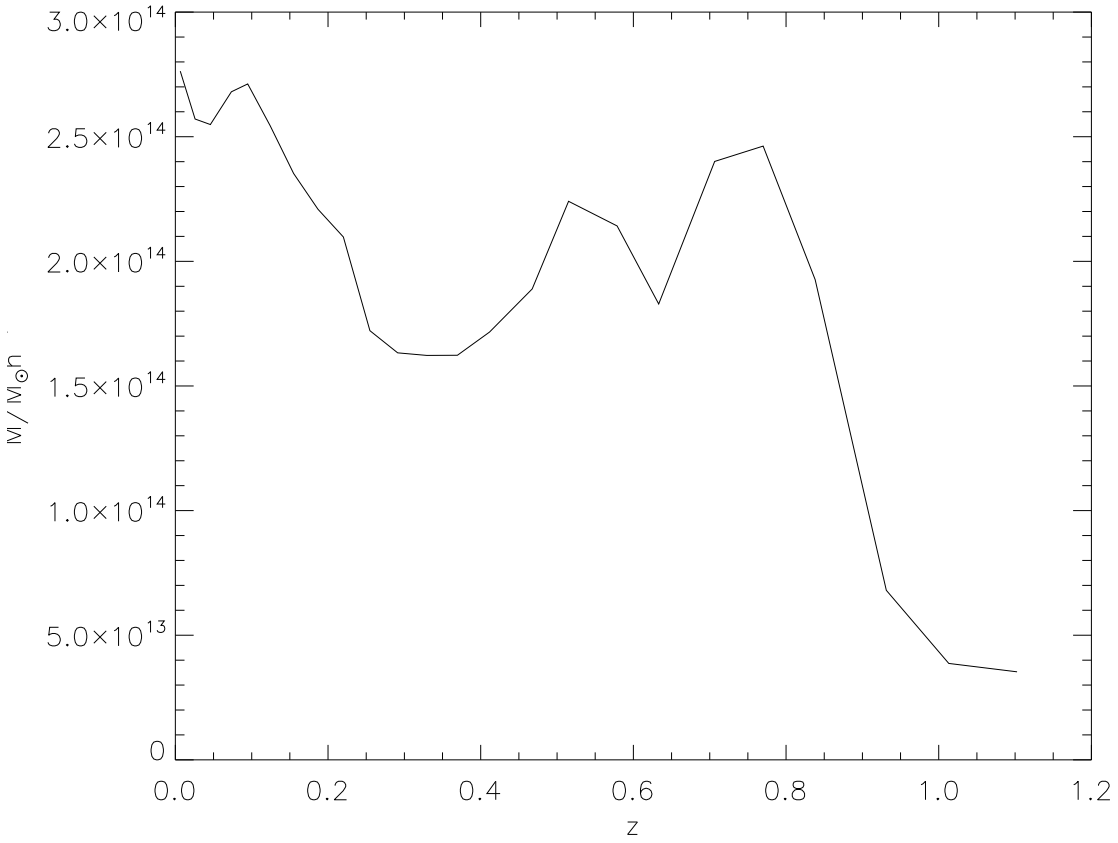

Figure 6.21: The formation history of cluster 1527, the recent merger history of which suggests it would have a cool core, however it underwent a major merger prior to its second, minor merger.

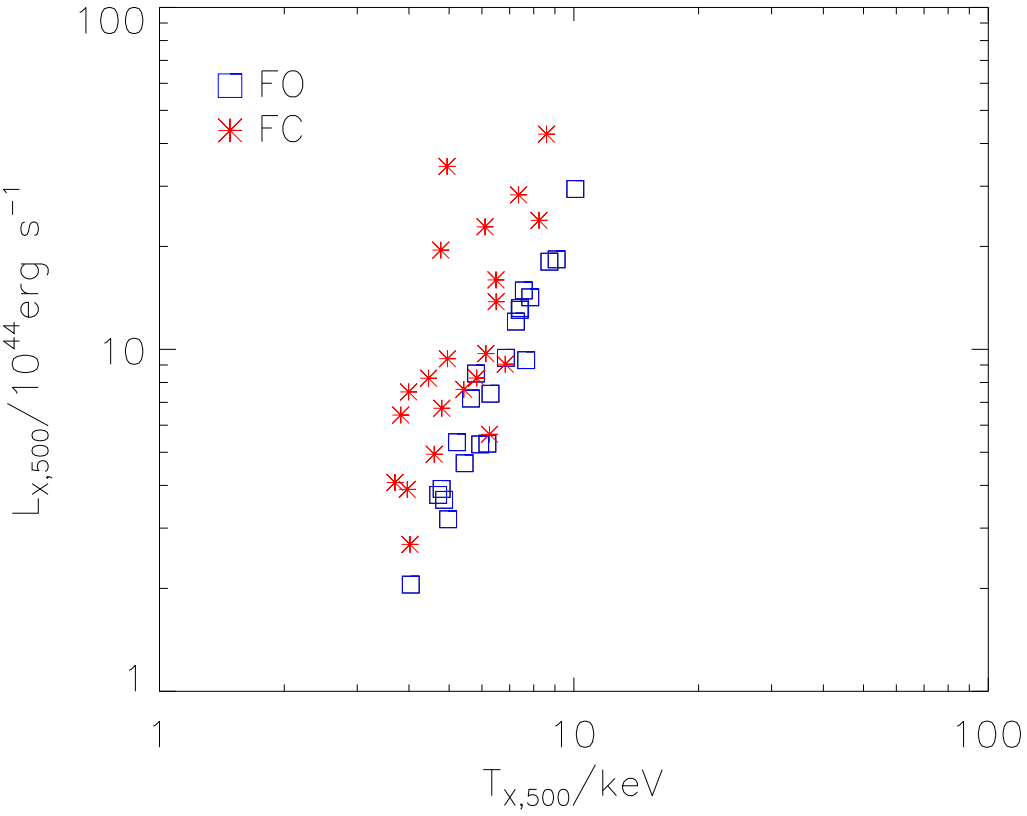

Figure 6.22: The change in the scatter from the FO run to the FC in the $L_X - T$ plane. The red stars show the FC clusters, and the blue squares show their FO counterparts. Several of the FC clusters appear to have been scattered to higher luminosities.

6.3.4 The luminosity-temperature relation

The luminosity-temperature relation for the FO simulation failed to show the observed scatter. This was to be expected, since the population consisted solely of non-cool core clusters and it is believed that an important driver for this scatter is the differing core regions of cool core and non-cool core clusters (O'Hara et al., 2006; Chen et al., 2007). We now examine whether the FC simulation shows greater scatter in the luminosity temperature relation than the FO simulation does.

Since there are insufficient objects in the FC simulation to produce its own scaling relation, we examine the relationship between the positions of the FC clusters and the corresponding FO clusters in the $L_X - T$ plane.

Figure 6.22 shows the positions of the FC clusters on the $L_X - T$ plane atop the FO clusters. It appears that several of them are scattered towards higher luminosities than is usual for their temperatures. This is to be expected for cool core clusters whose cores are

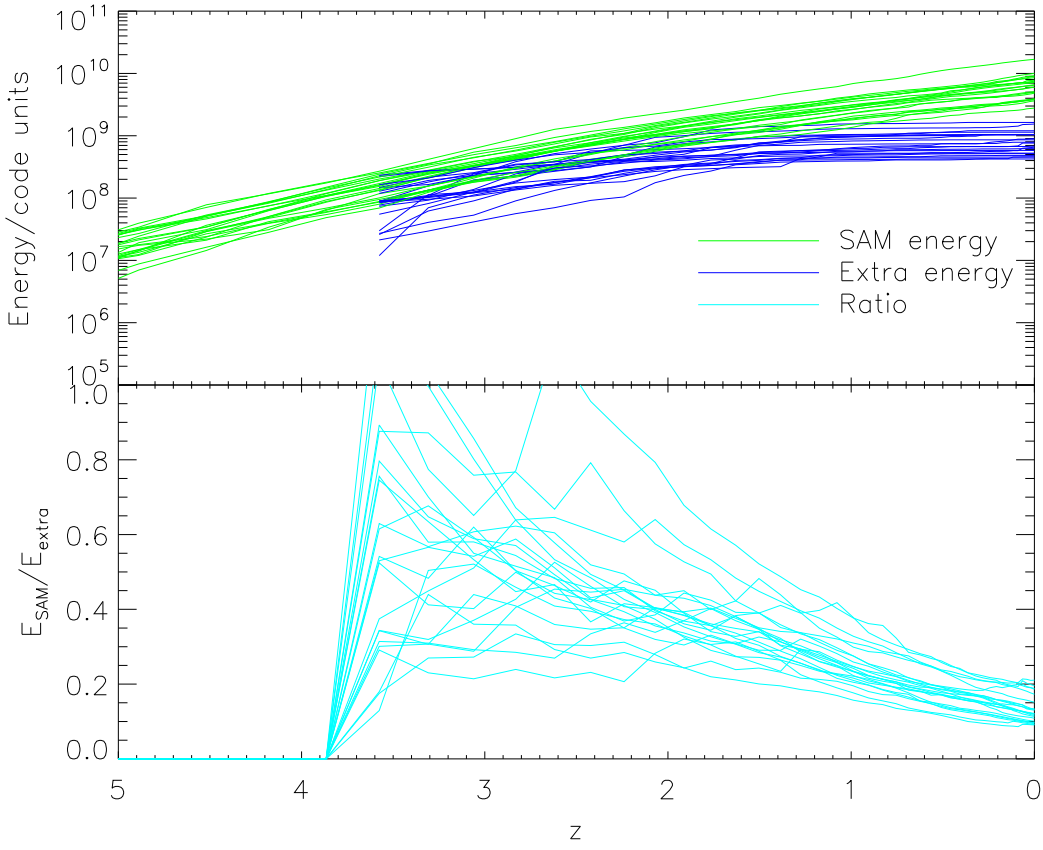

Figure 6.23: The cumulative energy injection in the FC run as a function of redshift. The green lines show the SAM energy, the blue lines show the extra energy and the cyan lines show the ratio of the two.

a source of much luminosity. Excising the cores reduces this scatter, as has been seen in observations (Markevitch, 1998, for example).

6.3.5 Energy Requirements

We now turn to look at the amount of additional energy required by the FC scheme, which appears to be reasonable - typically of order 10% of the energy injected by the feedback prescription.

Most of this energy is injected at high redshift (as can be seen in figure 6.23) with very little energy added since $z = 2$. Prior to this, the additional energy injection is typically equal to that injected from the feedback with both schemes showing the same behaviour at high redshift. The ratio of extra energy to feedback energy drops after $z = 2$ due to the continued injection of feedback energy and the aforementioned drop in extra energy.

This cessation in the extra heating will have been the result of all the overcooled gas

in the cluster centres having been removed. The need for additional energy at early times rather than late ones suggests that the discrepancy between the semi-analytic cooling function and the cluster scale radiative cooling is greatest at early times. This is not surprising, since the metallicity evolution scheme we use (and therefore the evolution of the cooling function) is very simplistic.

6.4 Conclusions

The feedback scheme of Short and Thomas (2009), when combined with a radiative cooling prescription such as that in the PC model results in an overcooling of the particles in the clusters' centres. We attempted to correct for this either by decoupling of hot and cold gas, or additional heating of the cold gas particles. After considering several mechanisms we chose a model in which we heated cold particles within $0.1R_{500}$ of a cluster's centre up to six times the cluster's gas mass-weighted temperature, in a box with a linearly evolving universal metallicity. Doing this prevents the cooling catastrophe which occurs without this additional heating and brings the clusters' temperature and entropy profiles into close agreement those observed in the REXCESS sample (Pratt et al., 2009a).

The energy requirements of this method are reasonable - typically $\approx 10\%$ of the energy the clusters receive from the semi-analytic heating. This additional heat may plausibly be the result of a mismatch between the semi-analytic gas cooling and the cluster scale radiative cooling, and could be produced by star formation occurring in the cold, dense clumps of gas. This additional energy injection happens at high redshift and is typically finished by $z = 2$.

When considering a sample of 22 clusters uniformly distributed in the mass range $2 \times 10^{14} M_{\odot} h^{-1} < M_{500} < 9 \times 10^{14} M_{\odot} h^{-1}$, this model succeeds in producing distinct populations of cool core (9 objects) and non-cool core (13 objects) clusters which is a first in a simulated cluster sample. Entropy, temperature and density profiles for the sample all show the clear distinction between cool core and non-cool core cluster within the central $0.15R_{500}$. The size of this central region is in agreement with that observed by Maughan (2007); Pratt et al. (2009a); and others, however the peak in the temperature profiles for the cool core clusters is at a much greater radius than is observed.

Gas fraction profiles also show a clear difference between the two populations, but the profiles for the cool core clusters are not in perfect agreement with observations in their centres.

Comparing the positions of the 22 selected objects on the $L-T$ plane with the positions

of their counterparts from the FO simulation shows an increase in the scatter of the FC clusters. This is caused by several of the objects being scattered to higher temperatures for their luminosity, with others staying in similar positions to their FO counterparts. This increase in scatter is in agreement with observations.

An examination of the clusters' histories reveals that non-cool core clusters have generally undergone a significant merger since $z = 0.4$ and cool core clusters have not (although there is no correlation between the size of this merger and "cool core-ness"). This is in agreement with previous assertions that cool core clusters are relaxed objects.

Chapter 7

Conclusions

This thesis presents the Millennium Gas simulations, and uses them to study the effects of different energy injection and radiative cooling schemes on populations of galaxy clusters.

Chapter 3 presentes the details of the simulations, describes the data reduction procedure and the generated data, and compares the results of the different simulations with X-ray observations of galaxy clusters, both at $z = 0$ and out to $z = 1$. The comparison between the observed data and the PC and FO simulations at low redshift shows that both were in good agreement with the observations, although neither simulation produced cool core clusters. In the PC simulation, this is because the preheating scheme is so severe that it blasts out any nascent cool core clusters, and in the case of the FO run, the lack of radiative cooling means that no cool cores could ever form.

At high redshift, however, the PC and FO runs make different predictions for the evolution of both the cluster profiles and scaling relations. The PC run predicts negative evolution (with respect to self-similarity) in the electron number density profiles, and positive evolution in the temperature and entropy profiles, whereas the FC run predicts no evolution. The two models predict opposite senses of the evolution in the normalisation of the $L-T$ and $T-M$ scalings, with the FC run predicting positive and negative evolution respectively. High redshift observational data is, at present, insufficient to determine which model is a better fit.

Chapter 4 takes a closer look at the hot gas fractions in cluster samples taken from the Millennium Gas simulations, comparing them with observations and examining the differing predictions for high redshift clusters.

Both the PC and FO runs produced clusters whose gas fraction profiles were in good agreement with those of non-cool core clusters in the REXCESS sample (Pratt et al., 2009a), but were well below the profiles of cool core clusters from Vikhlinin et al. (2006)

and Allen et al. (2008).

Integrated gas fractions within r_{500} are in reasonable agreement with observations (particularly in clusters above $5 \times 10^{14} h^{-1} M_{\odot}$), but the simulated cluster gas fractions show a greater dependence on mass within r_{2500} than is observed. We provide a fitting function to predict the mean cluster gas fraction for a given mass cluster.

Stellar fractions produced in both simulations show a smaller mass dependence than is observed, in agreement with previous work. The stellar fractions of the large simulated clusters are close to those observed (~ 0.013), rising in low mass objects, but much more slowly than in observed systems.

The evolution of the cluster gas fraction is then used as a discriminant between the FO and PC models by using the fitting function to predict the gas fraction for clusters in the *Chandra* sample (Maughan et al., 2008) based on their mass and redshift, and comparing the predicted gas fractions to the measures ones. Doing this, we can see that the observational data is fully consistent with the FO predictions, but is in disagreement with the PC predictions. From this, we conclude that a model of continual heating is preferred to an epoch of preheating at high redshift. Additionally, we conclude that the dependence of cluster gas fraction on the physical model limits its use as a cosmological probe.

Chapter 5 seeks to explain the scatter about the mean gas fraction in terms of other global cluster properties. The statistical techniques used to examine the dataset were explained. The mass limit above which cluster gas fraction ceases to be a function of mass was examined and shown to be in broad agreement with the measurements of McCarthy et al. (2007) and Allen et al. (2008).

Every variable conceivably causing scatter in the gas fraction was examined and no strong correlation between any variable, or group of variables likely to cause the scatter, could be found. However, there is a strong, positive correlation with the product of the scatter about the $L - T$ relation and the scatter about the $T - M$ relation, which can be strengthened if the variables are raised to the appropriate powers.

Chapter 6 attempts to combine the FO simulation with the radiative cooling scheme in the PC simulation. This is done by the addition of a heating source affecting only the overcooled particles in the cluster and heating them sufficiently to remove them from the cooling cycle. This requires typically 10% of the energy injected by the feedback scheme.

After doing this, the resulting model is able to produce both cool core and non-cool core clusters which, although showing less of a clear distinction than is observed, have

temperature, electron number density and entropy profiles in good agreement with those of the REXCESS sample (Pratt et al., 2009a).

The histories of both these classes of object are examined, and whilst no correlation between the "cool coreness" of a cluster (defined by the power-law slope of its inner temperature and entropy profiles) and its recent change in mass, non-cool core clusters have generally undergone a significant merger since $z = 0.4$ and cool core clusters had not. This supports previous assertions (e.g. Allen et al., 2008) than cool core clusters are relaxed objects.

7.1 Summary

The key results of this thesis are those contained in chapters 4 and 6 - that a continual injection of energy gives a closer match to cluster evolution than an epoch of preheating; and an appropriate feedback scheme, in combination with radiative cooling, can simulate a population of galaxy clusters containing both cool core and non-cool core objects, the difference between classes appearing to be caused by their recent merger history. The results in chapter 5 suggest that there may be a systematic bias in cluster observations towards those objects with a high gas fraction. This is not surprising.

7.2 Remaining problems

Whilst having answered some questions, the results in this thesis have raised further problems. Perhaps most notably is concerning the interpretation of cluster gas fraction observations. The high sensitivity of the gas fraction to the underlying physical processes makes the use of clusters to study the Universal gas fraction problematic - at least whilst the underlying physical processes are not well understood. Because of this, it may be better to assume a concordance cosmology, then use gas fraction observations to constrain cluster physics, rather than to use the observations to constrain the cosmology.

The feedback-plus-cooling model from chapter 6 is in need of further refinement. Whilst it is the first model to convincingly produce both cool core and non-cool core clusters, the two populations are not as distinct as those from observations. In addition to this, the gas fraction profiles, particularly for CC clusters, are not a good match to observations. The metallicity evolution assumed in the FC model is very simple, and unlikely to be anything more than a first order approximation to the true metallicity evolution. The semi-analytic model underpinning the feedback scheme is able to model the galaxy scale

metallicity (the regime in which the metallicity does change), so it is possible to integrate this into the feedback scheme to give a realistic metallicity evolution. Work on this is already underway.

The size of the sample used in chapter 6 is a weakness, but fortunately one that is easily remedied with sufficient computational resources. A larger sample size - at least as large as that of the FO simulation - would produce convincing scaling relations, and also allow a robust statistical analysis of the processes producing cool core, or non-cool core clusters.

Bibliography

Aarseth, S. J. (1963). Dynamical evolution of clusters of galaxies, I. *Monthly Notices of the Royal Astronomical Society*, 126:223–+. 8

Abell, G. O. (1958). The Distribution of Rich Clusters of Galaxies. *Astrophysical Journal, Supplement*, 3:211–+. 3

Abell, G. O., Corwin, Jr., H. G., and Olowin, R. P. (1989). A catalog of rich clusters of galaxies. *Astrophysical Journal, Supplement*, 70:1–138. 3

Allen, S. W., Rapetti, D. A., Schmidt, R. W., Ebeling, H., Morris, R. G., and Fabian, A. C. (2008). Improved constraints on dark energy from Chandra X-ray observations of the largest relaxed galaxy clusters. *Monthly Notices of the Royal Astronomical Society*, 383:879–896. 4, 50, 59, 62, 63, 68, 70, 89, 92, 93, 111, 139, 148, 149

Allen, S. W., Schmidt, R. W., Ebeling, H., Fabian, A. C., and van Speybroeck, L. (2004). Constraints on dark energy from Chandra observations of the largest relaxed galaxy clusters. 353:457–467. 59, 92

Allen, S. W., Schmidt, R. W., and Fabian, A. C. (2001). The X-ray virial relations for relaxed lensing clusters observed with Chandra. *Monthly Notices of the Royal Astronomical Society*, 328:L37–L41. 29

Allen, S. W., Schmidt, R. W., and Fabian, A. C. (2002). Cosmological constraints from the X-ray gas mass fraction in relaxed lensing clusters observed with Chandra. 334:L11–L15. 59

Andersson, K. et al. (2010). X-ray Properties of the First SZE-selected Galaxy Cluster Sample from the South Pole Telescope. 92

Andreon, S. (2010). The stellar mass fraction and baryon content of galaxy clusters and groups. *Monthly Notices of the Royal Astronomical Society*, 407:263–276. 75, 76

Arnaud, M. and Evrard, A. E. (1999). The L_X-T relation and intracluster gas fractions of X-ray clusters. *Monthly Notices of the Royal Astronomical Society*, 305:631–640. 6

Arnaud, M., Pointecouteau, E., and Pratt, G. W. (2007). Calibration of the galaxy cluster $M_{500} - Y_X$ relation with XMM-Newton. 474:L37–L40. 7, 43, 47, 70, 74

Ascasibar, Y., Sevilla, R., Yepes, G., Müller, V., and Gottlöber, S. (2006). Adiabatic scaling relations of galaxy clusters. 371:193–203. 33

Bade, N., Engels, D., Voges, W., Beckmann, V., Boller, T., Cordis, L., Dahlem, M., Englhauser, J., Molthagen, K., Nass, P., Studt, J., and Reimers, D. (1998). The Hamburg/RASS Catalogue of optical identifications. *Astronomy and Astrophysics, Supplement*, 127:145–152. 3

Bagla, J. S. and Padmanabhan, T. (1997). Cosmological N-body simulations. *Pramana*, 49:161–+. 24

Balestra, I., Tozzi, P., Ettori, S., Rosati, P., Borgani, S., Mainieri, V., Norman, C., and Viola, M. (2007). Tracing the evolution in the iron content of the intra-cluster medium. *Astronomy and Astrophysics*, 462:429–442. 124

Balogh, M. L., McCarthy, I. G., Bower, R. G., and Eke, V. R. (2008). Testing cold dark matter with the hierarchical build-up of stellar light. 385:1003–1014. 75

Balogh, M. L., Pearce, F. R., Bower, R. G., and Kay, S. T. (2001). Revisiting the cosmic cooling crisis. *Monthly Notices of the Royal Astronomical Society*, 326:1228–1234. 113

Barnes, J. and Hut, P. (1986). A hierarchical O(N log N) force-calculation algorithm. *Nature*, 324:446–449. 24

Baugh, C. M. (2006). A primer on hierarchical galaxy formation: the semi-analytical approach. *Reports on Progress in Physics*, 69:3101–3156. 35

Bernstein, G. M., Nichol, R. C., Tyson, J. A., Ulmer, M. P., and Wittman, D. (1995). The Luminosity Function of the Coma Cluster Core for $-25 ¡ M/R ¡ -9.4$. 110:1507–+. 73

Bialek, J. J., Evrard, A. E., and Mohr, J. J. (2001). Effects of Preheating on X-Ray Scaling Relations in Galaxy Clusters. 555:597–612. 92

Böhringer, H., Schuecker, P., Pratt, G. W., Arnaud, M., Ponman, T. J., Croston, J. H., Borgani, S., Bower, R. G., Briel, U. G., Collins, C. A., Donahue, M., Forman, W. R.,

Finoguenov, A., Geller, M. J., Guzzo, L., Henry, J. P., Kneissl, R., Mohr, J. J., Matsushita, K., Mullis, C. R., Ohashi, T., Pedersen, K., Pierini, D., Quintana, H., Raychaudhury, S., Reiprich, T. H., Romer, A. K., Rosati, P., Sabirli, K., Temple, R. F., Viana, P. T. P., Vikhlinin, A., Voit, G. M., and Zhang, Y. (2007). The representative XMM-Newton cluster structure survey (REXCESS) of an X-ray luminosity selected galaxy cluster sample. 469:363–377. 62

Böhringer, H. and Werner, N. (2010). X-ray spectroscopy of galaxy clusters: studying astrophysical processes in the largest celestial laboratories. *Astronomy and Astrophysics Reviews*, 18:127–196. 3

Borgani, S., Dolag, K., Murante, G., Cheng, L., Springel, V., Diaferio, A., Moscardini, L., Tormen, G., Tornatore, L., and Tozzi, P. (2006). Hot and cooled baryons in smoothed particle hydrodynamic simulations of galaxy clusters: physics and numerics. *Monthly Notices of the Royal Astronomical Society*, 367:1641–1654. 33

Borgani, S., Governato, F., Wadsley, J., Menci, N., Tozzi, P., Quinn, T., Stadel, J., and Lake, G. (2002). The effect of non-gravitational gas heating in groups and clusters of galaxies. 336:409–424. 34

Borgani, S., Murante, G., Springel, V., Diaferio, A., Dolag, K., Moscardini, L., Tormen, G., Tornatore, L., and Tozzi, P. (2004). X-ray properties of galaxy clusters and groups from a cosmological hydrodynamical simulation. 348:1078–1096. 75

Bower, R. G., McCarthy, I. G., and Benson, A. J. (2008). The flip side of galaxy formation: a combined model of galaxy formation and cluster heating. *Monthly Notices of the Royal Astronomical Society*, 390:1399–1410. 36

Bradt, H., Naranan, S., Rappaport, S., and Spada, G. (1968). Celestial Positions of X-Ray Sources in Sagittarius. *The Astrophysical Journal*, 152:1005–+. 4

Bryan, G. L. and Norman, M. L. (1998). Statistical Properties of X-Ray Clusters: Analytic and Numerical Comparisons. *The Astrophysical Journal*, 495:80–+. 20

Burns, J. O., Hallman, E. J., Gantner, B., Motl, P. M., and Norman, M. L. (2008). Why Do Only Some Galaxy Clusters Have Cool Cores? *The Astrophysical Journal*, 675:1125–1140. 83

Byram, E. T., Chubb, T. A., and Friedman, H. (1966). Cosmic X-ray Sources, Galactic and Extragalactic. *Science*, 152:66–71. 4

Carballo, R., Warwick, R. S., Barcons, X., Gonzalez-Serrano, J. I., Barber, C. R., Martinez-Gonzalez, E., Perez-Fournon, I., and Burgos, J. (1995). The ROSAT UK Medium Sensitivity Survey: optical identification and relation to X-ray spectral properties. *Monthly Notices of the Royal Astronomical Society*, 277:1312–1326. 3

Cavaliere, A. and Fusco-Femiano, R. (1976). X-rays from hot plasma in clusters of galaxies. *Astronomy and Astrophysics*, 49:137–144. 21

Cavaliere, A. G., Gursky, H., and Tucker, W. H. (1971). Extragalactic X-ray Sources and Associations of Galaxies. *Nature*, 231:437–438. 4

Chen, Y., Reiprich, T. H., Böhringer, H., Ikebe, Y., and Zhang, Y. (2007). Statistics of X-ray observables for the cooling-core and non-cooling core galaxy clusters. *Astronomy and Astrophysics*, 466:805–812. 6, 7, 143

Cole, S. (1991). Modeling galaxy formation in evolving dark matter halos. *The Astrophysical Journal*, 367:45–53. 113

Connolly, A. J., Szalay, A. S., Dickinson, M., Subbarao, M. U., and Brunner, R. J. (1997). The Evolution of the Global Star Formation History as Measured from the Hubble Deep Field. *The Astrophysical Journal, Letters*, 486:L11+. 124

Crain, R. A., Eke, V. R., Frenk, C. S., Jenkins, A., McCarthy, I. G., Navarro, J. F., and Pearce, F. R. (2007). The baryon fraction of ΛCDM haloes. *Monthly Notices of the Royal Astronomical Society*, 377:41–49. 33, 65, 92

Dai, X., Bregman, J. N., Kochanek, C. S., and Rasia, E. (2010). On the Baryon Fractions in Clusters and Groups of Galaxies. *The Astrophysical Journal*, 719:119–125. 103

Davé, R., Oppenheimer, B. D., and Sivanandam, S. (2008). Enrichment and pre-heating in intragroup gas from galactic outflows. 391:110–123. 75

Davis, M., Efstathiou, G., Frenk, C. S., and White, S. D. M. (1985). The evolution of large-scale structure in a universe dominated by cold dark matter. *The Astrophysical Journal*, 292:371–394. 8

De Lucia, G. and Blaizot, J. (2007). The hierarchical formation of the brightest cluster galaxies. *Monthly Notices of the Royal Astronomical Society*, 375:2–14. 36

Eisenhardt, P. R. M., Brodwin, M., Gonzalez, A. H., Stanford, S. A., Stern, D., Barmby, P., Brown, M. J. I., Dawson, K., Dey, A., Doi, M., Galametz, A., Jannuzi, B. T.,

Kochanek, C. S., Meyers, J., Morokuma, T., and Moustakas, L. A. (2008). Clusters of Galaxies in the First Half of the Universe from the IRAC Shallow Survey. 684:905–932. 34

Eke, V. R., Navarro, J. F., and Frenk, C. S. (1998). The Evolution of X-Ray Clusters in a Low-Density Universe. 503:569–+. 33

Ettori, S., De Grandi, S., and Molendi, S. (2002). Gravitating mass profiles of nearby galaxy clusters and relations with X-ray gas temperature, luminosity and mass. *Astronomy and Astrophysics*, 391:841–855. 6

Ettori, S., Dolag, K., Borgani, S., and Murante, G. (2006). The baryon fraction in hydrodynamical simulations of galaxy clusters. *Monthly Notices of the Royal Astronomical Society*, 365:1021–1030. 9, 30, 65, 75

Ettori, S., Morandi, A., Tozzi, P., Balestra, I., Borgani, S., Rosati, P., Lovisari, L., and Terenziani, F. (2009). The cluster gas mass fraction as a cosmological probe: a revised study. *ArXiv e-prints*. 59, 87

Ettori, S., Tozzi, P., Borgani, S., and Rosati, P. (2004). Scaling laws in X-ray galaxy clusters at redshift between 0.4 and 1.3. *Astronomy and Astrophysics*, 417:13–27. 29, 52, 53

Ettori, S., Tozzi, P., and Rosati, P. (2003). Constraining the cosmological parameters with the gas mass fraction in local and z¿0.7 galaxy clusters. *Astronomy and Astrophysics*, 398:879–890. 92

Evrard, A. E. (1997). The intracluster gas fraction in X-ray clusters - Constraints on the clustered mass density. *Monthly Notices of the Royal Astronomical Society*, 292:289–+. 92

Evrard, A. E. and Henry, J. P. (1991). Expectations for X-ray cluster observations by the ROSAT satellite. *The Astrophysical Journal*, 383:95–103. 34

Fabjan, D., Borgani, S., Tornatore, L., Saro, A., Murante, G., and Dolag, K. (2010). Simulating the effect of active galactic nuclei feedback on the metal enrichment of galaxy clusters. *Monthly Notices of the Royal Astronomical Society*, 401:1670–1690. 75

Feldmeier, J. J., Mihos, J. C., Morrison, H. L., Harding, P., Kaib, N., and Dubinski, J. (2004). Deep CCD Surface Photometry of Galaxy Clusters. II. Searching for Intracluster Starlight in Non-cD clusters. 609:617–637. 73

Feldmeier, J. J., Mihos, J. C., Morrison, H. L., Rodney, S. A., and Harding, P. (2002). Deep CCD Surface Photometry of Galaxy Clusters. I. Methods and Initial Studies of Intracluster Starlight. 575:779–800. 73

Felten, J. E., Gould, R. J., Stein, W. A., and Woolf, N. J. (1966). X-Rays from the Coma Cluster of Galaxies. *The Astrophysical Journal*, 146:955–958. 4

Finoguenov, A., Jones, C., Böhringer, H., and Ponman, T. J. (2002). ASCA Observations of Groups at Radii of Low Overdensity: Implications for the Cosmic Preheating. *The Astrophysical Journal*, 578:74–89. 6, 34

Frenk, C. S., White, S. D. M., Efstathiou, G., and Davis, M. (1985). Cold dark matter, the structure of galactic haloes and the origin of the Hubble sequence. *Nature*, 317:595–597. 8

Gastaldello, F., Buote, D. A., Humphrey, P. J., Zappacosta, L., Bullock, J. S., Brighenti, F., and Mathews, W. G. (2007). Probing the Dark Matter and Gas Fraction in Relaxed Galaxy Groups with X-Ray Observations from Chandra and XMM-Newton. *The Astrophysical Journal*, 669:158–183. 92

Gingold, R. A. and Monaghan, J. J. (1977). Smoothed particle hydrodynamics - Theory and application to non-spherical stars. *Monthly Notices of the Royal Astronomical Society*, 181:375–389. 26

Giodini, S., Pierini, D., Finoguenov, A., Pratt, G. W., Boehringer, H., Leauthaud, A., Guzzo, L., Aussel, H., and the COSMOS collaboration (2009). Stellar and Total Baryon Mass Fractions in Groups and Clusters Since Redshift 1. 703:982–993. 74

Gladders, M. D., López-Cruz, O., Yee, H. K. C., and Kodama, T. (1998). The slope of the cluster elliptical red sequence: A probe of cluster evolution. *The Astrophysical Journal*, 501(2):571. 3

Gladders, M. D. and Yee, H. K. C. (2000). A new method for galaxy cluster detection. i. the algorithm. *The Astronomical Journal*, 120(4):2148. 3

Gonzalez, A. H., Zabludoff, A. I., and Zaritsky, D. (2005). Intracluster Light in Nearby Galaxy Clusters: Relationship to the Halos of Brightest Cluster Galaxies. 618:195–213. 73

Gonzalez, A. H., Zabludoff, A. I., Zaritsky, D., and Dalcanton, J. J. (2000). Measuring the Diffuse Optical Light in Abell 1651. 536:561–570. 73

Gonzalez, A. H., Zaritsky, D., and Zabludoff, A. I. (2007). A Census of Baryons in Galaxy Clusters and Groups. 666:147–155. 74

Grego, L., Carlstrom, J. E., Reese, E. D., Holder, G. P., Holzapfel, W. L., Joy, M. K., Mohr, J. J., and Patel, S. (2001). Galaxy Cluster Gas Mass Fractions from Sunyaev-Zeldovich Effect Measurements: Constraints on Ω_M. *The Astrophysical Journal*, 552:2–14. 92

Hartley, W. G., Gazzola, L., Pearce, F. R., Kay, S. T., and Thomas, P. A. (2008). Nature versus nurture: the curved spine of the galaxy cluster X-ray luminosity-temperature relation. *Monthly Notices of the Royal Astronomical Society*, 386:2015–2021. 7, 33

Hénon, M. (1964). L'évolution initiale d'un amas sphérique. *Annales d'Astrophysique*, 27:83–+. 8

Herschel, W. (1785). O the Construction of the Heavens. *Royal Society of London Philosophical Transactions Series I*, 75:213–266. 3

Hinshaw, G., Weiland, J. L., Hill, R. S., Odegard, N., Larson, D., Bennett, C. L., Dunkley, J., Gold, B., Greason, M. R., Jarosik, N., Komatsu, E., Nolta, M. R., Page, L., Spergel, D. N., Wollack, E., Halpern, M., Kogut, A., Limon, M., Meyer, S. S., Tucker, G. S., and Wright, E. L. (2009). Five-Year Wilkinson Microwave Anisotropy Probe Observations: Data Processing, Sky Maps, and Basic Results. *Astrophysical Journal, Supplement*, 180:225–245. 14

Hogg, D. W. (1999). Distance measures in cosmology. *ArXiv Astrophysics e-prints*. 15

Horner, D. J., Perlman, E. S., Ebeling, H., Jones, L. R., Scharf, C. A., Wegner, G., Malkan, M., and Maughan, B. (2008). The WARPS Survey. VII. The WARPS-II Cluster Catalog. *Astrophysical Journal, Supplement*, 176:374–413. 83

Jansen, F., Lumb, D., Altieri, B., Clavel, J., Ehle, M., Erd, C., Gabriel, C., Guainazzi, M., Gondoin, P., Much, R., Munoz, R., Santos, M., Schartel, N., Texier, D., and Vacanti, G. (2001). XMM-Newton observatory. I. The spacecraft and operations. *Astronomy and Astrophysics*, 365:L1–L6. 4

Jeans, J. H. (1902). The Stability of a Spherical Nebula. *Royal Society of London Philosophical Transactions Series A*, 199:1–53. 18

Jernigan, J. G. and Porter, D. H. (1989). A tree code with logarithmic reduction of force terms, hierarchical regularization of all variables, and explicit accuracy controls. *Astrophysical Journal, Supplement*, 71:871–893. 24

Kaiser, N. (1986). Evolution and clustering of rich clusters. *Monthly Notices of the Royal Astronomical Society*, 222:323–345. 20

Kaiser, N. (1991). Evolution of clusters of galaxies. *The Astrophysical Journal*, 383:104–111. 34

Kay, S. T. (2004). The entropy distribution in clusters: evidence of feedback? *Monthly Notices of the Royal Astronomical Society*, 347:L13–L17. 114

Kay, S. T., da Silva, A. C., Aghanim, N., Blanchard, A., Liddle, A. R., Puget, J.-L., Sadat, R., and Thomas, P. A. (2007). The evolution of clusters in the CLEF cosmological simulation: X-ray structural and scaling properties. 377:317–334. 9, 30, 75, 83, 105, 114

King, I. (1962). The structure of star clusters. I. an empirical density law. *Astronomical Journal*, 67:471–+. 21

Kitzbichler, M. G. and White, S. D. M. (2008). A calibration of the relation between the abundance of close galaxy pairs and the rate of galaxy mergers. 391:1489–1498. 75

Kotov, O. and Vikhlinin, A. (2005). XMM-Newton Observations of Evolution of Cluster X-Ray Scaling Relations at z=0.4-0.7. *The Astrophysical Journal*, 633:781–790. 52, 53

Kotov, O. and Vikhlinin, A. (2006). Chandra Sample of Galaxy Clusters at z = 0.4-0.55: Evolution in the Mass-Temperature Relation. *The Astrophysical Journal*, 641:752–755. 52, 53

Kravtsov, A. V., Nagai, D., and Vikhlinin, A. A. (2005). Effects of Cooling and Star Formation on the Baryon Fractions in Clusters. *The Astrophysical Journal*, 625:588–598. 65

Kravtsov, A. V., Vikhlinin, A., and Nagai, D. (2006). A New Robust Low-Scatter X-Ray Mass Indicator for Clusters of Galaxies. *The Astrophysical Journal*, 650:128–136. 3, 7

Krick, J. E., Bernstein, R. A., and Pimbblet, K. A. (2006). Diffuse Optical Light in Galaxy Clusters. I. Abell 3888. 131:168–184. 73

Laganá, T. F., Lima Neto, G. B., Andrade-Santos, F., and Cypriano, E. S. (2008). Star formation efficiency in galaxy clusters. 485:633–644. 74

LaRoque, S. J., Bonamente, M., Carlstrom, J. E., Joy, M. K., Nagai, D., Reese, E. D., and Dawson, K. S. (2006). X-Ray and Sunyaev-Zel'dovich Effect Measurements of the Gas Mass Fraction in Galaxy Clusters. 652:917–936. 59

Larson, D., Dunkley, J., Hinshaw, G., Komatsu, E., Nolta, M. R., Bennett, C. L., Gold, B., Halpern, M., Hill, R. S., Jarosik, N., Kogut, A., Limon, M., Meyer, S. S., Odegard, N., Page, L., Smith, K. M., Spergel, D. N., Tucker, G. S., Weiland, J. L., Wollack, E., and Wright, E. L. (2011). Seven-year Wilkinson Microwave Anisotropy Probe (WMAP) Observations: Power Spectra and WMAP-derived Parameters. *Astrophysical Journal, Supplement*, 192:16–+. viii, 14

Lloyd-Davies, E. J., Ponman, T. J., and Cannon, D. B. (2000). The entropy and energy of intergalactic gas in galaxy clusters. *Monthly Notices of the Royal Astronomical Society*, 315:689–702. 6, 34, 123

Lloyd-Davies, E. J., Romer, A. K., Hosmer, M., Mehrtens, N., Davidson, M., Sabirli, K., Mann, R. G., Hilton, M., Liddle, A. R., Viana, P. T. P., Campbell, H. C., Collins, C. A., Dubois, E. N., Freeman, P., Hoyle, B., Kay, S. T., Kuwertz, E., Miller, C. J., Nichol, R. C., Sahlen, M., Stanford, S. A., and Stott, J. P. (2010). The XMM Cluster Survey: X-ray analysis methodology. *ArXiv e-prints*. 4

Lucy, L. B. (1977). A numerical approach to the testing of the fission hypothesis. *Astronomical Journal*, 82:1013–1024. 26

Lumb, D. H., Bartlett, J. G., Romer, A. K., Blanchard, A., Burke, D. J., Collins, C. A., Nichol, R. C., Giard, M., Marty, P. B., Nevalainen, J., Sadat, R., and Vauclair, S. C. (2004). The XMM-NEWTON Ω project. I. The X-ray luminosity-temperature relation at z¿0.4. *Astronomy and Astrophysics*, 420:853–872. 53

Mantz, A., Allen, S. W., Ebeling, H., Rapetti, D., and Drlica-Wagner, A. (2010a). The observed growth of massive galaxy clusters - II. X-ray scaling relations. *Monthly Notices of the Royal Astronomical Society*, 406:1773–1795. 59

Mantz, A., Allen, S. W., Rapetti, D., and Ebeling, H. (2010b). The observed growth of massive galaxy clusters - I. Statistical methods and cosmological constraints. *Monthly Notices of the Royal Astronomical Society*, 406:1759–1772. 59

Markevitch, M. (1998). The L X-T Relation and Temperature Function for Nearby Clusters Revisited. *The Astrophysical Journal*, 504:27–+. 144

Markevitch, M., Gonzalez, A. H., Clowe, D., Vikhlinin, A., Forman, W., Jones, C., Murray, S., and Tucker, W. (2004). Direct Constraints on the Dark Matter Self-Interaction Cross Section from the Merging Galaxy Cluster 1E 0657-56. *The Astrophysical Journal*, 606:819–824. 6

Maughan, B. J. (2007). The $L_X - Y_X$ Relation: Using Galaxy Cluster X-Ray Luminosity as a Robust, Low-Scatter Mass Proxy. *The Astrophysical Journal*, 668:772–780. 3, 7, 52, 53, 126, 145

Maughan, B. J., Jones, C., Forman, W., and Van Speybroeck, L. (2008). Images, Structural Properties, and Metal Abundances of Galaxy Clusters Observed with Chandra ACIS-I at 0.1<z<1.3. *Astrophysical Journal, Supplement*, 174:117–135. 53, 56, 57, 80, 82, 83, 84, 86, 87, 90, 114, 148

Maughan, B. J., Jones, L. R., Ebeling, H., and Scharf, C. (2006). The evolution of the cluster X-ray scaling relations in the Wide Angle ROSAT Pointed Survey sample at 0.6¡z¡1.0. *Monthly Notices of the Royal Astronomical Society*, 365:509–529. 52, 53

Mazzotta, P., Rasia, E., Moscardini, L., and Tormen, G. (2004). Comparing the temperatures of galaxy clusters from hydrodynamical N-body simulations to Chandra and XMM-Newton observations. 354:10–24. 38

McCarthy, I. G., Babul, A., Bower, R. G., and Balogh, M. L. (2008). Towards a holistic view of the heating and cooling of the intracluster medium. *Monthly Notices of the Royal Astronomical Society*, 386:1309–1331. 30

McCarthy, I. G., Bower, R. G., and Balogh, M. L. (2007). Revisiting the baryon fractions of galaxy clusters: a comparison with WMAP 3-yr results. *Monthly Notices of the Royal Astronomical Society*, 377:1457–1463. 92, 93, 111, 148

Meneghetti, M., Rasia, E., Merten, J., Bellagamba, F., Ettori, S., Mazzotta, P., Dolag, K., and Marri, S. (2010). Weighing simulated galaxy clusters using lensing and X-ray. *Astronomy and Astrophysics*, 514:A93+. 83

Messier, C. (1784). *Connaissance des Temps*. 3

Mo, H. J., Yang, X., van den Bosch, F. C., and Katz, N. (2005). Pre-heating by previrialization and its impact on galaxy formation. 363:1155–1166. 77

Monaghan, J. J. (2005). Smoothed particle hydrodynamics. *Reports on Progress in Physics*, 68(8):1703. 27

Monaghan, J. J. and Gingold, R. A. (1983). Shock Simulation by the Particle Method SPH. *Journal of Computational Physics*, 52:374–+. 28

Monaghan, J. J. and Lattanzio, J. C. (1985). A refined particle method for astrophysical problems. *Astronomy and Astrophysics*, 149:135–143. 26

Morandi, A., Ettori, S., and Moscardini, L. (2007). X-ray and Sunyaev-Zel'dovich scaling relations in galaxy clusters. *Monthly Notices of the Royal Astronomical Society*, 379:518–534. 52, 53

Motl, P. M., Burns, J. O., Loken, C., Norman, M. L., and Bryan, G. (2004). Formation of Cool Cores in Galaxy Clusters via Hierarchical Mergers. *The Astrophysical Journal*, 606:635–653. 9, 29

Muanwong, O., Kay, S. T., and Thomas, P. A. (2006). Evolution of X-Ray Cluster Scaling Relations in Simulations with Radiative Cooling and Nongravitational Heating. 649:640–648. 9, 30, 31, 33, 124

Muanwong, O., Thomas, P. A., Kay, S. T., and Pearce, F. R. (2002). The effect of cooling and preheating on the X-ray properties of clusters of galaxies. 336:527–540. 9, 29, 30

Muanwong, O., Thomas, P. A., Kay, S. T., Pearce, F. R., and Couchman, H. M. P. (2001). The Effect of Radiative Cooling on Scaling Laws of X-Ray Groups and Clusters. *The Astrophysical Journal, Letters*, 552:L27–L30. 9, 29

Nagai, D., Kravtsov, A. V., and Vikhlinin, A. (2007). Effects of Galaxy Formation on Thermodynamics of the Intracluster Medium. 668:1–14. 75, 83

Navarro, J. F., Frenk, C. S., and White, S. D. M. (1995). Simulations of X-ray clusters. 275:720–740. 9, 21, 29, 33, 103

Navarro, J. F., Frenk, C. S., and White, S. D. M. (1997). A Universal Density Profile from Hierarchical Clustering. 490:493–+. 8, 169

O'Hara, T. B., Mohr, J. J., Bialek, J. J., and Evrard, A. E. (2006). Effects of Mergers and Core Structure on the Bulk Properties of Nearby Galaxy Clusters. *The Astrophysical Journal*, 639:64–80. 7, 143

Pacaud, F., Pierre, M., Adami, C., Altieri, B., Andreon, S., Chiappetti, L., Detal, A., Duc, P., Galaz, G., Gueguen, A., Le Fèvre, J., Hertling, G., Libbrecht, C., Melin, J., Ponman, T. J., Quintana, H., Refregier, A., Sprimont, P., Surdej, J., Valtchanov, I.,

Willis, J. P., Alloin, D., Birkinshaw, M., Bremer, M. N., Garcet, O., Jean, C., Jones, L. R., Le Fèvre, O., Maccagni, D., Mazure, A., Proust, D., Röttgering, H. J. A., and Trinchieri, G. (2007). The XMM-LSS survey: the Class 1 cluster sample over the initial 5deg^2 and its cosmological modelling. *Monthly Notices of the Royal Astronomical Society*, 382:1289–1308. 52, 53

Peacock, J. (1999). *Cosmological Physics*. Cambridge University Press, Cambridge, U.K.; New York, U.S.A. 17

Pearce, F. R., Thomas, P. A., and Couchman, H. M. P. (1994). Head-On Mergers of Systems Containing Gas. 268:953–+. 60

Pearce, F. R., Thomas, P. A., Couchman, H. M. P., and Edge, A. C. (2000). The effect of radiative cooling on the X-ray properties of galaxy clusters. *Monthly Notices of the Royal Astronomical Society*, 317:1029–1040. 9, 29, 114

Peebles, P. J. E. (1970). Structure of the Coma Cluster of Galaxies. *Astronomical Journal*, 75:13–+. 8

Peebles, P. J. E. (1983). The sequence of cosmogony and the nature of primeval departures from homogeneity. *The Astrophysical Journal*, 274:1–6. 8

Peebles, P. J. E. (1993). *Principles of Physical Cosmology*. Princeton University Press. 15

Peterson, J. R. and Fabian, A. C. (2006). X-ray spectroscopy of cooling clusters. *Physics Reports*, 427:1–39. 126

Piffaretti, R. and Valdarnini, R. (2008). Total mass biases in X-ray galaxy clusters. *Astronomy and Astrophysics*, 491:71–87. 83

Ponman, T. J., Cannon, D. B., and Navarro, J. F. (1999). The thermal imprint of galaxy formation on X-ray clusters. *Nature*, 397:135–137. 6, 34, 123

Poole, G. B., Babul, A., McCarthy, I. G., Fardal, M. A., Bildfell, C. J., Quinn, T., and Mahdavi, A. (2007). The impact of mergers on relaxed X-ray clusters - II. Effects on global X-ray and Sunyaev-Zel'dovich properties and their scaling relations. *Monthly Notices of the Royal Astronomical Society*, 380:437–454. 3, 7

Pratt, G. W., Arnaud, M., Piffaretti, R., Boehringer, H., Ponman, T. J., Croston, J. H., Voit, G. M., Borgani, S., and Bower, R. G. (2009a). Gas entropy in a representative sample of nearby X-ray galaxy clusters (REXCESS): relationship to gas mass fraction.

ArXiv e-prints. x, xii, 5, 62, 64, 70, 89, 114, 115, 117, 119, 120, 126, 130, 132, 134, 136, 145, 147, 149

Pratt, G. W., Croston, J. H., Arnaud, M., and Böhringer, H. (2009b). Galaxy cluster X-ray luminosity scaling relations from a representative local sample (REXCESS). *Astronomy and Astrophysics*, 498:361–378. 6, 29, 42, 43, 45, 46, 48, 53, 56, 57

Predehl, P., Hasinger, G., Böhringer, H., Briel, U., Brunner, H., Churazov, E., Freyberg, M., Friedrich, P., Kendziorra, E., Lutz, D., Meidinger, N., Pavlinsky, M., Pfeffermann, E., Santangelo, A., Schmitt, J., Schuecker, P., Schwope, A., Steinmetz, M., Strüder, L., Sunyaev, R., and Wilms, J. (2006). eROSITA. In *Society of Photo-Optical Instrumentation Engineers (SPIE) Conference Series*, volume 6266 of *Society of Photo-Optical Instrumentation Engineers (SPIE) Conference Series*. 4

Puchwein, E., Sijacki, D., and Springel, V. (2009). Simulations of AGN Feedback in Galaxy Clusters and Groups. In S. Heinz & E. Wilcots, editor, *American Institute of Physics Conference Series*, volume 1201 of *American Institute of Physics Conference Series*, pages 297–300. 30

Puchwein, E., Springel, V., Sijacki, D., and Dolag, K. (2010). Intracluster stars in simulations with AGN feedback. *ArXiv e-prints: 1001.3018*. 30, 75

Quinn, P. J., Salmon, J. K., and Zurek, W. H. (1986). Primordial density fluctuations and the structure of galactic haloes. *Nature*, 322:329–335. 8

Rasia, E., Ettori, S., Moscardini, L., Mazzotta, P., Borgani, S., Dolag, K., Tormen, G., Cheng, L. M., and Diaferio, A. (2006). Systematics in the X-ray cluster mass estimators. *Monthly Notices of the Royal Astronomical Society*, 369:2013–2024. 83

Reiprich, T. H. and Böhringer, H. (2002). The Mass Function of an X-Ray Flux-limited Sample of Galaxy Clusters. *The Astrophysical Journal*, 567:716–740. 6

Ritchie, B. W. and Thomas, P. A. (2001). Multiphase smoothed-particle hydrodynamics. *Monthly Notices of the Royal Astronomical Society*, 323:743–756. 27

Rowley, D. R., Thomas, P. A., and Kay, S. T. (2004). The merger history of clusters and its effect on the X-ray properties of the intracluster medium. *Monthly Notices of the Royal Astronomical Society*, 352:508–522. 7

Sadat, R., Blanchard, A., Vauclair, S. C., Lumb, D. H., Bartlett, J., Romer, A. K., Bernard, J.-P., Boer, M., Marty, P., Nevalainen, J., Burke, D. J., Collins, C. A., and

Nichol, R. C. (2005). The XMM-Newton Ω project. *Astronomy and Astrophysics*, 437:31–38. 59

Salomé, P., Combes, F., Edge, A. C., Crawford, C., Erlund, M., Fabian, A. C., Hatch, N. A., Johnstone, R. M., Sanders, J. S., and Wilman, R. J. (2006). Cold molecular gas in the Perseus cluster core. Association with X-ray cavity, Hα filaments and cooling flow. *Astronomy and Astrophysics*, 454:437–445. 116

Sanderson, A. J. R., O'Sullivan, E., and Ponman, T. J. (2009). A statistically selected Chandra sample of 20 galaxy clusters - II. Gas properties and cool core/non-cool core bimodality. *Monthly Notices of the Royal Astronomical Society*, 395:764–776. 114, 126, 128, 137

Sanderson, A. J. R., Ponman, T. J., Finoguenov, A., Lloyd-Davies, E. J., and Markevitch, M. (2003). The Birmingham-CfA cluster scaling project - I. Gas fraction and the $M-T_X$ relation. *Monthly Notices of the Royal Astronomical Society*, 340:989–1010. 69, 70, 72

Seljak, U. and Zaldarriaga, M. (1996). A Line-of-Sight Integration Approach to Cosmic Microwave Background Anisotropies. *The Astrophysical Journal*, 469:437–+. 32

Short, C. J. and Thomas, P. A. (2009). Combining Semianalytic Models with Simulations of Galaxy Clusters: The Need for Heating from Active Galactic Nuclei. 704:915–929. 32, 35, 37, 114, 145

Short, C. J., Thomas, P. A., Young, O. E., Pearce, F. R., Jenkins, A., and Muanwong, O. (2010). The evolution of galaxy cluster X-ray scaling relations. *Monthly Notices of the Royal Astronomical Society*, 408:2213–2233. 51

Sijacki, D., Pfrommer, C., Springel, V., and Enßlin, T. A. (2008). Simulations of cosmic-ray feedback by active galactic nuclei in galaxy clusters. *Monthly Notices of the Royal Astronomical Society*, 387:1403–1415. 30

Somerville, R. S., Hopkins, P. F., Cox, T. J., Robertson, B. E., and Hernquist, L. (2008). A semi-analytic model for the co-evolution of galaxies, black holes and active galactic nuclei. *Monthly Notices of the Royal Astronomical Society*, 391:481–506. 35

Spergel, D. N., Bean, R., Doré, O., Nolta, M. R., Bennett, C. L., Dunkley, J., Hinshaw, G., Jarosik, N., Komatsu, E., Page, L., Peiris, H. V., Verde, L., Halpern, M., Hill, R. S., Kogut, A., Limon, M., Meyer, S. S., Odegard, N., Tucker, G. S., Weiland, J. L., Wollack, E., and Wright, E. L. (2007). Three-Year Wilkinson Microwave Anisotropy

Probe (WMAP) Observations: Implications for Cosmology. *Astrophysical Journal, Supplement*, 170:377–408. 13

Springel, V. (2005). The cosmological simulation code GADGET-2. *Monthly Notices of the Royal Astronomical Society*, 364:1105–1134. 22, 33

Springel, V. and Hernquist, L. (2003). Cosmological smoothed particle hydrodynamics simulations: a hybrid multiphase model for star formation. *Monthly Notices of the Royal Astronomical Society*, 339:289–311. 27, 30

Springel, V., White, S. D. M., Jenkins, A., Frenk, C. S., Yoshida, N., Gao, L., Navarro, J., Thacker, R., Croton, D., Helly, J., Peacock, J. A., Cole, S., Thomas, P., Couchman, H., Evrard, A., Colberg, J., and Pearce, F. (2005). Simulations of the formation, evolution and clustering of galaxies and quasars. 435:629–636. viii, 8, 25, 32, 97

Springel, V., White, S. D. M., Tormen, G., and Kauffmann, G. (2001). Populating a cluster of galaxies - I. Results at [formmu2]z=0. *Monthly Notices of the Royal Astronomical Society*, 328:726–750. 97

Stadel, J. G. (2001). *Cosmological N-body simulations and their analysis*. PhD thesis, UNIVERSITY OF WASHINGTON. 24

Stanek, R., Rasia, E., Evrard, A. E., Pearce, F., and Gazzola, L. (2010). Massive Halos in Millennium Gas Simulations: Multivariate Scaling Relations. 715:1508–1523. 33, 77

Sun, M., Voit, G. M., Donahue, M., Jones, C., Forman, W., and Vikhlinin, A. (2009). Chandra Studies of the X-Ray Gas Properties of Galaxy Groups. *The Astrophysical Journal*, 693:1142–1172. 43, 47, 69, 70, 72, 74

Sunyaev, R. A. and Zel'dovich, Y. B. (1970). Small-Scale Fluctuations of Relic Radiation. *Astrophysics and Space Science*, 7:3–19. 6

Sutherland, R. S. and Dopita, M. A. (1993). Cooling functions for low-density astrophysical plasmas. 88:253–327. 34, 39

Thomas, P. A. and Couchman, H. M. P. (1992). Simulating the formation of a cluster of galaxies. *Monthly Notices of the Royal Astronomical Society*, 257:11–31. 33

Tittley, E. R. and Couchman, H. M. P. (2000). Hierarchical clustering and the baryon distribution in galaxy clusters. *Monthly Notices of the Royal Astronomical Society*, 315:834–838. 101, 103, 105

Tormen, G., Bouchet, F. R., and White, S. D. M. (1997). The structure and dynamical evolution of dark matter haloes. *Monthly Notices of the Royal Astronomical Society*, 286:865–884. 8

Tozzi, P., Rosati, P., Ettori, S., Borgani, S., Mainieri, V., and Norman, C. (2003). Iron Abundance in the Intracluster Medium at High Redshift. 593:705–720. 34

van Albada, G. B. (1961). Evolution of clusters of galaxies under gravitational forces. *Astronomical Journal*, 66:590–+. 1

Viana, P. T. P., Kay, S. T., Liddle, A. R., Muanwong, O., and Thomas, P. A. (2003). The power spectrum amplitude from clusters revisited: σ_8 using simulations with pre-heating and cooling. *Monthly Notices of the Royal Astronomical Society*, 346:319–326. 9, 30

Vikhlinin, A., Burenin, R. A., Ebeling, H., Forman, W. R., Hornstrup, A., Jones, C., Kravtsov, A. V., Murray, S. S., Nagai, D., Quintana, H., and Voevodkin, A. (2009). Chandra Cluster Cosmology Project. II. Samples and X-Ray Data Reduction. 692:1033–1059. 6, 7

Vikhlinin, A., Kravtsov, A., Forman, W., Jones, C., Markevitch, M., Murray, S. S., and Van Speybroeck, L. (2006). Chandra Sample of Nearby Relaxed Galaxy Clusters: Mass, Gas Fraction, and Mass-Temperature Relation. *The Astrophysical Journal*, 640:691–709. 50, 62, 63, 69, 70, 72, 74, 80, 89, 92, 118, 139, 147

Vikhlinin, A., van Speybroeck, L., Markevitch, M., Forman, W. R., and Grego, L. (2002). Evolution of the Cluster X-Ray Scaling Relations since z¿0.4. *The Astrophysical Journal, Letters*, 578:L107–L111. 53

Viola, M., Monaco, P., Borgani, S., Murante, G., and Tornatore, L. (2007). How does gas cool in DM halos? *ArXiv e-prints*, 710. 9, 29

Voit, G. M., Kay, S. T., and Bryan, G. L. (2005). The baseline intracluster entropy profile from gravitational structure formation. 364:909–916. 33

Warren, M. S., Quinn, P. J., Salmon, J. K., and Zurek, W. H. (1992). Dark halos formed via dissipationless collapse. I - Shapes and alignment of angular momentum. *The Astrophysical Journal*, 399:405–425. 8

Weinberg, S. (1972). *Gravitation and Cosmology: Principles and Applications of the General Theory of Relativity*. 12

Weiner, B. J., Coil, A. L., Prochaska, J. X., Newman, J. A., Cooper, M. C., Bundy, K., Conselice, C. J., Dutton, A. A., Faber, S. M., Koo, D. C., Lotz, J. M., Rieke, G. H., and Rubin, K. H. R. (2009). Ubiquitous Outflows in DEEP2 Spectra of Star-Forming Galaxies at z = 1.4. 692:187–211. 34

Weisskopf, M. C., Brinkman, B., Canizares, C., Garmire, G., Murray, S., and Van Speybroeck, L. P. (2002). An Overview of the Performance and Scientific Results from the Chandra X-Ray Observatory. *Publications of the ASP*, 114:1–24. 4

White, D. A., Jones, C., and Forman, W. (1997). An investigation of cooling flows and general cluster properties from an X-ray image deprojection analysis of 207 clusters of galaxies. *Monthly Notices of the Royal Astronomical Society*, 292:419–+. 29

White, S. D. M. (1976). The dynamics of rich clusters of galaxies. *Monthly Notices of the Royal Astronomical Society*, 177:717–733. 8

White, S. D. M., Navarro, J. F., Evrard, A. E., and Frenk, C. S. (1993). The baryon content of galaxy clusters: a challenge to cosmological orthodoxy. *Nature*, 366:429–433. 92

Wu, X., Xue, Y., and Fang, L. (1999). The $L_X - T$ and $L_X - \sigma$ Relationships for Galaxy Clusters Revisited. *The Astrophysical Journal*, 524:22–30. 6

Young, O. E., Thomas, P. A., Short, C. J., and Pearce, F. (2011). Baryon fractions in clusters of galaxies: evidence against a pre-heating model for entropy generation. *Monthly Notices of the Royal Astronomical Society*, pages 127–+. 59

Zel'Dovich, Y. B. (1970). Gravitational instability: An approximate theory for large density perturbations. *Astronomy and Astrophysics*, 5:84–89. 28

Zibetti, S., White, S. D. M., Schneider, D. P., and Brinkmann, J. (2005). Intergalactic stars in z˜ 0.25 galaxy clusters: systematic properties from stacking of Sloan Digital Sky Survey imaging data. 358:949–967. 73

Appendix A

Mass determination via hydrostatic equilibrium

Since

$$\frac{1}{\rho} = -\frac{GM(r)}{r^2}$$

and

$$P = \frac{\rho}{\mu m_H} kT,$$

$$M(r) = -\frac{r^2}{G\rho}\frac{\mathrm{d}}{\mathrm{d}r}\left(\frac{\rho kT}{\mu m_H}\right)$$

$$\Rightarrow M(r) = -\frac{r^2 k}{G\rho\mu m_H}\left(T\frac{\mathrm{d}\rho}{\mathrm{d}r} + \rho\frac{\mathrm{d}T}{\mathrm{d}r}\right)$$

$$\Rightarrow M(r) = -\frac{r^2 k}{G\mu m_H} T\left(\frac{1}{\rho}\frac{\mathrm{d}\rho}{\mathrm{d}r} + \frac{1}{T}\frac{\mathrm{d}T}{\mathrm{d}r}\right)$$

$$\Rightarrow M(r) = -\frac{kTr}{G\mu m_H}\left(\frac{\mathrm{d}\log\rho}{\mathrm{d}\log r} + \frac{\mathrm{d}\log T}{\mathrm{d}\log r}\right)$$

Appendix B

Measuring cluster concentration

The central concentration of clusters can be determined by measuring the mass at two different over-densities, for example M_{2500} and M_{500}. Together, these uniquely determine the parameters of the NFW profile (Navarro et al., 1997) without any need to fit the profile as a function of radius.[1] To test the effectiveness of this procedure, we show in Figure B.1 the value of r_{200} predicted by the NFW fit (i.e. the NFW scale radius, a, times the concentration, x_{200}) versus the actual value. As can be seen, the two agree very well, confirming that the clusters are well-fit by the NFW profile out to this radius.

Cluster concentrations are often thought to have a dependence upon cluster mass, with more massive clusters having lower concentrations. That is indeed the case, but we find a much stronger correlation with cluster formation time, as illustrated in Figure B.2. Here the formation time is taken to be the value of the expansion factor when the total mass of all the subhalos that will go on to make up the cluster equal one fifth of the final cluster mass, but other definitions give similar correlations. We plot expansion factor rather than age as this gives a more linear correlation. The results are shown here for the GO simulation; those for the PC and FO runs are very slightly different because of the contribution of the baryons to the total mass.

On removing the best-fitting correlation (shown as a solid line in the figure), the residual concentration shows no dependence on mass. The correlation with mass is thus a secondary one that follows because low mass clusters tend to form at lower expansion factors than more massive ones.

[1] We provide IDL routines to do this at `http://astronomy.susx.ac.uk/~petert/nfw.pro`.

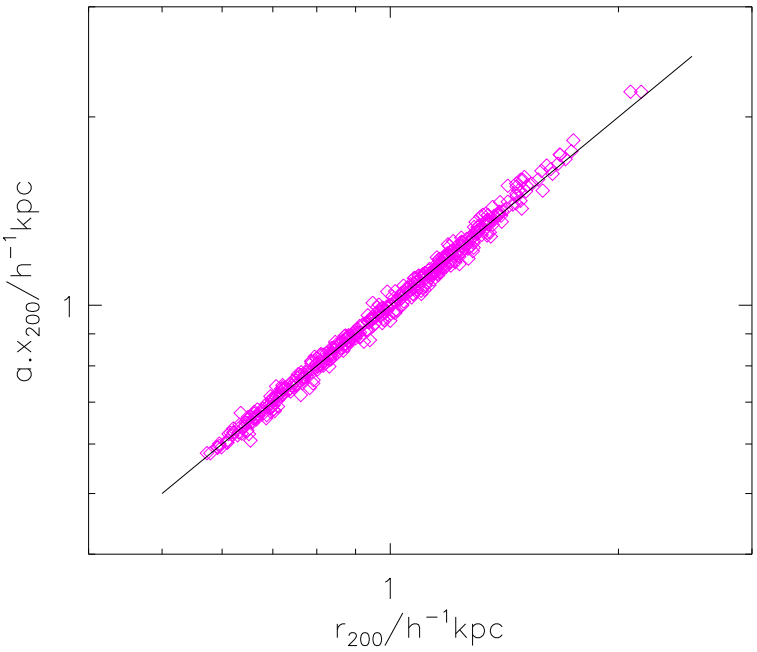

Figure B.1: The abscissa shows the actual value of r_{200} for each of the clusters, whilst the ordinate shows the value predicted from M_{2500} and M_{500} assuming an NFW profile.

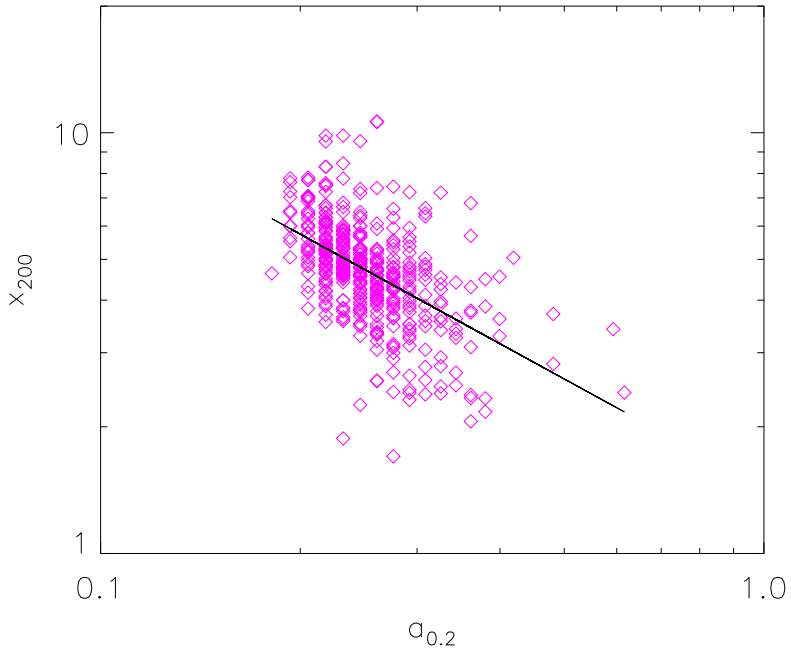

Figure B.2: Cluster concentration versus the expansion factor at the time that the clusters have accumulated one fifth of their final mass. The solid line shows the best-fitting power-law correlation.

Appendix C

IDL code for minimising scatter

An IDL routine to reduce the scatter in a variable with respect to a group of others by solving equation 5.7

```
pro minimise,data,dimension

; A program to minimise the variation in a given dimension of your
; data.

; data should be a 2-d matrix
; dimension should be an integer



; Determine the means for all the fields in the data set
dimen=size(data,/dimen)
Nobj=dimen[0] ;& Mattr=dimen[1]

column_mean=total(data,1)/Nobj
temp=replicate(1.0,Nobj)
X=(data-temp # transpose(column_mean))

; now have a matrix at which each data point is x_i - mean(x)_i
; Form a pseudo-covariance matrix.
Xi=X[*,dimension] ; column vector being the dimension column of X
; put something in here in case you want to look at the first or last column
if dimension ne 0 and dimension ne n_elements(X[0,*])-1 then begin
```

```
   Xj1=X[*,0:dimension-1]
   Xj2=X[*,dimension+1:n_elements(X[0,*])-1]
   Xj=[[Xj1],[Xj2]]
endif
if dimension eq 0 then Xj=X[*,1:n_elements(X[0,*])-1]

if dimension eq n_elements(X[0,*])-1 then Xj=X[*,0:n_elements(X[0,*])-2]



A=dblarr(n_elements(Xj[0,*]),n_elements(Xj[0,*]))
B=dblarr(n_elements(Xj[0,*]))

A=Xj ## transpose(Xj)
B=Xi ## transpose(Xj)

choldc,A,p,/double
alpha=cholsol(A,p,B,/double)
print,alpha
print,'std(Xi)=',stddev(Xi)
Xi_new=Xi-Xj#alpha
help,Xi_new
;plot alpha times variable
print,'std(Xi_new)=',stddev(Xi_new)
end
```

Appendix D

Formation time queries

To select the snapshot at which the main progenitor acquired at least a given fraction of the final halo's mass:

```
select DES.haloId as des_id,
min(PROG.snapnum)-1 as snapnum_half
        from   MPAHaloTrees..MHalo DES,
        MPAHaloTrees..MHalo PROG
        where
         DES.snapnum = 63 and
DES.np>20000 and
PROG.haloId between DES.firstProgenitorID and DES.lastProgenitorId and
PROG.np > $fraction*DES.np
   group by DES.haloID
```

To select the snapshot at which the total mass of the progenitors is a given fraction of the final halo's mass:

```
select L.haloID as haloId,
       min(L.snapnum) as snapnum
into   HalfMass
from   (select DES.haloId as haloId,
               DES.np as npDes,
               PROG.snapnum as snapnum,
               sum(PROG.np) as npSum
        from   MPAHaloTrees..MHalo DES,
```

```
            MPAHaloTrees..MHalo PROG
      where  DES.snapnum = 63
         and DES.ix between 0 and 4
         and DES.np>20000
         and PROG.haloId between DES.haloId and DES.lastProgenitorId
      group by Des.HaloId,
            DES.np,
            PROG.snapnum) L
where  L.npSum > $fraction*L.npDes
group by L.haloID
```

Appendix E

SQL halo merger query

An SQL query to return the time of a cluster's last major merger.

```
select DES.haloId as haloId,
       max(PROG2.snapnum) as snapnum
into   HalfMassJump
from   MPAHaloTrees..MHalo DES,
       MPAHaloTrees..MHalo PROG1,
       MPAHaloTrees..MHalo PROG2
where  DES.snapnum = 63
   and DES.np>20000
   and PROG1.haloId between DES.haloId and DES.lastProgenitorId
   and PROG1.haloId = DES.haloId + 63 - PROG1.snapnum
   and PROG2.haloId between DES.haloId and DES.lastProgenitorId
   and PROG2.haloId = DES.haloId + 63 - PROG2.snapnum
   and PROG2.firstProgenitorId = Prog1.haloId
   and PROG1.np < 0.5*PROG2.np
group by DES.haloID
```